

010  
10110  
1010101  
010101010

# Technology for biocomputational devices based on molecular motors

FRIDA WILHELMINA LINDBERG  
DIVISION OF SOLID STATE PHYSICS | LUND UNIVERSITY

0011010101010  
01010101011101  
0010001010111  
010010111010  
11010110101  
0100101010  
101010





Technology for biocomputational devices based on molecular motors



# Technology for biocomputational devices based on molecular motors

*Doctoral thesis*

Frida Wilhelmina Lindberg



**LUND**  
UNIVERSITY

Division of Solid State Physics

Department of Physics

DOCTORAL DISSERTATION

by due permission of the Faculty of Engineering at Lund University, Sweden.  
To be publicly defended on Friday, June 7<sup>th</sup>, 2019 at 09:15 in Rydbergsalen,  
Sölvegatan 14, Lund, for the degree of Doctor of Philosophy.

*Faculty opponent*

Dr. Mihai Irimia-Vladu  
Joanneum Research

<b>Organization</b> LUND UNIVERSITY  Division of Solid State Physics Department of Physics P.O. Box 118, SE-221 00 Lund, Sweden	<b>Document name: DOCTORAL DISSERTATION</b>
	<b>Date of issue: 2019-04-25</b>  Author: Frida Wilhelmina Lindberg
<b>Title and subtitle: Technology for biocomputational devices based on molecular motors</b>	
<b>Abstract:</b>  For many multivariable problems there are no efficient algorithms for finding solutions. To this day, conventional electronic computers mainly solve problems in a sequential manner. This sequential operation prevents problem-solving within a reasonable time-frame due to superpolynomial, and sometimes even exponential, time complexities. Developing powerful parallel computation techniques has therefore gained increasing attention in science and industry to overcome this fundamental limitation.  This thesis is aimed towards developing network-based biocomputation using molecular motors for solving combinatorial problems in a massively parallel manner. Molecular motors have been previously used to compute a small scale subset sum problem encoded into a network of channels and junctions <sup>1</sup> . Here we tackle some of the engineering requirements of upscaling this system. Specifically, we have developed reliable surface treatments for chemical modification, the regeneration of surfaces for a more sustainable fabrication process, the development of high throughput fabrication with nanometre scale resolution, the design optimisation of the graphical encoding and the development of two architectural elements: programmable gates for versatile networks, and electric sensors for label free detection of filaments.  We show how the material chemistry of molecular motor devices can be altered in a controlled way to ensure selective protein binding, only promoting motility in designated areas. To reuse these devices, we developed a method to regenerate the surfaces with a non-destructive approach, which prolongs their life-time and enables them to be used multiple times. We also present a new device system using two new polymer resists with tuneable motility properties.  To be able to fabricate large-scale, high-resolution devices within a reasonable time-frame we optimised the patterning parameters for electron beam lithography. We also show that nanoimprint lithography can be used as a high-throughput, high-resolution fabrication method to pattern the type of structures needed for molecular motor devices. By adjusting the structural design and imprinting parameters we are able to fabricate high aspect ratio patterns that successfully promote motility.  We also demonstrate a method of translating the exact cover problem into the subset sum problem. We present the design optimisation of a large-scale network (~1000 solutions) encoding the two combinatorial problems mentioned, and our progress towards finding a solution using the molecular motor system actin-myosin II as exploratory agents.  Additionally, we describe a method of creating switchable motility to create programmable network-junctions to be able to compute different mathematical encodings. Such dynamic encodings are a necessity for any viable computer. Finally, we present the advancements towards creating an electric sensor for detection of cytoskeletal filaments, using a carbon nanotube as a tripwire, to enable a reliable readout method for highly parallel problem solving.  We conclude with a discussion of future challenges and prospects for network-based biocomputation employing molecular motors in the light of our findings presented here.	
<b>Key words: Molecular motors, nanofabrication, biocomputation, nanostructures</b>	
<b>ISBN:</b> 978-91-7895-131-4 (print) 978-91-7895-132-1 (pdf)	<b>Language:</b> English

I, the undersigned, being the copyright owner of the abstract of the above-mentioned dissertation, hereby grant to all reference sources permission to publish and disseminate the abstract of the above-mentioned dissertation.

Signature 

Date 2019-04-25

# Technology for biocomputational devices based on molecular motors

Frida Wilhelmina Lindberg



**LUND**  
UNIVERSITY

Cover photo by Frida Wilhelmina Lindberg

Back cover photo by Ivan Maximov

pp 1-98 © Frida Wilhelmina Lindberg

Paper 1 © 2018 American Chemical Society (open access)

Paper 2 © 2019 Materials and Research Express (gold open access)

Paper 3 © by the Authors (Manuscript unpublished)

Paper 4 © by the Authors (Manuscript unpublished)

Paper 5 © by the Authors (Manuscript unpublished)

Faculty of Engineering  
Department of Physics  
Division of Solid State Physics

ISBN

978-91-7895-131-4 (print)

978-91-7895-132-1 (pdf)

Printed in Sweden by Media-Tryck, Lund University  
Lund 2019



Media-Tryck is an environmentally certified and ISO 14001:2015 certified provider of printed material. Read more about our environmental work at [www.mediatryck.lu.se](http://www.mediatryck.lu.se)

**MADE IN SWEDEN** 

*To my mother, who showed me how to climb  
Mount Everest without oxygen*

# Table of Contents

<b>Abstract</b> .....	<b>10</b>
<b>Populärvetenskaplig sammanfattning</b> .....	<b>12</b>
<b>Popular science summary</b> .....	<b>14</b>
<b>List of papers</b> .....	<b>16</b>
<b>Abbreviations</b> .....	<b>18</b>
<b>Acknowledgements</b> .....	<b>20</b>
<b>1 Introduction</b> .....	<b>22</b>
<b>2 Background</b> .....	<b>30</b>
2.1 Molecular motor proteins .....	30
2.1.1 The actin-myosin II system .....	31
2.1.2 The microtubule-kinesin system .....	34
2.2 Patterning techniques for molecular motor devices.....	35
2.2.1 Electron beam lithography.....	35
2.2.2 Nanoimprint lithography .....	37
2.3 Solving combinatorial problems .....	38
2.3.1 Alternative parallel computation techniques .....	39
2.3.2 Computing with molecular motors .....	40
<b>3 Surface treatment</b> .....	<b>41</b>
3.1 Motivation and previous work.....	41
3.2 Controlled surface modification (Paper I) .....	43
3.3 Investigation of new polymer resists .....	46
3.4 Surface regeneration (Paper IV) .....	49
3.5 Concluding remarks.....	54
<b>4 Patterning nanostructures</b> .....	<b>55</b>
4.1 Motivation and previous work.....	55
4.2 Process optimisation for EBL (Paper III) .....	56
4.3 NIL for molecular motor structures (Paper II).....	58
4.4 Concluding remarks.....	63

<b>5</b>	<b>Computing with molecular motors</b> .....	<b>64</b>
5.1	Motivation and previous work.....	64
5.2	Conversion of EXCOV into SSP.....	65
5.3	Introducing “reset” junctions.....	65
5.4	Reducing the network size.....	66
5.5	Implementing the 1000 solution network.....	68
5.6	Concluding remarks.....	72
<b>6</b>	<b>Architectural elements</b> .....	<b>73</b>
6.1	Motivation and previous work.....	73
6.1.1	Switchable junctions for programmable gating.....	73
6.1.2	Electric sensors for label free detection.....	74
6.2	Programmable gating (Paper V).....	75
6.3	Electrical detection.....	79
6.4	Concluding remarks.....	84
<b>7</b>	<b>Conclusions and outlook</b> .....	<b>85</b>
	<b>References</b> .....	<b>89</b>

# Abstract

For many multivariable problems there are no efficient algorithms for finding solutions. To this day, conventional electronic computers mainly solve problems in a sequential manner. This sequential operation prevents problem-solving within a reasonable time-frame due to superpolynomial, and sometimes even exponential, time complexities. Developing powerful parallel computation techniques has therefore gained increasing attention in science and industry to overcome this fundamental limitation.

This thesis is aimed towards developing network-based biocomputation using molecular motors for solving combinatorial problems in a massively parallel manner. Molecular motors have been previously used to compute a small scale subset sum problem encoded into a network of channels and junctions<sup>1</sup>. Here, we tackle some of the engineering requirements of upscaling this system. Specifically, we have developed; reliable surface treatments for chemical modification, the regeneration of surfaces for a more sustainable fabrication process, the development of high throughput fabrication with nanometre scale resolution, the design optimisation of the graphical encoding and the development of two architectural elements: programmable gates for versatile networks, and electric sensors for label free detection of filaments.

We show how the material chemistry of molecular motor devices can be altered in a controlled way to ensure selective protein binding, only promoting motility in designated areas. To reuse these devices, we developed a method to regenerate the surfaces with a non-destructive approach, which prolongs their life-time and enables them to be used multiple times. We also present a new device system using two new polymer resists with tuneable motility properties.

To be able to fabricate large-scale, high-resolution devices within a reasonable time-frame we optimised the patterning parameters for electron beam lithography. We also show that nanoimprint lithography can be used as a high-throughput, high-resolution fabrication method to pattern the type of structures needed for molecular motor devices. By adjusting the structural design and imprinting parameters we are able to fabricate high aspect ratio patterns that successfully promote motility.

We also demonstrate a method of translating the exact cover problem into the subset sum problem. We present the design optimisation of a large-scale network (~1000

solutions) encoding the two combinatorial problems mentioned, and our progress towards finding a solution using the molecular motor system actin-myosin II as exploratory agents.

Additionally, we describe a method of creating switchable motility to create programmable network-junctions to be able to compute different mathematical encodings. Such dynamic encodings are a necessity for any viable computer. Finally, we present the advancements towards creating an electric sensor for detection of cytoskeletal filaments, using a carbon nanotube as a tripwire, to enable a reliable readout method for highly parallel problem solving.

We conclude with a discussion of future challenges and prospects for network-based biocomputation with molecular motors in the light of our findings presented here.

# Populärvetenskaplig sammanfattning

Molekylära motorprotein är små biologiska motorer som kan liknas med vilken annan motor som helst i det att de omvandlar energi till rörelse. De finns överallt i våra celler och deras huvudroll är att organisera logistiken inne i cellerna. Många molekylära motorsystem består av två delar: ett spår och en motor som spatserar på spåret. Idag kan vi ta ut hela motorsystemet ur cellen och fästa motorerna på en valfri yta. Efter extraheringen, kan spåren klippas sönder till trådliknande filament, och om vi tillför motorerna bränsle kan de gripa tag i filamenten och transportera dem, ungefär som en rockstjärna som surfar på publikhavet.

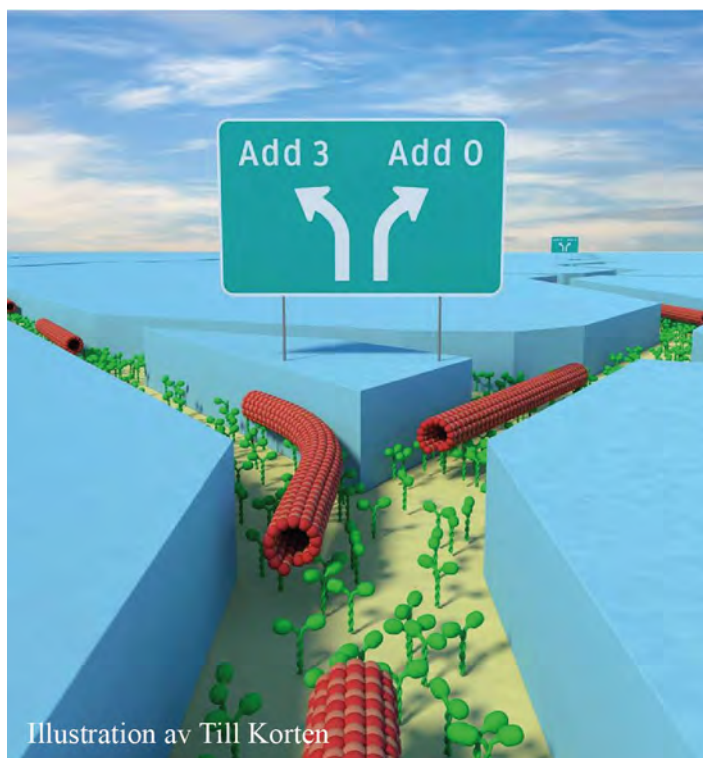
Det här är ju i sig själv ganska fascinerande, men vi skulle också vilja tillämpa det till något lite mer användbart i praktiken. Vad sägs om att försöka ge sig på ett riktigt, riktigt stort matematiskt problem som vanliga seriedatorer kämpar med att lösa? Sådana problem är exempelvis viktiga i optimeringen av rutter och elektriska kretsar, i kodknäckning och i skapandet av nya specifika läkemedel genom att man kan studera vilken form olika proteiner tar beroende på de ingående aminosyrorerna. Även om det låter näst intill otroligt, så är det faktiskt möjligt att utföra beräkningar med molekylära motorer och det är egentligen inte särskilt svårt. Tricket är att skapa en fysisk struktur av sitt matematiska problem, ungefär som en labyrint. Det är det vi kallar nätverksbaserad beräkning med molekylära motorer.

Nätverksbaserad beräkning med molekylära motorer består i princip bara av ett nätverk av sammansatta vägar, precis som vägarna vi kör våra bilar på. Filamenten matas in i ena änden av nätverket, eller vid särskilda positioner, och kan därefter komma ut vid olika platser beroende på vilken väg de väljer inne i nätverket. Varje rutt motsvarar olika beräkningar, och genom att filamenten går på upptäcktsfärd genom hela nätverket kan vi få reda på alla lösningar på en och samma gång. Givetvis gäller det då att vägarna är konstruerade på ett särskilt sätt så de verkligen kodar för olika beräkningar. Det gör vi bl. a. genom att tillsätta särskilda trafikregler som våra upptäcktsresande filament måste följa.

Nästa utmaning är att få våra filament att följa trafikreglerna. Genom att ha väldigt smala leder, kan vi skapa enkelriktade vägar där det inte går att göra U-svängar. Om vi istället breddar vägarna, öppnar vi upp för även mötande trafik. Vi kan också skapa rondeller och tillfälliga avspärningar som definierar vilka rutter som är tillåtna. Önskad svängar kan t.ex. motverkas genom att ha väldigt skarpa korsningar där filamenten bara fortsätter längs med den väg de kommer ifrån. Ett

ännu bättre sätt att förhindra oönskade svängar vore att använda sig av tunnelsystem med broar, men att implementera det kräver ytterligare teknikutveckling innan det är görbart. De mer drastiska avspärningarna kan användas för att ändra på vilka vägar som är tillgängliga. Detta innebär ju som tidigare skrivet, att vi ändrar på vilken beräkning vi utför, vilket gör hela nätverkssystemet flexibelt. Vi kan också skapa vägtullar som registrerar förbigående filament. Om dessa placeras vid de olika utgångarna kan vi registrera resultaten på våra beräkningar.

Som ni kanske redan misstänker så är molekylära motorer inte särskilt stora, vilket innebär att filamenten de driver behöver väldigt, väldigt små vägbanor. I den här avhandlingen beskriver jag hur dessa kan tillverkas med två olika metoder och hur vi selektivt kan placera våra motorer på gatorna inne i vår labyrint. Jag kommer att beskriva hur vi kan skapa reglerbara avspärningar som kan öppnas och stängas, och en tänkbar metod för att implementera elektriska tullar för att räkna förbigående filament. Dessutom kommer jag att beskriva hur vår labyrint ser ut i mer detalj och kommer att försöka förklara varför det är viktigt att utveckla parallella beräkningsmetoder som denna.



**Figur.** Röda filament på upptäcktsfärd genom ett nätverk. Filamenten transporteras ovanpå gröna molekylära motorer. Varje rutt i nätverket representerar en särskild beräkning, vilket innebär att vi kan finna alla lösningar parallellt.

# Popular science summary

Molecular motor proteins are small biological motors, similar to any other motor in that they convert energy into motion. They are omnipresent in our cells, and one of their main roles is to govern the logistics inside the cell. Many motor systems consist of two parts: a track and a motor walking on this track. Today, we can extract the entire motor system and glue the motors to a surface of our choice. Once extracted, the tracks can be cut up into filament-like structures and if we supply our motors with fuel, they're able to latch onto the filaments and kick them forward, like a crowd-surfing rock-star.

As fascinating as this is on its own, we would also like to apply this crowd-surfing to something practically useful. How about tackling a really, really big mathematical problem which our serially computing electronic computers struggle to calculate? Such problems are for instance important for optimising routes and circuits, to break encrypted codes and to create new specific target drugs by studying the shape of different protein compositions. Unbelievable as it may sound, it's actually possible to compute with molecular motors, and it's not really that complicated. The trick is to create a physical structure of this mathematical problem, sort of like a purposefully constructed maze. We call this network-based computation with molecular motors.

Network-based computation with molecular motors is in principle just a network of connected roads, just like the streets we drive our cars on. The filaments enter at a certain point and can exit at different streets depending on what pathway they select. Each street represents a different calculation, and so, by randomly exploring all possible paths we can solve the encoded problem in a massively parallel manner using our filaments as exploratory agents. Of course, the organisation of the streets is carefully designed and there are certain traffic rules that the agents have to obey.

So how can we make our agents follow traffic rules? By using very narrow roads, we can create one-way streets where U-turns are forbidden. If we broaden the streets however, also meeting traffic is allowed. Furthermore, we can implement roundabouts and roadblocks and define what paths are allowed and what paths are not. Turns can for instance be prevented by using very sharp crossing angles, causing agents to just pass straight by. An even better way to prevent turns would be to use tunnels and bridges, though implementing this requires further technology development. The more drastic roadblocks (or gates) can be used to change what

streets are accessible, which in turn means we change the calculation. We can also create check-points, similar to toll-stops or modern parking garages. These check-points don't do much more than register the passing of an exploring agent. However, if we place these check-points at the exiting streets, we can obtain information about what streets were accessible inside the network, which provides us with the correct solutions to the maze.

As you might have gathered already, molecular motors are not very large in size, meaning that the filaments they propel need very, very small roads. In this thesis I describe how we can build these small roads using two different methods and how we can selectively place our motors inside our maze of streets. I describe how we can create switchable roadblocks that can be opened and closed, and I describe our progress toward implementing electric check-points for detecting passing filaments. Furthermore, I describe the maze layout in more detail and explain why it is important to develop parallel computation techniques such as this.

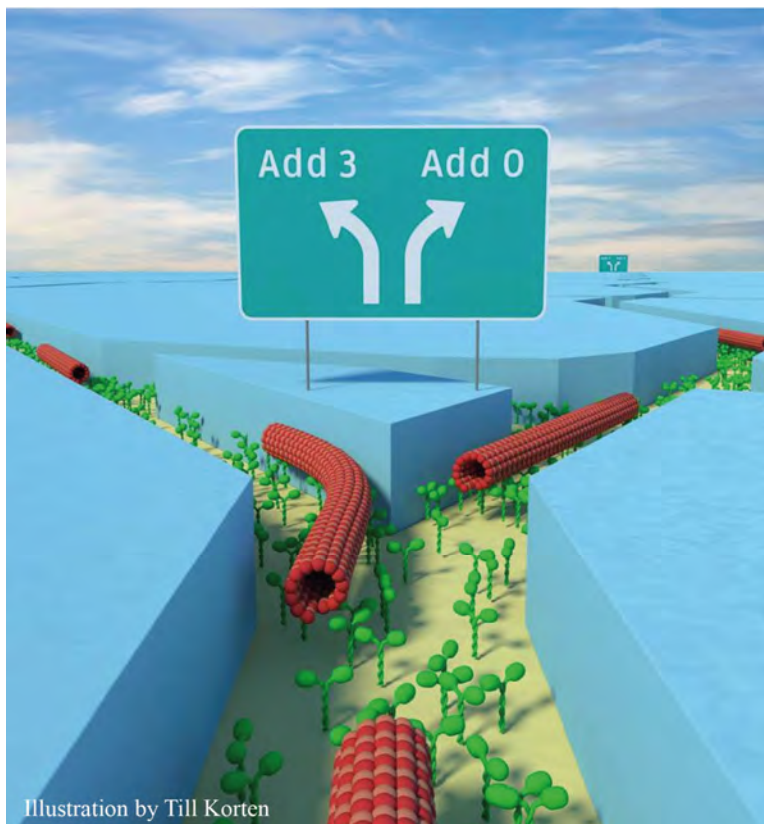


**Figure.** Red filaments crowd-surfing on green motors, exploring all possible paths inside a network. Each path represents a different calculation, enabling the encoded problem to be computed in a massively parallel manner.

# List of papers

This thesis is based on the following papers, referred to as Paper I-V in the text.

**I. Controlled Surface Silanization for Actin-Myosin Based Nanodevices and Biocompatibility of New Polymer Resists**

F. W. Lindberg, M. Norrby, M. A. Rahman, A. Salhotra, H. Takatsuki, S. Jeppesen, H. Linke, A. Månsson

*Langmuir* 34(30) 8777-8784 (2018).

I designed the project and performed the device fabrication and contributed to the motility assay experiments and analysis. I wrote the paper with input from co-authors.

**II. Design and development of nanoimprint-enabled structures for molecular motor devices**

F. W. Lindberg, T. Korten, A. Löfstrand, M. A. Rahman, M. Graczyk, A. Månsson, H. Linke, I. Maximov

*Materials Research Express* 6(2) 025057 (2019).

I designed the project and performed the device fabrication and contributed to the motility assay experiments and analysis. I wrote the paper with input from co-authors.

**III. Nanofabrication technologies for molecular-motor-powered network-based biocomputation structures**

C. Meinecke, T. Korten, F. W. Lindberg, H. Linke, G. Heldt, D. Reuter, S. Diez, S. E. Schulz

*Manuscript*

I designed and performed the device fabrication and analysis for the actin-myosin devices, contributed to the motility assay experiments and analysis and helped write the paper.

**IV. Regeneration of assembled molecular motor-based bionanodevices**

M. A. Rahman, C. Reuther, F. W. Lindberg, M. Mengoni, H. Linke, S. Diez, A. Månsson

*Manuscript*

I designed and performed the device processing of the actin-myosin devices and helped write the paper.

**V. Nanoscaled patterning of active molecular motor structured surfaces for switchable motility**

F. W. Lindberg\*, J. Zhu\*, T. Korten, C. Meinecke, S. Diez, H. Linke

*Manuscript*

I designed and performed some of the device fabrication and analysis and wrote the paper with input from co-authors.

\*Equal contribution

**Related publications**

The following papers are relevant, but outside the scope of this thesis.

**VI. Nanowires for Biosensing: Lightguiding of Fluorescence as a Function of Diameter and Wavelength**

D. Verardo, F. W. Lindberg, N. Anttu, C. S. Niman, M. Lard, A. P. Dabkowska, A. Månsson, T. Nylander, C. Prinz, H. Linke

*Nano Letters 18(8) 4796-4802 (2018)*

I performed the fabrication and growth of the nanowire samples and some of the analysis. I helped write the paper.

# Abbreviations

ATP	adenosine triphosphate
ADP	adenosine diphosphate
CNT	carbon nanotube
CNFET	carbon nanotube field effect transistor
CVD	chemical vapour deposition
DNA	deoxyribonucleic acid
EBL	electron beam lithography
EXCOV	exact cover
FET	field effect transistor
HMM	heavy meromyosin
IPS	intermediate polymer stamp
IVMA	in vitro motility assay
MEK	methyl ethyl ketone
NBC	network-based computation
NIL	nanoimprint lithography
NP	non-deterministic polynomial time
PEG	poly(ethylene glycol)
PMMA	poly(methyl methacrylate)
PMSF	phenylmethane sulfonyl fluoride
PNIPAM	poly( <i>N</i> -isopropylacrylamide)
PGMA	poly(glycidyl methacrylate)
T-NIL	thermal nanoimprint lithography
TEM	transmission electron microscope

TMCS	trimethylchlorosilane
SDS	sodium dodecyl sulphate
SSP	subset sum problem
UN	United Nations
UV	ultra violet
UV-NIL	ultra violet nanoimprint lithography
UVL	ultra violet lithography
3D	three dimensional

# Acknowledgements

Looking back at all the hard work, I know I would not be where I am today without the support and help from those around me. There are a few people I would like to give special thanks to:

To begin with, I would like to say thank you to my dearest supervisors, Heiner Linke and Alf Månsson, who told me that nothing is impossible and who opened up an entirely new world to me. Nothing will ever be the same again. Thank you for giving me space and freedom to grow and learn, and to catch me and guide me when I needed it the most. I am forever grateful for all you have done for me.

I've had the great pleasure of working with the best team for none less than two EU-projects in a row. A special thank you to Till Korten, you are real a champion and your skills seemingly endless, thank you for always being so helpful and supportive. To Stefan Diez, you light up the room with your presence and deep knowledge, and to Dan Nicolau Jr who mesmerises and amazes me. To Adam Micolich, your creativity and innovation is so extremely inspiring, there is never a dull moment working with you. To Marlene Norrby, Ashik Rahman and Aseem Salhotra, thank you for never giving up and always staying positive and supportive when I a hundred times over have yelled "this will be the one, I have a great feeling about this one!" Without your hard work this project would not have come this far, I owe you a great thank you. To Cordula Reuther, Sönke Steenhusen, Christoph Meinecke, Danny Reuter, Georg Heldt, Thomas Blaudeck, Venu Vemula and Hillel Kugler, it has been such a pleasure to work with you and to get to know you, your expertise has really driven us forward. And to my wonderful bio4comp fellows in Lund for making hard work so enjoyable, Jingyuan Zhu, Pradheebha Surendiran and Roman Lyttleton, thank you. Especially Roman, the endless hours we've spent in the lab, day and night and all the hours we spent on the phone and e-mail when you lived in Oz, your support and hard work has meant the world to me. And to Gerda Rentschler, the way you keep track of every detail and keep us all together and looking perfect, your tireless efforts are nothing less than amazing.

To Adam Burke and Mercy Lard, the first few years would not have been the same without you, thank you for everything.

To the people who keep the wheels turning, our past and present brilliant lab and administrative staff, I could spend pages and pages on how much you have helped

me through the years, I am so incredibly grateful to each and every one of you, especially to the ones I have pestered the most over the years: Louise Baldetorp, Charlotte Solberg, Anders Kvennefors, Mariusz Graczyk, Håkan Lapovski, George Rydnemalm, Janne Mårtensson, Johanna Mosgeller, Sören Jeppesen, Maria Huffman, Ivan Maximov, Dmitry Suyatin, Bengt Mueller, Peter Blomqvist, Mia Hedin, Margareta Forsberg, Eva Lenhoff, Marica Kolobaric, Abdul-Rehman Hakam and Line Lundfald, but also to all those who I have not mentioned by name here, a great thank you to you all, so much of what I have learnt over the years I owe to you and I am truly blessed to have learnt from such experts.

To my office mates Mercy, Gustav, Dmitry, Trung, Xulu, Vilgaile, I-ru, Nicklas, Laura, David, Florinda, Elke, Rebekah, Cassie and Inga, there is a special, deep bond between people who've shared an office together. Thank you for all the laughs we've had over the years. And to all my other wonderful colleagues at ftf, Reza, Oskar, Artis, Kush, Damiano, Lukas, Irene, Thanos, Bao, Anette, Neimantas, Malin, Anders, Kalle, Sara, Maria, Christelle, Stefan, Enrique, Pyry, Gaute, Jason, Magnus, Olof, Robert, David, Bekmurat, Jonatan, Sven, Zhen and the list goes on, thank you for making every day so perfect, for wonderful collaborations and heart-warming conversations filled with support and solidarity, thank you all for sharing your knowledge so freely and for such great inspiration.

An extra thank you to my trainers and coaches over the years, who taught me that I can do anything I set my mind to, that hard work pays off and that stopping is not an option, who inspire me to push harder and be the very best I can be every day and to never give up. This I take with me forever, and apply to all of life, including work and academia.

And finally, to my family and loved ones, Molly, Normha, Pentti, Nadia, Sarah, Henrik, Jenny, Johan, Jan, Annica, Nix, Nox and Lady for always being present or just one phone call away, I love you all and I would not be the person I am today without you.

Frida Wilhelmina Lindberg, Lund 2019

# 1 Introduction

Nanotechnology is often described as the manipulation of matter at a very small scale, in the range 1 to 100 nanometres ( $1-100 \cdot 10^{-9}$  m). It is an interdisciplinary field, where the laws of physics, biology, chemistry, materials science and engineering all blend and have to be considered together. The following text is a truly interdisciplinary thesis within nanotechnology, where all the fields mentioned above have been taken into consideration. The goal of this work has been to develop the requirements for a large-scale parallel computer based on molecular motors for solving combinatorial problems.

Naturally, the complexity of any computational problem grows when the number of variables that need to be observed increases. For mathematical problems with a combinatorial nature, an increase in the number of variables causes a superpolynomial, and sometimes even exponential, growth in time complexity. Let's assume a doctor, Sarah, is specialised in treating people suffering from the plague. The United Nations (UN) needs her to travel across the world to train and treat people as soon as possible. Sarah can therefore, not afford to re-visit a country as this would cause an international diplomatic crisis and outrage of why UN-funding is misdirected to privilege one country over another. What route can Sarah take, allowing her to cover all countries, exactly once as fast as possible before the disease spreads further? To find the answer to this question, all possible routes need to be explored. And as the number of countries Sarah needs to visit increases, so does the computational complexity and thus, the problem blows up exponentially.

Combinatorial problems like the one Sarah encountered, are known as non-deterministic polynomial time (NP) problems, problems with multiple solutions that cannot be verified within a polynomial timeframe<sup>2</sup>. These problems are very challenging for electronic computers that work in a sequential manner as often, no efficient algorithms exist and instead, parallel computation techniques are needed. To this date, existing parallel computation techniques such as, parallel electronic computers<sup>3,4</sup>, DNA computation<sup>5-7</sup>, microfluidics based computation<sup>8</sup> and quantum computation<sup>9</sup>, all have their own drawbacks and limitations for upscaling into more complex systems (further discussed in Chapter 2).

In this thesis we further explore a parallel computation method based on molecular motors. Molecular motors are a class of proteins that convert chemical energy into mechanical motion in a highly energy-efficient manner<sup>1,10,11</sup>, enabling them to

propel their corresponding cytoskeletal filamentous proteins. In the *in vitro* motility assay<sup>12–15</sup> (IVMA) the motors are first isolated in functional form from the cell and can then be adsorbed onto a surface with maintained function. The IVMA has enabled many new insights into the physiological properties of molecular motor systems<sup>16–19</sup>, and has also gained interest as a basis for nanotechnology applications<sup>1,20–23</sup>. The type of motility assay used here is the gliding assay<sup>15</sup>, where the molecular motors are immobilized on the substrate, while the filaments are propelled along the surface in a random motion. This motion can be directed by introducing chemically<sup>24,25</sup> and physically<sup>26–31</sup> confining tracks, which has led to the exploration of various lab-on-a-chip applications<sup>1,21,32,33</sup>.

In our motility assay system, we build a “flow cell” comprised of a thin, glass coverslip onto which we paste two pieces of tape spaced a few mm apart (**Figure 1.1**). The surfaces we study are mounted onto the tape, face down, enabling addition of protein and buffer solutions via capillary forces. We image the gliding assay through the glass coverslip using an inverted fluorescence microscope and fluorescently labelled actin filaments. To direct the motion of filaments, we use a combination of physically and chemically confining tracks. The nanostructures are created by lithography, providing channels with polymer walls. The channel floors are chemically treated to allow motor binding in a motility-promoting manner, while the walls are treated to inhibit this binding. The binding mechanism and motor confinement will be further discussed in Chapters 2 and 3, and the patterning of nanostructures is further discussed in Chapter 4.

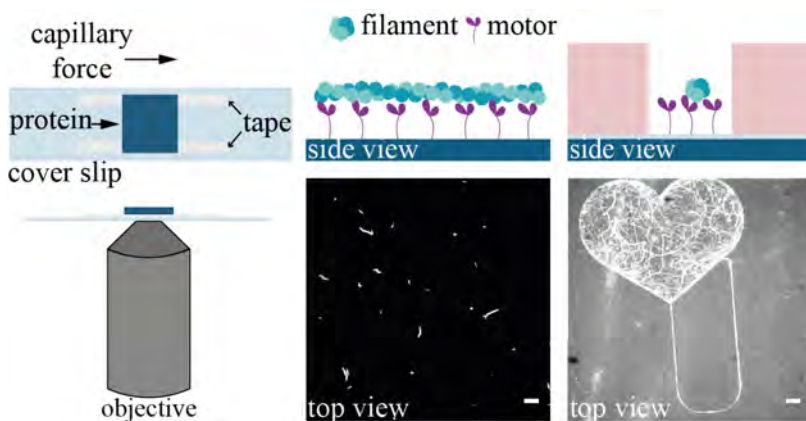


**Figure 1.1.** Schematic illustrations and fluorescence micrographs of (left) a flow cell and our experimental set-up, (middle) an *in vitro* motility assay on a flat surface and (right) on a structured surface. The flow cell consists of a glass slide with two pieces of tape onto which the sample is mounted upside down, creating an enclosed volume for the protein assays. The flow cell is mounted face down onto a microscope and imaged using a fluorescence microscope. Motors bound to a flat surface propel filaments in a random motion through active transport. The fluorescently labelled filaments appear as bright snakes on the dark surface. The nanostructured surface physically and chemically confines the motor system, only allowing the filaments to move from the large heart into the channel and back again. The lower right micrograph shows the maximum intensity of a 60 s time-lapse movie. The scale bar is 5  $\mu\text{m}$  in both fluorescence micrographs.

The use of molecular motor systems for network-based computation (NBC) was first reported in 2016<sup>1</sup>, in the form of a proof-of-principle small scale network solving a simple combinatorial problem known as the subset sum problem. The subset sum problem<sup>34</sup> (SSP) asks what sums are attainable given a set of numbers. For instance, given the set (2, 3, 9), the possible sums and correct solutions, correspond to (0), 2, 3, 5, 9, 11, 12, 14. For small sets, such as the one demonstrated<sup>1</sup>, it seems trivial and unnecessary to create a computer to find the solutions. However, the SSP is of a combinatorial nature as all combinations of numbers must be explored by brute force in order to find the correct answers. Therefore, the solution space and thus, the time required to solve the problem grows exponentially,  $2^n$ , with the number of integers<sup>6,34,35</sup>,  $n$ .

The motor systems are confined by a network of channels (**Figure 1.2**) consisting of two types of junctions: pass and split. The pass junctions are basic cross-overs, where filaments are supposed to continue along the straight path from which they came. At split junctions however, the filaments can turn and thus, spread across the network. The position of the split junctions define what numbers are encoded in the network, as this defines how far right a filament can travel before making a turn, and thus, at what positions filaments can exit the network. The farther right the filaments exit the higher the resulting sum.

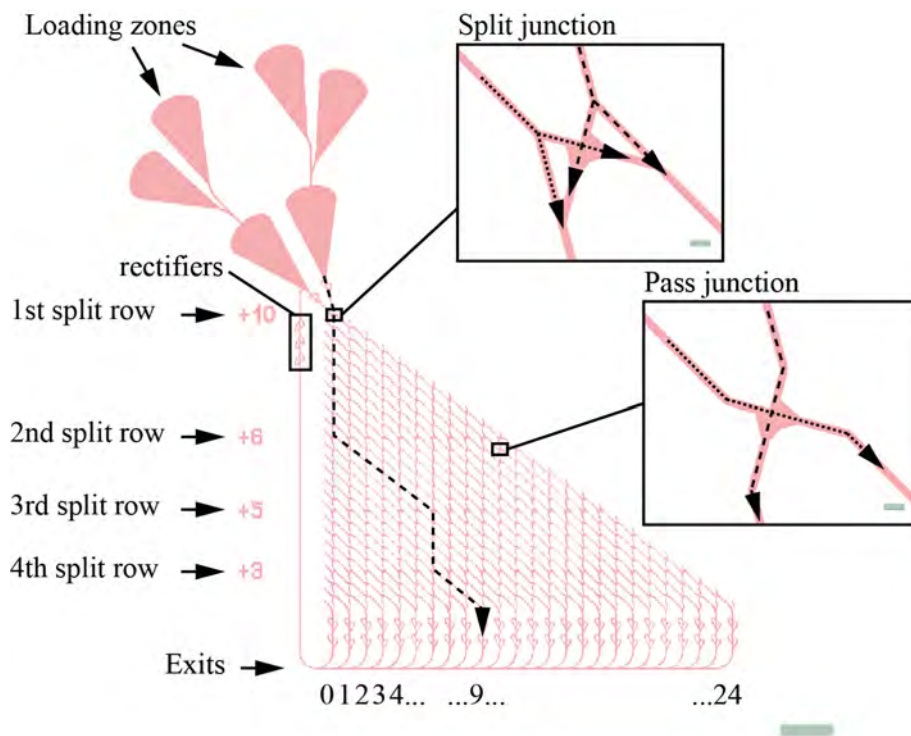


**Figure 1.2.** Schematic layout of a biocomputational network of the combinatorial problem subset sum encoding the numbers (10, 6, 5, 3). Filaments enter the network of split and pass junctions through large areas called loading zones. If the filaments try to enter the network from the wrong way, they are re-directed by rectifiers<sup>1</sup>. At the pass junctions the filaments travel straight along the path they came from, and at split junctions they can turn either left (straight down) or right. The farther right (when looking at the network at from above) a filament moves, the higher the resulting sum. The number of pass junctions between two split rows match the numbers encoded. In the example path (dashed line) the filament travels straight through the first split junction encoding the number 10 (nothing is added). At the second split junction, encoding the number 6, the filament turns and moves right 6 pass junctions (+6). At the third split junction, encoding the number 5, the filament turns again and moves down (nothing is added), but at the fourth split junction, encoding the number 3, the filament turns right again and travels even farther right, 3 pass junctions (+3), and eventually exits at exit number  $6+3=9$ . The scalebar in the split and pass junction figures is 500 nm. The scalebar in the big figure is 25  $\mu\text{m}$ .

In this thesis we mainly use the relatively small<sup>36</sup> ( $\sim 10$  nm wide) actin-myosin II system. The semiflexible<sup>11,37</sup> filamentous actin is propelled by proteolytically cleaved myosin-II fragments (known as heavy meromyosin (HMM)), at high speeds<sup>11</sup>. To some extent, we also use the microtubule-kinesin system which has larger<sup>11</sup> ( $\sim 25$  nm wide) and more rigid microtubules<sup>11,37</sup> that are propelled by kinesin-1 motors at about 10-fold lower velocities<sup>38</sup>. The networks for the actin-myosin II system are fabricated with polymer resist channel walls that are patterned by electron beam lithography on channel floors made of  $\text{SiO}_2/\text{Si}$  substrates which are chemically modified to promote motility (described further in Chapter 3). This thesis tackles some of the engineering requirements related to upscaling the proof-

of-principle network demonstrated in 2016<sup>1</sup> and also demonstrates a method to translate another combinatorial problem, exact cover, into the SSP and describes our progress towards solving a larger scale network in the ~1000 solution range.

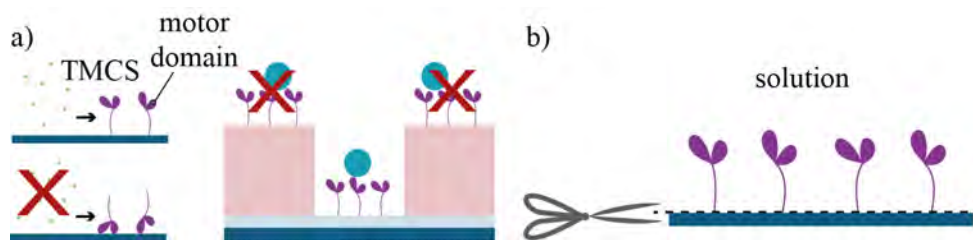


**Figure 1.3.** Schematic illustration of a) molecular motor-binding to a surface. To chemically confine the motor systems we need to ensure the motors bind in an upright, motility-promoting manner with the motor domains protruding into the solution. b) To enable a sustainable fabrication method we developed a procedure to cleave the motors off the surface, allowing the samples to be reused without disassembling the flow cell.

To chemically confine molecular motor systems, the surface chemistry must differ between the motility promoting (channel floor) and motility inhibiting (channel wall) area. Furthermore, the material chemistry must be compatible with the molecular motor system used, both in relation to toxicity as well as protein binding to ensure the motors bind with the motor domain protruding into solution (**Figure 1.3a**). The binding mechanism of HMM to a surface is complex and depends on both the surface charge<sup>39</sup> and the surface hydrophobicity<sup>40-42</sup>. Previous studies<sup>39,43</sup> have shown that trimethylchlorosilane (TMCS) functionalised SiO<sub>2</sub> surfaces created by chemical vapour deposition (CVD) promote high-quality actin filament motility. In these studies, the CVD process occurred in a fully saturated TMCS system. Initially, we used a similar process but noticed inconsistencies in sample behaviour with respect to both measured contact angles and the actin filament sliding velocities for different sample batches. We linked these observations to the limitations of the CVD process performed in a relatively uncontrolled environment. To provide more reliable results, we developed a CVD tool to enable silanisation in a more controlled manner, enabling us to tailor the surface hydrophobicity without changing the chemical composition of the surface (Paper I).

Furthermore, the re-use of nanostructured devices within molecular motor-based applications is highly desirable due to the expensive and time-consuming fabrication procedures, as well as from a sustainable perspective, as less material is used and samples shipped elsewhere can be recycled and used for multiple experiments. We therefore, developed a process for chemically cleaning the nanostructures (**Figure 1.3b**) from old proteins without disassembling the nanofluidic flow cells using a combination of the non-selective protease Proteinase K and the non-ionic surfactant Triton X100 (Paper IV).

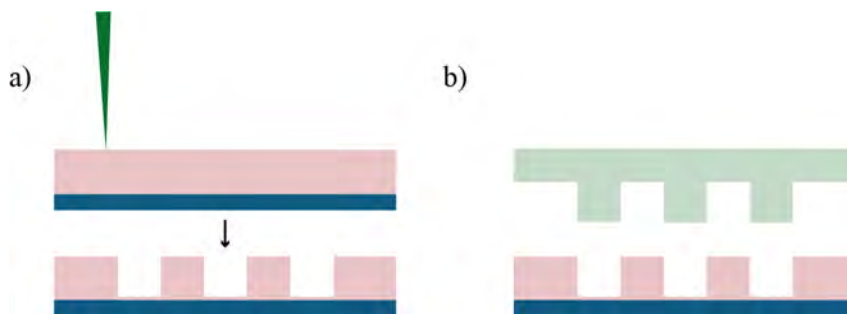


**Figure 1.4.** Schematic illustration of a) electron beam lithography and b) nanoimprint lithography for molecular motor devices. In electron beam lithography an electron beam is scanned across the surface, selectively exposing specific regions, causing cross-linking or cleavage of the polymer, making it more or less soluble in a developer. In nanoimprint lithography a polymer is heated above its glass transition temperature and a stamp is pressed down to physically imprint structures. Both methods enable high-resolution nanoscaled patterning.

The required dimensions for molecular motor structures depend on the motor system used. Channels can be designed so that they represent “one-way streets” by taking advantage of the persistence length of the filaments<sup>27,44</sup>, where an advantage of more rigid filaments are that wider channels can be used. The actin-myosin system requires high-resolution fabrication techniques based on the necessary feature size (channel widths around 200-300 nm<sup>27</sup>) to prevent U-turns. Such structures are patterned by electron beam lithography (EBL), where selective areas of a polymer are exposed with an electron beam causing cross-linking or cleavage of polymer chains (**Figure 1.4a**). This provides high flexibility in pattern design but at a very low throughput. We optimised the processing parameters for a new sensitive electron beam resist, CSAR62 in our currently available electron beam lithography system as well as a newly purchased system to improve the throughput of patterning larger-scale computational networks (Paper III).

Another fabrication method that can be used to achieve high-resolution patterns but with a higher throughput is nanoimprint lithography (NIL) where a stamp is used to imprint a polymer (**Figure 1.4b**). NIL was first used for fabricating narrow channels (100-400 nm) for molecular motor devices in 2005 by Bunk et al<sup>45</sup>. However, structures for molecular motors also require large open areas, “loading zones” (see **Figure 1.2**), to collect the filaments from solution and funnel them towards the connecting channels<sup>1,21</sup>. Such structures, with a large width relative to the height, are difficult to imprint with NIL as the imprinted polymer needs to be displaced across large distances<sup>46</sup>. We extended the previous imprinting study<sup>45</sup> for molecular motor devices to include a method of fabricating a new type of loading zone. By introducing pillars inside the loading zones, we could provide close by regions into which the resist could be displaced (Paper II). We also extended the previously results by optimising the process for a new imprinting resist, TU7, which has a low glass transition temperature allowing imprints below 100°C.

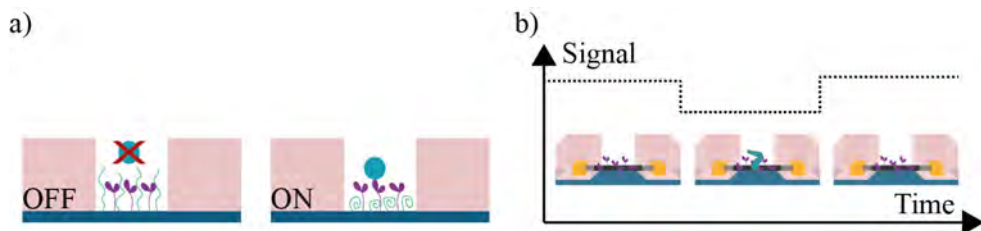


**Figure 1.5.** Schematic illustration of a) a programmable gate using the thermoresponsive polymer PNIPAM to switch between a blocked (OFF) and unblocked channel (ON) and b) a nanoFET with a carbon nanotube to create an electrical detection method enabling label-free and microscope-free experiments.

Allowing imprinting of large-scale networks and the re-generation of surfaces for multiple use, creates an attractive and sustainable computational method. However, to create a versatile computer that can be used to encode different numbers, a programmable gate is needed. Such a gate can be used to transform pass junctions into split junctions, and vice versa, by blocking and unblocking certain paths (**Figure 1.5a**). Initial studies<sup>47</sup> for blocking and promoting the motility of microtubules were done on Au patterned surfaces, and demonstrated the proof-of-principle of using a thermo-responsive polymer poly(N-isopropylacrylamide) (PNIPAM) to create physical roadblocks. At low temperatures, PNIPAM resides in an extended form, blocking the molecular motors, inhibiting motility. If the temperature is increased, the polymer curls up and exposes the motors, and the roadblock is lifted. We continued this work, aiming to create a gating mechanism inside our channel structures, to create switchable, and thus programmable, networks by selective patterning of a polymer linker for PNIPAM grafting (Paper V).

Another important enabler for large-scale biocomputation, is technology to detect a large number of filaments passing different check-points, e.g., at the network exits. If this detection is done electrically, the need for fluorescent labels becomes redundant, and neither labels nor microscopes need to be used. Additionally, electrical detection and read-out would enable a direct interface to traditional, electronic computers. We have begun development towards an electrical readout method using a single-walled carbon nanotube (CNT) as a nanoscale field effect transistor<sup>48</sup> (nanoFET) (**Figure 1.5b**). CNTs have previously been used as nanoFETs<sup>49–51</sup>, but to the best of our knowledge, not for detecting the passing of an unbound protein. A voltage is applied across the CNT, creating a current sensitive to the local charge environment. As a charged particle, e.g., a protein filament, passes in close proximity of the CNT, the charge environment changes which modulates the electric output signal. Therefore, the passing of a charged particle should be detectable as a function of time. Our molecular motor systems require buffer solutions with different ionic constituents. This affects the distance at which our protein charges can be detected as the electrolytes screen the electric potential.

We examined the effect of the local environment in terms of ionic strength; how close the filaments need to pass the CNT and the quality of motility at very low ionic strengths. We found that the CNTs have to be placed on top of pedestals to allow filaments being propelled above the surface to graze across the CNT, and that there is a trade-off between retaining function of the biological system and what gap size is possible between filament and CNT.

The developments presented in this thesis, provide stepping stones towards using large-scale biocomputational networks to solve combinatorial problems in a massively parallel manner. Further development of parallel computation techniques for solving these types of problems, opens up for exploring entirely new scientific questions that previously were impossible to manage within, e.g., artificial intelligence<sup>52,53</sup>, complex studies of protein folding<sup>54,55</sup>, network route optimisations<sup>56</sup> and many more.

The remaining chapters of this thesis are laid out as follows:

Chapter 2 introduces molecular motor systems, in particular the actin-myosin II and microtubule-kinesin I system in more detail, to provide a background for how these motor systems can be used in nanotechnology devices, in particular for computation. A theoretical background on the type of computational problems studied is also introduced. Furthermore, a brief review of the two main patterning techniques (EBL and NIL) used throughout this thesis is presented.

Chapter 3 focuses on the surface chemistry of the devices and describes how surfaces can be modified in a controllable manner to ensure selective motility (Paper I) and how surfaces can be cleaned and reused multiple times (Paper IV).

Chapter 4 describes the optimisation and development of nanopatterning for EBL (Paper III) and NIL (Paper II) to enable higher throughput fabrication of large networks without loss of structural resolution.

Chapter 5 demonstrates our efforts towards solving an upscaled network encoding the combinatorial problem exact cover. The algorithm for translating the exact cover problem into the previously demonstrated subset sum problem is presented as well as the design optimisation for this new network and preliminary results on a  $10^3$ -solution-space order.

Chapter 6 presents the progress towards developing a programmable gate for switching the number encoding inside a network (Paper V), and the progress towards developing an electric readout method using a CNT as a nanoFET.

Chapter 7 summarizes the results presented and describes future improvements and developments in this area.

# 2 Background

*This chapter aims to provide sufficient background knowledge for the reader to be able to understand the results presented in the chapters to follow, and to appreciate their scientific significance. A brief introduction to molecular motor systems is given, in particular the actin-myosin II and the microtubule-kinesin I system, together with a few notes on what to consider when selecting a new system. The second part of this chapter introduces the two main patterning techniques used in this thesis: electron beam lithography and nanoimprint lithography. The third and final part of this chapter presents the type of mathematical problems that are of interest in parallel computation and how these can be solved. A short introduction is given to some pertinent techniques including quantum computation and DNA computation, as well as an introduction of network-based computation with molecular motors.*

## 2.1 Molecular motor proteins

Molecular motors are proteins that govern the active and directed movement in all eukaryotic cells. The motors convert chemical energy of adenosine triphosphate (ATP) hydrolysis into mechanical motion in a highly energy-efficient manner<sup>1,10,11</sup>. In the *in vitro* motility assay<sup>12–15</sup> (IVMA) the motors are isolated from the cell and adsorbed onto a surface. In the presence of ATP, the corresponding cytoskeletal filaments are propelled in a random direction through active transport by the motors. This motion can be directed using chemically<sup>24,25</sup> and physically<sup>26–31</sup> confining tracks, but the efficiency of the guiding along these tracks is highly dependent on the persistence length of the filaments<sup>24,27,31,44</sup>, i.e., their flexural rigidity. The most important properties to consider when choosing a molecular motor system for nanotechnology applications are:

- Persistence length: defines the dimension requirements of the nanostructures. Very flexible filaments require narrow tracks<sup>24,27</sup> to ensure unidirectional motion but also enable very compact nanostructures as the filaments can turn through steeper radii. More rigid filaments allow for larger nanostructures which simplifies fabrication but puts constraints on

imaging techniques due to the increase in size as the structures will expand outside the imaging field of view.

- Filament gliding velocity: defines how fast filaments run through a device and what temperature range<sup>57</sup> the system needs to be operated in. It may be preferential to decrease the filament speed in certain devices or regions to facilitate readout or detection, while larger nanostructure systems could benefit statistically from higher velocities due to an increased current density of filaments.
- Processivity: defines if the filaments are more or less likely to detach from the motors and is usually negatively correlated with the gliding speed. Non-processive motors require many motors to propel the filaments, making it difficult for filaments to escape via side-wall interactions. These motors detach readily from their filaments, usually providing higher gliding velocities than processive motors.

### 2.1.1 The actin-myosin II system

Striated muscle tissue is composed of repeating units known as sarcomeres which consist of thin actin containing filaments and thicker myosin II containing filaments<sup>58</sup> (**Figure 2.1**). Upon activation, the filaments slide along each other driven by a cyclic binding-unbinding process between myosin motor domains and actin filaments. This, so called the cross-bridge cycle, is the molecular basis for muscles contraction<sup>59,60</sup>.

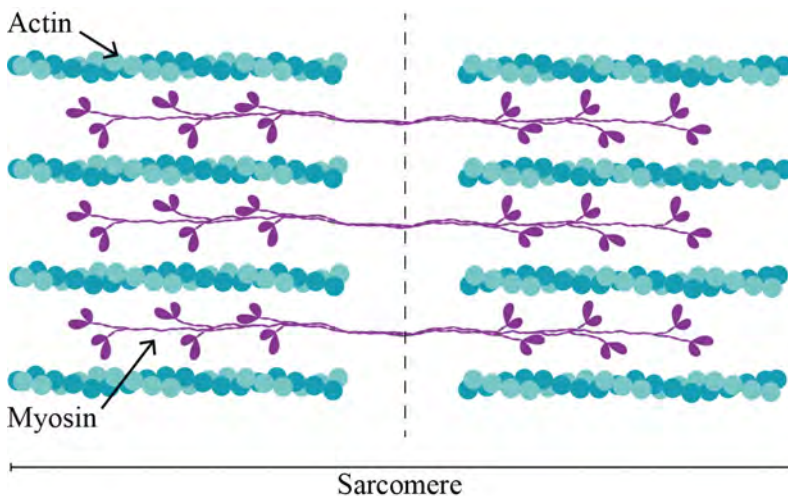


**Figure 2.1.** Schematic illustration of a sarcomere, showing the actin filaments in aqua shades and myosin filaments in purple. Figure freely interpreted from<sup>61</sup>.

The actin filaments consist of globular monomers, G-actin, arranged in a helical structure<sup>62</sup> which creates polar filaments, F-actin, with one end denoted the plus end or barbed end and the other the minus end or pointed end. During actin polymerization, the filament preferentially elongates by monomers binding to the plus end<sup>63</sup>, hence the terminology. Each actin filament has a diameter of  $\sim 9$  nm<sup>36</sup> and can grow several micrometres long. Due to their structural composition, actin filaments are semi-flexible on the length scale of a cell with a persistence length around 10-20  $\mu\text{m}$ <sup>11,37</sup>. In this thesis, mainly rhodamine-phalloidin labelled actin filaments have been used, which usually have a persistence length in the upper part of the mentioned range<sup>37,64,65</sup>.

The myosin super family consists of 35 different myosin classes<sup>66,67</sup>. In this thesis we have used (rabbit) skeletal muscle myosin II. Muscle myosin II forms thick bipolar filaments with globular units, heads, that are around 10 nm long and 5 nm wide. These heads contain the motor domains: a catalytic site for ATP turnover and positively charged surface loops with central roles in actin binding<sup>68</sup>. Myosin II can be proteolytically cleaved into subunits<sup>69</sup>, resulting in light meromyosin and heavy meromyosin (HMM). The HMM tail is negatively charged and forms a coiled-coil consisting of  $\alpha$ -helical segments of the two myosin heavy chains that make up the bulk of each myosin molecule<sup>70</sup>. **Figure 2.2** shows two transmission electron microscope (TEM) images of negatively stained myosin II (**a**) and HMM bound to actin filaments (**b**). Both samples have been stained with uranyl acetate<sup>71</sup> on square meshed TEM Cu grids with pioloform membranes. The concentration of myosin II is 2550  $\mu\text{g/ml}$  and the actin-HMM concentration is 630  $\mu\text{g/ml}$ , both contained in LISS buffer (1 mM  $\text{MgCl}_2$ , 10 mM MOPS, 0.1 mM  $\text{K}_2\text{EGTA}$  in 1M KOH) with 3M KCl. The images are taken with a JEOL JEM-1400 Plus TEM at 100 kV acceleration voltage.

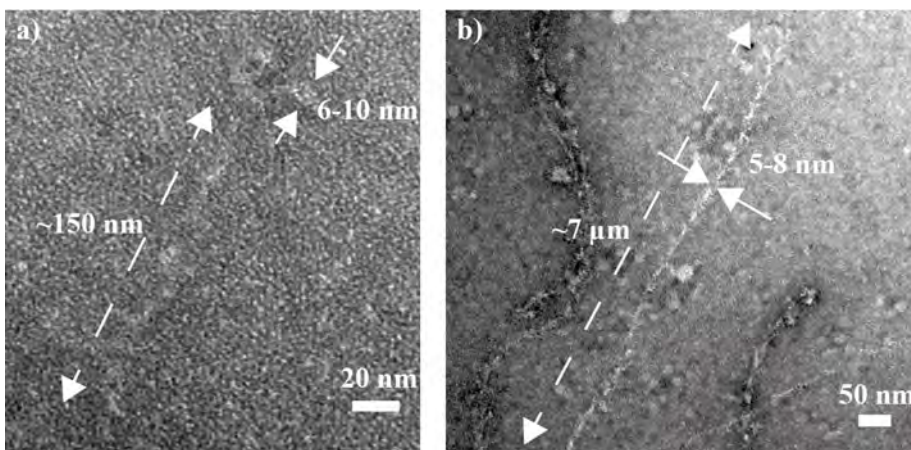


**Figure 2.2.** TEM images of negatively stained myosin II (a) and HMM bound to actin filaments (b).

### *The cross-bridge cycle*

The cross-bridge cycle is a cyclic process of binding and unbinding of myosin to actin powered by ATP. Upon binding of an ATP molecule, myosin undergoes a conformational change<sup>60,72</sup> that lowers the actin-myosin binding affinity (**Figure 2.3a**). Associated with hydrolysis of ATP into adenosine diphosphate (ADP) and inorganic phosphate ( $P_i$ ), the myosin motor undergoes a larger conformational change, forcing the head with its lever arm structure into a pre-power stroke, cocked position (**Figure 2.3b**). Initially, the myosin binding sites on actin filaments are blocked by two proteins: troponin and tropomyosin. When troponin binds  $Ca^{2+}$  it undergoes a conformational change<sup>73</sup> which in turn induces the position of tropomyosin to shift, allowing myosin to bind to actin. The binding of myosin to actin (**Figure 2.3c**) leads to an accelerated dissociation of  $P_i$  (**Figure 2.3d**) followed by the release of ADP (**Figure 2.3e**). These chemical changes are closely associated with a force-generating structural change; a swing of the lever arm creating a power-stroke, that pulls the actin filaments toward the centre of the sarcomere. The cycle is repeated if a new ATP molecule binds to the myosin motor. Thus, each cycle or “step” ( $\sim 10$  nm)<sup>74</sup> only consumes one ATP molecule under physiological conditions which corresponds to approximately 25 kT ( $100 \cdot 10^{-21}$  J)<sup>10,11</sup>. This makes these motors highly energy efficient with a maximum thermodynamic efficiency for an ensemble of motors of up to  $\sim 50\%$ <sup>10</sup>. Furthermore, myosin II always moves toward the plus end of an actin filament and is a non-processive motor, allowing propulsion of actin filaments at high velocities ( $\sim 10$   $\mu\text{m/s}$ )<sup>11</sup>.

As mentioned in the introduction, we use a combination of TMCS-derivatised channel floors and polymer channel walls to chemically and physically confine the actin-myosin II system in our devices.

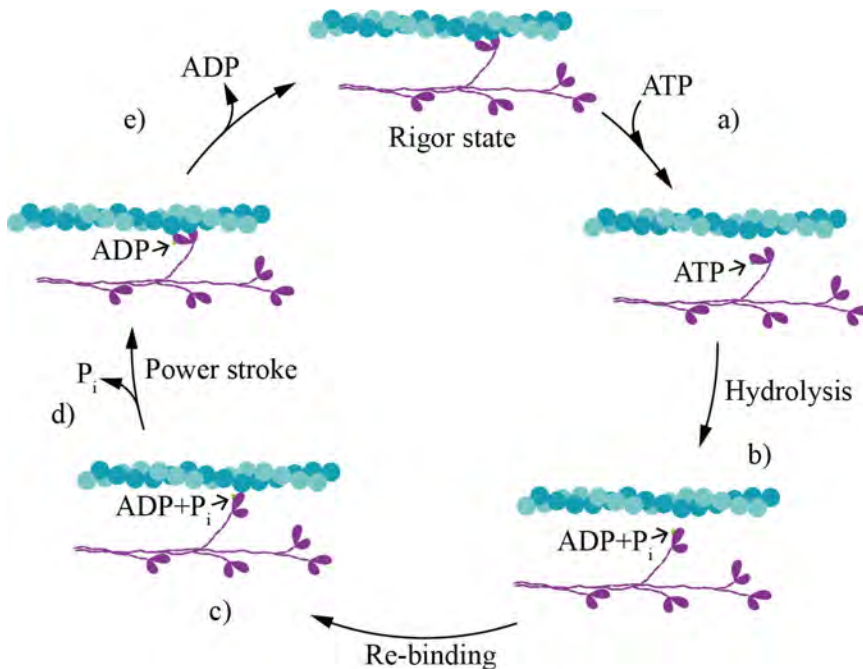


**Figure 2.3.** Schematic illustration of the cross-bridge cycle. a) The binding of ATP to myosin causes a weaker interaction between actin and myosin. b) The ATP molecule is hydrolysed into ADP and inorganic phosphate ( $P_i$ ), which causes a conformational change in the myosin, forcing the motor domain and its lever arm into a cocked position. c) The myosin head re-binds to the actin filament causing d) dissociation of inorganic phosphate from the catalytic site followed by a power-stroke, pulling on the actin filament, and e) ADP dissociates. As a new ATP molecule binds in the cycle is repeated. Figure freely interpreted from<sup>61</sup>.

### 2.1.2 The microtubule-kinesin system

Microtubules consist of tubulin protofilaments arranged in a 3-start helical structure running parallel to the axis of the filament<sup>75</sup>. This creates stiff, hollow tubes with a diameter of 25 nm<sup>11</sup> with a several millimetre long persistence length in solution<sup>11,37</sup>. If transported along kinesin motor tracks, microtubules have a shorter persistence length around 100  $\mu\text{m}$ <sup>76</sup> (albeit, this depends on the filament length). Similar to actin, microtubules have a plus and a minus end due to the asymmetry of the dimers.

Kinesin 1 is a motor protein highly involved in cargo transport within the cell<sup>77</sup>. Like myosin, kinesin has two heads containing the binding sites for microtubules<sup>78</sup>. The binding mechanism is similar to that of the actomyosin system<sup>60,72</sup> involving varying binding affinities coupled to different states in the ATP turnover cycle<sup>38</sup>. Unlike myosin-II, kinesin 1 is a processive motor<sup>11,38</sup> which means that at least one of the heads is bound to the microtubule at all times. Related to this processivity, kinesin-1 propels microtubules at a slow rate (1  $\mu\text{m/s}$ ). The step size is around 8 nm<sup>1</sup>.

Due to the longer persistence length of microtubules<sup>42</sup> as compared to actin filaments<sup>25</sup> wider channels, up to 19  $\mu\text{m}$  wide<sup>79</sup>, can be used in nanotechnology devices. However, any interaction of microtubules with the side-walls causes a re-direction of their pathway, both along and up the wall, which may lead to detachment<sup>25</sup>. Wider channels enable microtubules to approach the wall at larger angles, increasing the risk of detachment. Therefore, they are better guided in narrower tracks below 1  $\mu\text{m}$ <sup>25</sup>.

For the microtubule-kinesin system we use a combination of  $\text{SiO}_2$  channel walls and Au channel floors in our devices. The motility on the  $\text{SiO}_2$  can be suppressed by preventing kinesin binding through polyethylene glycol (PEG) treatment<sup>80</sup> and a high density of kinesin motors can be bound to Au to promote motility<sup>81</sup>. Thus, the combination of PEGylated  $\text{SiO}_2$  walls and Au floors provides a high contrast in motility on the floors as compared to the walls<sup>81</sup>.

## 2.2 Patterning techniques for molecular motor devices

The physical confinement of the molecular motor systems is done by nanoscale channels. For the actin-myosin II system the confining channels are made directly in polymer resist, whereas for the microtubule-kinesin I system, these channels are defined in polymer resist and subsequently etched down into  $\text{SiO}_2$ . The following section gives a brief introduction to the two lithography methods used in this thesis for defining the channel structures: electron beam lithography and nanoimprint lithography.

### 2.2.1 Electron beam lithography

Electron beam lithography (EBL) uses high-energy electrons to pattern a polymer resist, which enables patterning with a high resolution (sub 10 nm)<sup>82,83</sup>, using commercially available tools and materials. Unlike the most common forms of ultra violet lithography (UVL), EBL does not require the use of a mask for selective exposure. Instead, the structures are patterned by selective exposure in an adjustable pattern by an electron beam scanning across the surface (**Figure 1.4a**). Therefore, EBL is a very adaptable method well suited for research.

To create the electron beam, primary electrons are extracted from an electron source and accelerated towards the specimen with an energy corresponding to the acceleration voltage. The electron beam is focused by electromagnetic and/or electrostatic lenses as it travels towards the specimen. It travels through the electron column (all kept in high vacuum), creating a very small, few nanometres wide<sup>84</sup>,

focused electron probe. When the primary electrons reach the sample, they begin interacting with the resist.

There are two classes of resists, negative tone and positive tone resists<sup>85</sup>. Positive tone resists have long polymer chains that are cleaved upon electron beam exposure, making the exposed areas more soluble. Negative tone resists consist of shorter polymer chains that are cross-linked upon exposure, making these areas less soluble. Obviously, there are a range of different polymer chain lengths and compositions, affecting both the contrast and sensitivity for each resist while also making them more or less soluble in different types of developers.

There are different types of electron-matter interaction depending on the electron energy. Low-energy electrons can scatter both elastically and inelastically<sup>86</sup>. Elastic scattering will cause the primary electrons to slightly deflect, causing beam broadening. Inelastic scattering will generate (shorter-range) secondary electrons in the resist, which in turn may lead to proximity exposures. Higher energy electrons penetrate the sample deeper, all the way into the substrate. Here, they can backscatter and re-enter the resist layer, causing a larger proximity exposure, which can overexpose or even distort the pattern. If the acceleration voltage is increased, the number of inelastic scattering events in the resist will decrease as the electron energy increases, and less beam broadening will occur<sup>86</sup>. However, this increased substrate interaction will cause a longer-range proximity effect than at lower voltages. As the electron energy is increased, the sensitivity of the resist is decreased, i.e., the number of chain scissions or cross-links per electron will decrease, and higher exposure doses are required, due to that it is mostly scattered, low-energy electrons that interact with the resist. In turn, the exposure dose strongly affects the pattern quality, as a too low electron dose leads to underexposure, and the structure will not be fully patterned. A too high electron dose will cause an overexposure, resulting in broadening of the pattern, as well as possible feature collapses in very dense patterns. It is therefore, very important to choose the correct resist and developer for each purpose, as well as the appropriate hardware parameters. The overall pattern resolution will depend on the probe size, the type of resist and developer used, the type of electron scattering occurring as well as the range of any secondary electrons generated<sup>85</sup>.

Albeit the high flexibility of use, EBL also has several drawbacks. A drawback related to beam scanning is the long exposure time needed as compared to the flood-like exposure during projection UVL. Furthermore, depending on the exposure parameters and the resist material used, scattered electrons can be an issue by causing proximity effects<sup>85</sup>. Also, electrostatic charging may occur in non-conductive materials, causing defocusing of the electron beam (due to Coulomb interactions), which decreases the resolution<sup>85</sup>.

### 2.2.2 Nanoimprint lithography

Nanoimprint lithography (NIL) is a high-throughput technique suitable for large-scale fabrication while providing sub-10 nm resolution<sup>87,88</sup>. There are two main types of NIL, UV-NIL<sup>89</sup> and thermal NIL (T-NIL)<sup>88</sup>. In both instances, a polymer resist is heated above its glass transition temperature and a stamp is uniformly pressed down into the resist at a high pressure, transferring the stamp pattern into the polymer, by physically displacing the polymer and filling the stamp protrusions (**Figure 1.4b**). In T-NIL the polymer resist is cured by cooling, whereas in UV-NIL the polymer resist is cured using UV-light. Therefore, mainly negative tone resists are used for NIL. The mother-stamp for T-NIL is made out of a hard material, e.g., a metal or SiO<sub>2</sub> on Si<sup>90</sup>. However, the resist in UV-NIL needs to be flooded with UV-light to initiate the catalytic cross-linking reaction to cure the resist<sup>89</sup>. This means that the stamp or substrate needs to be transparent. In this thesis a hard mother-stamp is used to create a transparent intermediate polymer stamp (IPS<sup>®</sup>) by T-NIL. The IPS<sup>®</sup> is then used to imprint a UV-curable resist with UV-NIL. Usually, the stamp is not pushed into contact all the way down to the substrate, but a thin residual layer of resist is left to protect the structures. This residual layer can be removed by oxygen-plasma treatment. A schematic illustration of a NIL process is seen in **Figure 2.4**.

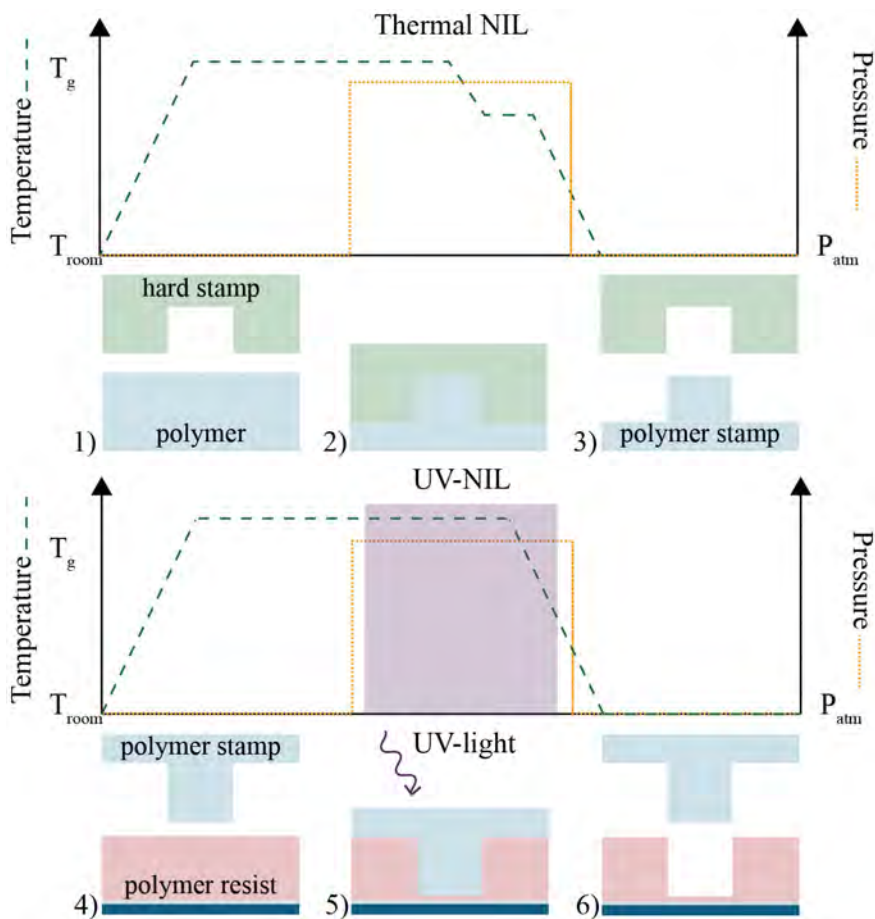


**Figure 2.4.** Schematic illustration of a NIL processes. In thermal imprinting 1) the polymer is heated above its glass transition temperature,  $T_g$ , and 2) imprinted with a hard stamp at an elevated pressure. The polymer is cured by cooling at the elevated pressure. The pressure is then decreased to atmospheric pressure and 3) the stamp is released. In UV-NIL 4) the resist is heated above  $T_g$  and 5) imprinted at an elevated pressure. The resist is cured by UV-light exposure before 6) releasing the stamp. Figure designed based on the process used in our imprinting tool.

## 2.3 Solving combinatorial problems

Many important mathematical problems are of combinatorial nature: the correct solution(s) consist of a combination of input objects. These problems are important in for instance, developing artificial intelligence<sup>52,53</sup>, optimal network routing<sup>56</sup>, game theory<sup>91</sup>, protein folding<sup>54</sup> and cryptography<sup>92</sup>.

A specific subarea of combinatorial problems is the non-deterministic polynomial time (NP) problems. These are problems with multiple solutions that cannot be

verified within a polynomial timeframe<sup>2</sup> as the number of input objects,  $n$ , increase, such as the Travelling Salesman problem Sarah encountered in the introduction. Polynomial time-complexities can be described as  $n^2$ , whereas many combinatorial problems that must be solved by brute force, such as the SSP, are described by an exponential time-complexity,  $2^n$ . Sequentially solving these problems quickly becomes intractable as a function of  $n$  due to the exponential scaling, and instead, parallel computation techniques are required. However, if different NP-problems can be reduced to other NP-problems by algorithms that scale polynomially<sup>93–95</sup>, they are considered complete, i.e., “NP-complete”. Thus, solving one NP-complete problem, offers in principle, a way to solve all problems in this class.

Apart from high-power consuming multi-core processing with electronic parallel computers<sup>3,4</sup>, there are several other alternative parallel computation techniques currently being explored. A few instances of these are: microfluidics based computation<sup>8</sup>, DNA computation<sup>5–7</sup> and quantum computation<sup>9</sup>, described briefly in the section below.

### 2.3.1 Alternative parallel computation techniques

Microfluidics based computation<sup>8</sup> is an NBC technique, in which liquids with fluorescent beads are pushed through channels to explore all possible paths encoding a mathematical problem<sup>8</sup>. External pressures are required<sup>96</sup> to maintain flow along the channels, and the pressure requirements increase impractically as a function of  $n$ . In addition, the architecture becomes intractably complex for larger instances, which prevents the technique from scaling well.

DNA (deoxyribonucleic acid) computation<sup>5–7</sup> uses large amounts of nucleotide (adenosine, thymidine, cytosine and guanidine) combinations, i.e., single stranded DNA, as computing agents. The solutions to the problem are encoded as unique nucleotide sequences and the agents compute by selectively combining with their complementary strands, creating double stranded DNA. This enables all excess single stranded DNA agents with the “wrong” sequence to be discarded. If the paired sequences are immobilized on the surface<sup>7</sup>, the doubled stranded DNA can be extracted and further sorted, so that only the correct solution(s) remain (if there is a correct solution). Another method<sup>97</sup> is to generate an output signal in the form of a single DNA strand with a specific sequence upon activation by DNA agents (complementary DNA strands). The DNA agents combine with partially doubled stranded DNA and then release the originally bound strand after branch migration has occurred, generating the output signal. Despite its versatility, high energy efficiency<sup>5</sup> and parallelism, the major drawback with DNA computation is the quite large error-rate<sup>98</sup>. As a consequence of this, impractical amounts of DNA<sup>7,99</sup> are required to ensure statistically significant results for large problems.

The basis of quantum computation is to process coherent quantum mechanical waves using “qubits”, which are quantum systems with two states that can be superpositioned<sup>9</sup>. Furthermore, in the world of quantum mechanics, the qubits can also be entangled providing even more states which makes this technique massively parallel. However, quantum computation is currently underdeveloped, though a huge effort is ongoing to develop new qubit systems and optimizing computational designs to limit decoherence-causing destructive noise.

### 2.3.2 Computing with molecular motors

All parallel computation methods mentioned in the previous section suffer from drawbacks, and are currently not able to solve large instances of NP-complete problems. We have chosen to explore the possibility of using molecular motors as computing agents in nanoscaled NBC systems, i.e., where the mathematical problem is graphically encoded into a network of channels and junctions (see example in **Figure 1.2**). Each pathway in the network corresponds to a different solution, which means that a large number of proteins can be used to compute problems in a massively parallel manner. Since the agents are self-propelled, no external forces (e.g., pressure difference or electricity) are needed.

A major benefit of computing with molecular motors is the low energy requirement. The self-propelling mechanical work, is fuelled by the chemical energy molecule ATP in a highly energy-efficient<sup>1</sup> manner, as mentioned in section 2.1. For comparison, the Landauer limit, stating the minimal energy cost due to heat generation for any computational system, and is defined as  $kT \ln 2 \approx 2.9 \cdot 10^{-22}$  J per binary operation<sup>100</sup>. The energy cost in molecular motor-powered computational systems can be defined as the amount of energy required to perform one computational operation, such as moving a cytoskeletal filament past one split-junction point to another. This in turn, is determined by the step size and energy cost per step which depends on the number of heads binding to each filament, as each unbinding event requires 1 ATP molecule (corresponding to  $25kT \approx 100 \cdot 10^{-21}$  J). The energy consumption per operation for a molecular motor-based NBC computer<sup>1</sup>, encoding the SSP (see example in **Figure 1.2**) of the 30 first prime numbers, is on average  $\sim 2 \cdot 10^{-14}$  J for both myosin II and kinesin 1 propelled filaments, i.e., the energy required to travel between two split junctions. This is much lower than for an electronic super computer which requires approximately  $2.3 - 5.3 \cdot 10^{-10}$  J per binary operation (see more detailed calculations in Nicolau et al.<sup>1</sup> supporting information S7), several orders of magnitude more than molecular motors. This makes molecular motor-based computation a very viable and worthwhile parallel computation technique, promising also for larger instances of NP-complete problems.

# 3 Surface treatment

*The material chemistry of molecular motor devices must be compatible with the sensitive biological systems used to ensure selective motility and protein binding. This chapter describes how we have optimized the chemical surface treatment of the channel floors (Paper I) and developed a method for cleaning and re-using our nanodevices (Paper IV). We also describe the initial results of a new device system using two different polymers as both channel walls and floors.*

## 3.1 Motivation and previous work

To enable selective motility in biomolecular devices (**Figure 1.3**), the surface chemistry of the channel floors must differ from that of the channel walls. This is achieved here, by using different materials for the floor as compared to the walls, where the motility on the walls is suppressed and the motility on the floors is promoted.

Both the surface charge<sup>39</sup> and surface hydrophobicity<sup>40–42</sup> affect the binding mechanism of HMM to a surface. As mentioned in Chapter 2, the HMM tail has an excess negative charge, whereas its two heads have an excess positive charge. Earlier studies<sup>101–103</sup> have shown motility on positively charged surfaces, suggesting that electrostatic forces promote the adsorption of the negatively charged HMM tail<sup>104,105</sup>. Further studies on the actin-myosin system<sup>29,39,42,43</sup>, indicate that more hydrophobic surfaces tend to promote actin motility due to HMM configurations with the heads extending out into solution<sup>39</sup>. This entropically driven adsorption<sup>40</sup> is believed to be related to partial unfolding<sup>41</sup> of the HMM tail, at the point where it was been cleaved off from light meromyosin by chymotrypsin.

There are several methods to change the surface hydrophobicity, e.g., by oxygen plasma treatment or through surface functionalization with different silanes<sup>43,102,106</sup>. Previous studies<sup>39,43</sup> have shown that trimethylchlorosilane (TMCS) functionalised surfaces promote high quality actin filament motility. The SiO<sub>2</sub> channel floors in the actin-myosin devices form silanols (SiOH) that are easily derivatized with e.g., TMCS. TMCS reacts with surface silanols and forms a monolayer of hydrophobic methyl groups through a chemical vapour deposition (CVD) process (**Figure 3.1**).

To introduce more hydroxyl groups, the SiO<sub>2</sub> surface can be activated with oxygen plasma. This oxygen plasma treatment also oxidizes the surrounding polymer walls used in our devices, making them more hydrophilic, allowing motility to be suppressed.

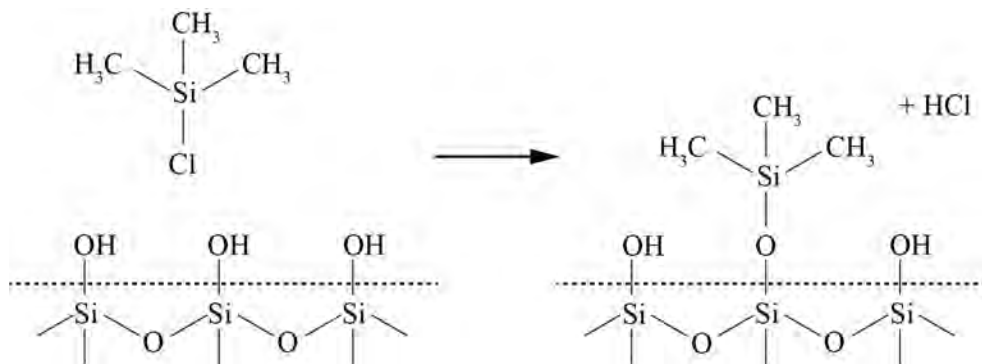


**Figure 3.1.** Schematic illustration of the trimethylchlorosilane (TMCS) reaction with hydroxyl groups on a SiO<sub>2</sub> surface. The chlorine group in TMCS reacts with hydroxyl groups on SiO<sub>2</sub> forming a monolayer of methyl groups (hydrophobic moieties).

In previous TMCS studies<sup>39,43</sup>, the CVD process occurred in a fully saturated TMCS system. Initially, we used a similar process but noticed inconsistencies in sample behaviour, with respect to both the measured static water contact angles and the actin filament sliding velocities for different sample batches. We linked these observations to the primitive nature of the used CVD process, performed in an uncontrolled environment in a glass jar or petri dish, in a glove-box used by multiple users for a large variety of different chemical procedures.

To provide more reliable results, with a consistent device performance in terms of motility on the SiO<sub>2</sub> channel floors, we developed a CVD tool to enable silanisation in a more controlled manner (Paper I), described in more detail in section 3.2 below. We found that the surface hydrophobicity could be tailored by varying the TMCS partial pressure and silanisation duration.

Hitherto, mainly poly(methyl metacrylate) (PMMA) has been used, both for EBL<sup>1,21</sup> and NIL<sup>45</sup> for actin-myosin II devices. Previous actin-myosin motility studies on different polymers<sup>20,29,30,107</sup> was published over a decade ago, and new and improved materials are constantly being developed. Therefore, we studied two new and improved polymer resists, CSAR62 and TU7, for channel wall structures patterned by EBL and NIL, respectively. We found that motility could be suppressed by oxygen plasma treatment, making both polymers a suitable material choice for channel walls. Moreover, no autofluorescence was observed during IVMA with rhodamine-phalloidin labelled actin filaments and both polymers supported motility when left un-treated by oxygen plasma, indicating a lack of protein-toxicity. We also

developed a new device system using a combination of the two polymers as channel floors and channel walls, completely removing the requirement of modifying the SiO<sub>2</sub> surface by silanisation. Albeit observing motility, the filament velocity was still lower on these surfaces as compared to that than on TMCS-derivatised SiO<sub>2</sub> and will need further development before being a viable contender. These studies are further described in section 3.3.

The re-use of nanostructured devices within molecular motor-based applications is highly desirable due to the expensive and time-consuming fabrication procedures, as well as from a sustainability perspective as less material is used and samples shipped elsewhere can be recycled for multiple experiments. Therefore, we developed a process for chemically cleaning the nanostructures from old proteins without disassembling the nanofluidic flow cells (Paper IV, section 3.4).

## 3.2 Controlled surface modification (Paper I)

**Figure 3.2** shows a 3D-render of our home-built CVD set-up for silanisation. The silanisation chamber is pumped down to vacuum pressure ( $10^{-2}$  bar) to reduce the amount of contamination and oxygen levels. The valve system enables nitrogen purging to clean the surfaces and the chamber, before and after silanisation. Since the TMCS is never exposed outside the system, the shelf-time of the silane can be expected to be prolonged and the tool can be located in a fume hood instead of inside a glove box. Furthermore, the valve system enables silanisation at various partial pressures of TMCS.

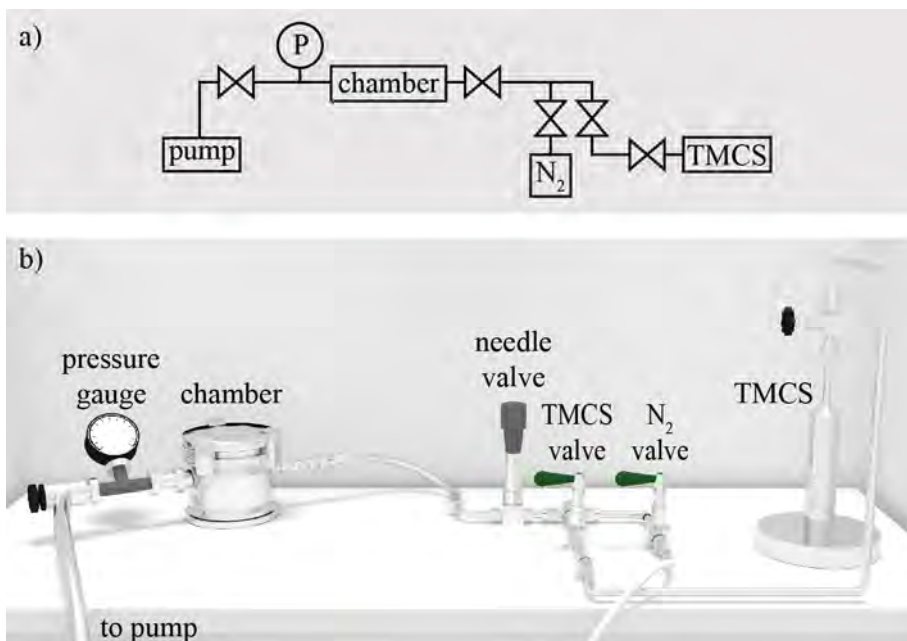


**Figure 3.2.** a) Schematic diagram and b) 3D-render of the chemical vapour deposition tool built for silanisation. The silanisation chamber is pumped down to vacuum pressure and flushed with  $N_2$  in repeated cycles to limit the amount of contamination. The partial pressure of TMCS in the chamber is controlled by valves.

Earlier studies<sup>23,42,108</sup> show an increase in the actin filament sliding velocity with an increasing water contact angle, up to  $\sim 80^\circ$ . At higher contact angles, the HMM proteins are likely to denature, causing a reduction in motility. Also other factors may affect the sliding velocity, including surface roughness<sup>43,109</sup>, due to friction or non-uniform coverage with HMM. All previous studies of motility variations vs contact angle have been done using a range of different surface materials. **Figure 3.3** shows how we were able to tailor the surface hydrophobicity using only one type of silane (TMCS) by varying the silanisation time and partial pressure of TMCS.

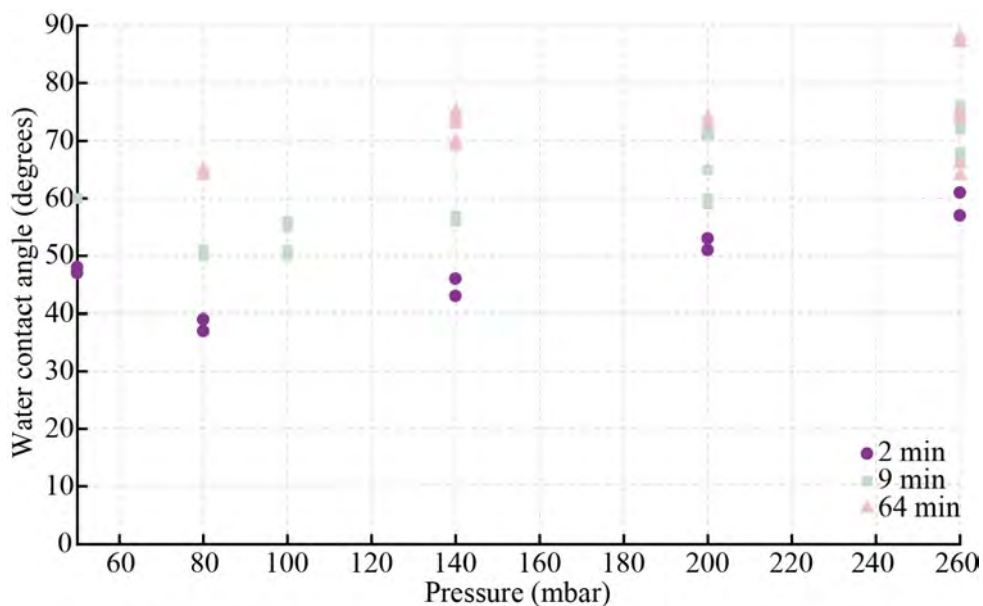


**Figure 3.3.** Water contact angle as a function of chamber pressure at different silanisation times. The chamber pressure is pumped down to  $10^{-2}$  mbar and increased by flowing in TMCS. The silanisation time is defined as the time after reaching the respective chamber pressure. The water contact angle increases with an increased chamber pressure and increased silanisation duration.

The measured water contact angle increased with the silanisation duration and chamber pressure, indicating a higher surface coverage of TMCS. The highest chamber pressure we could obtain was 260 mbar, which corresponds to a fully saturated TMCS system at room temperature. To study the actin filament sliding velocity at different degrees of TMCS coverage, we used two types of protein assay solutions, amc130 (ionic strength 130 mM with methylcellulose) and a60 (ionic strength 60 mM). The higher ionic strength in the amc130 solution promotes fewer, but longer actin filaments as the interaction strength between actin monomers is stronger. Furthermore, the amc130 solution contains methylcellulose which prevents actin filaments from diffusing away from the surface even if they are not tethered by HMM. **Figure 3.4** shows the obtained sliding velocities in both assay solutions for different water contact angles. At the lowest contact angles ( $10^\circ$  and  $28^\circ$ ), only the methylcellulose-containing amc130 solution showed motile actin filaments, albeit at reduced velocity. At these low contact angles on negatively charged  $\text{SiO}_2$ , the majority of the HMM molecules are expected to bind via their motor domains and not via their tail segment<sup>23,42,103,105</sup>, causing a decrease in the number of motility-promoting HMM molecules. The sliding velocities increasing with an increased contact angle is consistent with previous ideas<sup>23,105</sup>, suggesting that the fraction of HMM molecules bound via their tail domain increases with larger contact angles. However, despite the observed higher velocity of actin

filaments at higher contact angles, also the variability within the samples was larger. At  $86^\circ$  we could observe areas with little to no motility. Overall, the total number of motile filaments was also very low on these samples, suggesting stochastic variations in the density of adsorbed functional HMM molecules in different regions.

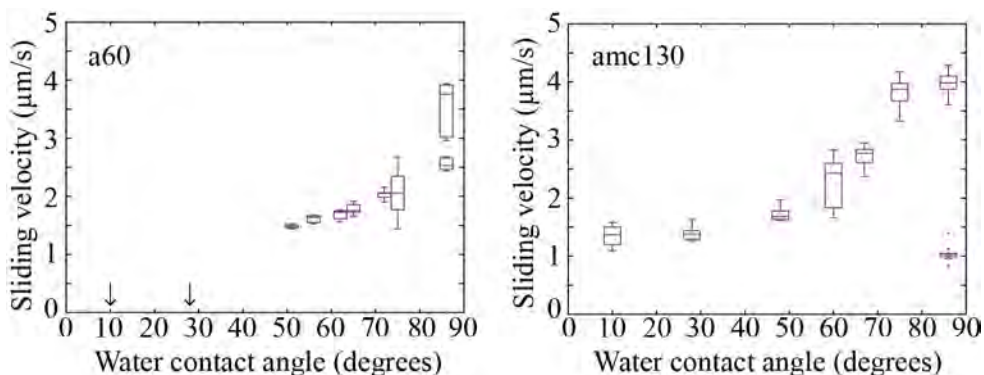


**Figure 3.4.** Actin filament sliding velocities at different water contact angles on TMCS-derivatised  $\text{SiO}_2$  surfaces using a60 and amc130 protein assay solutions. The sliding velocity increases with an increasing water contact angle. At the lowest contact angles in a60 no motility was observed (indicated by arrows). The motility experiments were performed at  $25.3 \pm 0.6^\circ\text{C}$  (a60) and  $24.8 \pm 0.9^\circ\text{C}$  (amc130). 10 filaments/contact angle were analysed. The central mark of the boxplot shows the median of the data set, the top edge of the box shows the 75<sup>th</sup> percentile and the lower edge of the box shows the 25<sup>th</sup> percentile. The whiskers show the most extreme data points not considered to be outliers, where an outlier is defined as a point greater than 1.5 times the interquartile range away from the top or bottom of the box (marked in red). Reprinted with permission from<sup>110</sup>. Copyright (2018) American Chemical Society.

### 3.3 Investigation of new polymer resists

The two main requirements for polymers to be able to be used for molecular motor-based nanotechnology devices are 1) the biocompatibility of the resist with the molecular motor system and 2) the ability to suppress motility to ensure selective motility only the nanostructured channels with TMCS. Furthermore, as the experiments utilise fluorescence microscopy, it is also important that the polymers are not autofluorescent.

Our standard devices are made with polymer walls and TMCS-derivatised  $\text{SiO}_2$  floors. Therefore, all test-devices also went through the necessary steps for processing nanostructured devices; baking, development, cross-linking etc. (details in Paper I). Post-processing, a few chips were exposed to oxygen plasma, and a subset of these were silanised with TMCS. We measured the static water contact angles of the differently treated samples (**Table 3.1**) and compared this to the actin filament velocity results obtained during IVMA experiments.

The oxygen plasma treated surfaces showed a large decrease in the contact angle as compared to the untreated chips. None of the surfaces were affected by the silanisation, indicating that the polymers are very suitable for selective HMM-binding onto the channel floors, and not to the polymer walls. This was confirmed by the results from the IVMA experiments, which showed no motility on the polymer surfaces that had been oxygen treated. Furthermore, we observed high-quality motility, with comparable actin-filament sliding velocities to that on TMCS derivatised SiO<sub>2</sub><sup>110</sup>, on both TU7 and CSAR62 (that had not been exposed to oxygen plasma). These results indicate that both resists are also biocompatible with our system.

**Table 3.1.** Water contact angle measurements on TU7, CSAR62 and SiO<sub>2</sub>.

	TU7 <sup>1</sup>	TU7 <sup>2</sup>	CSAR62 <sup>1</sup>	CSAR62 <sup>2</sup>	SiO <sub>2</sub> <sup>1</sup>
no TMCS	24±1°	65±1°	33±1°	71±1°	<5°
TMCS	26±1°	63±1°	35±1°	71±1°	67±1°

<sup>1</sup>Exposed to oxygen plasma at 5 mbar for 15 s.

<sup>2</sup>Not oxygen plasma treated

To further expand our device tool-box we made new devices with TU7 floors and CSAR62 walls. After spin-coating and baking the TU7, we cross-linked the polymer through a UVL flood exposure (365 nm, 20 s) and then spun a layer of CSAR62 on top. After a second bake, we patterned the top CSAR62 layer by EBL and performed an oxygen plasma treatment before developing the structures in O-xylene. By oxygen plasma treating the surface before development, we expected the top CSAR62 surface to be oxidized while the TU7 channel floors were protected by the undeveloped CSAR62. As a reference, we ran IVMAs on a non-plasma treated CSAR62 surface (showed motility) as well as a CSAR62 surface that had been oxygen plasma treated and then submerged in O-xylene (showed no motility), indicating our plasma treatment was unaffected by the development.

In the nanostructured surfaces with CSAR62 channel walls, we observed selective motility limited to the TU7 channel floors, however, at a reduced actin filament velocity and longevity. **Figure 3.5a** shows the summarised results of actin filament sliding velocities on TMCS derivatised SiO<sub>2</sub> reference surfaces for two temperatures (19°C and 26°C), on flat CSAR62 (also at two temperatures) and TU7 surfaces, and inside nanostructures made with CSAR62 walls with both TMCS derivatised SiO<sub>2</sub> channel floors as well as TU7 channel floors. As could be expected, the velocities are much higher in the higher temperature region. A noticeable difference between the two different types of nanostructured surfaces (CSAR62-TU7 and CSAR62-TMCS) is the much lower velocity on the TU7 floors as compared to the TMCS floors. **Figure 3.5b** shows atomic force micrographs of flat CSAR62, flat TU7 and the nanostructured CSAR62/TU7. The measured root mean square roughness was

similar for both TU7 and CSAR62 ( $0.47 \pm 0.05$  nm and  $0.41 \pm 0.02$ ), but both higher and more uneven for the TU7 channel floors ( $1.90 \pm 0.78$  nm) which likely contain a lot of resist residue due to lack of oxygen treatment after EBL exposure and development. These results are consistent with the idea that rougher surfaces might cause a decrease in the sliding velocity due to friction<sup>43,109</sup>. Further processing optimisations and nanostructuring in these polymer resists are discussed in section 4.4 (Paper III) and 4.5 (paper III).

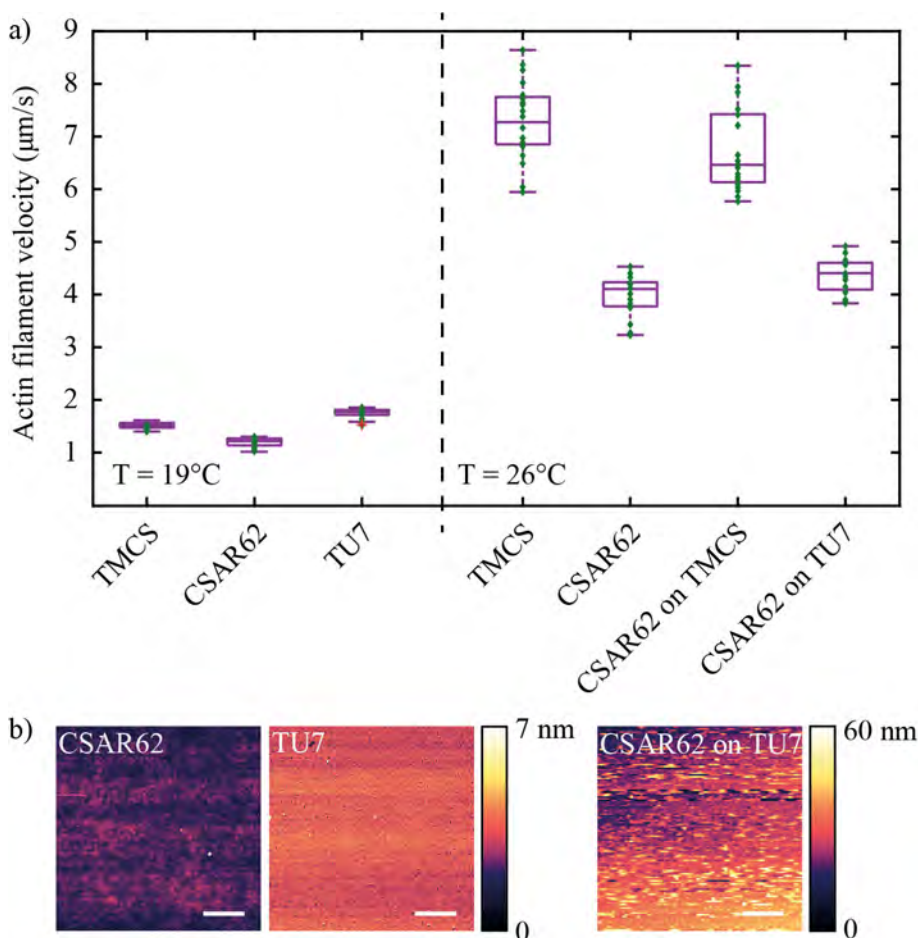


**Figure 3.5.** a) Actin filament sliding velocities on flat TMCS derivatised  $\text{SiO}_2$  surfaces, on flat CSAR62 surfaces and flat TU7 without oxygen plasma exposure, and on nanostructured TMCS-derivatised  $\text{SiO}_2$  and TU7 channel floors with CSAR62 walls. The motility experiments were performed at  $19^\circ\text{C}$  (left) and  $26^\circ\text{C}$  (right). 20 filaments/boxplot were analysed. The central mark of the boxplot shows the median of the data set, the top edge of the box shows the 75<sup>th</sup> percentile and the lower edge of the box shows the 25<sup>th</sup> percentile. The whiskers show the most extreme data points not considered to be outliers, where an outlier is defined as a point greater than 1.5 times the interquartile range away from the top or bottom of the box (marked in red). The green markers show all individual data points. b) Atomic force micrographs of flat CSAR62, flat TU7 and of the TU7 floor inside a larger structure in patterned CSAR62.

### 3.4 Surface regeneration (Paper IV)

During IVMA experiments, we have repeatedly observed how filaments tend to follow the sidewalls of nanostructures. To enable better studies of the effect of different chemical modifications of channel floors, independent of the influence of the walls, we developed some new structures which evenly distribute the filaments across a limited surface area. To try and re-direct the filaments away from the channel walls we introduced *bulges* or *petals*, creating flower-like structures. Before fabricating any real structures, we first ran Monte Carlo simulations (designs and analysis done by me, simulations done by Till Korten, see paper II for more details) to provide a prediction of the filament behaviour (**Figure 3.6**). These simulations were done for the microtubule-kinesin 1 system. In our initial designs we introduced a central pillar to try and increase the number of re-directing events further. However, according to the simulations, these pillars had no evident effect (compare A, B with C, D, E, F). The difference between A and B is a central circle squeezing the flower pattern to different extents, causing different angles at the petal intersections. Clearly, a smaller circle (and thus, higher angle) pushes the filaments more towards the centre. We varied the number of petals from 6 (A), 8 (G), 9 (H), 10 (I) to 12 (J) and found that more petals provide a more delocalised filament distribution. Thus, for the devices, we designed structures with different numbers of petals: 8 and 12, with different inner circle radii: 52, 54, 56, 58, 60  $\mu\text{m}$  and with varied petal radii between 10 and 15  $\mu\text{m}$ . **Figure 3.6K** and **Figure 3.6L** show the maximum projection of two fluorescence microscopy time-lapse movies of an actual device with microtubules evenly distributed across the surface.

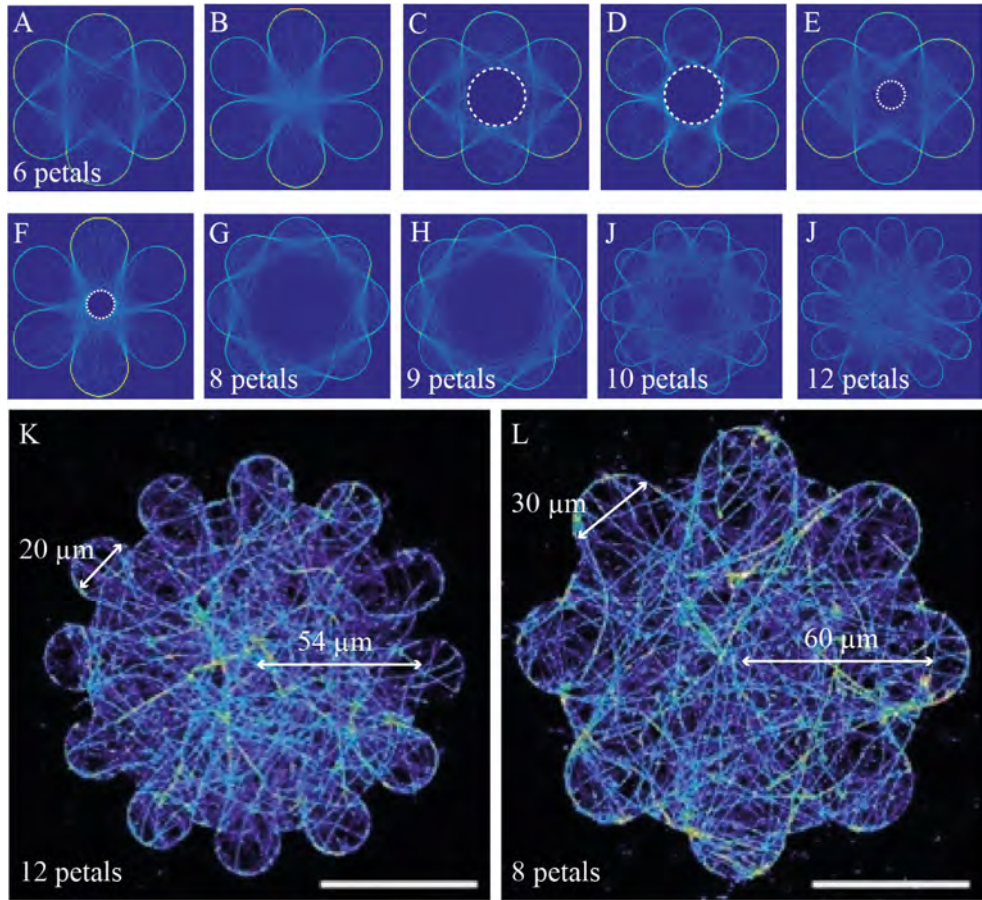


**Figure 3.6.** Heat maps from Monte Carlo simulations (A-J) and fluorescence micrographs (K-L) of microtubules in flower structures with varying properties regarding the number of petals, petal diameter and inner circle radius. Some structures also contain a central pillar (white dashed line). The scale bars in K and L are both 50 μm.

For our initial actin-myosin experiments, we used flat surfaces of TMCS-derivatised glass and SiO<sub>2</sub>, before moving on to large areas of un-patterned CSAR62 EBL resist, partially covering a TMCS-derivatised SiO<sub>2</sub> surface, and finally nanostructures with CSAR62 channel walls and TMCS-derivatised SiO<sub>2</sub> channel floors.

**Figure 3.7** schematically illustrates the developed protocol for surface regeneration involving the proteolytic enzyme proteinase K and the detergent Triton X100. Proteinase K is a non-selective, highly active protease that attacks the peptide bonds between several different amino acids<sup>111</sup>, and it has been used previously to cleave actin<sup>112</sup>. Therefore, we expected the proteinase K to appreciably lower the local protein concentration through proteolysis. Detergents weaken hydrophobic

interactions and are therefore, also likely to weaken the interaction between the HMM molecules and the surface.

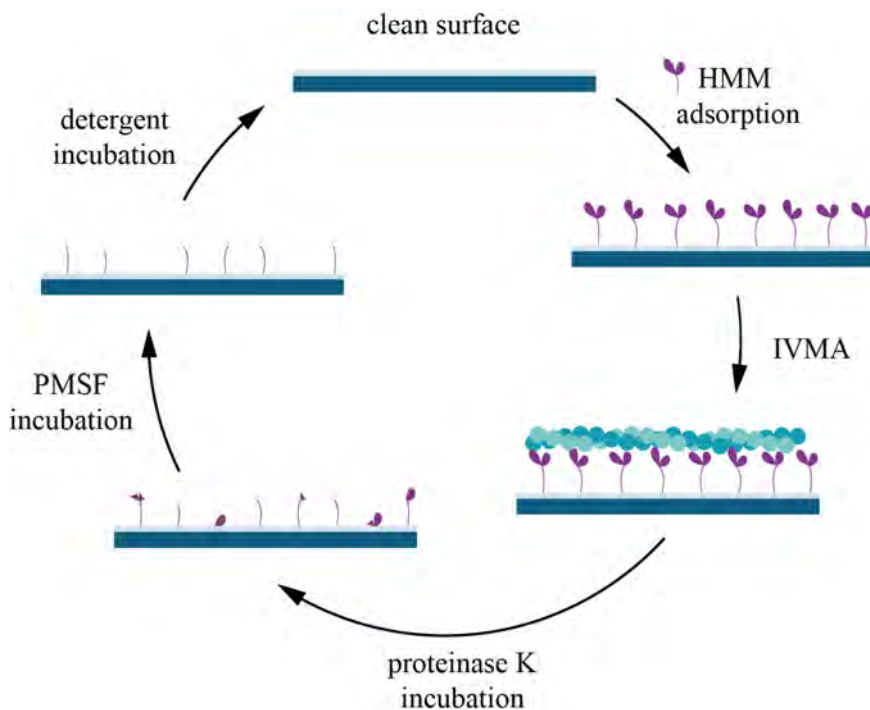


**Figure 3.7.** Schematic illustration of the surface regeneration process. HMM molecules are adsorbed onto a clean surface and an IVMA experiment is run. The sample is then incubated with the non-selective proteolytic enzyme proteinase K in order to cleave the HMM molecules into fragments. To inactivate proteinase K the sample is incubated with phenylmethane sulfonyl fluoride (PMSF) before finally cleaning the surface with the detergent Triton X100 to remove any remaining protein fragments.

**Figure 3.8** shows the regeneration results using different detergents and protocols. Our initial tests were done on TMCS derivatised glass surfaces and no detergent was used. However, we observed a decrease in the actin filament sliding velocity after regeneration, as well as an increased average filament length, while shorter filaments detached more rapidly. This led us to believe that the HMM density was lower on the regenerated surfaces, possibly due to steric hindrance to adsorption of fresh HMM by HMM remnants from the previous IVMA experiment. We were able to optimize this regeneration and obtain full surface recovery in terms of actin filament velocity by including an additional cleaning step with the detergent sodium dodecyl sulphate (SDS). This approach gave good motility quality even after multiple regeneration cycles. We then moved on to the partially covered CSAR62/TMCS-derivatised SiO<sub>2</sub> chips, with equally successful surface

regeneration of the TMCS-derivatised SiO<sub>2</sub> area without sacrificing the motility inhibition on the CSAR62 resist.

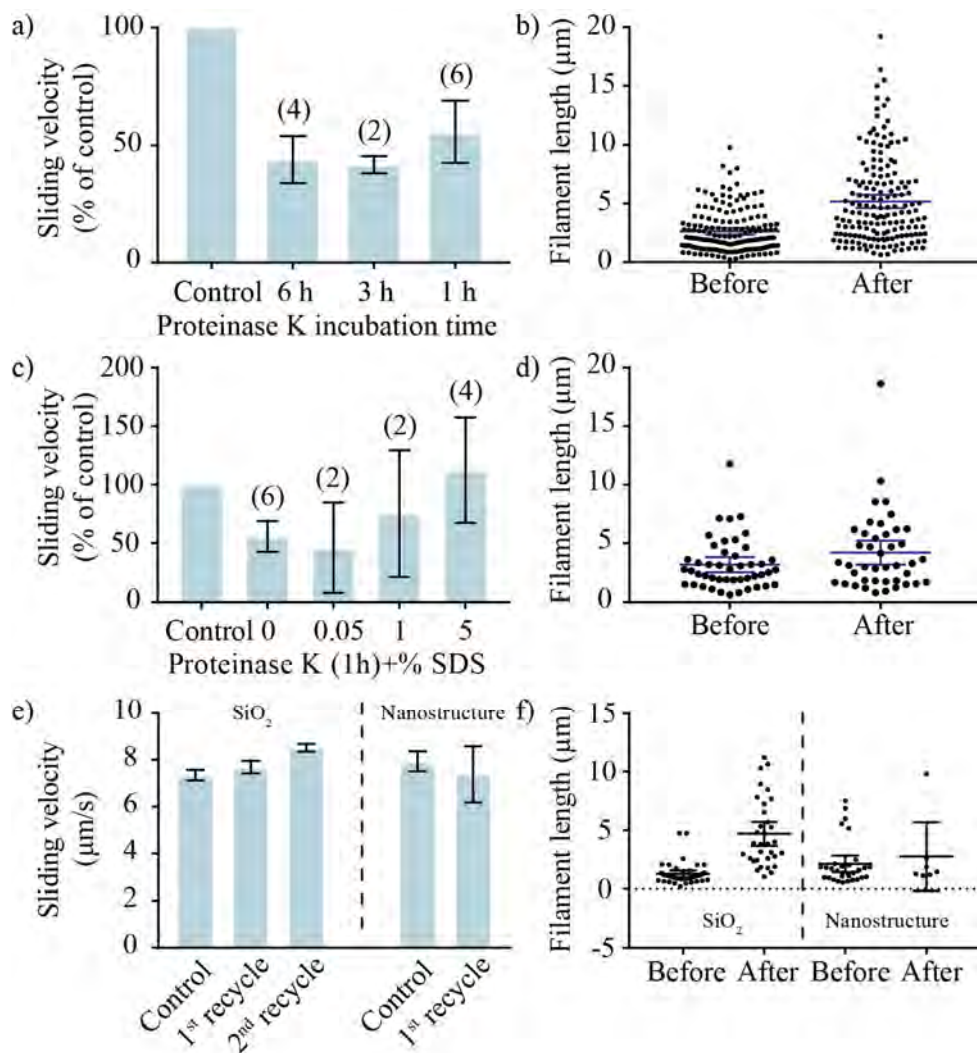


**Figure 3.8.** Actin filament velocity and length on TMCS-derivatised glass surfaces. a) For different incubation times with proteinase K, the number of surfaces are stated in parentheses (). Between 9-30 filaments were analysed for each experiment. b) Before and after regeneration with proteinase K (incubated 1 h) at 6 different experimental occasions. c) For 1 h proteinase K incubation followed by 5 min SDS treatment at 0, 0.05%, 1%, 5%, the number of surfaces are stated in parentheses (). Between 9-30 filaments were analysed for each experiment. The mean sliding velocities are normalised to the same surface before regeneration. d) Before and after regeneration with 1 h proteinase K incubation followed by 5 min 5% SDS treatment at 2 different experimental occasions. e) For 1 h proteinase K incubation followed by 5 min Triton X100 (0.05%) treatment on flat SiO<sub>2</sub> (1 surface, 18-25 filaments analysed) and in nanostructures (1 surface, 3-12 filaments analysed). f) Before and after regeneration with 1 h proteinase K incubation followed by 5 min Triton X100 (0.05%) treatment on flat SiO<sub>2</sub> and in nanostructures. All data are given as the mean  $\pm$ 95% confidence interval.

However, after the regeneration treatment of the nanostructures including CSAR62 channel walls and TMCS-derivatised SiO<sub>2</sub> channel floors, no motility could be observed. One possible basis for this decrease in performance could be interactions between the long hydrocarbon chains in SDS with the ester groups in CSAR62. Another reason could be the anionic nature of SDS, adversely affecting the performance of CSAR62, more prominent in the nanochannels than for larger surfaces. Therefore, we tested a new non-ionic detergent, Triton X100, which does not contain any long hydrocarbon chains. We were then able to obtain successfully regenerated surfaces with high-quality actin filament motility on both TMCS-derivatised glass and on nanostructured surfaces.

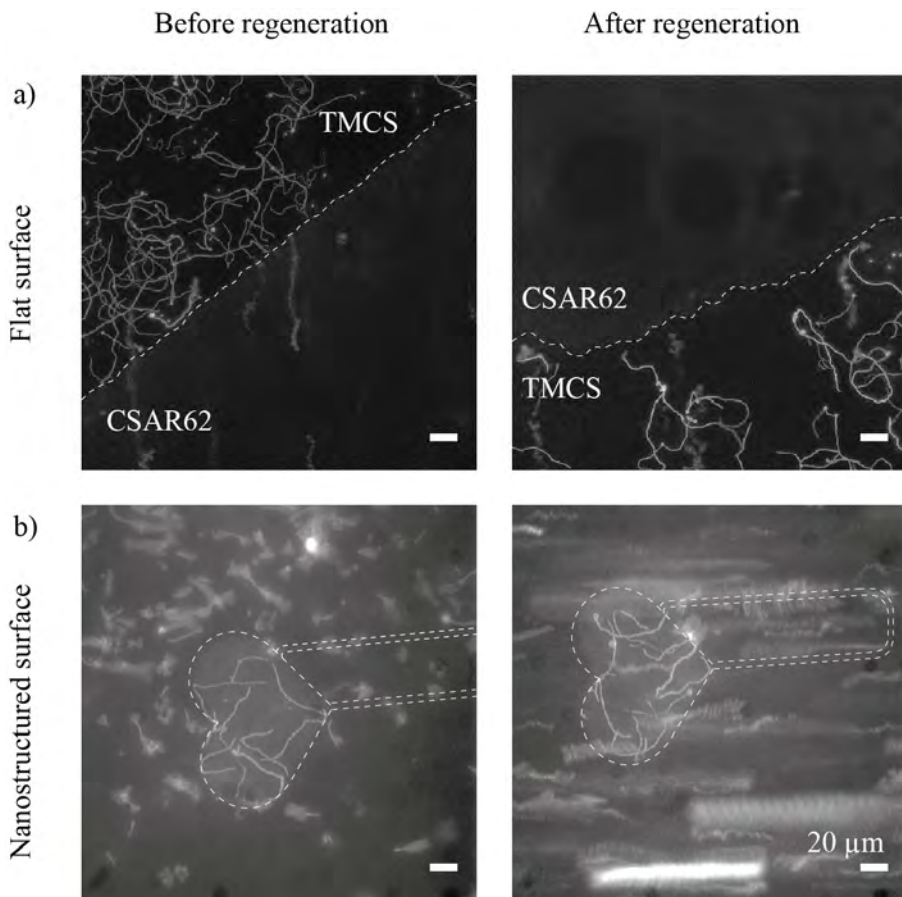


**Figure 3.9.** Maximum projections of fluorescence microscopy recordings (3.8 s) before and after regeneration of a) a partially covered CSAR62 and TMCS-derivatised SiO<sub>2</sub> using proteinase K and 5% SDS and b) nanostructures in CSAR62 with TMCS-derivatised SiO<sub>2</sub> floors using proteinase K and 0.05% Triton X100. The scalebar is 20 μm in all images. CSAR62 was spin-coated and then partially removed from the central region of the sample in a) and b) (both images are from the sample sample but at different locations).

### 3.5 Concluding remarks

By modifying the surface hydrophobicity in a controlled manner, we were able to tune the actin filament sliding velocity without changing the type of silane or material, which has greatly improved the yield of successful devices. We also demonstrated a novel method for fabricating nanodevices using the two polymer resists CSAR62 and TU7 as they both promote motility if they are left untreated, as well as inhibit motility if they are treated with oxygen plasma. Therefore, both resists serve well as channel walls inhibiting motility. However, channel floors made of motility-promoting (untreated) TU7 with motility-inhibiting (oxygen treated) CSAR62 walls need further optimization, likely by improving residual resist removal after EBL exposure. This may be done by further expanding the study to include different developers or chemical cleaning procedures. Moreover, we developed a technique for recycling molecular motor-based devices using the non-selective protease Proteinase K and surfactant Triton X100, creating a more sustainable fabrication process. These findings strengthen and expand the studies of chemically confining molecular motors in nanotechnology devices by including new materials and treatment protocols, the impact of which, is further discussed in the final chapter of this thesis.

# 4 Patterning nanostructures

*The scalable fabrication of our biocomputation devices require advanced nanofabrication techniques to provide nanometre-scale features, combined with a high throughput of larger scale samples for system development and experimental optimisation. This chapter describes the development of fabrication methods for patterning the channel walls for the actin-myosin II system by electron beam lithography and nanoimprint lithography.*

## 4.1 Motivation and previous work

The nanostructures used for physically confining molecular motor systems can be patterned by multiple techniques. The actin-myosin II system requires a high spatial resolution down to a few nanometres based on the necessary feature size (channel widths around 200-300 nm with details requiring sub 10 nm resolution, for junction details, see Chapter 2). Larger structures can be patterned by UVL, while the majority of the patterns need to be patterned by EBL. NIL can also be used to enable a higher fabrication throughput of larger devices, while still maintaining a high resolution.

The major drawbacks of UVL and NIL for our current experimental system is the requirement for a UVL mask for selectively exposing a photosensitive resist, and the necessity of a NIL stamp for imprinting features. This limits the flexibility in developing new structures within a reasonable time-frame, as new masks and stamps need to be fabricated for each new feature. However, when a suitable device design is defined, both these techniques can be used for large-scale fabrication in a feasible and sustainable manner. There are different UVL methods, the more commonly used tools use visible wavelengths providing a resolution  $\sim 50$  nm<sup>82</sup> due to diffraction limits, which makes this technique less suitable for actin-myosin devices. There are also more advanced methods like extreme UVL, pushing the resolution to sub 10 nm<sup>113,114</sup> by using very short wavelengths of light. However, for design development, EBL is still the preferred lithography method because of the flexibility, despite the longer exposure times required.

The device fabrication done by our group<sup>1</sup> prior to this thesis work, was relatively inexpensive and time-efficient due to the limited pattern size. However, the increased dimensions associated with an upscaled complexity, require optimisations for higher throughput fabrication (Paper III). We have therefore, optimised the EBL processing parameters and developed a process for fabricating devices by NIL.

To reduce EBL exposure times, we began with switching the EBL resist from PMMA to CSAR62, which has a higher sensitivity (allowing shorter exposure times). Similar to PMMA, CSAR62 is a methacrylate based polymer<sup>115</sup> but it has a higher contrast and resolution as compared to PMMA<sup>115,116</sup>. For PMMA, sub-10 nm<sup>117,118</sup> resolution is possible, but it requires higher electron doses for a given EBL system and developer. The exposure parameters for patterning actin-myosin II structures in CSAR62 are presented in Paper III and section 4.2.

NIL has previously been used for fabricating narrow channels (100-400 nm) for actin-myosin II devices in PMMA by Bunk et al.<sup>45</sup>. PMMA has a glass transition temperature around 95-106°C, and was in Bunk et al.<sup>45</sup> imprinted at 200°C. At temperatures above 100°C, thermal expansion can cause pattern deformations if the substrate and stamp are not thermally matched<sup>119</sup>. Here we use a new imprinting resist, TU7, developed by Obducat, with a lower glass transition temperature that can be imprinted at 75°C.

Furthermore, structures for molecular motors also require large open areas, loading zones (see **Figure 1.2**), to collect the filament agents from solution and funnel them towards the connecting channel network<sup>1,21</sup>. These loading zones are difficult to imprint by NIL, as areas with a large width relative to the height require the displacement of polymer across large distances<sup>46</sup>. We extended the previous study, to include a method of fabricating a new type of loading zone that was re-designed to contain nanoscaled pillars to provide close by regions into which the resist could be displaced (Paper II). By choosing the resist layer as thin as possible, we were able to optimise the stamp filling, allowing polymer to displace into the pillars. We managed to obtain motility inside the loading zones, albeit, at a lower velocity as compared to EBL patterned loading zones. Interestingly, after simulating the filament movement (simulations done by Till Korten, analysed by me) inside the new loading zones containing pillars, we found that the overall filament movement can be shifted to distribute the filaments evenly across the surface or towards one side. The developed imprinting process is described in Paper II and in section 4.3.

## 4.2 Process optimisation for EBL (Paper III)

**Figure 4.1** shows a dose test for exposing CSAR62 at 20 kV acceleration voltage. Previously, we were exposing PMMA950K at 20 kV with dose 250  $\mu\text{C}/\text{cm}^2$  and

developing in a 3:1 mixture of isopropanol and methyl isobutyl ketone mixture. By switching to CSAR62, we were able to reduce the exposure dose (using the same acceleration voltage, 20 kV) down to  $60 \mu\text{C}/\text{cm}^2$  when developed in O-xylene, which enables  $\sim 4$  times shorter exposures, while maintaining a high resolution.

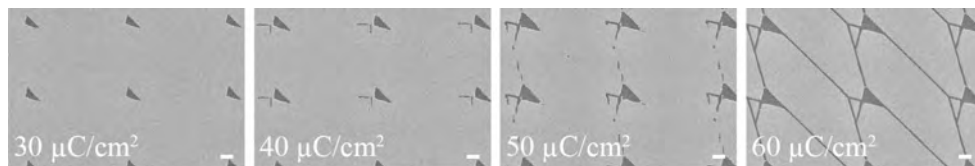


**Figure 4.1.** Scanning electron micrographs of CSAR62 exposed at 30, 40, 50 and  $60 \mu\text{C}/\text{cm}^2$  at 20 kV, and developed in O-xylene. The scalebar is  $1 \mu\text{m}$  in all images.

To further decrease the exposure times, we tried increasing the aperture size in the electron column. This can however, cause a decrease in resolution due to a broader electron probe. Therefore, we performed IVMA experiments to examine if this possible decrease in resolution would affect the actin filament motility in our channels, most importantly if we would still observe unidirectional motion. **Figure 4.2** shows two fluorescence micrographs of patterns exposed with 10 and  $20 \mu\text{m}$  apertures. No noticeable loss in feature details and no U-turns were observed in the higher aperture structures, indicating we could expose our structures using a larger aperture, here  $20 \mu\text{m}$  instead of  $10 \mu\text{m}$ . This in turn increased our beam current from  $\sim 0.014 \text{ nA}$  to  $\sim 0.12 \text{ nA}$ , increasing our throughput by a factor of 8.5.

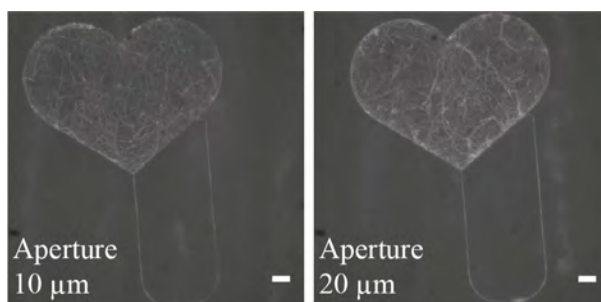


**Figure 4.2.** Fluorescence micrographs of patterns exposed with a  $10 \mu\text{m}$  aperture and  $20 \mu\text{m}$  aperture at 20 kV. The images show the maximum intensity for a 60 s time-lapse movie of an actin-myosin IVMA experiment. The scalebar is  $5 \mu\text{m}$  in both images.

A few years into this thesis work, our lab bought a new EBL system with a higher acceleration voltage, 50 kV, that, together with a  $40 \mu\text{m}$  aperture, provided beam currents of  $\sim 0.60 \text{ nA}$ . Thus, this would enable an even higher throughput due to faster exposure times. However, as mentioned in Chapter 2, higher acceleration voltages will decrease the number of forward-scattered primary electrons, and

higher electron doses will be required. Furthermore, the increased electron energy will cause the beam to penetrate deeper into the substrate, causing more backscattered and secondary electrons generating proximity exposures. To examine the pattern broadening at different doses, we performed a new dose test ranging from  $175 \mu\text{C}/\text{cm}^2$  to  $275 \mu\text{C}/\text{cm}^2$  in steps of  $25 \mu\text{C}/\text{cm}^2$ . We also switched the developer to amyl acetate which is supposed to provide an even higher contrast between exposed and unexposed CSAR62<sup>116</sup>. However, amyl acetate also leaves large amounts of residue on the channel floor as compared to O-xylene<sup>116</sup>, which is why O-xylene was used as a developer in the double resist (CSAR62/TU7) IVMA experiment described in section 3.3. As seen in **Figure 4.3**, we found that it was possible to achieve well defined features at  $250 \mu\text{C}/\text{cm}^2$  with an acceptable pattern broadening (40-50 nm).

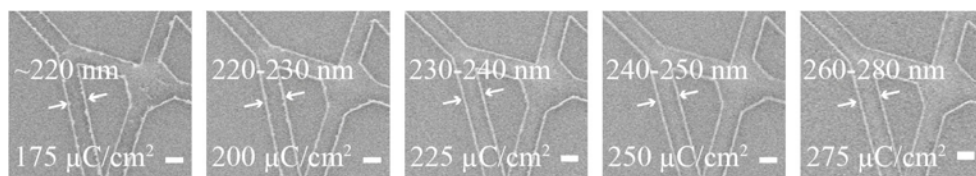


**Figure 4.3.** Scanning electron micrographs of CSAR62 exposed at 175, 200, 225, 250 and 275  $\mu\text{C}/\text{cm}^2$  at 50 kV developed in amyl acetate. The scalebar is 250 nm in all images.

### 4.3 NIL for molecular motor structures (Paper II)

**Figure 4.4** shows heat maps of Monte Carlo simulations (analysis done by me, simulations by Till Korten, TUD, see details in Paper II) estimating what effect a structural re-design of the loading zone with pillars would have on the actin filament behaviour. We found that the structural design and placement of the pillars can be used to tailor the emptying rate (**Figure 4.5**) from the loading zone as well as filament guidance. Designs A, B, F and G all have three sharp corners which seems to provide a larger difference in the emptying rate between the hexagonal and square placed pillar patterns as compared to designs D and E, which just have one sharp corner. Furthermore, the completely symmetrical pillar shapes in designs H and I are nearly identical, both compared to each other as well as between the hexagonal and square patterns. According to the heatmaps in **Figure 4.4**, the latter two (completely symmetrical) designs also seem to distribute the filaments more evenly inside the loading zone. The patterns with a sharp corner pointing towards the exit both have an overall higher emptying rate than their corresponding patterns rotated  $180^\circ$  (compare A vs B, D vs E and F vs G), as well as a higher emptying rate in the square pattern repetition as compared to the hexagonal repetition. The most noticeable effect in both **Figure 4.4** and **Figure 4.5** can be seen between patterns F

and G which have three sharp corners and a concave arc in the pattern causing the filaments to clearly shift towards one side of the loading zone. The reason for this is likely that the filaments hitting the concave wall are constantly re-directed according to their impinging angle<sup>25</sup>. This coincides well with the simulations and experimental results described in section 3.4. Similar simulations to these have also been successfully used for predicting the behaviour of the actin-myosin II and microtubule-kinesin 1 system in nanostructures<sup>1,120</sup>.

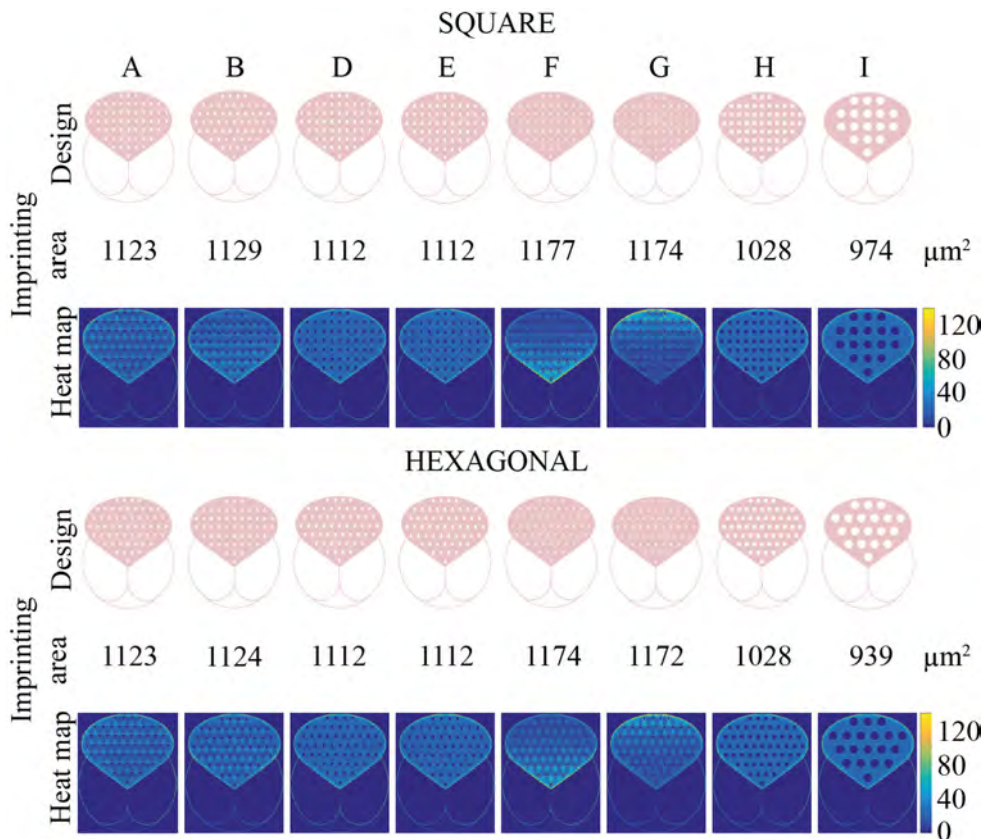


**Figure 4.4.** Loading zone designs for nanoimprint lithography. We created eight different pillar patterns placed in both a square and hexagonal pattern repetition. The heat maps show the filament distribution of 240 actin filaments (10  $\mu\text{m}$  persistence length) simulated for 1500 s, the colour bar corresponds to the number of filaments visiting each pixel. The imprinting area corresponds to the amount of open  $\text{SiO}_2$  available for HMM binding. Reprinted from<sup>121</sup>. Copyright (2019) IOPScience (gold open access).

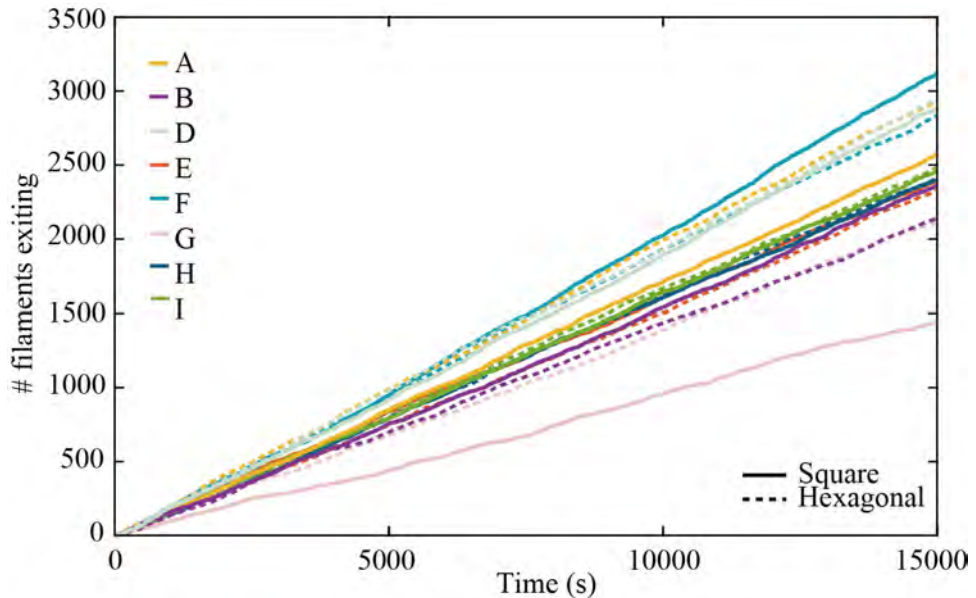


**Figure 4.5.** Emptying rate for the different loading zone designs shown as the number of filaments exiting as a function of time. The emptying rate varies depending on the pattern shape as well as the pattern repetition design (square or hexagonal). Reprinted from<sup>121</sup>. Copyright (2019) IOPScience (gold open access).

As mentioned, one of the difficulties for imprinting features with a large difference between height and width, is related to displacing large amounts of polymer. By including pillars into our design, we expected to provide regions into which polymer could be displaced. Furthermore, we aimed to limit the amount of displaced polymer by minimizing the resist layer thickness in order to obtain capillary flow upwards into the cavities, without suffering from insufficient filling during imprint. In standard NIL procedures, the resist layer is chosen thicker than the stamp protrusions to prevent damaging the stamp and deforming the pattern. However, by using a soft intermediate polymer stamp, IPS<sup>®</sup>, this risk is eliminated. To test this approach, we spin-coated TU7-220 at various spin-speeds ranging from 1000-3000 rpm. To imprint our structures, we fabricated a hard stamp in SiO<sub>2</sub> on a 4" Si wafer. A new IPS<sup>®</sup> for imprinting TU7 was made through thermal NIL for each wafer using the hard stamp. **Figure 4.6** shows the resulting TU7-220 thickness for different spin-speeds and scanning electron micrographs of the structures. Only the thickest TU7-220 layer used (~350 nm, still thinner than the 380 nm stamp cavities) provided sufficient filling of the stamp protrusions.

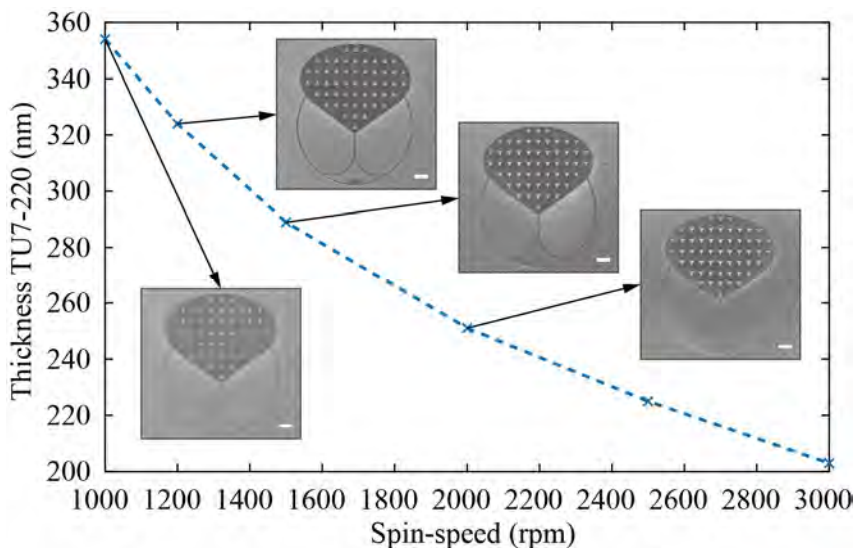


**Figure 4.6.** Spin-curve of TU7-220 and scanning electron micrographs of the imprinted structures for each resist thickness. The structures in the thickest TU7 were imprinted without defects, while the thinner layers had an increasing number of air-pockets present due to insufficient stamp filling. The scalebar is 10  $\mu\text{m}$  in all images. Reprinted from<sup>121</sup>. Copyright (2019) IOPScience (gold open access).

To measure the residual layer, we made a small scratch across the samples. **Figure 4.7** shows AFM scans of the residual removal of TU7 at different reactive ion etching times in oxygen plasma. It is important that the residual TU7 layer is completely removed as the underlying  $\text{SiO}_2$  must be fully exposed to enable silanisation and HMM binding.

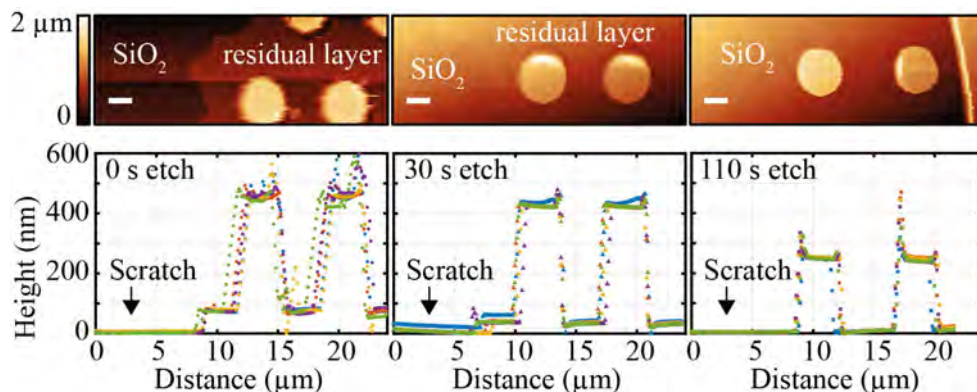


**Figure 4.7.** Atomic force measurement scans of the residual TU7 layer in the imprinted structures. The colours in the graphs represent different (single pixel) profile scans across the pillars. The scalebar is 2  $\mu\text{m}$  in all images. Reprinted from<sup>121</sup>. Copyright (2019) IOPScience (gold open access).

Scanning electron micrographs of the resulting structures are seen in **Figure 4.8** together with a series of fluorescence micrographs during an IVMA experiment with actin-myosin. We were able to obtain motility inside both the loading zones and the channels, with a good spread of filaments across the entire loading zone. However, the total number of filaments observed was very low, and we observed several detachment events upon head-on collisions, similar to previous findings<sup>24,47</sup>. The decrease in filament number may be related to a lower surface area (see **Figure 4.4**) as compared to loading zones without any pillars (which have an area of  $1200 \mu\text{m}^2$ ), in combination with filament detachment due to an increased number of collisions caused by the increase in wall surface.

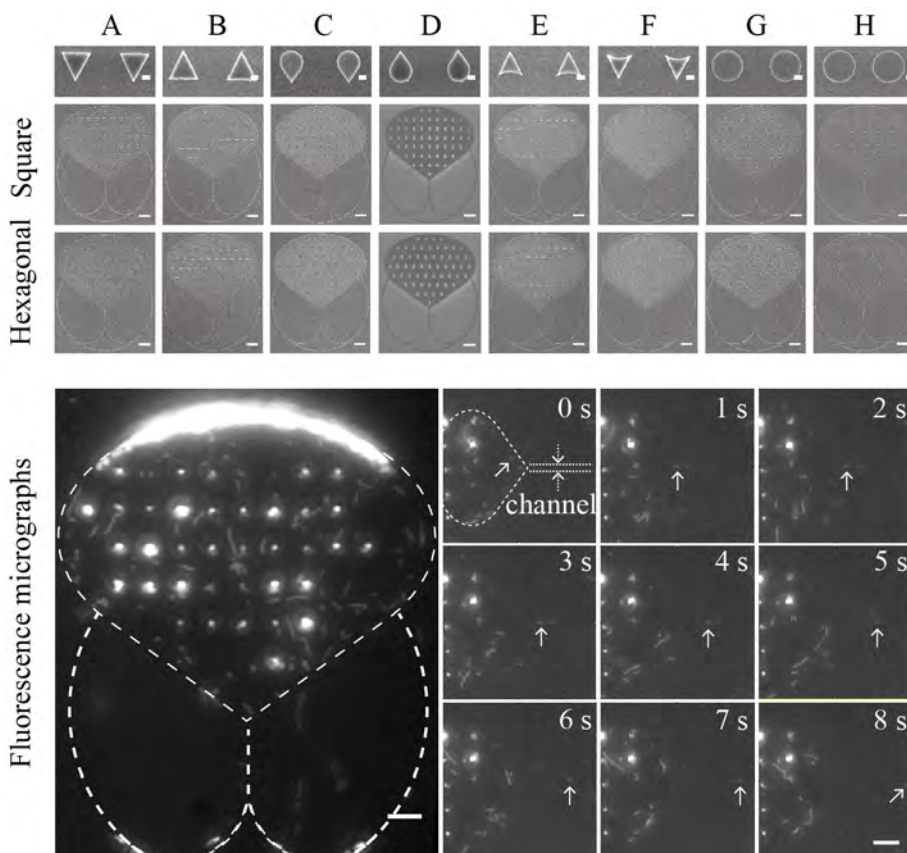


**Figure 4.8.** Scanning electron micrographs of the imprinted structures and fluorescence micrographs of an IVMA experiment with actin-myosin II showing a wide-spread filament distribution across the surface and a sequence of snap shots showing how an actin filament moves from the loading zones into a nanochannel. The scalebar for the zoom-in SEM images is  $1 \mu\text{m}$  and  $10 \mu\text{m}$  for the larger SEM images. The scalebar for the fluorescence micrograph is  $5 \mu\text{m}$  in all images. Reprinted from<sup>121</sup>. Copyright (2019) IOPScience (gold open access).

## 4.4 Concluding remarks

We demonstrated that CSAR62 is a suitable resist for patterning molecular motor-based devices by electron beam lithography, providing higher throughput than PMMA-based devices in the EBL systems used for this work. Furthermore, it is possible to fabricate both loading zones and channels in TU7 using NIL. However, the latter fabrication process needs further optimization before it can be used as a reliable method, both to improve motility inside the loading zones and to expand the imprinting to include large networks of channels. A very interesting effect to consider for future applications is the possibility of directing the motion of filaments by placing structures in specific formations, e.g., to separate different sensing areas. Moreover, it is important to keep studying the processing parameters of new resist materials as they will keep expanding the current limitations of devices and what structures are possible to fabricate. These findings strengthen and expand the studies of physically confining molecular motors in nanotechnology devices by developing processing methods in two new resists for high-throughput fabrication by EBL and NIL.

# 5 Computing with molecular motors

*This chapter describes the progress toward computing in large-scale networks using molecular motors. The so-called exact cover (EXCOV) problem is presented in more detail and the conversion into the subset sum problem is described. We present the measures taken to realise large-scale computation with molecular motors as well as the progress towards experimentally solving a ~1000-solution parallel computation network.*

## 5.1 Motivation and previous work

NBC with molecular motors was first published in 2016<sup>1</sup>, solving a small proof-of-principle SSP<sup>34</sup>, which asks what sums are possible to create from a given set of numbers (see example in Chapter 1). As described in the previous study<sup>1</sup>, we use a channel network with two different types of junctions, split and pass, to direct the motion of our agents. The filaments are collected from the buffer in the large loading zones which guide them into the networks (see **Figure 1.2**). Filaments entering a pass junction are only allowed to travel straight, following the path from which they came. At the split junctions, the filaments can turn either right or travel straight down (looking at the network from above). If they go right a number is added, and if they go straight down, no number is added. The value of the added number matches the number of pass junctions the filament will pass until the next split junction. Each exit at the end of the network, corresponds to a different solution in increasing order, meaning that the farther right a filament travels (when viewing the network from above), the higher the resulting sum of numbers added. By using these traffic rules, the problem encoded can be solved in a massively parallel manner within polynomial time, without knowing the solutions in advance, i.e., the numbers and solutions will be defined by the junction positions.

During the course of this thesis, we expanded this encoding to include the exact cover problem (EXCOV), by a theoretically converting (conversion developed by our collaborators<sup>122</sup>) the EXCOV problem into the SSP. The aims were to (i) implement a larger experimental network with around 1000 solutions (compared to tens previously)<sup>1</sup>, and (ii) to demonstrate the conversion of one NP-complete problem into another for NBC with molecular motors.

## 5.2 Conversion of EXCOV into SSP

The EXCOV problem asks if an exact cover of numbers can be created of a given set of sets. For instance, given the sets (1,3), (2,3), (2,4), (3,4), the exact cover corresponds to a combination of sets that, together, include each number (1-4) exactly once. In the problem Sarah encountered in the introduction, the exact cover would be the set of trips where she visits each country exactly once and thus, prevents a diplomatic crisis and mass extinction. To convert the number sets into an SSP network, we first translate each set into a binary number, where each bit represents an element in the set. In the set (1,3), position 1 and 3 will be represented by a 1, and position 2 and 4 (absent in the set) will be represented by a 0, i.e., 1 0 1 0. The set (2,3) will be represented by a 1 in position 2 and 3, and by a 0 in position 1 and 4, i.e., 0 1 1 0, see more examples in **Table 5.1**. Thereafter, each binary number is translated into its decimal number, providing a new set of numbers, which are encoded in an SSP network (see **Figure 1.2**).

**Table 5.1.** Translation of a small example of EXCOV subsets into a SSP set.

	Set	Binary number	Conversion	Decimal number
Set 1	(1,3)	1 0 1 0	$2^3+2^1$	10
Set 2	(2,3)	0 1 1 0	$2^2+2^1$	6
Set 3	(2,4)	0 1 0 1	$2^2+2^0$	5
Set 4	(3,4)	0 0 1 1	$2^1+2^0$	3
Exact cover	(1,2,3,4)	1 1 1 1	$2^3+2^2+2^1+2^0$	15

Using this encoding, the exact cover of the numbers (1-4) corresponds to the binary number (1 1 1 1) = 15. Thus, we know what sum an exact cover corresponds to, and therefore, only need to look at this network exit to find out whether or not an exact cover exists. If filaments exit at this exit, then the set of sets contains an exact cover, which for this small instance corresponds to Set 1 and Set 3.

## 5.3 Introducing “reset” junctions

As described in the introduction, the channel network consists of two types of junctions: split and pass junctions. A drawback of the binary conversion introduced in the previous section is the case of carrying numbers. When adding binary numbers,  $1+0=1$ ,  $0+0=0$  and  $0+1=1$ , but  $1+1=0$ , carrying 1 to the next bit, see example in **Table 5.2**.

**Table 5.2.** Binary addition with and without carrying numbers.

Binary addition without carry	Binary addition with carry
1 0 0 1 0 0 1	1 0 1 1 0 0 1
<u>+ 0 1 1 0 1 0 0</u>	<u>+ 0 1 1 0 1 0 0</u>
1 1 1 1 1 0 1	1 0 0 0 1 1 0 1

If numbers are carried, a subset of sets can add up to what seemingly is an exact cover but may include multiples of an element, e.g. the subsets (1,3)=1 0 1 0, (3)=0 0 1 0, (3,4)=0 0 1 1 do not contain an exact cover (as the number 2 is missing and element 3 is present in multiple sets) but still sum up to the binary number (1 1 1 1) due to carry. To avoid carrying of numbers, a third junction-type was introduced: reset junctions<sup>122</sup>, to replace split junctions where binary carry-over could occur. At reset junctions, filaments from both junction inlets exit one collective path downward, meaning no addition can occur (**Figure 5.1**).

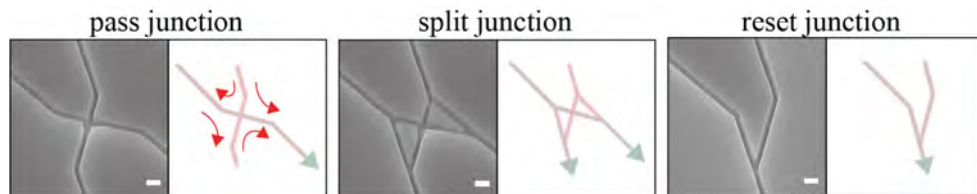


**Figure 5.1.** Scanning electron micrographs and schematic illustrations of the different junction types used in the biocomputational network. The green dashed lines mark the allowed paths and the red full lines mark illegal paths. At pass junctions the filaments continue along the same path they came from. At split junctions the filaments can turn right to add a number or travel straight down (nothing is added). At reset junctions the filaments can only travel straight down and no numbers are added. The scalebar is 500 nm for all micrographs.

## 5.4 Reducing the network size

The position of the split rows define what numbers are encoded in the network, as they define how far right a filament can travel before encountering the next split junction (see example in **Figure 1.2**). The subsets given in **Table 5.3** encodes an EXCOV problem with a solution-space of about 1000 solutions, meaning that a brute force approach would need to check about 1000 possible solutions. The encoded numbers are placed in descending order inside the network. This means that the first addition combination encountered in the sets seen in **Table 5.3** corresponds to whether or not to add 244. This is followed by the option of adding 234, 228, 224 and so on for each combination, see **Figure 5.2**. However, we do not need to encode all solutions. The number combinations creating sums above 255 as well as their corresponding exits can be discarded as they all contain multiples of the same number/bit (see **Table 5.3** and dashed lines in **Figure 5.2**). Therefore, these

sections of the network can be removed. Instead, the numbers that cannot be combined to create an exact cover can be used as entrance points. In **Figure 5.2** these numbers correspond to columns 0, 224, 228, 234 and 244. The remaining network is so small, that the agents entering at 0 cannot reach exit 255, and therefore, this entrance does not need to be part of the network. By introducing multiple inlets, we not only reduce the network size, but we also decrease the bottle-neck effect of feeding in filaments to a large network through just one inlet.

**Table 5.3.** Translation of a large example of EXCOV subsets into a SSP set.

	Set	Binary number	Conversion	Decimal number
Set 1	(7,8)	0 0 0 0 0 0 1 1	$2^1+2^0$	3
Set 2	(6,8)	0 0 0 0 0 1 0 1	$2^2+2^0$	5
Set 3	(6,7)	0 0 0 0 0 1 1 0	$2^2+2^1$	6
Set 4	(6,7,8)	0 0 0 0 0 1 1 1	$2^2+2^1+2^0$	7
Set 5	(5,8)	0 0 0 0 1 0 0 1	$2^3+2^0$	9
Set 6	(4,6,8)	0 0 0 1 0 1 0 1	$2^4+2^2+2^0$	21
Set 7	(1,2,3)	1 1 1 0 0 0 0 0	$2^7+2^6+2^5$	224
Set 8	(1,2,3,6)	1 1 1 0 0 1 0 0	$2^7+2^6+2^5+2^2$	228
Set 9	(1,2,3,5,7)	1 1 1 0 1 0 1 0	$2^7+2^6+2^5+2^3+2^1$	234
Set 10	(1,2,3,4,6)	1 1 1 1 0 1 0 0	$2^7+2^6+2^5+2^4+2^2$	244
Exact cover	(1,2,3,4,5,6,7)	1 1 1 1 1 1 1 1	$2^7+2^6+2^5+2^4+2^3+2^2+2^1+2^0$	255

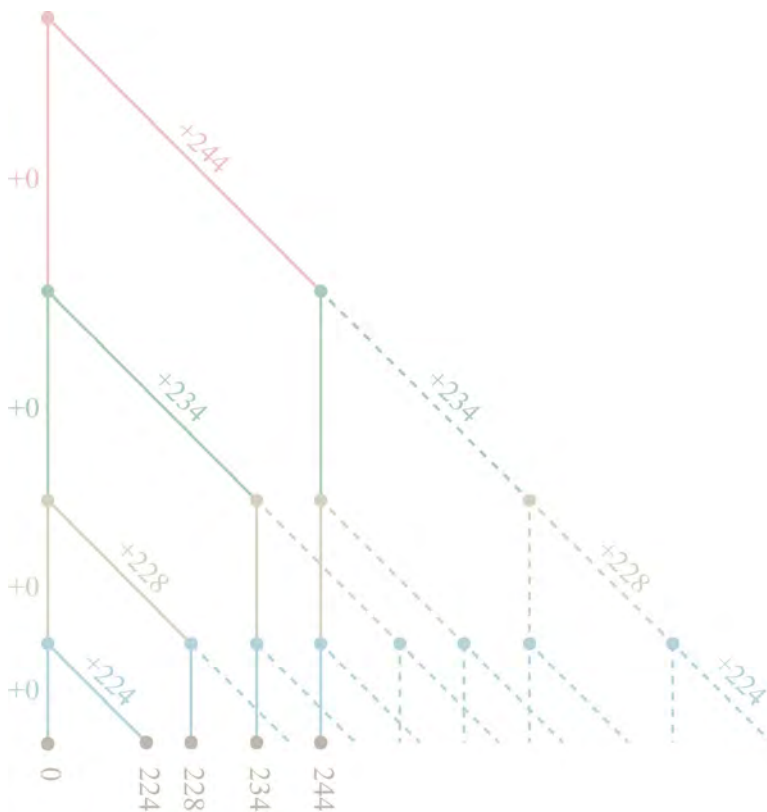


**Figure 5.2.** Top section of the network encoding the four largest decimal numbers in Table 5.3. The full lines correspond to possible paths, while the dashed lines create sums above the EXCOV sum 255. Split junctions are marked with a filled circle. At each split junction the filaments can either turn right to add a number or move downwards (no number is added). The farther right a filament moves the higher the resulting sum. Exits corresponding to sums larger than 255 can be removed as these sums contain multiple elements of the same number. Instead, a smaller network can be created, with inlets at the marked exits, increasing the number of filaments that can be fed into the network simultaneously and reducing the trajectory path of each filament.

## 5.5 Implementing the 1000 solution network

We fabricated an SSP network encoding the sets in **Table 5.3**, with the network size-reductions described in the previous section. This network encodes an EXCOV problem with  $\sim 1000$  solutions, although, only one exit, the exact cover exit, is of interest (255). The resulting design and network are seen in **Figure 5.3**. The network was fabricated in CSAR62 resist by EBL and treated with the optimised silanisation method described in Chapter 3.

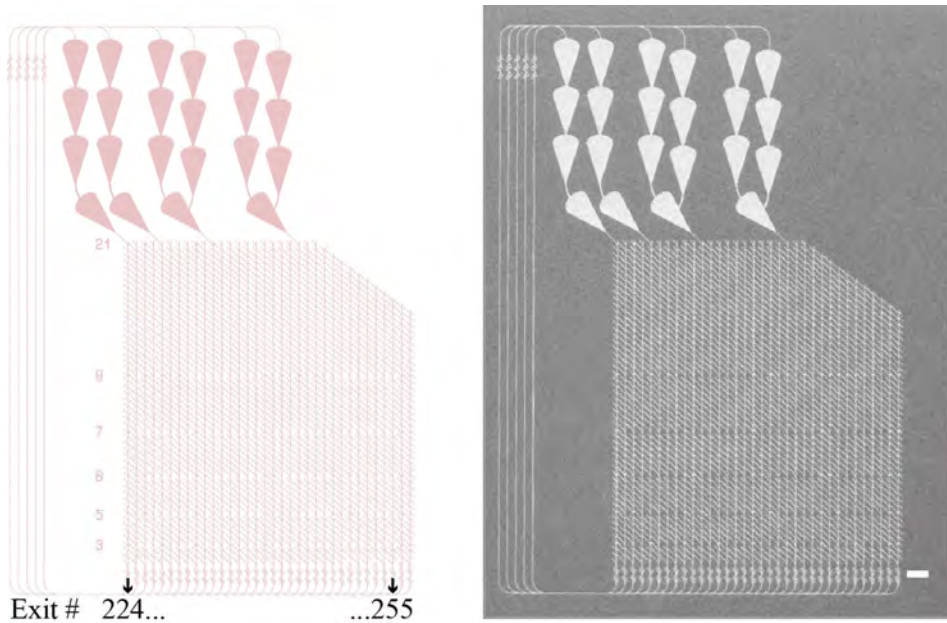


**Figure 5.3.** EBL pattern and scanning electron micrograph of the SSP sets described in **Table 5.3** after reducing the size of the networks by removing exits and number combinations above 257 (256-257 could also be removed but we left these). The scalebar in the micrograph is 20  $\mu\text{m}$ . N.B. the numbers were not exposed.

We performed motility tests using HMM (120  $\mu\text{g/ml}$ ) and Rhodamine-Phalloidin labelled actin filaments (100 nM) at 22°C. The number of filaments exiting was counted by hand and is seen in **Figure 5.4**. The pink bars represent incorrect solutions and the green bars represent correct solutions. In principle, if filaments did not make any wrong turns, we would only need one filament exiting at each correct exit to find all possible solutions to the SSP. For the EXCOV problem, this means we would only need to observe a single filament exiting at the exact cover exit.

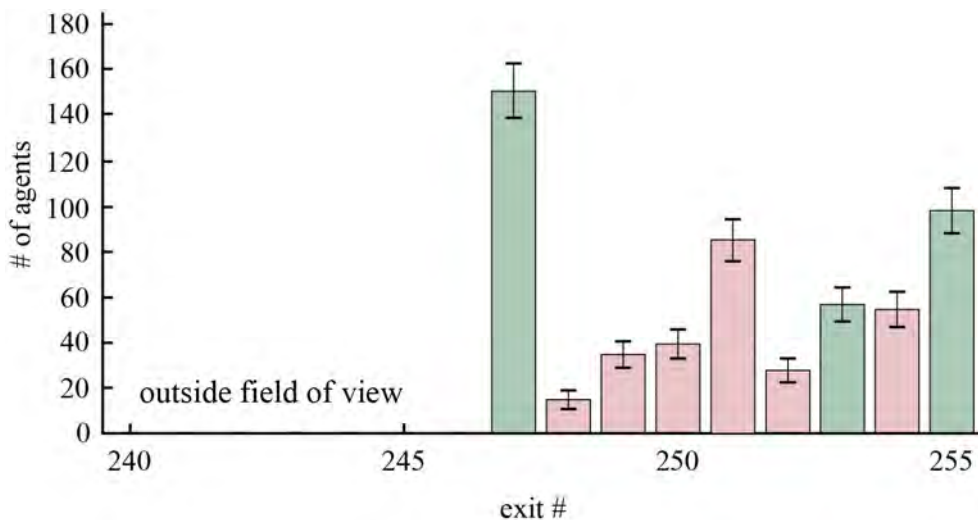


**Figure 5.4.** Histogram showing the number of filaments exiting at exits 247-255. The bars show the total number of filaments exiting each exit in seven different data sets. The error bars show the square root of the number of actin filaments per exit.

Unfortunately, in these first test devices, a large number of filaments exit at incorrect solutions, which creates false positives that prevent the true positives from being distinguishable with statistical significance. These errors arise from filaments making wrong turns in pass junctions causing them to enter illegal paths. Nicolau et al.<sup>1</sup> describe how the fraction of useable filaments,  $f(x)$ , decreases exponentially with the number of pass junction crossings,  $x$ , depending on the fractional error-rate,  $E$ :

$$f(x) = (1 - E)^x. \quad (1)$$

To calculate the error-rate we counted, by hand, the number of filaments making wrong turns in our largest data set (**Figure 5.1**). We observed 89 wrong turns out of 2306 counted filaments, providing an error-rate of 3.86% (fractional error-rate 0.0386). Nicolau et al.<sup>1</sup> found that, based on **Eq. 1**, the correct results could still be distinguished from the background noise if  $f \geq 0.15$ . In the network seen in **Figure 5.3**, the fraction of useable filaments is  $\sim 0.17$  (45 pass junction crossings), indicating that the correct results would be just about distinguishable (although not considering the number of filaments, only the error-rate and number of pass junctions). We used the error-rate to simulate the results (simulations done by Till Korten, TUD) of the filament distribution (**Figure 5.5c**) in a network with the same error-rate (here also considering the number of filaments exiting). The simulation result coincides well with the obtained experimental results (**Figure 5.5b** and **Figure 5.4**). **Figure 5.5a** shows a summed stack of the maximum intensity of a 300 s time-lapse movie of the

analysed set. The EXCOV exit has been marked with two loading zones (these are not connected to the network).

Despite our efforts to reduce the size of the network, and thus, the number of pass junction encounters, the error-rates still seem to be too high to be able to distinguish the correct solutions with the total number of filaments we were able to test so far. One reason for this difference compared what Nicolau et al.<sup>1</sup> found, is likely caused by the reset junctions presented in section 5.3. As the reset junctions concentrate filaments from two paths, this also means concentration of erroneous filaments making the error-rate distribution difficult to predict. However, reset junctions are still required to prevent errors in the calculation caused by carrying numbers. A possible solution would be to discard filaments that try to turn right at positions with reset junctions, although, this would mean that the overall signal would be decreased due to a decrease in the number of filaments. Furthermore, discarding of filaments is also problematic from an engineering perspective, as this would require yet further junction crossings, pass junctions, which may lead to an even more complex error-rate distribution. Therefore, an important necessity for network-based biocomputing to progress in the future is to reduce the number of wrong turns filaments make in the pass junctions. We have begun exploring options using 3D junctions, however, this lays beyond the scope of this thesis.

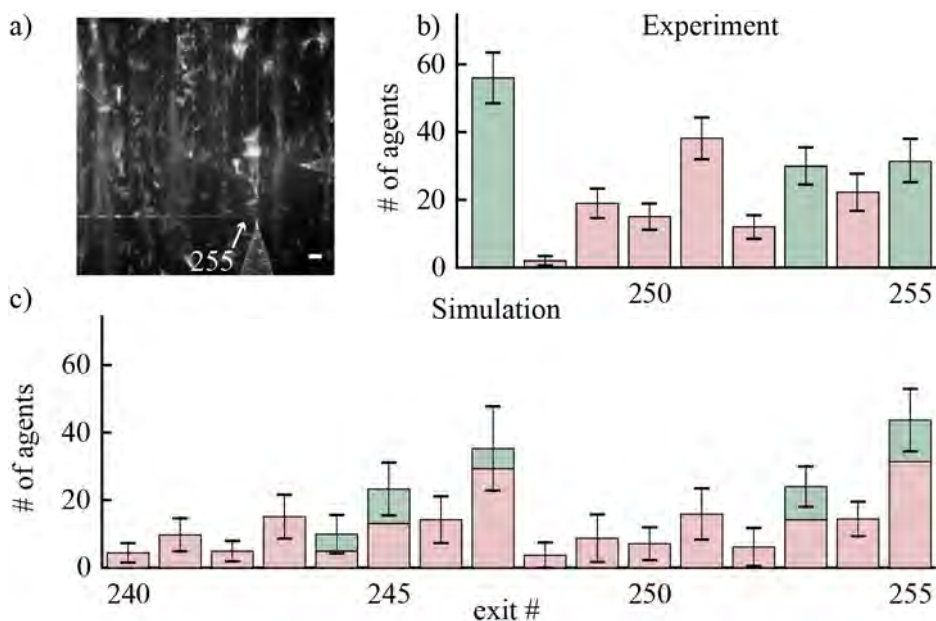


**Figure 5.5.** a) Fluorescence micrograph (scalebar 15 μm) showing the maximum intensity of a 200 s time-lapse movie at the lower right corner of the EXCOV network shown in **Figure 5.3**. The exact cover exit (255) has been marked with two loading zones. b) Experimental data for the analysed set showing the number of filaments exiting at each exit 247-255. Correct solutions are marked in green and incorrect solutions are marked in pink. c) Simulated data for error-rate 3.86%. The pink bars represent erroneous filaments that have taken illegal paths.

## 5.6 Concluding remarks

By translating sets of numbers into binary numbers and then back to a single decimal number we were able to create a theoretical conversion of the EXCOV problem into the SSP. We introduce a new network design including a new type of junction to avoid carrying numbers in binary addition, and describe how to optimise the size of the network. By minimising the size of the network, we managed to reduce the number of pass junction crossings, which contribute to a decreased fractional number of filaments. However, despite our efforts to reduce the number of pass junctions, the error-rates are still too high to clearly distinguish between correct and incorrect solutions, and need further optimisations before we can solve the encoded EXCOV problem in a statistically significant manner. Nevertheless, these developments will enable successfully solving of larger scale problems within the nearby future once the error-rates of the pass junctions can be reduced.

# 6 Architectural elements

*This chapter describes the development of two architectural elements for NBC with molecular motors. The first section presents the progress towards developing a method for creating a programmable gate, with the aim to enable versatile networks where the mathematical numbers encoded can be tuned by switching between pass and split junctions. The second section of this chapter describes the progress towards developing an electric readout method for detection of filaments passing certain check-points by using a CNT as a nanoscale field effect transistor.*

## 6.1 Motivation and previous work

### 6.1.1 Switchable junctions for programmable gating

The numbers in the mathematical problem encoded in our current network design (**Figure 1.2** and **Figure 5.3**), are defined by the placement of split and pass junctions. Different number sets have split rows located at different positions, and at different distances relative to each other. Currently, this is hard-coded into the network design during fabrication of the structures. By creating a programmable gate to transform pass junctions into split junctions and vice versa, we aim to be able to vary both the numbers within the sets, as well as the number of numbers encoded in the same network. This is highly desirable in upscaled versions of biocomputational devices, as it enables a broad variety of permutations for a dynamic algorithm using a standard large-scale network, patterned by e.g., NIL.

Previous studies of physically blocking and unblocking kinesin-1 motors have been done using the thermally activated polymer poly(N-isopropylacrylamide) (PNIPAM) on Au patterned surfaces<sup>47</sup>. These studies demonstrate the proof-of-principle of creating physical roadblocks on chemically confined tracks. PNIPAM resides in an extended form at low temperatures, blocking the motors, and curls up at higher temperatures, unblocking the motors. If the PNIPAM density is too low, the motors will still be able to bind and propel filaments. However, if the PNIPAM density is too high, motility will be completely inhibited as no motors will be able

to bind to the surface. Thus, the motor-blocking properties are determined by the density of the polymer, which can be tuned by the PNIPAM grafting temperature<sup>123</sup>.

We extended the previous PNIPAM study<sup>47</sup> by combining physical and chemical confinement of the motor system inside SiO<sub>2</sub> channels with Au floors (Paper V). To enable a switchable gating mechanism for transforming junctions between split and pass formation, we only patterned selective areas using a polymer linker for PNIPAM grafting.

## 6.1.2 Electric sensors for label free detection

In large-scale networks, a large number of filaments need to be detected at e.g., the network exits (**Figure 1.2**). For very big networks, optical readout methods are intractable, and pose limitations regarding network size as they expand outside the microscope field of view. An alternative method is instead to use nanoscale field effect transistors<sup>48</sup> (nanoFETs) for electrical detection. This would remove the need of fluorescence microscopes altogether by enabling label-free detection and thus, also eliminate drawbacks related to fluorophore bleaching and restrictions on the use of auto-fluorescent materials. Furthermore, an electrical readout method provides a better interface with electronic computers which may be of importance for future hybrid computers.

A transistor is a three-terminal device, where the conductance between two terminals is dependent on the voltage applied to a third terminal. A voltage,  $V_{SD}$ , is applied across the electrical source and drain contacts, generating a current,  $I_{SD}$ , through the transistor channel. The number of available charge carriers, and hence the current through the device, can be tuned by applying a second voltage,  $V_G$ . A schematic example of a nanoFET in a liquid is illustrated in **Figure 6.1**.

Several different types of nanoFETs have been realised based on e.g., silicon nanowires (SiNWs) or carbon nanotubes (CNTs). SiNW FETs have been used to detect changes in the pH<sup>48</sup>, by functionalising them with groups sensitive to protonation and deprotonation at different pH-values, chemically gating the SiNWs. They have also been used to detect reversible protein binding<sup>48</sup> by functionalising the SiNWs with complementary proteins, and to detect DNA hybridisation by functionalising the wires with target DNA<sup>124,125</sup>. CNT FETs (aka CNFETs), have also been used to detect DNA hybridisation in a similar manner, even down to a single molecule level<sup>49</sup>. Furthermore, CNFETs have been used for bacterial lectin detection using glycoconjugated CNTs<sup>50</sup>, and for detecting cancer biomarkers<sup>51</sup> by functionalisation of complementary proteins.

In this thesis, we try to use a (non-functionalised) single-walled CNFET to detect the passing of an actin filament (a charge particle) as a function of time due to a change in the local charge environment. To the best of our knowledge, this would

be the first nanoFET detecting an unbound protein, and would provide a reliable readout method for determining the number of filaments passing. To the date of the printing of this thesis, we have not yet been able to measure the crossing of an actin filament. So far, we have studied the buffer requirements in terms of ionic strength for a functioning biological system and for electrical detection to be possible. We also expect that the CNT needs to be raised up to the travelling height of the actin filaments to ensure that the charged filaments pass close enough (within the Debye length) to be detected. Therefore, we developed a process for fabricating pedestals for this purpose.

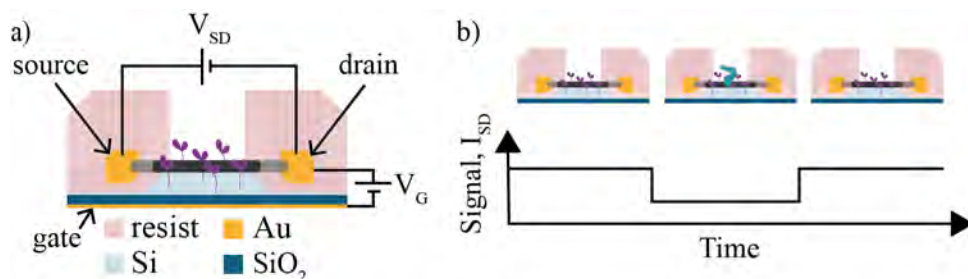


**Figure 6.1.** Schematic illustration of a nanoscale field effect transistor inside a nanochannel. a) A current,  $I_{SD}$ , is passed through the transistor by applying a voltage,  $V_{SD}$ , across the source and drain contacts. Charge carriers can be injected or depleted increasing or decreasing the conductivity through the transistor channel by applying a second voltage,  $V_G$ , across the transistor and e.g., a back gate. b) As a charged particle (here an actin filament) passes in close proximity of the transistor, the electric output signal ( $I_{SD}$ ) changes as a result of the a change in the local charge environment.

## 6.2 Programmable gating (Paper V)

**Figure 6.2** shows a schematic illustration of a programmable gate designed to switch between a pass and a split junction using the polymer PNIPAM. At low temperatures PNIPAM is extended and the junction corresponds to a pass junction. At higher temperatures, PNIPAM curls up and the junction is intended to transform into a split junction.

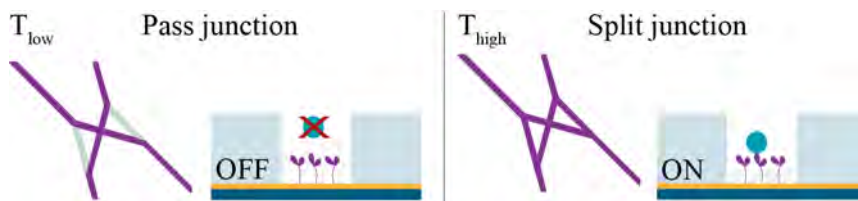


**Figure 6.2.** Schematic illustration of a switchable gate using a thermo-responsive polymer. At low temperatures the junction corresponds to a pass junction as the molecular motors are blocked by the polymer. At high temperatures the junction is transformed into a split junction as the polymer curls up, exposing the motors, enabling filament binding.

The gating mechanism only works if the PNIPAM polymer is grafted in specific regions, otherwise motility would be blocked and unblocked everywhere. To selectively graft a carboxy-terminated version of PNIPAM we used the negative tone resist poly-glycidyl methacrylate<sup>126</sup> (PGMA) as a coupling agent<sup>127</sup>, which can be patterned by EBL and developed in methyl ethyl ketone (MEK). To prevent the filaments from encountering a large step inside the channels, we diluted PGMA in anisole to two concentrations (1% and 6%), to try and obtain an as thin layer as possible. On flat surfaces, both PGMA concentrations provided uniform films (~15 nm for 1% PGMA and ~146 nm for PGMA 6%), however, on the structured surfaces we observed polymer accumulation inside the channels for the higher PGMA concentration (Figure 6.3).

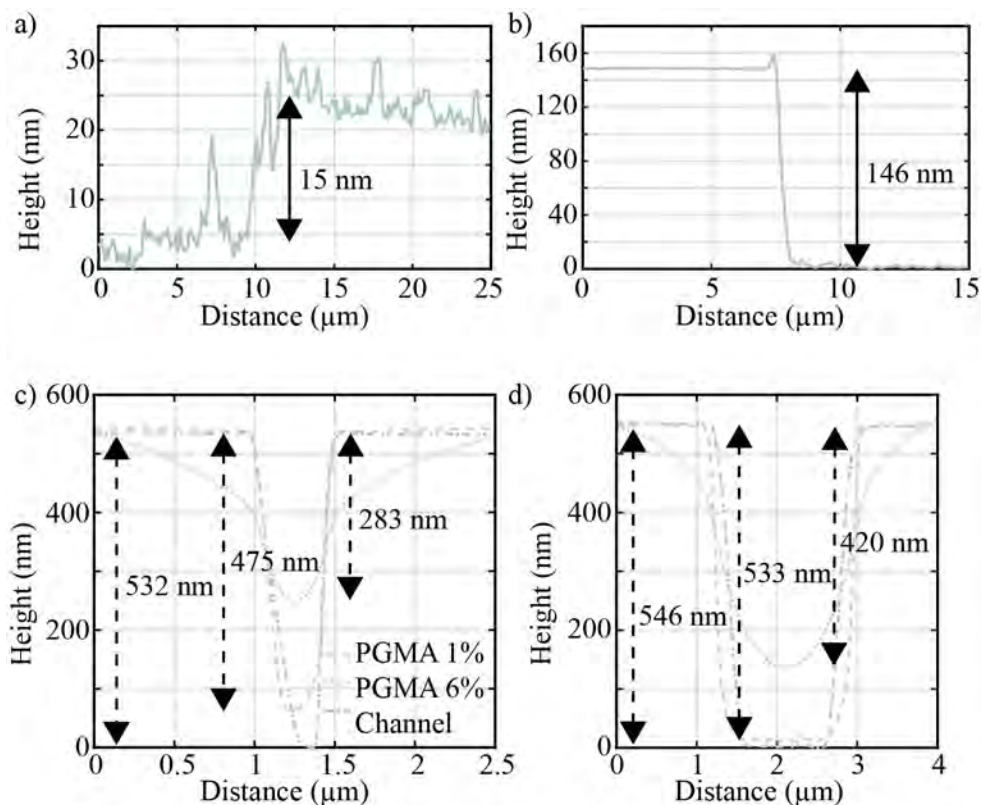


**Figure 6.3.** Profile graphs extracted from AFM scans on nanostructured surfaces (1 scan = 50 px wide). A scratch was made on a flat region of the surface to measure the thickness of a) PGMA 1% (~15 nm) and b) PGMA 6% (~146 nm). Both PGMA 1% and 6% accumulated in the c) 500 nm wide channels, but in the d) 2 μm wide channels, only PGMA 6% was accumulated. N.B. The thinner channels suffer from AFM artefacts making it difficult to see the precise contours due to broadening effects of the AFM tip in high aspect ratio structures.

**Figure 6.4a** shows the dose test done for PGMA to find the suitable EBL exposure parameters. The doses tested ranged from  $12 \mu\text{C}/\text{cm}^2$  to  $60 \mu\text{C}/\text{cm}^2$  and, as can be seen in the optical micrograph, the pattern was overexposed for all doses but the lowest one. Furthermore, we found that a thin (7 nm) layer of PGMA always remains on the unexposed surface (measured by ellipsometry) despite longer development times (**Figure 6.4b**) and can only be removed by oxygen plasma treatment.

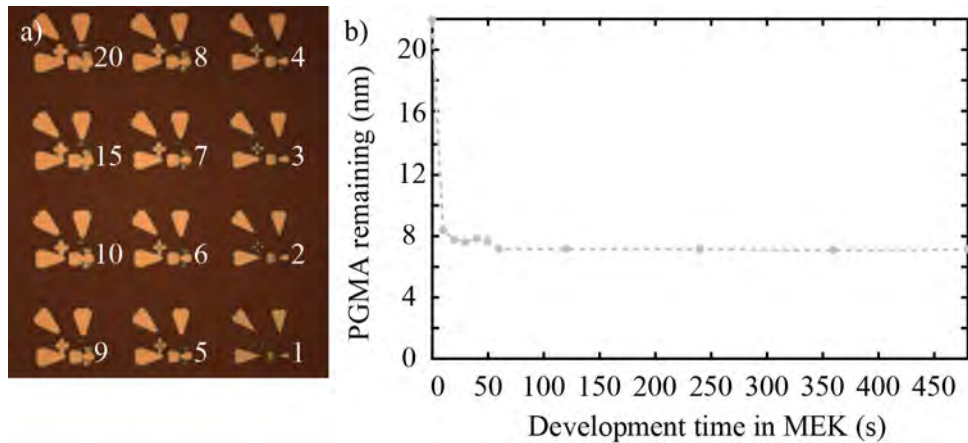


**Figure 6.4.** a) Optical micrograph of an EBL dose test showing the dose factor in white, base dose =  $12 \mu\text{C}/\text{cm}^2$ . b) Unexposed PGMA remaining on the surface after different development times in MEK.

**Figure 6.5** shows the resulting PGMA (1%) pattern inside a nanochannel after EBL exposure at  $12 \mu\text{C}/\text{cm}^2$ . The PGMA thickness is around 27 nm, although, the exact thickness is difficult to measure due to possible AFM tip broadening effects. However, as seen in **Figure 6.3**, the resist will accumulate more inside smaller channels. The PGMA thickness can be reduced further (post patterning) by etching with oxygen plasma.

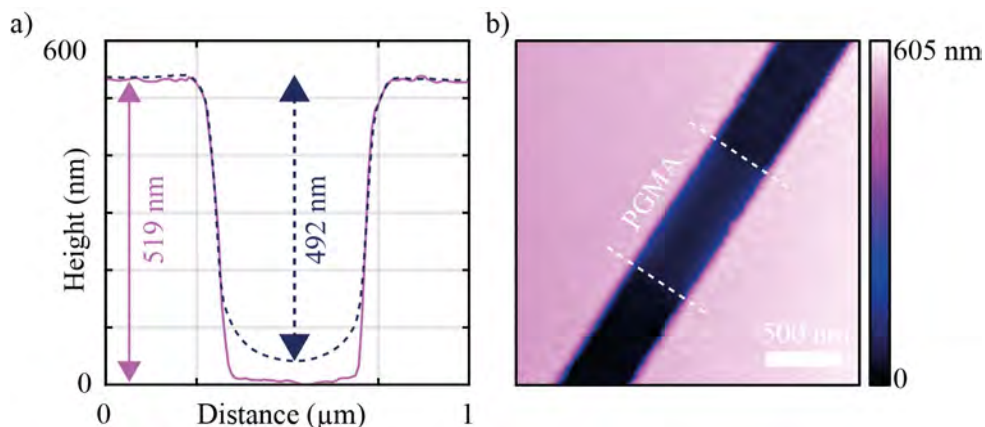


**Figure 6.5.** a) Profile plot of the b) atomic force micrograph showing the patterned PGMA patch inside a nanochannel.

**Figure 6.6** shows how motility is first inhibited (filaments are blurry) on a PNIPAM patch grafted on PGMA when the polymer is in its extended form ( $T = 25^\circ\text{C}$ ). When the temperature is increased ( $T = 35^\circ\text{C}$ ), the PNIPAM collapses, and motility is promoted (filaments appear as straight lines). **Figure 6.6** also shows how the PNIPAM grafting temperature affects the motor blocking properties. When using  $140^\circ\text{C}$  as the grafting temperature, there are still some motile filaments visible on the extended-PNIPAM patch, indicating that some filaments are still being propelled. At grafting temperature,  $T_{\text{grafting}} = 143^\circ\text{C}$ , no motile filaments can be observed on the extended-PNIPAM patch, indicating successful motor-blocking. However, at the number of filaments is lower on the contracted PNIPAM patch at  $T_{\text{grafting}} = 143^\circ\text{C}$  as compared to at  $T_{\text{grafting}} = 140^\circ\text{C}$ , indicating that the PNIPAM density could likely be further optimised between  $140\text{--}143^\circ\text{C}$ . However, these results provide a good baseline for studying switching inside nanochannels, where the system is likely to also be slightly different. The next step is to perform IVMA experiments on selectively patterned nanochannels. We are currently awaiting the first results of these experiments.

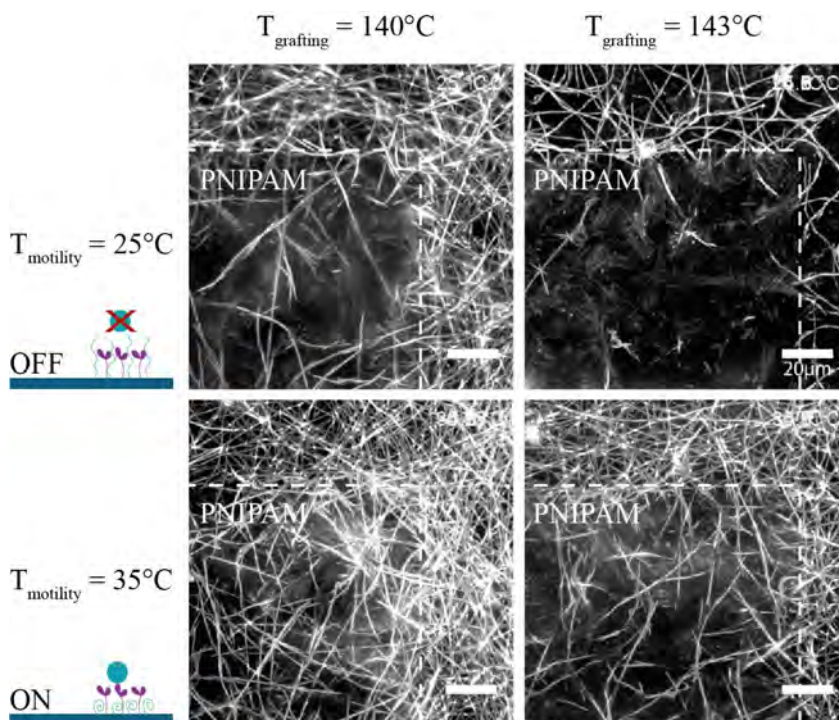


**Figure 6.6.** Data demonstrating local switching of motility on PNIPAM patches grafted on patterned PGMA. The fluorescent micrographs show the maximum projection of 85 s long movies of the local PNIPAM grafting tests. At  $T = 25^\circ\text{C}$  the PNIPAM is in an extended form, blocking the molecular motors and inhibiting motility (filaments appear blurry on the patch). At  $T = 35^\circ\text{C}$  the PNIPAM collapses and exposes the molecular motors, thus, enabling motility across the polymer patch (filaments appear as straight lines). The two columns show how the grafting temperature affects the blocking properties of PNIPAM as the polymer density varies. At the lower grafting temperature,  $T = 140^\circ\text{C}$ , the PNIPAM density is slightly lower and does not completely block all motors as compared to the higher grafting temperature,  $T = 143^\circ\text{C}$ , where no filaments move across the polymer patch. The scalebar is  $20\ \mu\text{m}$  in all images.

## 6.3 Electrical detection

An important consideration for electrical detection of charged particles, in a liquid using CNFETs, is the distance at which a particle with a specific charge is detectable. This depends on the sensitivity of the CNFET, the electric noise present in the measurement and the ionic strength of the liquid.

The sensitivity of a CNFET detector can be defined as the change in charge required to cause a detectable change in the electrical output signal ( $I_{SD}$ ), i.e., the current flowing through the CNT. This will depend on several things, including the electrical properties of the transistor itself and the type of electric contacts used. By changing the gate voltage, we can tune the region we will operate in, see **Figure 6.7**.

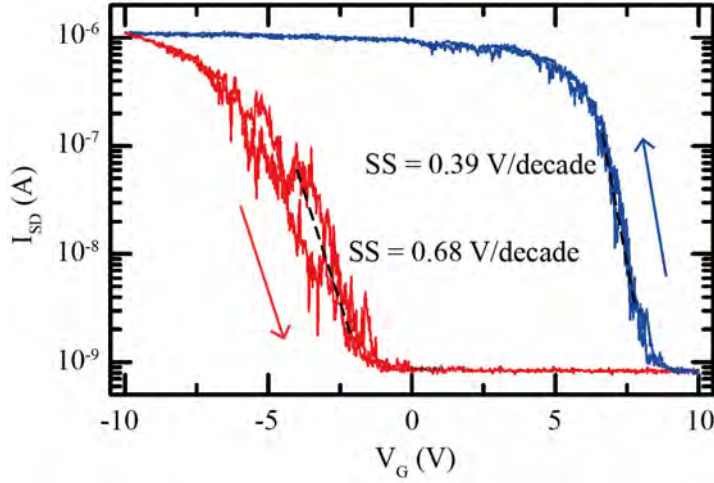


**Figure 6.7.** Measured source-drain current ( $I_{SD}$ ) of a single-walled CNFET as a function of the gate voltage ( $V_G$ ) with an applied source-drain voltage of 5 V. The dotted line shows the log linear region with a subthreshold swing of 0.39 V/decade. The arrows indicate the direction of the gate voltage-sweep. Reprinted with permission from Roman Lyttleton’s doctoral thesis<sup>128</sup>.

Here, the most sensitive region can be approximated by the log linear regime (dotted line in **Figure 6.7**), where a small change in  $V_G$  causes a large change in  $I_{SD}$ . For our best devices (developed and fabricated by Roman Lyttleton, UNSW), the subthreshold swing is 0.39 V/decade<sup>128</sup>, i.e., introducing a 390 mV voltage will change the  $I_{SD}$  by a factor 10. At typical currents of 0.5-1  $\mu\text{A}$ , our devices show an inherent pink noise width of 5-10%<sup>128</sup> of the applied current (external noise was filtered out by encapsulating the set-up in a Faraday cage). Therefore, for charged species to be detectable, they need to cause a 10% change in  $I_{SD}$ , i.e., by a factor 1.1. In the log linear regime, the current is proportional to the gate voltage as:

$$I_{SD} \propto e^{AV_G} \rightarrow \Delta I_{SD} \propto e^{A\Delta V_G} \quad (2)$$

meaning that if  $\Delta V_G = 0.39$  V causes  $\Delta I_{SD} = 10$ , then  $A \approx -5.76$ . A 10% change means  $\Delta I_{SD} = 1.1$ , which with  $A \approx -5.76$  means that  $\Delta V_G \approx 0.02$  V. Thereby, the voltage step required to detect an actin filament is 20 mV. The next question is, at what distance away from the CNT does a charged actin filament passing by exert a 20 mV potential on the CNFET?

As a measure for that we first consider the Debye length, which is defined as the length for which the electric potential of a local surplus charge decreases by  $1/e$ . The Debye length is strongly dependent on the local charges present in the liquid, here, the ionic strength of the solution, as electrolytes screen the electric potential.

The higher the ionic strength, the more heavily the electric potential from a charged filament will be screened by the intermediary electrolyte between the filament and the detector. Therefore, we want to reduce the ionic strength of our protein solutions, increasing the Debye length, which will reduce the screening effect. However, there is a biological limit to the minimum ionic strength, dictated by the biology of the molecular motor system.

**Figure 6.8** shows a simulation of how the voltage step in the output signal changes with the gap size between the filament and CNT by accounting for the Debye screening in some commonly used buffer solutions, and assuming an actin filament with a linear charge density of  $-4000 \text{ e}/\mu\text{m}^{129,130}$  (simulations done by Adam Micolich, UNSW, Manuscript in preparation). The 20 mV detection limit is marked with a red dashed line.

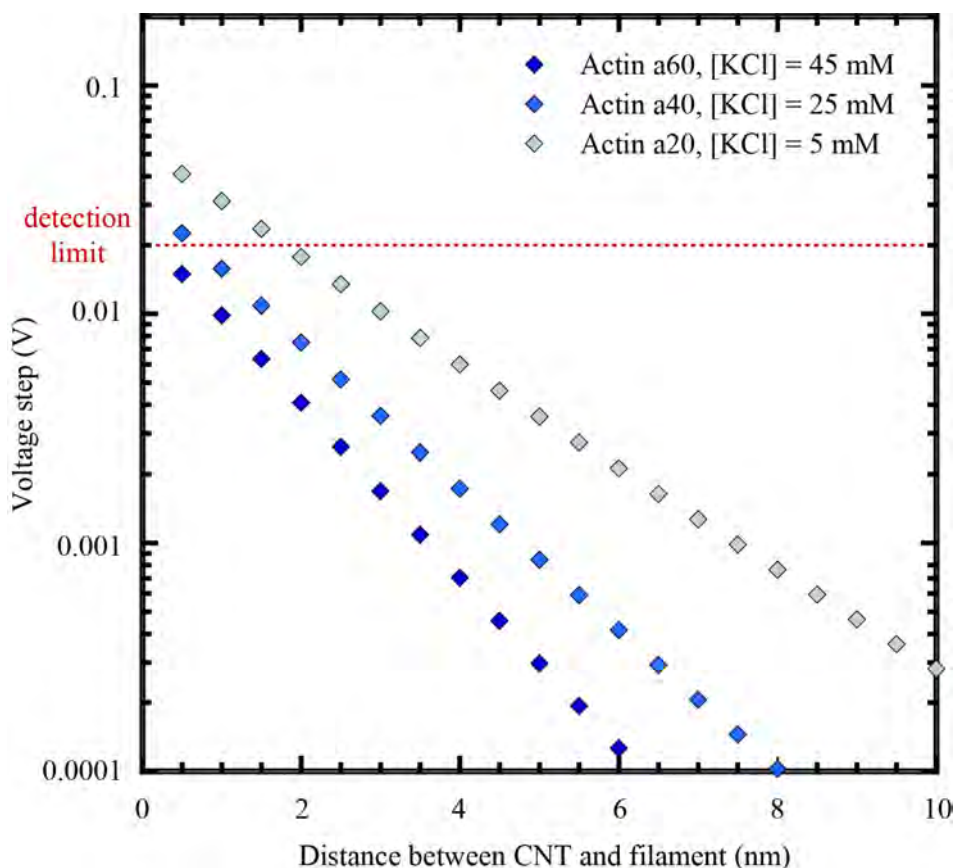


**Figure 6.8.** Simulation showing the change in potential exerted on the CNT depending on the distance between the passing actin filaments and the CNT for different buffer solutions. The red dashed line marks the detection limit (20 mV) of the current actin-myosin II CNFET devices with a sensitivity of 0.39 V/decade and pink noise  $\sim 10\%$ .

The main contribution to the ionic strength for the actin myosin system is the concentration of  $\text{KCl}^{128}$ . According to the simulations in **Figure 6.8**, the actin filaments are unlikely to be detectable in the current devices, with the  $\text{KCl}$  concentrations in the typically used a60 buffer (45 mM), but possibly in the a40 buffer (25 mM) as well as the a20 buffer (5 mM). Decreasing the  $[\text{KCl}]$  will also cause a decrease in actin filament gliding velocity as previously described<sup>131</sup>. To this end, we performed IVMA experiments to compare the motility at two different  $\text{KCl}$  concentrations, using the standard 45 mM  $\text{KCl}$  buffer and an extreme 0 mM  $\text{KCl}$  buffer. **Figure 6.9** highlights the threefold drop in velocity when decreasing the  $[\text{KCl}]$  from 45 mM to 0. The fluorescence micrographs also show an increased fragmentation of actin filaments at the lower  $[\text{KCl}]$ , consistent with the idea that the interaction strength between actin monomers is appreciably reduced at lower ionic strengths.

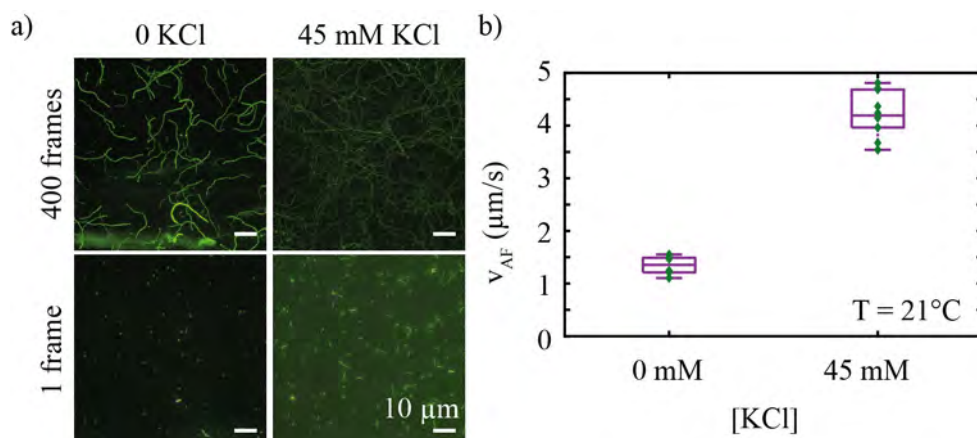


**Figure 6.9.** a) Fluorescence micrographs at 0 mM  $\text{KCl}$  and 45 mM  $\text{KCl}$  concentration. The bottom images show one frame. For the lower ionic strength, increased filament fragmentation is clearly visible. The top images show the sum of 400 frames. They show a clear difference in the actin filament path length, where the higher ionic strength provides much faster filaments. This is confirmed by point tracking 10 filaments and analysing their velocities in b) which shows that the actin filament velocity,  $v_{AF}$ , is around x3 higher at 45 mM  $\text{KCl}$  concentration as compared to at 0 mM  $\text{KCl}$ . The central mark of the boxplot shows the median of the data set, the top edge of the box shows the 75<sup>th</sup> percentile and the lower edge of the box shows the 25<sup>th</sup> percentile. The whiskers show the most extreme data points not considered to be outliers, where an outlier is defined as a point greater than 1.5 times the interquartile range away from the top or bottom of the box (none visible in the graph). Individual data points are shown in green.

HMM propels actin  $\sim 38 \text{ nm}^{105}$  above the surface, making the filament almost completely electrically screened if the CNT is placed on the channel floor. As seen in **Figure 6.8**, the allowed gap between the CNT and filament can be increased by decreasing the ionic strength, but as seen in **Figure 6.9** we want to use an as high  $[\text{KCl}]$  as possible to prevent a decrease in velocity and an increase in filament fragmentation. To bring the CNT and filaments as close together as possible, optimally completely removing the gap, we placed the CNTs on  $\text{SiO}_2$  pedestals. To

create the SiO<sub>2</sub> pedestals we selectively protected the pedestal area with EBL resist and lowered the surrounding channel floor by wet-etching with hydrogen fluoride (HF).

To examine what effect the HF-etch might have on the actin filament motility, we performed IVMAs with nanostructures comparing the etched and non-etched surfaces. **Figure 6.10** shows the summed stacks of the maximum intensity for 60 s of a non-etched and HF-etched nanostructured surface as well as the actin filament sliding velocity. No detectable difference in motility could be observed in terms of filament gliding velocity, indicating that the resulting surface supports appropriate HMM binding. This means it is possible to create SiO<sub>2</sub> pedestals for the actin-myosin system by this approach.

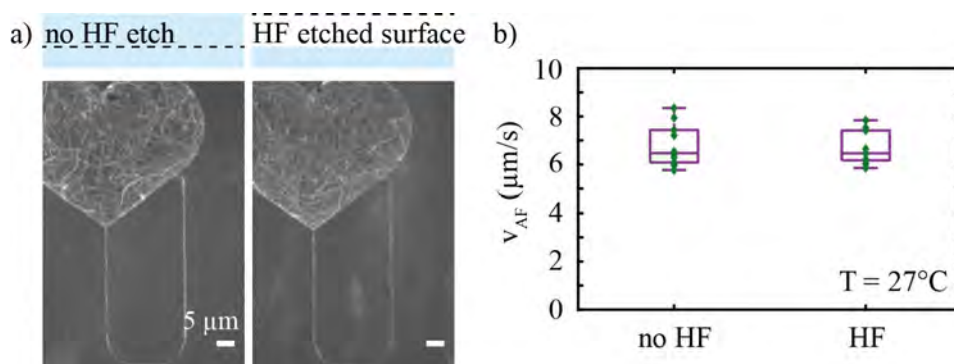


**Figure 6.10.** a) Fluorescence micrographs of non-etched and HF-etched SiO<sub>2</sub> surfaces inside polymer nanostructures. b) Actin filament sliding velocity on non-etched and HF-etched SiO<sub>2</sub> surfaces (n=10 filaments). No difference in motility quality in terms of actin filament sliding velocity is observed. See boxplot details in **Figure 6.9**. Individual data points are shown in green.

As the purpose of the pedestals is to bring the CNT and actin filament in closer contact, a major drawback would be if the filament was simply raised and actively transported across by HMM bound to the pedestal surface. To avoid this, we plan to cover the pedestals with a thin non-motile layer of parylene-C (~3 nm). The simulations in **Figure 6.8** take this additional passivating layer into account. We performed IVMA experiments on parylene-C surfaces (supplied by Jan Gluschke, UNSW) treated with oxygen plasma and found that it is possible to completely suppress motility on these surfaces, similar to the polymer walls (see **Figure 3.5**).

Finally, a basic, but key requirement for electrically detecting the actin filaments, is to be able to perform simultaneous optical and electric measurements and to correlate these two signals. To be able to bond the samples and connect them to our electronic instrumentation and to prevent the fragile cover slips from breaking due to the extra weight of the additional electronics, we created a set of 3D-printed sample holders

to support the samples in the correct positions and enable easy handling. The most successful holder is demonstrated in **Figure 6.11**.

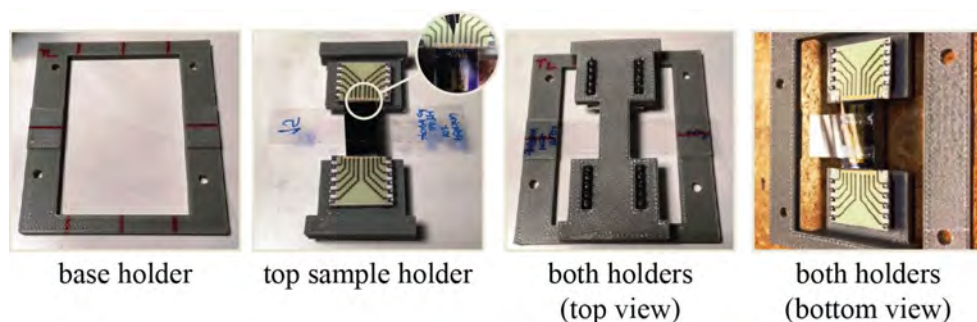


**Figure 6.11.** Pictures of the 3D-printed sample holders supporting the flow cell and sample to avoid that the flow cells break. The first image shows the base holder and the second images shows the top holder with the sample glued between two packages. The inset shows the bond wires electrically connecting the sample and package. The third image shows the top view of both holders together, and displays how the cover slip is supported by the base holder. The electric pins connected to the package protrude out through holes in the top sample holder. The fourth image shows both holders from the bottom view.

## 6.4 Concluding remarks

By using a polymer linker, PGMA, to graft selective areas with the thermo-responsive polymer PNIPAM, we successfully show local on/off switching of microtubule-kinesin 1 motility. We describe the development of the PGMA processing parameters on both flat surfaces, larger patches and inside nanoscale channels. These findings provide a stepping stone towards developing dynamic encodings for NBC with molecular motors.

To electrically detect actin filaments passing specific check-points we have begun the development of a nanoFET based on a single-walled CNT. We describe how actin filaments need to pass in close proximity of the CNTs to be detectable, and how this distance varies with the local charge environment. To reduce the distance between the filament and the CNT, we have developed a method of raising the CNTs onto SiO<sub>2</sub> pedestals that suppress motility. Furthermore, to support the cover slips and samples from the additional weight of the electronics we created easy-to-handle 3D-printed holders. Though not yet successful in measuring an actin filament passing, these results provide major steps towards an electrical readout method, although further device optimisation is most likely necessary to increase the sensitivity of the devices to enable a detectable change in the electric output.

# 7 Conclusions and outlook

This thesis focuses on the processing and fabrication development of devices for NBC with molecular motors.

In the first section of the thesis we describe three techniques that strengthen and expand the study of chemically confining molecular motors. We describe a method to improve the modification of the surface chemistry for selective protein binding by using a dedicated CVD system, where the content of TMCS, and silanisation duration can be varied. This enables a reliable surface treatment providing a high yield of motile samples, and provides an opportunity to study surface interactions of proteins on different surfaces with different hydrophobicity, without changing the chemical compound.

During the investigation of two new lithography resists we discovered that it is also possible to fabricate nanostructures without the necessity of silanisation altogether. Instead, we use the intrinsic, motility promoting properties of the negative tone NIL resist TU7, and the possibility to suppress motility on the EBL resist CSAR62 by oxidation with oxygen plasma. The filament velocity and the number of filaments across the surface is still low, but could potentially be improved by reducing the surface roughness and EBL resist-residues by using a different developer or by other chemical cleaning without loss of function.

Furthermore, we developed a method for chemically cleaning our devices from salt residue and motors, to be able to re-use our devices without the necessity of additional processing modifications. By recycling devices, we are able to decrease the overall time and material consumption, providing a more sustainable fabrication process.

As with many other parallel computation techniques, solving combinatorial problems with molecular motors is limited by various practical limitations, i.e., there are certain engineering aspects that require improvement before being able to create a viable contender that can outperform an electronic computer. One basic aspect is being able to upscale the fabrication of the physically confining structures without loss of resolution. In the second section of the thesis we present two methods for improving the throughput of molecular motor-based devices.

We switched to a more sensitive resist, CSAR62, as compared to the previously used PMMA, and describe the optimisation of the EBL patterning parameters. We

also developed a new method for patterning the large aspect ratio loading zone structures by NIL in TU7.

By redesigning the loading zones to include pillar-structures we could create areas into which polymer could be displaced during imprint. We also found that these newly introduced pillars can be used to tailor the directionality of the overall filament movement, a very useful feature within e.g., sensing applications. **Figure 7.1** shows a possible design for a sensor exploiting this directionality. The loading zone pillars here, correspond to design F in **Figure 4.4**, and will push the filaments from the large central circle towards each sensing area. An alternative design would be to use structures that cause a variety of emptying rates. These structures could for instance, be fabricated by a combination of UVL and NIL.

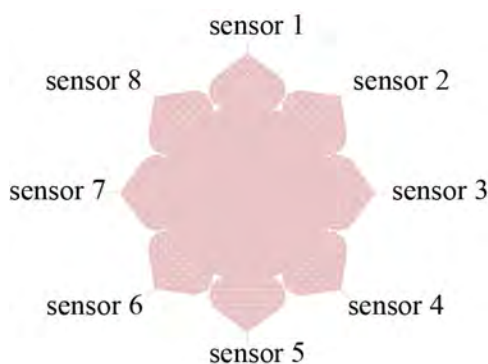


**Figure 7.1.** Possible biosensor design utilising the directional properties of the pillar-shapes and configuration described in design F, **Figure 4.4**. The filaments in solution would diffuse down into the large open central (pink) area and be pushed toward each sensor due to the shape and position of the (white) pillars.

Within this thesis we also present an algorithm for translating the NP-complete problem EXCOV into another NP-complete problem, the SSP. We describe a method of reducing the network size to reduce the number of filaments required, and we describe how challenges related to carrying numbers in binary addition can be avoided. We try to solve a large-scale network with  $\sim 1000$  solutions, but the current error-rates i.e., wrong turns within the network, are too high to find a statistically significant solution.

To reduce the error-rates and thus, the number of filaments required, we are currently developing a new type of junction with three dimensional crossings, fabricated by two photon polymerisation technology. In such a structure, filaments will move across “bridges” and through “tunnels” (**Figure 7.2**). If successful, this would enable complete elimination of the risk of filaments taking a wrong turn at pass junction crossings. However, these types of junctions are not compatible with the switchable junctions described in Chapter 6.

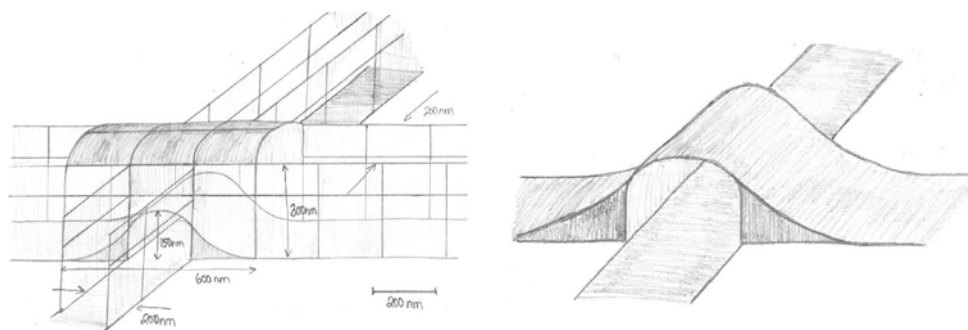


**Figure 7.2.** Schematic illustrations of a 3D-junction that eliminates the risk of filaments making wrong turns at pass junctions. By creating bridges and tunnels, there is only one possible pathway for the filaments.

Another draw-back with the current network design is the relatively slow input of exploring agents. Despite describing a method of increasing the number of locations at which filaments are fed in, they are still all inserted at the top of the network through a limited number of entrance points. For very large networks, this will cause a major bottle-neck due to the vast number of filaments required to solve large networks. To remove this bottle-neck, we are currently working on a method to split and grow our filamentous agents while in the network. However, if any information is stored on the filament itself, a split and regrowth process will continuously cause this information to dilute.

Storing data on filaments is important in problems that require information about what paths have been explored, e.g., in the travelling salesman problem Sarah encountered in the introduction. In principle, all NP-complete problems can be translated into each other, and the network encoding presented in this thesis might not always be the most optimum design for all problems. At the moment, we are working on a second, compact network design for solving the Boolean Satisfiability problem, which we translate into the travelling salesman problem. The current design (not shown here) will however, only work if the filaments can be tagged with information on where they have been. Any methods for splitting and re-growing filaments must therefore, also include the transfer of this information. However, we are currently unable to store and manipulate information on our filaments. Nevertheless, in the future, barcoding by bleaching fluorophores or tagging by e.g., attaching DNA oligonucleotides might be feasible options.

In the final section of this thesis we described the development of two architectural elements for NBC with molecular motors, a programmable gating mechanism and an electric sensor.

We describe a new method of selectively grafting the thermo-responsive polymer PNIPAM on nanostructures, allowing local switching of motility by creating physical roadblocks, veiling and unveiling the surface-bound molecular motors. By

introducing switchable paths, we can create dynamic encodings that allow different numbers and a different number of numbers to be encoded within the same algorithm. This allows the fabrication of very versatile devices that can be patterned with a standard, predefined, large-scale network structure e.g., using high throughput NIL. In combination with our regeneration process, these advancements are steps towards real-life applications of NBC with molecular motors due to the reduced fabrication costs and upscaling properties.

There are also other methods one could envisage to tune the motility. One possible method would be to not physically block the motors but instead switch the motor function itself. Another method could be to include a tuneable surface chemistry to selectively collapse the motors, e.g., by changing the surface hydrophobicity, or to change the binding affinity. A precondition for any future method is however, that it must be reversible to ensure maximum flexibility.

The NBC method presented in this thesis relies on an optical readout and counting filaments by hand. In collaboration with a group of students, our research group is currently developing a deep learning algorithm for analysis of filaments in our IVMA experiments, regarding the number of exiting events, the number of wrong turns, the relationship between certain filament behaviour and specific filament dimensions or device structures. This would simplify the data analysis during development, and provide the possibility to map a wide range of variables providing massive information on how our system can be optimised further. Naturally, only visible information can be analysed, restricting the amount of area that can be studied simultaneously as we are limited by the microscope field of view. For counting the filament exit events, we would instead like to employ an electrical readout method using a single-walled CNT as a nanoFET as this removes the restraints of using a microscope all together.

Though we are yet to integrate these nanoFETs and detect filaments exiting, we describe how close by filaments need to pass in order to be detectable. We also describe methods of how the filaments can be brought within this range, by raising the CNT onto pedestals, and by decreasing the ionic strength to decrease the screening of the electric potential. Furthermore, we show a way to perform optical and electrical measurements simultaneously without breaking the samples due to the additional weight of the electronics.

These improvements, together with other, new and promising ideas, have the potential to boost the field of NBC using not only molecular motors as agents, but also other agents, such as bacteria, artificial motors or perhaps some other self-propelling, highly energy-efficient agent. I do believe, that solving combinatorial problems beyond what has been possible so far, is actually within reach in the nearby future.

# References

1. Nicolau, D. V. J. *et al.* Parallel computation with molecular motor-propelled agents in nanofabricated networks. *PNAS* **113**, 2591–2596 (2016).
2. Goldreich, O. *P, NP, and NP-Completeness-The Basics of Computational Complexity.* (Cambridge university press, 2010).
3. Mukhanov, O. A. Energy-efficient single flux quantum technology. *IEEE Trans. Appl. Supercond.* **21**, 760–769 (2011).
4. Madden, P. H. Dispelling the myths of parallel computing. *IEEE Des. Test* **30**, 58–64 (2013).
5. Adleman, L. M. Molecular Computation of Solutions to Combinatorial Problems. *Science (80-. )*. **266**, 1021–1024 (1994).
6. Lipton, R. J. DNA Solution of Hard Computational Problems. *Science (80-. )*. **268**, 542–545 (1995).
7. Braich, R. S. *et al.* Solution of a 20-variable 3-SAT problem on a DNA computer. *Science* **296**, 499–502 (2002).
8. Chiu, D. T., Pezzoli, E., Wu, H., Stroock, a D. & Whitesides, G. M. Using three-dimensional microfluidic networks for solving computationally hard problems. *Proc. Natl. Acad. Sci. U. S. A.* **98**, 2961–2966 (2001).
9. Ladd, T. *et al.* Quantum computers. *Nature* **464**, 45–53 (2010).
10. Barclay, C. J. Estimation of cross-bridge stiffness from maximum thermodynamic efficiency. *J. Muscle Res. Cell Motil.* **19**, 855–864 (1998).
11. Korten, T., Månsson, A. & Diez, S. Towards the application of cytoskeletal motor proteins in molecular detection and diagnostic devices. *Curr. Opin. Biotechnol.* **21**, 477–488 (2010).
12. Kron, S. J. & Spudich, J. A. Fluorescent actin filaments move on myosin fixed to a glass surface. *Proc. Natl. Acad. Sci. U. S. A.* **83**, 6272–6276 (1986).
13. Howard, J., Hudspeth, A. J. & Vale, R. D. Movement of microtubules by single kinesin molecules. *Nature* **342**, 154–158 (1989).
14. Sheetz, M. P. & Spudich, J. A. Movement of myosin-coated fluorescent beads on actin cables in vitro. *Nature* **303**, 31–35 (1983).
15. Kron, S. J., Toyoshima, Y. Y., Uyeda, T. Q. P. & Spudich, J. A. Assays for

- Actin Sliding Movement over Myosin-Coated Surfaces. *Methods Enzymol.* **196**, 399–416 (1991).
16. Kishino, A. & Yanagida, T. Force measurements by micromanipulation of a single actin filament by glass needles. *Nature* **334**, 74–76 (1988).
  17. Murphy, C. T., Rock, R. S. & Spudich, J. A. A myosin II mutation uncouples ATPase activity from motility and shortens step size. *Nat. Cell Biol.* **3**, 311–315 (2001).
  18. Toyoshima, Y. Y. *et al.* Myosin subfragment-1 is sufficient to move actin filaments in vitro. *Nature* **328**, 536–539 (1987).
  19. Homsher, E., Kim, B., Bobkova, A. & Tobacman, L. S. Calcium regulation of thin filament movement in an in vitro motility assay. *Biophys. J.* **70**, 1881–1892 (1996).
  20. Bunk, R. *et al.* Actomyosin motility on nanostructured surfaces. *Biochem. Biophys. Res. Commun.* **301**, 783–788 (2003).
  21. Lard, M. *et al.* Ultrafast molecular motor driven nanoseparation and biosensing. *Biosens. Bioelectron.* **48**, 145–152 (2013).
  22. ten Siethoff, L. *et al.* Molecular motor propelled filaments reveal light-guiding in nanowire arrays for enhanced biosensing. *Nano Lett.* **14**, 737–742 (2014).
  23. Månsson, A. Translational actomyosin research: Fundamental insights and applications hand in hand. *J. Muscle Res. Cell Motil.* **33**, 219–233 (2012).
  24. Sundberg, M. *et al.* Actin filament guidance on a chip: Toward high-throughput assays and lab-on-a-chip applications. *Langmuir* **22**, 7286–7295 (2006).
  25. Clemmens, J. *et al.* Mechanisms of microtubule guiding on microfabricated kinesin-coated surfaces: Chemical and topographic surface patterns. *Langmuir* **19**, 10967–10974 (2003).
  26. Hiratsuka, Y., Tada, T., Oiwa, K., Kanayama, T. & Uyeda, T. Q. P. Controlling the direction of kinesin-driven microtubule movements along microlithographic tracks. *Biophys. J.* **81**, 1555–1561 (2001).
  27. Bunk, R. *et al.* Guiding motor-propelled molecules with nanoscale precision through silanized bi-channel structures. *Nanotechnology* **16**, 710–717 (2005).
  28. Hess, H. *et al.* Molecular Shuttles Operating Undercover: A New Photolithographic Approach for the Fabrication of Structured Surfaces Supporting Directed Motility. *Nano Lett.* **3**, 1651–1655 (2003).
  29. Nicolau, D. V., Suzuki, H., Mashiko, S., Taguchi, T. & Yoshikawa, S. Actin motion on microlithographically functionalized myosin surfaces and tracks.

- Biophys. J.* **77**, 1126–1134 (1999).
30. Suzuki, H., Yamada, A., Oiwa, K., Nakayama, H. & Mashiko, S. Control of actin moving trajectory by patterned poly(methylmethacrylate) tracks. *Biophys. J.* **72**, 1997–2001 (1997).
  31. Månsson, A., Bunk, R., Sundberg, M. & Montelius, L. Self-organization of motor-propelled cytoskeletal filaments at topographically defined borders. *J. Biomed. Biotechnol.* **2012**, (2012).
  32. Lin, C.-T., Kao, M.-T., Kurabayashi, K. & Meyhofer, E. Self-Contained, Biomolecular Motor-Driven Protein Sorting and Concentrating in an Ultrasensitive Microfluidic Chip. *Nano Lett.* **8**, 1041–1046 (2008).
  33. Katira, P. & Hess, H. Two-stage capture employing active transport enables sensitive and fast biosensors. *Nano Lett.* **10**, 567–572 (2010).
  34. Bokhari, S. S. Parallel solution of the subset-sum problem: an empirical study. *Concurr. Comput. Pract. Exp.* **24**, 2241–2254 (2012).
  35. Hodge, R. *The molecules of life: DNA, RNA and proteins*. (Infobase publishing, 2009).
  36. Holmes, K. C., Popp, D., Gebhard, W. & Kabsch, W. Atomic model of the actin filament. *Nature* **347**, 44–49 (1990).
  37. Gittes, F., Mickey, B., Nettleton, J. & Howard, J. Flexural rigidity of microtubules and actin filaments measured from thermal fluctuations in shape. *J. Cell Biol.* **120**, 923–934 (1993).
  38. Hackney, D. D. Highly processive microtubule-stimulated ATP hydrolysis by dimeric kinesin head domains. *Nature* **377**, 448–450 (1995).
  39. Albet-Torres, N. *et al.* Mode of heavy meromyosin adsorption and motor function correlated with surface hydrophobicity and charge. *Langmuir* **23**, 11147–11156 (2007).
  40. Nakanishi, K., Sakiyama, T. & Imamura, K. On the adsorption of proteins on solid surfaces, a common but very complicated phenomenon. *Biosci. Bioeng.* **91**, 233–244 (2001).
  41. van der Veen, M., Stuart, M. C. & Norde, W. Spreading of proteins and its effect on adsorption and desorption kinetics. *Colloids Surfaces B Biointerfaces* **54**, 136–142 (2007).
  42. Hanson, K. L. *et al.* Polymer surface properties control the function of heavy meromyosin in dynamic nanodevices. *Biosens. Bioelectron.* **93**, 305–314 (2017).
  43. Sundberg, M. *et al.* Silanized surfaces for in vitro studies of actomyosin function and nanotechnology applications. *Anal. Biochem.* **323**, 127–138 (2003).

44. Clemmens, J. *et al.* Motor-protein roundabouts : Microtubules moving on kinesin-coated tracks through engineered networks. *Lab Chip* **4**, 83–86 (2004).
45. Bunk, R. *et al.* Guiding molecular motors with nano-imprinted structures. *Jpn. J. Appl. Phys.* **44**, 3337–3340 (2005).
46. Scheer, H.-C. Problems of the nanoimprinting technique for nanometer scale pattern definition. *J. Vac. Sci. Technol. B Microelectron. Nanom. Struct.* **16**, 3917 (1998).
47. Schroeder, V., Korten, T., Linke, H., Diez, S. & Maximov, I. Dynamic Guiding of Motor-Driven Microtubules on Electrically Heated, Smart Polymer Tracks. *Nano Lett.* **13**, 3434–3438 (2013).
48. Cui, Y., Wei, Q., Park, H. & Lieber, C. M. Nanowire nanosensors for highly sensitive and selective detection of biological and chemical species. *Science* (80-. ). **293**, 1289–1292 (2001).
49. Sorgenfrei, S. *et al.* Label-free single-molecule detection of DNA-hybridization kinetics with a carbon nanotube field-effect transistor. *Nat. Nanotechnol.* **6**, 126–132 (2011).
50. Vedala, H. *et al.* Nanoelectronic Detection of Lectin-Carbohydrate Interactions Using Carbon Nanotubes. *Nano Lett.* **11**, 170–175 (2010).
51. Lerner, M. B. *et al.* Hybrids of a Genetically Engineered Antibody and a Carbon Nanotube Transistor for Detection of Prostate Cancer Biomarkers. *ACS Nano* **6**, 5143–5149 (2012).
52. Governatori, G., Olivieri, F., Scannapieco, S., Rotolo, A. & Cristani, M. Strategic argumentation is NP-complete. in *Frontiers in Artificial Intelligence and Applications* **263**, 399–404 (2013).
53. Verma, T. S. & Pearl, J. Deciding Morality of Graphs is NP-complete. in *Uncertainty in Artificial Intelligence* 391–399 (1993). doi:10.1016/b978-1-4832-1451-1.50052-4
54. Fraenkel, A. S. Complexity of protein folding. *Bull. Math. Biol.* **55**, 1199–1210 (1993).
55. Berger, B. & Leighton, T. Protein Folding in the Hydrophobic-Hydrophilic ( HP ) Model is NP-Complete. *J. Comput. Biol.* **5**, 27–40 (1998).
56. Yan, G., Zhou, T., Hu, B., Fu, Z.-Q. & Wang, B.-H. Efficient routing on complex networks. *Phys. Rev. E* **73**, 046108 (2006).
57. Homsher, E., Wang, F. & Sellers, J. R. Factors affecting movement of F-actin filaments propelled by skeletal muscle heavy meromyosin. *Am. J. Physiol.* **262**, C714–C723 (1992).
58. Huxley, A. F. Muscle structure and theories of contraction. *Prog Biophys*

- Biophys Chem* **7**, 255–318 (1957).
59. Huxley, H. E. The Mechanism of Muscular Contraction. *Science* (80-. ). **164**, 1356–1366 (1969).
  60. Rayment, I. *et al.* Structure of the Actin-Myosin Complex and Its Implications for Muscle Contraction. *Science* (80-. ). **261**, 58–65 (1993).
  61. Alberts, B. *et al.* *Essential cell biology*. (Garland Science, 2010).
  62. Moore, P. B., Huxley, H. E. & DeRosier, D. J. Three-dimensional reconstruction of F-actin, thin filaments and decorated thin filaments. *J. Mol. Biol.* **50**, 279–296 (1970).
  63. Jockusch, B. M. *The Actin Cytoskeleton*. (Springer, 2017).
  64. Bengtsson, E. *et al.* Myosin-Induced Gliding Patterns at Varied [MgATP] Unveil a Dynamic Actin Filament. *Biophys. J.* **111**, 1465–1477 (2016).
  65. Vikhorev, P. G., Vikhoreva, N. N. & Månsson, A. Bending flexibility of actin filaments during motor-induced sliding. *Biophys. J.* **95**, 5809–5819 (2008).
  66. Odronitz, F. & Kollmar, M. Drawing the tree of eukaryotic life based on the analysis of 2,269 manually annotated myosins from 328 species. *Genome Biol.* **8**, R196 (2007).
  67. Hartman, M. A. & Spudich, J. a. The myosin superfamily at a glance. *J. Cell Sci.* **125**, 1627–1632 (2012).
  68. Bordas, J. *et al.* Extensibility and symmetry of actin filaments in contracting muscles. *Biophys. J.* **77**, 3197–207 (1999).
  69. Margossian, S. & Lowey, S. Preparation of myosin and its subfragments from rabbit skeletal-muscle. *Methods Enzymol.* **85**, 55–71 (1982).
  70. Lu, R. C. Identification of a region susceptible to proteolysis. *PNAS* **77**, 2010–2013 (1980).
  71. Mellema, J. E., Van Bruggen, E. F. J. & Gruber, M. Uranyl oxalate as a negative stain for electron microscopy of proteins. *Biochim. Biophys. Acta* **140**, 180–182 (1967).
  72. Kodama, T. Thermodynamic analysis of muscle ATPase mechanisms. *Physiol. Rev.* **65**, 467–551 (1985).
  73. Ebashi, S., Ebashi, F. & Kodama, A. Troponin as the Ca<sup>++</sup>-receptive Protein in the Contractile System. *J. Biochem.* **62**, 137–138 (1967).
  74. Walcott, S., Warshaw, D. M. & Debold, E. P. Mechanical coupling between myosin molecules causes differences between ensemble and single-molecule measurements. *Biophys. J.* **103**, 501–510 (2012).
  75. Howard, J. *Mechanics of motor proteins and the cytoskeleton*. (Sinauer

- Associates, 2001).
76. Nitta, T. & Hess, H. Dispersion in active transport by kinesin-powered molecular shuttles. *Nano Lett.* **5**, 1337–1342 (2005).
  77. Goldstein, L. S. B. & Philp, A. V. The road less traveled: Emerging principles of kinesin motor utilization. *Annu. Rev. cell Dev. Biol.* **15**, 141–83 (1999).
  78. Rice, S. *et al.* A structural change in the kinesin motor protein that drives motility. *Nature* **402**, 778–84 (1999).
  79. Nitta, T. *et al.* Comparing guiding track requirements for myosin-and kinesin-powered molecular shuttles. *Nano Lett.* **8**, 2305–2309 (2008).
  80. Zhang, M., Desai, T. & Ferrari, M. Proteins and cells on PEG immobilized silicon surfaces. *Biomaterials* **19**, 953–960 (1998).
  81. van den Heuvel, M. G. L., Butcher, C. T., Smeets, R. M. M., Diez, S. & Dekker, C. High rectifying efficiencies of microtubule motility on Kinesin-coated gold nanostructures. *Nano Lett.* **5**, 1117–1122 (2005).
  82. Gangnaik, A. S., Georgiev, Y. M. & Holmes, J. D. New Generation Electron Beam Resists: A Review. *Chem. Mater.* **29**, 1898–1917 (2017).
  83. Manfrinato, V. R. *et al.* Resolution limits of electron-beam lithography towards the atomic scale. *Nano Lett.* **13**, 1555–1558 (2013).
  84. Raith GmbH, Dortmund. Available at: [www.raith.com](http://www.raith.com).
  85. Stepanova, M. & Dew, S. *Nanofabrication: Techniques and Principles*. (Springer, 2012). doi:10.1007/978-3-7091-0424-8
  86. Kyser, D. F. & Ting, C. H. Voltage dependence of proximity effects in electron beam lithography. *J. Vac. Sci. Technol.* **16**, 1305–8 (1979).
  87. Chou, S. Y., Krauss, P. R., Zhang, W., Guo, L. & Zhuang, L. Sub-10 nm imprint lithography and applications. *J. Vac. Sci. Technol.* **15**, 2897–2904 (1997).
  88. Chou, S., Krauss, P. & Renstrom, P. Imprint of sub-25nm vias and trenches in polymers. *Appl. Phys. Lett.* **67**, 3114 (1995).
  89. Tang, M.-J., Xie, H.-M., Li, Y.-J., Li, X.-J. & Wu, D. A New Grating Fabrication Technique on Metal Films Using UV-Nanoimprint Lithography. *Chinese Phys. Lett.* **29**, 098101 (2012).
  90. Guo, L. J. Recent progress in nanoimprint technology and its applications. *J. Phys. D. Appl. Phys.* **37**, R123–R141 (2004).
  91. Rey, A., Rothe, J. & Marple, A. Path-Disruption Games: Bribery and a Probabilistic Model. *Theory Comput. Syst.* **60**, 222–252 (2017).
  92. Diffie, W. & Hellman, M. E. New Directions in Cryptography. *IEEE Trans.*

- Inf. Theory* **22**, 644–654 (1976).
93. Cook, S. A. The complexity of theorem proving procedures. *Proc. 3rd Annu. ACM Symp. Theory Comput.* 151–158 (1971).
  94. Levin, L. A. Universal Sequential Search Problems. *Probl. Inf. Transm.* **9**, 115–116 (1973).
  95. Karp, R. M. *Reducibility among combinatorial problems. Complexity of Computer Computations* (Plenum, 1972). doi:10.1007/978-3-540-68279-0\_8
  96. Whitesides, G. M. The origins and the future of microfluidics. *Nature* **442**, 368–373 (2006).
  97. Qian, L. & Winfree, E. Scaling up digital circuit computation with DNA strand displacement cascades. *Science (80-. )*. **332**, 1196–1201 (2011).
  98. Boneh, D., Dunworth, C., Lipton, R. J. & Sgall, J. On the computational power of DNA. *Discret. Appl. Math.* **71**, 79–94 (1996).
  99. Ouyang, Q., Kaplan, P. D., Liu, S. & Libchaber, A. DNA solution of the maximal clique problem. *Science (80-. )*. **278**, 446–449 (1997).
  100. R Landauer. Irreversibility and Heat Generation in the Computing Process. *IBM J. Res. Dev.* **5**, 183–191 (1961).
  101. Jaber, J. a., Chase, P. B. & Schlenoff, J. B. Actomyosin-Driven Motility on Patterned Polyelectrolyte Mono- and Multilayers. *Nano Lett.* **3**, 1505–1509 (2003).
  102. Harada, Y., Sakurada, K., Aoki, T., Thomas, D. D. & Yanagida, T. Mechanochemical coupling in actomyosin energy transduction studied by in vitro movement assay. *J. Mol. Biol.* **216**, 49–68 (1990).
  103. Albet-Torres, N., Gunnarsson, A., Persson, M., Balaz, M. & Höök, F. Molecular motors on lipid bilayers and silicon dioxide: different driving forces for adsorption. *Soft Matter* **6**, 3211–3219 (2010).
  104. Ramsden, J. J., Roush, D. J., Gill, D. S., Kurrat, R. & Willson, R. C. Protein Adsorption Kinetics Drastically Altered by Repositioning a Single Charge. *J. Am. Chem. Soc.* **117**, 8511–8516 (1995).
  105. Persson, M. *et al.* Heavy meromyosin molecules extending more than 50 nm above adsorbing electronegative surfaces. *Langmuir* **26**, 9927–9936 (2010).
  106. Warrick, H. M. *et al.* In vitro methods for measuring force and velocity of the actin-myosin interaction using purified proteins. *Methods Cell Biol.* **39**, 1–21 (1993).
  107. Rivelino, D. *et al.* Acting on actin: The electric motility assay. *Eur. Biophys. J.* **27**, 403–408 (1998).

108. Nicolau, D. V. *et al.* Surface hydrophobicity modulates the operation of actomyosin-based dynamic nanodevices. *Langmuir* **23**, 10846–10854 (2007).
109. van Zalinge, H. *et al.* Surface-Controlled Properties of Myosin Studied by Electric Field Modulation. *Langmuir* **31**, 8354–8361 (2015).
110. Lindberg, F. W. *et al.* Controlled Surface Silanization for Actin-Myosin Based Nanodevices and Biocompatibility of New Polymer Resists. *Langmuir* **34**, 877–8784 (2018).
111. Betzel, C., Gour, P. P. & Saenger, W. Three-dimensional structure of proteinase K at 0.15-nm resolution. *Eur. J. Biochem.* **178**, 155–171 (1988).
112. Higashi-Fujime, S., Suzuki, M., Titani, K. & Hozumi, T. Muscle actin cleaved by Proteinase K: Its polymerization and In Vitro motility. *J. Biochem.* **112**, 568–572 (1992).
113. Fan, D. & Ekinci, Y. Photolithography reaches 6 nm half-pitch using extreme ultraviolet light. *J. Micro/Nanolithography, MEMS, MOEMS* **15**, 33505 (2016).
114. Tallents, G., Wagenaars, E. & Pert, G. Optical lithography: Lithography at EUV wavelengths. *Nat. Photonics* **4**, 809–811 (2010).
115. Schirmer, M. *et al.* Chemical Semi-Amplified positive E-beam Resist (CSAR 62) for highest resolution. *Proc. SPIE* **8886**, 88860D–88860D–7 (2013).
116. Thoms, S. & Macintyre, D. S. Investigation of CSAR 62, a new resist for electron beam lithography. *J. Vac. Sci. Technol. B-Nanotechnology Microelectron.* **32**, 1–7 (2014).
117. Van Der Gaag, B. P. & Scherer, A. Microfabrication below 10 nm. *Appl. Phys. Lett.* **56**, 481–483 (1990).
118. Yasin, S., Hasko, D. G. & Ahmed, H. Comparison of MIBK/IPA and water/IPA as PMMA developers for electron beam nanolithography. *Microelectron. Eng.* **61–62**, 745–753 (2002).
119. Guo, J. L. Nanoimprint lithography: methods and material requirements. *Adv. Mater.* **19**, 495–513 (2007).
120. Nitta, T., Tanahashi, A., Hirano, M. & Hess, H. Simulating molecular shuttle movements: Towards computer-aided design of nanoscale transport systems. *Lab Chip* **6**, 881–885 (2006).
121. Lindberg, F. W. *et al.* Design and development of nanoimprint-enabled structures for molecular motor devices. *Mater. Res. Express* **6**, (2019).
122. Korten, T., Diez, S. & Jr, D. N. *Encoding Exact Cover Into Network Form and Solving it by Biocomputation.* (2019).

123. Ionov, L., Stamm, M. & Diez, S. Reversible switching of microtubule motility using thermoresponsive polymer surfaces. *Nano Lett.* **6**, 1982–1987 (2006).
124. Gao, A. *et al.* Silicon-nanowire-based CMOS-compatible field-effect transistor nanosensors for ultrasensitive electrical detection of nucleic acids. *Nano Lett.* **11**, 3974–3978 (2011).
125. Gao, A. *et al.* Enhanced sensing of nucleic acids with silicon nanowire field effect transistor biosensors. *Nano Lett.* **12**, 5262–5268 (2012).
126. Taniguchi, Y. *et al.* PGMA as a High Resolution , High Sensitivity Negative Electron Beam Resist. *Jpn J Appl Phys* **18**, 1143–1148 (1979).
127. Synytska, A., Stamm, M., Diez, S. & Ionov, L. Simple and Fast Method for the Fabrication of Switchable Bicomponent Micropatterned Polymer Surfaces. *Langmuir* **23**, 5205–5209 (2007).
128. Lyttleton, R. W. Development of solid-state nanodevices for studying proteins. (University of New South Wales, 2018).
129. Sanders, L. K. *et al.* Control of electrostatic interactions between F-actin and genetically modified lysozyme in aqueous media. *Proc. Natl. Acad. Sci.* **104**, 15994–15999 (2007).
130. Tuszyński, J. A., Portet, S., Dixon, J. M., Luxford, C. & Cantiello, H. F. Ionic Wave Propagation along Actin Filaments. *Biophys. J.* **86**, 1890–1903 (2004).
131. Balaz, M. & Månsson, A. Detection of small differences in actomyosin function using actin labeled with different phalloidin conjugates. *Anal. Biochem.* **338**, 224–236 (2005).



Paper I







## Controlled Surface Silanization for Actin-Myosin Based Nanodevices and Biocompatibility of New Polymer Resists

Frida W. Lindberg,<sup>†</sup> Marlene Norrby,<sup>‡</sup> Mohammad A. Rahman,<sup>‡</sup> Aseem Salhotra,<sup>‡</sup> Hideyo Takatsuki,<sup>‡</sup> Sören Jeppesen,<sup>†</sup> Heiner Linke,<sup>†</sup> and Alf Månsson<sup>\*,‡</sup>

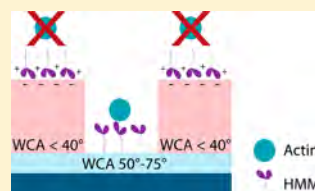
<sup>†</sup>NanoLund and Solid State Physics, Lund University, Box 118, Lund SE-221 00, Sweden

<sup>‡</sup>Department of Chemistry and Biomedical Sciences, Linnaeus University, Kalmar SE-391 82, Sweden

### Supporting Information

**ABSTRACT:** Molecular motor-based nanodevices require organized cytoskeletal filament guiding along motility-promoting tracks, confined by motility-inhibiting walls. One way to enhance motility quality on the tracks, particularly in terms of filament velocity but also the fraction of motile filaments, is to optimize the surface hydrophobicity. We have investigated the potential to achieve this for the actin-myosin II motor system on trimethylchlorosilane (TMCS)-derivatized SiO<sub>2</sub> surfaces to be used as channel floors in nanodevices. We have also investigated the ability to suppress motility on two new polymer resists, TU7 (for nanoimprint lithography) and CSAR 62 (for electron beam and deep UV lithography), to be used as channel walls.

We developed a chemical-vapor deposition tool for silanizing SiO<sub>2</sub> surfaces in a controlled environment to achieve different surface hydrophobicities (measured by water contact angle). In contrast to previous work, we were able to fabricate a wide range of contact angles by varying the silanization time and chamber pressure using only one type of silane. This resulted in a significant improvement of the silanization procedure, producing a predictable contact angle on the surface and thereby predictable quality of the heavy meromyosin (HMM)-driven actin motility with regard to velocity. We observed a high degree of correlation between the filament sliding velocity and contact angle in the range 10–86°, expanding the previously studied range. We found that the sliding velocity on TU7 surfaces was superior to that on CSAR 62 surfaces despite similar contact angles. In addition, we were able to suppress the motility on both TU7 and CSAR 62 by plasma oxygen treatment before silanization. These results are discussed in relation to previously proposed surface adsorption mechanisms of HMM and their relationship to the water contact angle. Additionally, the results are considered for the development of actin-myosin based nanodevices with superior performance with respect to actin-myosin functionality.



### 1. INTRODUCTION

Molecular motor proteins are responsible for active transport and directed movement in eukaryotic cells. In the *in vitro* motility assay,<sup>1–4</sup> isolated motor-proteins are adsorbed on appropriate surfaces where they propel their corresponding cytoskeletal filament.<sup>5,6</sup> In addition to giving great insight into the biophysical and physiological properties of molecular motor systems,<sup>7–10</sup> this assay has enabled a variety of nanotechnology applications such as biocomputation<sup>5</sup> and biosensing.<sup>5,11–15</sup> In these instances, key advantages are self-propulsion without the need for bulky accessory equipment such as pumps and, not the least, high energy efficiency<sup>5,6</sup> (energy used per calculation or separation operation) compared to competing techniques, e.g., micro- and nanofluidics.

One molecular motor system used in nanotechnology applications is the actin-myosin II motor system of muscle.<sup>16–18</sup> In these applications, filamentous actin is generally propelled by surface-adsorbed proteolytic myosin II motor fragments, primarily heavy meromyosin<sup>14</sup> (HMM). The mechanism underlying the adsorption of HMM on a surface is complex and depends on several factors including the surface hydrophobicity<sup>19–21</sup> and the surface charge.<sup>22</sup> The surface

hydrophobicity can be altered by surface functionalization with different silanes.<sup>23–25</sup> On the basis of previous results, trimethylchlorosilane (TMCS)-derivatized surfaces have been found to promote high-quality actin-myosin motility superior to that on other surface chemistries.<sup>22,24</sup>

Use of molecular motors in nanotechnological applications requires organized guiding of transported filaments (filament motility) along tracks,<sup>26</sup> e.g., to concentrate analyte molecules in localized detector areas<sup>12</sup> or for computational network exploration.<sup>5</sup> Such guiding can be achieved by selective immobilization of functional motors only on the tracks and not in the surrounding areas. The selectivity can be achieved by different surface chemistries<sup>27–29</sup> on the tracks and the surroundings. However, physical<sup>11,30–34</sup> patterning of tracks, e.g., the use of physical walls, also supports effective guiding. Optimally, a combination of the two approaches should be used,<sup>27,35</sup> with channel floors supporting motility, surrounded by nonmotile, confining channel walls. To obtain unidirectional movement of actin filaments without U-turns, the

Received: April 30, 2018

Revised: July 3, 2018

Published: July 3, 2018

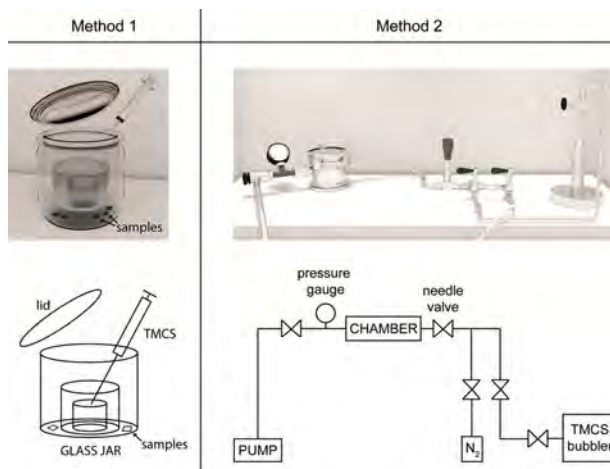


**Figure 1.** 3D render and schematic illustration of silanization method 1 and method 2. In method 1 the silanization is done inside a glass jar using a fully saturated TMCS system. In method 2 the silanization chamber is pumped down to vacuum pressure, whereupon TMCS is flown in. The influx of TMCS can be controlled by the valves, enabling silanization at different chamber pressures.

channel tracks must be narrow<sup>11</sup> (<300 nm). These narrow tracks can be fabricated in polymer resists using nanoimprint lithography<sup>36</sup> or electron-beam lithography,<sup>30</sup> to surround, e.g., TMCS-derivatized SiO<sub>2</sub> floors<sup>11</sup> with polymer resist walls.

Hitherto, TMCS silanization has been performed without control of the TMCS pressure,<sup>5,24,30</sup> and no studies have been done to measure the motility quality regarding filament velocity on different surface hydrophobicities obtained using one given silane type. We hypothesize that the surface hydrophobicity can be controlled by controlling the chamber pressure during silanization, giving a detailed insight into how different degrees of TMCS-based silanization affects the actin-myosin function.

Furthermore, previous actin-myosin motility studies have been performed using five different positive-tone resists<sup>11,33,34,37</sup> for electron-beam lithography and two negative-tone resists<sup>11</sup> for nanoimprint lithography. However, the latest results for new resists were published over a decade ago,<sup>11</sup> and new lithography materials are constantly being developed and need to be studied because they hold several advantages with respect to contrast, resolution, chemical safety, and tailoring of suitable motor-based nanodevices for each application. New polymer resists with interesting properties in these respects are CSAR 62, a high-resolution positive-tone resist for electron-beam lithography and deep-UV lithography, and TU7, which is a negative-tone resist with a low molding temperature especially designed for nanoimprint lithography.

In this Article, we investigate the combination of these new materials and processes to achieve controlled surface functionalizations for improved actin-myosin based nanodevices. Specifically, we investigate the motility quality (particularly sliding velocity but also fraction of motile filaments) on SiO<sub>2</sub> surfaces derivatized by TMCS, using a controlled CVD process with the capability to regulate the chamber pressure. Furthermore, we examine the potential of using CSAR 62 and TU7 as channel walls in nanodevices.

We found that the myosin-driven actin motility was not inhibited by the presence of the CSAR 62 and TU7 resists but that it could be suppressed on both resist surfaces by oxygen plasma treatment. This is an essential property of materials to be useful in the production of walls and surrounding areas in nanodevices. We were also able to obtain surfaces with predictable hydrophobicity and equally predictable actin filament sliding velocity by using controlled chemical-vapor deposition to obtain different water contact angles. These results confirm our hypothesis concerning effective control of filament velocity and, thus, motility quality by controlling the degree of silanization by TMCS. The results also support and expand previous ideas about the basis for the relationship between surface contact angle and HMM-propelled actin-filament motility.<sup>14,22</sup> Together, the findings provide a strong foundation for the improvement of actin-myosin based nanodevices produced by either electron-beam or nanoimprint lithography.

## 2. EXPERIMENTAL SECTION

**2.1. Chip Preparation.** All chips were fabricated using 10 × 10 mm<sup>2</sup> Si(100) substrates. The substrates were ashed in oxygen plasma at 5 mbar for 60 s and cleaned in acetone and isopropanol for 3 min each in an ultrasonic bath at room temperature followed by drying under nitrogen flow. CSAR 62 (Allresist GmbH, Strausberg, Germany) was spin-coated at 3000 rpm and baked on a hotplate at 160 °C for 120 s. TU7 (Obducat AB, Lund, Sweden) was spin-coated at 1500 rpm and baked on a hotplate at 95 °C for 60 s. All chips underwent the same chemical treatment as they would have undergone if patterned by the respective lithography technique. The CSAR 62 chips were immersed in the developer *o*-xylene for 5 min and dried under nitrogen flow. The TU7 chips were imprinted with an unpatterned, soft intermediate polymer stamp (IPS) at 75 °C with a pressure of 20 bar while being exposed to 4 × 5 s UV-light pulses every 10 s. The pressure was maintained for 2 min and then decreased to ambient conditions while cooling. Prior to silanization, half the batch of polymer chips was ashed in oxygen plasma for 15 s at 5 mbar and the other half was not.

The SiO<sub>2</sub> chips used for examining the contact angle variation at different TMCS chamber pressures were also fabricated using 10 × 10 mm<sup>2</sup> Si(100) substrates. A 70 nm thick SiO<sub>2</sub> layer was first deposited by atomic layer deposition. Prior to silanization, all these chips were ashed in oxygen plasma for 15 s at 5 mbar.

A patterned 250 nm thick CSAR 62 surface on 70 nm SiO<sub>2</sub> with 200 nm wide channels was also prepared using the same parameters as specified above but here including an electron-beam lithography exposure (dose 60 μC/cm<sup>2</sup>, beam current 0.1 nA).

**2.2. Silanization Method 1.** The polymer chips and SiO<sub>2</sub> reference were silanized using the previous, less-controlled silanization method (here delineated as method 1) in a glass jar in a glovebox (Figure 1). A few drops of trimethylchlorosilane (Sigma-Aldrich, Missouri, U.S.A.) were added using a needle and syringe to a beaker inside the glass jar, which was then shut and kept closed until the treatment was terminated. The silanization was performed for two different times: 10 and 30 min.

**2.3. Silanization Method 2.** To examine the filament velocity variation on SiO<sub>2</sub> surfaces with different surface hydrophobicities, a controlled chemical-vapor deposition (CVD) system was developed, in the following referred to as silanization method 2 (Figure 1). All gas lines, valves, and the deposition chamber were built in stainless steel (SS). An oil-free scroll pump was connected to a valve and a pressure gauge and then to the chamber using couplings with viton gaskets. The deposition chamber lid was sealed by a viton O-ring. Between the chamber and the N<sub>2</sub> and TMCS gas lines we placed a SS needle valve with Swagelok fittings. The N<sub>2</sub> gas line and the TMCS stainless steel bubbler (SAFC Hightech, Bromborough, U.K.) were separated by manual SS on/off valves.

The chips to be silanized were placed inside the deposition chamber, which was then pumped down to a chamber pressure of 10<sup>-2</sup> mbar. Prior to TMCS deposition, the chamber was purged in one cycle with N<sub>2</sub> gas. To silanize, we opened the TMCS bubbler and then the TMCS valve separating the gas source and the chamber. The needle valve was kept fully open during the entire silanization process. The TMCS bubbler was closed when the desired chamber pressure was reached to maintain a stable pressure for the duration of silanization. Both the silanization time and pressure were varied to obtain a series of samples with different water contact angles (see Supporting Information for more details). After silanization, the chamber and gas lines up to the bubbler and N<sub>2</sub> valves were pumped down again to 10<sup>-2</sup> mbar and purged with N<sub>2</sub> gas in 3 cycles.

**2.4. Contact Angle Measurements.** To determine the hydrophobicity of the surface after various treatments, we performed static contact angle measurements at 22 °C using a Theta Lite Tensiometer. A sessile drop of ultrapure (type 1) water was dropped onto the surface using a manual one-touch dispenser. The droplet was imaged using a FireWire camera with telecentric optics and monochromatic LED-based background lighting. We used the OneAttention software (Biolin Scientific, Västra Frölunda, Sweden) to perform computer analysis of the drop profile and extract the contact angle data from the Young equation.

**2.5. Atomic Force Microscopy Measurements.** The surface roughness and texture of both TU7 (after imprinting) and CSAR 62 were examined using an atomic force microscope (Dimension 3100, Veeco Digital Instruments, Inc., Plainview, N.Y.). The scans were obtained in contact mode using a Pointprobe silicon-SPM-Sensor with rotated tip (180°) with an Al coating on the detector side. The surfaces were scanned before silanization. Each scan was done on a 5 × 5 μm<sup>2</sup> area (256 × 256 pixels) and analyzed in Gwyddion (GNU GPL developed by the Czech Metrology Institute). The surface topography was analyzed from line scans in the raw data before smoothing in terms of the root-mean-square (RMS) on four different chips, with 10 lines per chip.

**2.6. Protein Preparations.** Muscles were obtained from New Zealand White rabbits (KB Lidköpings Kaninfarm, Lidköping, Sweden). The animals were sacrificed following the standard procedure approved by the Ethical Committee for Animal Experiments, Linköping, Sweden (reference no. 73-14), and performed in accordance with National and European legislation. White hind leg

muscles were used for extraction of myosin II from fast skeletal muscles and back muscles for extraction of actin.

Immediately upon dissection, the muscles were rinsed in ice-cold 0.15 M NaCl and myosin was then isolated essentially as described by Kron et al.<sup>4</sup> and Sata et al.<sup>38</sup> Heavy meromyosin (HMM) was obtained by chymotryptic cleavage of myosin II using the method described by Okamoto and Sekine.<sup>39</sup> Actin acetone powder was prepared and subsequent isolation of actin was performed as described by Pardee and Spudis.<sup>40</sup> The final concentration of proteins was determined using a spectrophotometer, and the purity was assessed by sodium dodecyl sulfate polyacrylamide gel electrophoresis (SDS-PAGE). Actin filaments were labeled with rhodamine-phalloidin (Technologies, U.S.A.; Cat. no. R415) essentially as described by Kron et al.<sup>4</sup> and Balaz and Månsson.<sup>41</sup>

**2.7. Motility Assay and Data Collection.** We performed *in vitro* motility assays<sup>42</sup> using flow cells built out of a microscope coverslip (no. 0, Menzel-Gläser, Braunschweig, Germany) and an appropriately functionalized silicon chip separated with a spacer of a 60 μm thick double-sided tape (3M, Saint Paul, MN). The chips were mounted upside down, on top of the spacer, so that the functionalized surface formed the top surface of the flow cell.

The flow cell was incubated with HMM and rhodamine-phalloidin labeled actin filaments according to a protocol modified from that described previously.<sup>42</sup> The following incubation steps were used: 120 μg/mL HMM (2–5 min), 1 mg/mL BSA (2 min), and 5–10 nM rhodamine-phalloidin labeled actin filaments (2 min). The ionic strength was either 60 (a60) or 130 mM, where the solution of the latter ionic strength contained 0.64% methyl cellulose (aMC130). The ionic strength was regulated by varying the KCl concentrations. We did not use blocking actin or affinity purification to block or remove ATP-insensitive HMM heads<sup>43</sup> (“dead heads”). The MgATP concentration used was 1 mM in all assay solutions.

The motility assay was imaged using a Nikon TE300 inverted microscope with mercury-lamp illumination, Nikon 100 × 1.4 NA oil immersion objective, TRITC filter set (excitation, 532–554 nm; emission, 570–613 nm; dichroic cut-on, 562 nm), and a Hamamatsu EMCCD camera. The recordings were analyzed using a custom-developed MATLAB (MathWorks, Natick, MA)<sup>13</sup> program to examine the actin filament sliding velocity. The boxplots shown in Figures 2 and 4 are generated using MATLABs boxplot function,

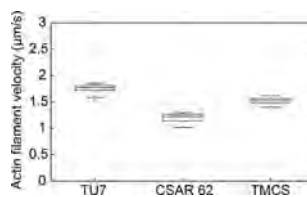


**Figure 2.** Measured actin filament velocities on TU7, CSAR 62, and TMCS-derivatized SiO<sub>2</sub> silanization using method 1. No motility was observed on plasma oxygen-treated TU7 and CSAR 62. The TU7 and CSAR 62 surfaces in the graph have not been plasma-ashed, and both promote actin filament motility. The highest velocity was observed on TU7. The motility experiments were performed at 19.2 ± 0.4 °C on 2 chips per polymer, and 20 filaments per chip were analyzed.

where the central mark shows the median, the top edge of the box shows the 75th percentile, and the lower edge of the box shows the 25th percentile. The whiskers show the most extreme data points not considered to be outliers (outliers (+) are marked in red). An outlier is defined as a point greater than 1.5 times the interquartile range away from the top or bottom of the box. The number of filaments and filament lengths in each recording were analyzed using *in-house* developed ImageJ<sup>44,45</sup> plug-ins.

### 3. RESULTS AND DISCUSSION

**3.1. Motility on TU7 and CSAR 62 Resist.** In the manufacturing of nanodevices utilizing the actin-myosin motility, the floors of the motility nanochannels are first opened up by electron-beam lithography or nanoimprint lithography of the covering resist.<sup>5,12</sup> This is followed by plasma ashing of the entire surface to remove resist remnants in the channels before silanization and to modify the surface chemistry of the surrounding resist areas. To mimic and evaluate this procedure, we measured contact angles on the two resists before and after silanization for both plasma-ashed (PA) and nonplasma-ashed (NPA) chips as well as on plasma-ashed SiO<sub>2</sub> reference chips (Table 1).

**Table 1. Measured Contact Angles of Plasma-Ashed (PA) and Nonplasma-Ashed (NPA) TU7, CSAR 62, and SiO<sub>2</sub> Surfaces after TMCS Silanization Using Method 1 for Different Time Durations<sup>a</sup>**

TMCS (min)	TU7 PA	TU7 NPA	CSAR 62 PA	CSAR 62 NPA	SiO <sub>2</sub> PA
0	24 ± 1°	65 ± 1°	33 ± 1°	71 ± 1°	<5° <sup>b</sup>
10	26 ± 1°	63 ± 1°	35 ± 0°	71 ± 1°	67 ± 1°
30	25 ± 2°	63 ± 1°	33 ± 1°	69 ± 0°	69 ± 2°

<sup>a</sup>The values are given as the average of contact angles ± standard deviations measured on two different surfaces. <sup>b</sup>The water contact angle was below the measurement limit, ~5°.

The results show that the contact angle of the resists was unaffected by silanization. The contact angles for the nonplasma-ashed chips with polymer resists were similar to those previously found to be optimal for HMM adsorption in functional form using a range of surface derivations.<sup>21,22,24,46</sup> In this mode of HMM adsorption, the C-terminal tail segment of HMM is believed to partially unfold,<sup>20</sup> associated with entropically driven adsorption<sup>19</sup> on moderately hydrophobic areas (e.g., those derivatized with TMCS). The actin filament sliding velocities for the nonplasma-ashed TU7 and CSAR 62 chips are shown in Figure 2. The results from the 10 and 30 min silanization have been merged into one boxplot as no difference was observed regarding the actin filament sliding velocity or contact angle, which coincides well with previous reports<sup>24</sup> for silanization in what was believed to be a fully TMCS-saturated system. The sliding velocity on TU7 was higher than that on CSAR 62 despite the contact angle on the latter resist being very close to that found previously<sup>21,22</sup> to be optimal for motility. The observation of motility on both TU7 and CSAR 62 demonstrates that neither of the resists is toxic to the proteins.

We investigated if different surface roughnesses may be the basis for different motility qualities on TU7 and CSAR 62. Thus, Sundberg et al.<sup>24</sup> proposed that a rougher surface may cause a decrease in the sliding velocity due to friction or a nonuniform HMM surface density. Furthermore, van Zalinge et al.<sup>47</sup> suggested that chemical interactions of the force-producing HMM motor domains with protruding parts of the surface may cause a decrease in sliding velocity with increased surface roughness. However, Albet-Torres et al.<sup>22</sup> did not detect clear differences in motility quality between surfaces with different roughnesses. The surface roughnesses on TU7 and CSAR 62 were investigated by atomic force microscopy (AFM) imaging. Figure 3 shows two representative AFM scans of TU7 (A) and CSAR 62 (B) surfaces. The measured RMS

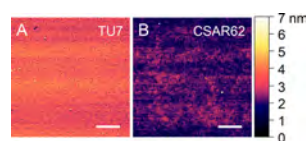


**Figure 3.** AFM scans of (A) TU7 and (B) CSAR 62 surfaces after smoothing the data. The root-mean-square (RMS) surface roughness (determined from raw data before smoothing) on CSAR 62 ( $0.41 \pm 0.02$  nm) was similar to that measured on TU7 ( $0.47 \pm 0.05$  nm). The scale bar is  $1 \mu\text{m}$  in both images.

surface roughness on TU7 was  $0.47 \pm 0.05$  nm (mean of 10 measurements on 4 different surfaces ± standard deviation) and that on CSAR 62 was  $0.41 \pm 0.02$  nm, i.e., the same within the uncertainty of the measurement. In these experiments, the CSAR 62 surface exhibited a lower HMM-propelled actin filament sliding velocity than TU7, despite having a higher contact angle than the latter surface. The similarity in surface roughness between TU7 and CSAR 62 suggests that the difference in velocity between these two surfaces is not due to differences in surface roughness; other factors are likely to be important.<sup>21,48</sup> Finally, the velocities were similar on TMCS-derivatized SiO<sub>2</sub> and nonplasma-ashed TU7 despite lower contact angle on the latter surface. The results could fit with the idea that an appreciably smoother surface like TMCS<sup>24</sup> promotes a higher sliding velocity. On the other hand, the differences in velocity between TU7 and CSAR 62 and the similarities between TMCS and TU7 support the view that also other factors than the contact angle and surface roughness are important.<sup>14,21,22,47</sup> More detailed studies in the future as previously performed for other polymer materials<sup>21,48</sup> would be of value, e.g., analyzing the difference in water uptake and polymer mechanical properties at the macromolecular chain level. In this connection it is of interest<sup>21</sup> to investigate if there are differences in total HMM density as well as in the fraction of active HMM molecules on the different polymers. Whereas a detailed investigation of these issues is outside the scope of the present study, we obtained evidence against different densities of actin propelling HMM molecules on TU7 and CSAR 62 by studying the sliding velocity of actin filaments as a function of filament length (see Supporting Information, Figure S1). This relationship is known to reflect the number of myosin heads that are available for binding and propulsion of the actin filament,<sup>49–51</sup> i.e., not including those heads that are prevented from taking part in such interactions. We found no length dependence of the velocity on either of the surfaces, consistent with the idea that the lower velocity on CSAR 62 is not attributed to a lower density of active HMM molecules.

Large decreases (~40°) in the contact angle were observed on both TU7 and CSAR 62 after plasma ashing (Table 1), and we were able to fully suppress the motility on both resists if they were treated with oxygen plasma prior to silanization. This is expected because the oxygen plasma oxidizes the resist surface and makes it more hydrophilic<sup>52</sup> by introducing primarily hydroxyl groups. Furthermore, previous reports<sup>53,54</sup> have also shown that oxygen plasma treatment may induce modifications in the polymer surface that render it positively or negatively charged, although no surface charge measurements were performed on these surfaces. This issue is further discussed later.

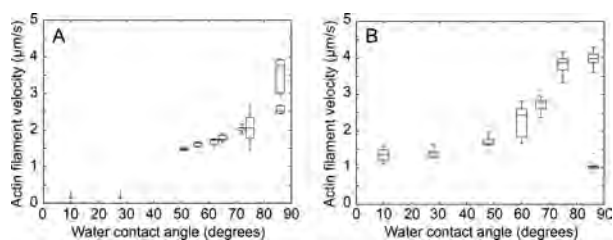


**Figure 4.** Actin filament velocities on TMCS-derivatized  $\text{SiO}_2$  surfaces using a60 (A) and aMC130 (B) assay solution. The actin filament sliding velocity increases with an increasing water contact angle in both assay solutions. No motility was observed at the lower angles in a60 solution (indicated by arrows). At the highest contact angle tested, the motility quality showed greater variability. The motility experiments were performed at  $25.3 \pm 0.6$  °C (A) and  $24.8 \pm 0.9$  °C (B), and 10 filaments were analyzed per contact angle.

### 3.2. Actin Filament Velocities at Different Surface Energies.

As illustrated in Figure 4, the actin filament sliding velocity increased with increasing contact angle (up to a factor of 3) and thereby with the degree of silanization. This is consistent with previous findings<sup>22</sup> that the velocity increases with the contact angle up to  $75^\circ$  on surfaces silanized using different silanes. The present results extend the previous findings in several respects. First, the entire range of contact angles in the present study were produced using just one silane, namely, TMCS, by varying the chamber pressure and the silanization time. In the previous study, several silanes were used to obtain a range of contact angles. Second, in previous work,<sup>22</sup> the correlation between the contact angle and the velocity was only studied in an aMC130 solution and up to a contact angle of  $\sim 75^\circ$ . Here, we also used a60 solution and succeeded to consistently extend the range of contact angles up to  $86^\circ$ . The differences between the assay solutions is that filaments are usually longer, on average, in aMC130 solution due to higher ionic strength (130 mM) and the filaments are held down to the surface by the presence of methylcellulose (MC). The latter effect allows maintained motility, albeit at reduced velocity,<sup>49</sup> also if very few myosin motor domains are available to bind actin. Importantly, however, the presence of methylcellulose does not affect the maximum myosin-propelled filament velocity for long filaments as previously tested at an ionic strength of  $\sim 60$  mM.<sup>43</sup> The fact that MC prevents diffusion of actin filaments away from the surface even if they are not tethered by myosin motors can explain why motility was observed on surfaces with very low contact angles ( $10^\circ$  and  $28^\circ$ ) in aMC130 solution but not in a60 solution. At such low contact angles on negative surfaces like  $\text{SiO}_2$ , a large fraction of the HMM molecules are believed to adsorb on the surface via their motor domains,<sup>14,21,55,56</sup> reducing the number of motor domains available for actin interaction. Overall, our results show an increased velocity with an increasing contact angle in the range  $10^\circ$ – $86^\circ$ . This is consistent with the idea<sup>14,55</sup> that the fraction of the HMM molecules that are adsorbed in an actin-propelling configuration, via their tail domain, increases with the surface contact angle at the expense of head-based adsorption.

In this context it is of interest to note that the idea of electrostatic surface adsorption of the myosin heads on negatively charged surfaces<sup>22,50,55–57</sup> has received unexpected support from very recent studies of severe cardiac diseases (hypertrophic cardiomyopathy; HCM) due to myosin mutations.<sup>58</sup> Thus, it is now clear that, in addition to the positively charged actin-binding loops, the myosin motor

domains contain an additional region, the “myosin mesa”, with numerous conserved positively charged amino acids that are hot spots for HCM-causing mutations. The myosin mesa is believed to be critical for formation of the so-called super-relaxed state of myosin.<sup>59</sup> This is a physiologically important myosin state to effectively relax a muscle cell. In this state, the positively charged myosin mesa region binds to the partner myosin head of a given molecule as well as to negatively charged regions on the thick (myosin) filament backbone, effectively sequestering the heads on a surface away from the actin filaments. Interestingly, the ATP-turnover kinetics of the super-relaxed state shows strong resemblances<sup>59</sup> to that detected for myosin heads bound to negatively charged  $\text{SiO}_2$  surfaces.<sup>55</sup> The finding provides strong evidence that electrostatic interactions due to positive charges on myosin are of great physiological relevance, causing quite strong binding also at physiological ionic strengths (higher than those used here). This finding, together with the similarity in ATP-turnover kinetics, strongly supports our previously proposed ideas<sup>22,50,55–57</sup> about the basis for poor actin-myosin motility on negatively charged surfaces. If these hypotheses are correct, one would expect that the mentioned myosin mutations that reduce the positive charge density in the myosin mesa region would reduce the contact angle dependence (related to surface charge<sup>22</sup>) of actin-myosin motility. This is of interest to test in future studies using silanized surfaces of the types manufactured here. Detailed studies of this type may actually give new mechanistic insights into the effects of severe disease-causing mutations.

In previous work,<sup>14,21,46</sup> increased velocity with increasing contact angle has generally only been observed on surfaces of contact angles up to  $81^\circ$ .<sup>57</sup> Higher contact angles have been associated with reduced sliding velocity and reduced fraction of motile actin filaments, likely due to protein denaturation. In contrast, we here found increased velocity on average when the contact angle was increased from  $75^\circ$  to  $86^\circ$ . This effect is most easily explained by a further increase of the fraction of HMM molecules that are adsorbed on the surface via their hydrophobic tail domain instead of via their head domain. Total internal reflection fluorescence based ATPase assays<sup>60</sup> suggested that the fraction of the HMM molecule with head up was  $>70\%$  on a TMCS surface of  $70^\circ$  contact angle, leaving room for further increase of this fraction by increased contact angle up to  $86^\circ$ . One possible explanation for previously observed reduction in motility at contact angles  $> 75$ – $80^\circ$  is the increased tendency for the motor domains of HMM to denature on the polymer surfaces used in these studies.<sup>21,46</sup>

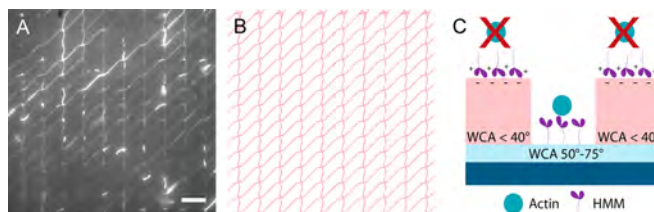


**Figure 5.** Summed stack (225 frames) of a fluorescence microscopy recording (A) of a nanostructured surface patterned in 250 nm thick CSAR 62 on top of 70 nm SiO<sub>2</sub> and the network design (B) with CSAR 62 in white and SiO<sub>2</sub> in pink; scale bar 10  $\mu\text{m}$  for (A) and (B). Negligible number of actin filaments, and no motility was observed on the plasma oxygen-treated CSAR 62 (black areas in A). Many actin filaments (white lines in A) and selective motility were observed, however, on the TMCS-derivatized SiO<sub>2</sub> surface inside the nanochannels, likely related to different binding configurations of the myosin motors on the surface (C).

The polymers have higher surface area (related to higher roughness) and are softer than TMCS-derivatized SiO<sub>2</sub>, which may form the basis for such an effect.

It should be pointed out that, whereas the average velocity increased with contact angle in the range of 75°–86°, increased velocity was not universally observed (Figure 4). Thus, there was variability between the motility quality on different parts of a surface at the highest contact angle both regarding the actin filament sliding velocity and the number of motile filaments (see Supporting Information, Figure S2). For instance, whereas the velocity in some regions of a surface with contact angle 86° was appreciably higher than that at 75°, there was no motility on other parts of the surface, i.e., the actin filaments were attached but immobile in the latter regions and in some regions no filaments were present at all. These observations may fit with a critical balance between improved motility due to HMM tail adsorption and blocked motility due to head denaturation. One of these phenomena may dominate in one region whereas the other phenomenon may dominate in other regions, e.g., depending on stochastic variation in the early density of adsorbed HMM molecules in the different regions. Verification of this hypothesis could possibly be achieved using appropriately fluorescence-labeled HMM to probe spatial variability of the HMM density. However, this seemingly simple but, in reality, rather complex approach is outside the scope of the present study.

For the use of TMCS derivatization in actin-myosin nanodevices, it is valuable to know that motility is generally maintained on TMCS-derivatized surfaces even for the most extensive silanization that is readily achieved using our controlled CVD system (method 2). However, the variability in motility between different regions of a surface and between different surfaces at a contact angle of 86° suggests that it is safer to aim for contact angles in the range 70–75° for optimal actin-myosin function if filaments with high velocity are desired. However, for the study of actin filament behavior or in sensing applications, a lower filament velocity may be required, and thus, lower contact angles can be used. Further, the velocity variations could possibly also be useful in measurements where a range of temperatures are used, but a constant velocity is desired. The different water contact angles can be achieved by using different chamber pressures and silanization times (see Figure S3 for more details). This is not achievable in a predictable way using method 1.

As a confirmation of the above findings, we studied motility on surfaces where we had first used electron-beam lithography to pattern the surfaces with 200 nm wide CSAR 62 channels

on top of SiO<sub>2</sub>. On such surfaces, selective motility was observed on the TMCS-derivatized SiO<sub>2</sub> channel floors but not on the CSAR 62-coated areas (Figure 5), after plasma ashing and silanization using parameters corresponding to a water contact angle of  $\sim 75^\circ$ . The measured average velocity of actin filaments in a60 solution in these structures at 22 °C was  $3.7 \pm 0.3 \mu\text{m/s}$  ( $n = 10$  filaments), i.e., slightly higher than that on unpatterned TMCS. This work further substantiates previous results that a surface with low contact angle and negative charge<sup>55,56</sup> is associated with poor HMM-propelled actin filament sliding. This is likely due to adsorption of the HMM molecules via electrostatic attraction between their actin-binding positively charged surface loops and negative charges on the surface<sup>56,61–63</sup> that prevent the myosin motor domains to propel actin filaments (Figure 5C).

#### 4. CONCLUSIONS

We have shown that it is possible to adsorb HMM in a motility-promoting manner on two new lithography resists, TU7 for nanoimprint lithography and CSAR 62 for electron-beam and deep-UV lithography, showing that the resists are nontoxic for the proteins. We have also shown that these resists can be treated with oxygen plasma to reduce the contact angle with completely suppressed actin binding by the adsorbed HMM molecules. Importantly, the suppression of actin binding is unaffected by silanization treatment. These findings support the use of the mentioned resists, with several advantages compared to previously used polymers in terms of resolution, contrast, and molding temperature for fabrication of nanodevices where selective actin-myosin based transportation is critical, in, e.g., diagnostics<sup>12,15</sup> and biocomputation.<sup>5</sup> We also demonstrated a method for silanizing surfaces at different chamber pressures. We have shown that this provides the ability to obtain surfaces with a controlled variation in surface hydrophobicities most likely related to different TMCS coverage. In vitro motility studies using these surfaces corroborate and extend previously proposed models for HMM adsorption on SiO<sub>2</sub>-based surfaces with different contact angles. The data also provide a well-defined window for silanization parameters to achieve optimal function on TMCS-derivatized surfaces in nanodevices. In view of recent studies in the literature, these results provide a model system for new potential applications in the study of disease-causing mutations.

## ■ ASSOCIATED CONTENT

### Supporting Information

The Supporting Information is available free of charge on the ACS Publications website at DOI: 10.1021/acs.langmuir.8b01415.

Actin filament sliding velocity on TU7 and CSAR 62 as function of the actin filament length, water contact angle as a function of chamber pressure at different silanization times, and number of filaments and filament lengths at different water contact angles (PDF)

## ■ AUTHOR INFORMATION

### Corresponding Author

\*E-mail: alf.mansson@lnu.se.

### ORCID

Frida W. Lindberg: 0000-0001-5617-6337

### Notes

The authors declare no competing financial interest.

## ■ ACKNOWLEDGMENTS

This work has received funding from the European Union's Horizon 2020 research and innovation programme under Grant agreement no. 732482 (Bio4Comp); from NanoLund; from the Swedish Research Council (Projects 2015-05290 and 2015-0612); and from Linnaeus University, Faculty of Health and Life Sciences.

## ■ REFERENCES

- (1) Kron, S. J.; Spudich, J. A. Fluorescent Actin Filaments Move on Myosin Fixed to a Glass Surface. *Proc. Natl. Acad. Sci. U. S. A.* **1986**, *83* (17), 6272–6276.
- (2) Howard, J.; Hudspeth, A. J.; Vale, R. D. Movement of Microtubules by Single Kinesin Molecules. *Nature* **1989**, *342* (6246), 154–158.
- (3) Sheetz, M. P.; Spudich, J. A. Movement of Myosin-Coated Fluorescent Beads on Actin Cables in Vitro. *Nature* **1983**, *303* (5912), 31–35.
- (4) Kron, S. J.; Toyoshima, Y. Y.; Uyeda, T. Q. P.; Spudich, J. A. Assays for Actin Sliding Movement over Myosin-Coated Surfaces. *Methods Enzymol.* **1991**, *196* (1986), 399–416.
- (5) Nicolau, D. V., Jr.; Lard, M.; Korten, T.; van Delft, F. C. M. J. M.; Persson, M.; Bengtsson, E.; Månsson, A.; Diez, S.; Linke, H.; Nicolau, D. V. Massively-Parallel Computation with Molecular Motor-Propelled Agents in Nanofabricated Networks. *Proc. Natl. Acad. Sci. U. S. A.* **2016**, *113* (10), 2591–2596.
- (6) Barclay, C. J. Estimation of Cross-Bridge Stiffness from Maximum Thermodynamic Efficiency. *J. Muscle Res. Cell Motil.* **1998**, *19* (8), 855–864.
- (7) Kishino, A.; Yanagida, T. Force Measurements by Micro-manipulation of a Single Actin Filament by Glass Needles. *Nature* **1988**, *334* (6177), 74–76.
- (8) Murphy, C. T.; Rock, R. S.; Spudich, J. A. A Myosin II Mutation Uncouples ATPase Activity from Motility and Shortens Step Size. *Nat. Cell Biol.* **2001**, *3* (3), 311–315.
- (9) Toyoshima, Y. Y.; Kron, S. J.; McNally, E. M.; Niebling, K. R.; Toyoshima, C.; Spudich, J. A. Myosin Subfragment-1 Is Sufficient to Move Actin Filaments in Vitro. *Nature* **1987**, *328* (6130), 536–539.
- (10) Homsher, E.; Kim, B.; Bobkova, A.; Tobacman, L. S. Calcium Regulation of Thin Filament Movement in an in Vitro Motility Assay. *Biophys. J.* **1996**, *70* (April), 1881–1892.
- (11) Bunk, R.; Klinth, J.; Montelius, L.; Nicholls, I. A.; Omling, P.; Tägerud, S.; Månsson, A. Actomyosin Motility on Nanostructured Surfaces. *Biochem. Biophys. Res. Commun.* **2003**, *301* (3), 783–788.
- (12) Lard, M.; ten Siethoff, L.; Kumar, S.; Persson, M.; te Kronnie, G.; Linke, H.; Månsson, A. Ultrafast Molecular Motor Driven

Nanoseparation and Biosensing. *Biosens. Bioelectron.* **2013**, *48*, 145–152.

(13) ten Siethoff, L.; Lard, M.; Generosi, J.; Andersson, H. S.; Linke, H.; Månsson, A. Molecular Motor Propelled Filaments Reveal Light-Guiding in Nanowire Arrays for Enhanced Biosensing. *Nano Lett.* **2014**, *14*, 737–742.

(14) Månsson, A. Translational Actomyosin Research: Fundamental Insights and Applications Hand in Hand. *J. Muscle Res. Cell Motil.* **2012**, *33* (3–4), 219–233.

(15) Korten, T.; Månsson, A.; Diez, S. Towards the Application of Cytoskeletal Motor Proteins in Molecular Detection and Diagnostic Devices. *Curr. Opin. Biotechnol.* **2010**, *21* (4), 477–488.

(16) Huxley, H. E. The Mechanism of Muscular Contraction. *Science (Washington, DC, U. S.)* **1969**, *164* (3886), 1356–1366.

(17) Huxley, A. F.; Simmons, R. M. Proposed Mechanism of Force Generation in Striated Muscle. *Nature* **1971**, *233* (5321), 533–538.

(18) Huxley, A. F. Muscular Contraction. *J. Physiol.* **1974**, *243* (1), 1–43.

(19) Nakanishi, K.; Sakiyama, T.; Imamura, K. On the Adsorption of Proteins on Solid Surfaces, a Common but Very Complicated Phenomenon. *Biosci. Bioeng.* **2001**, *91* (3), 233–244.

(20) van der Veen, M.; Stuart, M. C.; Norde, W. Spreading of Proteins and Its Effect on Adsorption and Desorption Kinetics. *Colloids Surf, B* **2007**, *54* (2), 136–142.

(21) Hanson, K. L.; Fulga, F.; Dobroiu, S.; Solana, G.; Kaspar, O.; Tokarova, V.; Nicolau, D. V. Polymer Surface Properties Control the Function of Heavy Meromyosin in Dynamic Nanodevices. *Biosens. Bioelectron.* **2017**, *93*, 305–314.

(22) Albet-Torres, N.; O'Mahony, J.; Charlton, C.; Balaz, M.; Lisboa, P.; Aastrup, T.; Månsson, A.; Nicholls, I. A. Mode of Heavy Meromyosin Adsorption and Motor Function Correlated with Surface Hydrophobicity and Charge. *Langmuir* **2007**, *23* (22), 11147–11156.

(23) Harada, Y.; Sakurada, K.; Aoki, T.; Thomas, D. D.; Yanagida, T. Mechanochemical Coupling in Actomyosin Energy Transduction Studied by in Vitro Movement Assay. *J. Mol. Biol.* **1990**, *216* (1), 49–68.

(24) Sundberg, M.; Rosengren, J. P.; Bunk, R.; Lindahl, J.; Nicholls, I. A.; Tägerud, S.; Omling, P.; Montelius, L.; Månsson, A. Silanized Surfaces for in Vitro Studies of Actomyosin Function and Nanotechnology Applications. *Anal. Biochem.* **2003**, *323* (1), 127–138.

(25) Warrick, H. M.; Simmons, R. M.; Finer, J. T.; Uyeda, T. Q.; Chu, S.; Spudich, J. A. In Vitro Methods for Measuring Force and Velocity of the Actin-Myosin Interaction Using Purified Proteins. *Methods Cell Biol.* **1993**, *39*, 1–21.

(26) Månsson, A.; Sundberg, M.; Bunk, R.; Balaz, M.; Nicholls, I. A.; Omling, P.; Tegenfeldt, J. O.; Tägerud, S.; Montelius, L. Actin-Based Molecular Motors for Cargo Transportation in Nanotechnology-Potentials and Challenges. *IEEE Trans. Adv. Packag.* **2005**, *28* (4), 547–555.

(27) Sundberg, M.; Bunk, R.; Albet-Torres, N.; Kvennefors, A.; Persson, F.; Montelius, L.; Nicholls, I. A.; Ghatnekar-Nilsson, S.; Omling, P.; Tägerud, S.; et al. Actin Filament Guidance on a Chip: Toward High-Throughput Assays and Lab-on-a-Chip Applications. *Langmuir* **2006**, *22* (17), 7286–7295.

(28) Clemmens, J. J.; Hess, H.; Lipscomb, R.; Hanein, Y.; Böhringer, K. F.; Matzke, C. M.; Bachand, G. D.; Bunker, B. C.; Vogel, V. Mechanisms of Microtubule Guiding on Microfabricated Kinesin-Coated Surfaces: Chemical and Topographic Surface Patterns. *Langmuir* **2003**, *19* (26), 10967–10974.

(29) Månsson, A.; Bunk, R.; Sundberg, M.; Montelius, L. Self-Organization of Motor-Propelled Cytoskeletal Filaments at Topographically Defined Borders. *J. Biomed. Biotechnol.* **2012**, *2012*, 647265.

(30) Bunk, R.; Sundberg, M.; Månsson, A.; Nicholls, I. A.; Omling, P.; Tägerud, S.; Montelius, L. Guiding Motor-Propelled Molecules with Nanoscale Precision through Silanized Bi-Channel Structures. *Nanotechnology* **2005**, *16*, 710–717.

(31) Clemmens, J.; Hess, H.; Doot, R.; Matzke, C. M.; Bachand, G. D.; Vogel, V. Motor-Protein Roundabouts: Microtubules Moving on

Kinesin-Coated Tracks through Engineered Networks. *Lab Chip* **2004**, *4* (D), 83–86.

(32) Hess, H.; Matzke, C. M.; Doot, R. K.; Clemmens, J.; Bachand, G. D.; Bunker, B. C.; Vogel, V. Molecular Shuttles Operating Undercover: A New Photolithographic Approach for the Fabrication of Structured Surfaces Supporting Directed Motility. *Nano Lett.* **2003**, *3* (12), 1651–1655.

(33) Nicolau, D. V.; Suzuki, H.; Mashiko, S.; Taguchi, T.; Yoshikawa, S. Actin Motion on Microlithographically Functionalized Myosin Surfaces and Tracks. *Biophys. J.* **1999**, *77* (2), 1126–1134.

(34) Suzuki, H.; Yamada, A.; Oiwa, K.; Nakayama, H.; Mashiko, S. Control of Actin Moving Trajectory by Patterned Poly-(Methylmethacrylate) Tracks. *Biophys. J.* **1997**, *72* (5), 1997–2001.

(35) Hiratsuka, Y.; Tada, T.; Oiwa, K.; Kanayama, T.; Uyeda, T. Q. P. Controlling the Direction of Kinesin-Driven Microtubule Movements along Microlithographic Tracks. *Biophys. J.* **2001**, *81* (3), 1555–1561.

(36) Bunk, R.; Carlberg, P.; Månsson, A.; Nicholls, I. A.; Omling, P.; Sundberg, M.; Tägerud, S.; Montelius, L. Guiding Molecular Motors with Nano-Imprinted Structures. *Jpn. J. Appl. Phys.* **2005**, *44* (5A), 3337–3340.

(37) Riveline, D.; Ott, A.; Jülicher, F.; Winkelmann, D. A.; Cardoso, O.; Lacapère, J. J.; Magnúsdóttir, S.; Viovy, J. L.; Gorre-Talini, L.; Prost, J. Acting on Actin: The Electric Motility Assay. *Eur. Biophys. J.* **1998**, *27* (4), 403–408.

(38) Sata, M.; Sugiura, S.; Yamashita, H.; Momomura, S.; Serizawa, T. Dynamic Interaction Between Cardiac Myosin Isoforms Modifies Velocity of Actomyosin Sliding In Vitro. *Circ. Res.* **1993**, *73* (4), 696–704.

(39) Okamoto, Y.; Sekine, T. A Streamlined Method of Subfragment One Preparation from Myosin. *J. Biochem.* **1985**, *98* (4), 1143–1145.

(40) Pardee, J. D.; Aspudich, J. Purification of Muscle Actin. *Methods Enzymol.* **1982**, *85*, 164–181.

(41) Balaz, M.; Månsson, A. Detection of Small Differences in Actomyosin Function Using Actin Labeled with Different Phalloidin Conjugates. *Anal. Biochem.* **2005**, *338* (2), 224–236.

(42) Persson, M.; Gullberg, M.; Tolf, C.; Lindberg, A. M.; Månsson, A.; Kocer, A. Transportation of Nanoscale Cargoes by Myosin Propelled Actin Filaments. *PLoS One* **2013**, *8* (2), e55931.

(43) Homsher, E.; Wang, F.; Sellers, J. R. Factors Affecting Movement of F-Actin Filaments Propelled by Skeletal Muscle Heavy Meromyosin. *Am. J. Physiol.* **1992**, *262* (3), C714–C723.

(44) Rueden, C. T.; Schindelin, J.; Hiner, M. C.; DeZonia, B. E.; Walter, A. E.; Arena, E. T.; Eliceiri, K. W. ImageJ2: ImageJ for the Next Generation of Scientific Image Data. *BMC Bioinf.* **2017**, *18*, 529.

(45) Schindelin, J.; Arganda-Carreras, I.; Frise, E.; Kaynig, V.; Longair, M.; Pietzsch, T.; Preibisch, S.; Rueden, C.; Saalfeld, S.; Schmid, B.; et al. Fiji: An Open-Source Platform for Biological-Image Analysis. *Nat. Nat. Methods* **2012**, *9* (7), 676–682.

(46) Nicolau, D. V.; Solana, G.; Kekic, M.; Fulga, F.; Mahanivong, C.; Wright, J.; dos Remedios, C. G. Surface Hydrophobicity Modulates the Operation of Actomyosin-Based Dynamic Nanodevices. *Langmuir* **2007**, *23* (21), 10846–10854.

(47) van Zalinge, H.; Ramsey, L. C.; Aveyard, J.; Persson, M.; Månsson, A.; Nicolau, D. V. Surface-Controlled Properties of Myosin Studied by Electric Field Modulation. *Langmuir* **2015**, *31* (30), 8354–8361.

(48) van Zalinge, H.; Aveyard, J.; Hajne, J.; Persson, M.; Månsson, A.; Nicolau, D. V. Actin Filament Motility Induced Variation of Resonance Frequency and Rigidity of Polymer Surfaces Studied by Quartz Crystal Microbalance. *Langmuir* **2012**, *28* (42), 15033–15037.

(49) Uyeda, T. Q. P.; Kron, S. J.; Spudich, J. A. Myosin Step Size - Estimation from Slow Sliding Movement of Actin over Low Densities of Heavy Meromyosin. *J. Mol. Biol.* **1990**, *214* (3), 699–710.

(50) Månsson, A.; Balaz, M.; Albet-Torres, N.; Rosengren, K. J. In Vitro Assays of Molecular Motors - Impact of Motor-Surface Interactions. *Front. Biosci., Landmark Ed.* **2008**, *13*, 5732–5754.

(51) Månsson, A. Actomyosin Based Contraction: One Mechanokinetic Model from Single Molecules to Muscle? *J. Muscle Res. Cell Motil.* **2016**, *37* (6), 181–194.

(52) Chai, J.; Lu, F.; Li, B.; Kwok, D. Y. Wettability Interpretation of Oxygen Plasma Modified Poly(Methyl Methacrylate). *Langmuir* **2004**, *20* (25), 10919–10927.

(53) Coen, M. C.; Groening, P.; Dietler, G.; Schlapbach, L. Creation of a Conductive Surface Layer on Polypropylene Samples by Low-Pressure Plasma Treatments. *J. Appl. Phys.* **1995**, *77* (11), 5695–5701.

(54) Bridwell, L. B.; Giedd, R. E.; Wang, Y. Q.; Mohite, S. S.; Jahnke, T.; Brown, I. M.; Bedell, C. J.; Sofield, C. J. Ion Implantation of Polymers for Electrical Conductivity Enhancement. *Nucl. Instrum. Methods Phys. Res., Sect. B* **1991**, *56-57*, 656–659.

(55) Persson, M.; Albet-Torres, N.; Ionov, L.; Sundberg, M.; Höök, F.; Diez, S.; Månsson, A.; Balaz, M. Heavy Meromyosin Molecules Extending More than 50 Nm above Adsorbing Electronegative Surfaces. *Langmuir* **2010**, *26* (12), 9927–9936.

(56) Albet-Torres, N.; Gunnarsson, A.; Persson, M.; Balaz, M.; Höök, F.; Månsson, A. Molecular Motors on Lipid Bilayers and Silicon Dioxide: Different Driving Forces for Adsorption. *Soft Matter* **2010**, *6*, 3211–3219.

(57) Sundberg, M.; Balaz, M.; Bunk, R.; Rosengren-Holmberg, J. P.; Montelius, L.; Nicholls, I. A.; Omling, P.; Tägerud, S.; Månsson, A. Selective Spatial Localization of Actomyosin Motor Function by Chemical Surface Patterning. *Langmuir* **2006**, *22* (17), 7302–7312.

(58) Trivedi, D. V.; Adhikari, A. S.; Sarkar, S. S.; Ruppel, K. M.; Spudich, J. A. Hypertrophic Cardiomyopathy and the Myosin Mesa: Viewing an Old Disease in a New Light. *Biophys. Rev.* **2018**, *10* (1), 27–48.

(59) Hooijman, P.; Stewart, M. A.; Cooke, R. A. New State of Cardiac Myosin with Very Slow ATP Turnover: A Potential Cardioprotective Mechanism in the Heart. *Biophys. J.* **2011**, *100* (8), 1969–1976.

(60) Balaz, M.; Sundberg, M.; Persson, M.; Kvassman, J.; Månsson, A. Effects of Surface Adsorption on Catalytic Activity of Heavy Meromyosin Studied Using a Fluorescent ATP Analogue. *Biochemistry* **2007**, *46* (24), 7233–7251.

(61) Aoki, T.; Sowa, Y.; Yokota, H.; Hiroshima, M.; Tokunaga, M.; Ishii, Y.; Yanagida, T. Non-Contact Electrostatic Surface Force Imaging of Single Protein Filaments Using Intermolecular Force Microscopy. *Single Mol.* **2001**, *2* (3), 183–190.

(62) Bordas, J.; Svensson, A.; Rothery, M.; Lowy, J.; Diakun, G. P.; Boesecke, P. Extensibility and Symmetry of Actin Filaments in Contracting Muscles. *Biophys. J.* **1999**, *77* (6), 3197–3207.

(63) Ramsden, J. J.; Roush, D. J.; Gill, D. S.; Kurrat, R.; Willson, R. C. Protein Adsorption Kinetics Drastically Altered by Repositioning a Single Charge. *J. Am. Chem. Soc.* **1995**, *117* (5), 8511–8516.

## **SUPPORTING INFORMATION**

### **Controlled surface silanization for actin-myosin based nanodevices and biocompatibility of new polymer resists**

Frida W. Lindberg<sup>1</sup>, Marlene Norrby<sup>2</sup>, Mohammad A. Rahman<sup>2</sup>, Aseem Salhotra<sup>2</sup>, Hideyo Takatsuki<sup>2</sup>, Sören Jeppesen<sup>1</sup>, Heiner Linke<sup>1</sup>, Alf Månsson<sup>2</sup>

<sup>1</sup> Nano Lund and Solid State Physics, Lund University, Box 118, SE-221 00 Lund, Sweden.

<sup>2</sup> Department of Chemistry and Biomedical Sciences, Linnaeus University, Kalmar, SE-39182, Sweden.

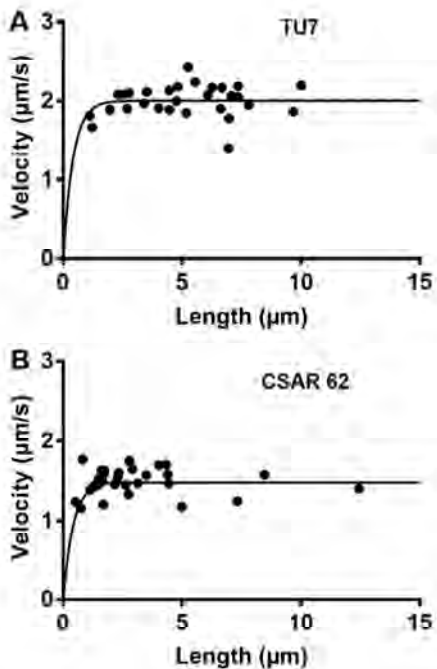


**Figure S1. HMM driven sliding velocity of actin filaments against filament length on resist polymers TU7 and CSAR 62. A.** Motility on non-plasma ashed TU7. **B.** Motility on non-plasma ashed CSAR 62. Experiments in A and B at (19.3-19.8)°C after HMM incubation concentration at 120 μg/ml in a60 solution. Velocities are average values obtained over a sliding time period of 3.0 s. Filament lengths,  $l$ , were obtained from intensity data as previously described<sup>1</sup>. The lines represent plots of the following equation<sup>2</sup>:  $\text{velocity} = v_0(1 - (1 - f)^{\rho dl})$  where  $v_0$  is the velocity for long actin filaments,  $f$  is the motor duty ratio (here taken as 0.02),  $\rho$  is the active motor density, here assumed similar (4000 μm<sup>-2</sup>) to that for a TMCS derivatized surface (contact angle 70°) and  $d=30$  nm<sup>3</sup>. Note, comparison between the experimental data and the theoretical plots are consistent with as high myosin head density on both TU7 and CSAR 62 as on TMCS derivatized SiO<sub>2</sub>.

### Number of filaments and filament lengths in a60 and aMC130 solution.

No motility was observed at the lowest water contact angles in a60 solution. Some motility was observed in aMC130 solution, although very few filaments were moving (**Figure S2 (A-B)**). As mentioned in the main paper, this is likely due to a large fraction of HMM molecules binding to the surface via their motor domains, causing very few motility-promoting heads. At a contact angle of 86°, the number of motile filaments and stationary filaments varied appreciably in different regions. Thus, the number of motile filaments was larger in some areas, whereas other areas showed no motility at all. The number of stationary filaments was similar in both a60 and aMC130, which can be explained by a similar number of “dead”, non-functional HMM heads. The total number of actin filaments being much lower in aMC130 solution as compared to a60 is attributable to the higher ionic strength in aMC130 (130 mM instead of 60 mM). The interaction strength between actin monomers is appreciably reduced by a lowered ionic strength, leading to appreciably higher motility-induced fragmentation of the filaments. This also explains why an increased ionic strength shifts the length distribution of the actin filaments observed after a period of myosin driven motion to higher values (**Figure S2 (C-D)**) despite similar initial incubation concentrations with both HMM and actin.

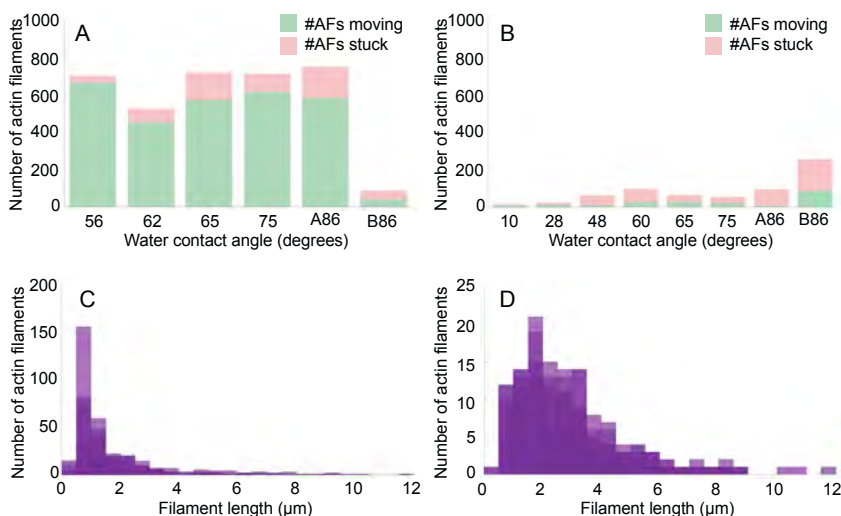


**Figure S2.** Fraction of motile actin filaments in a60 (A) and aMC130 (B) solution at different contact angles. The highest contact angle (86°) is divided in two sections, similar to **Figure 4** in the main paper as there was a large variation in both the velocity as well as the number of motile filaments in different areas of the sample. The number of longer filaments at different water contact angles is higher in aMC130 (C) as compared to a60 (D). Each bin represents 0.5  $\mu\text{m}$ , where the length of each filament (40 per recording) was measured by hand.

### Optimizing the CVD system for TMCS-derivatization.

The degree of silanization can be controlled by varying the chamber pressures and silanization duration with Method 2 (see main paper, Methods). This is illustrated by the measured contact angles at different chamber pressures and silanization times in **Figure S3**.

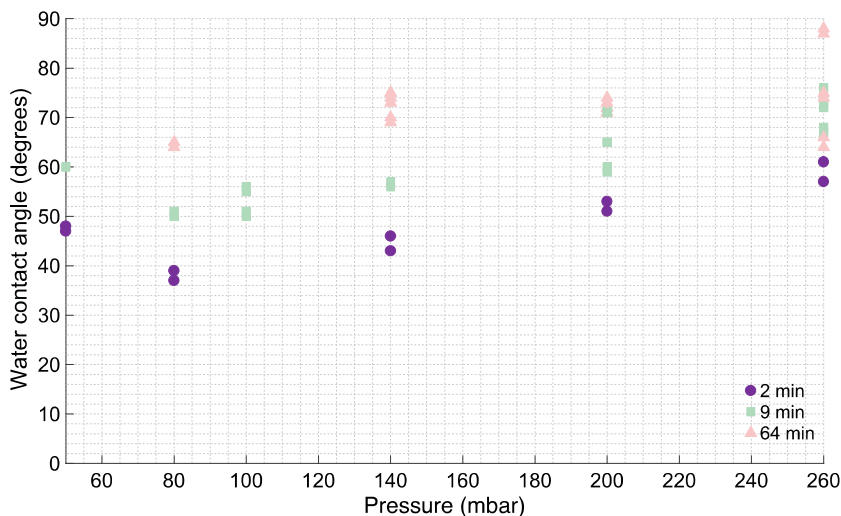


**Figure S3.** The water contact angle as a function of chamber pressure at different silanization times; 2 min (purple circle), 9 min (green square) and 64 min (pink triangle). The silanization time is defined as the time after reaching the desired chamber pressure (i.e., 50 mbar, 80 mbar, 140 mbar, 200 mbar and 260 mbar). The water contact angle increases at higher chamber pressures and longer silanization durations.

The highest chamber pressure obtained (260 mbar) corresponds to a fully saturated TMCS system at  $22.2 \pm 1^\circ\text{C}$ . The water contact angle increases when the silanization duration increases as well as when the chamber pressure is increased. By increasing the chamber pressure, we were able to obtain a higher water contact angle at reduced silanization duration. Similarly, at a fixed chamber pressure, the water contact angle increased with the silanization duration. We noticed that the water contact angle varies slightly as the bubbler is depleted, which manifests itself in a larger range of data points in some regions. A more optimised system could actively control the bubbler temperatures, e.g. using a heat bath. The system used in this paper was used at room temperature without any heating.

## References

- (1) Sundberg, M.; Balaz, M.; Bunk, R.; Rosengren-Holmberg, J. P.; Montelius, L.; Nicholls, I. A.; Omling, P.; Tägerud, S.; Månsson, A. Selective Spatial Localization of Actomyosin Motor Function by Chemical Surface Patterning. *Langmuir* **2006**, *22* (17), 7302–7312.
- (2) Uyeda, T. Q. P.; Kron, S. J.; Spudich, J. A. Myosin Step Size - Estimation from Slow Sliding Movement of Actin over Low Densities of Heavy Meromyosin. *J. Mol. Biol.* **1990**, *214* (3), 699–710.
- (3) Lard, M.; ten Siethoff, L.; Generosi, J.; Persson, M.; Linke, H.; Månsson, A. Nanowire-Imposed Geometrical Control in Studies of Actomyosin Motor Function. *IEEE Trans. Nanobioscience* **2015**, *14* (3), 289–297.



Paper II





# Materials Research Express



## PAPER

# Design and development of nanoimprint-enabled structures for molecular motor devices

### OPEN ACCESS

#### RECEIVED

27 September 2018

#### REVISED

24 October 2018

#### ACCEPTED FOR PUBLICATION

31 October 2018

#### PUBLISHED

30 November 2018

Frida W Lindberg<sup>1</sup> , Till Korten<sup>2,3</sup>, Anette Löfstrand<sup>1</sup>, Mohammad A Rahman<sup>4</sup>, Mariusz Graczyk<sup>1</sup>, Alf Månsson<sup>4</sup>, Heiner Linke<sup>1</sup> and Ivan Maximov<sup>1</sup>

<sup>1</sup> NanoLund and Solid State Physics, Lund University, Box 118, SE-221 00 Lund, Sweden

<sup>2</sup> B CUBE - Center for Molecular Bioengineering, Technische Universität Dresden, 01069 Dresden, Germany

<sup>3</sup> Max Planck Institute of Molecular Cell Biology and Genetics, Pfotenhauerstr. 108, 01307 Dresden Germany

<sup>4</sup> Department of Chemistry and Biomedical Sciences, Linnaeus University, Kalmar, SE-39182, Sweden

E-mail: [ivan.maximov@ftf.lth.se](mailto:ivan.maximov@ftf.lth.se)

Original content from this work may be used under the terms of the [Creative Commons Attribution 3.0 licence](https://creativecommons.org/licenses/by/4.0/).

Any further distribution of this work must maintain attribution to the author(s) and the title of the work, journal citation and DOI.



**Keywords:** nanoimprint lithography, molecular motors, actin-myosin, nanostructures, nanofabrication, nanodevice, patterning  
Supplementary material for this article is available [online](#)

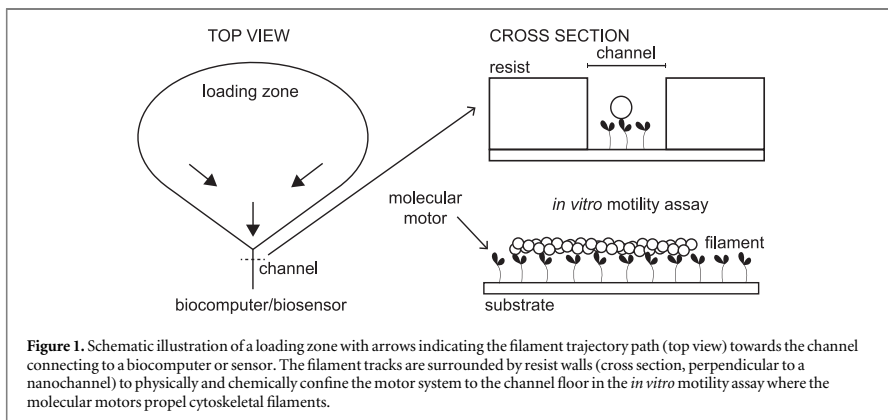
## Abstract

Devices based on molecular motor-driven cytoskeletal filaments, e.g., actin filaments, have been developed both for biosensing and biocomputational applications. Commonly, these devices require nanoscaled tracks for guidance of the actin filaments which has limited the patterning technique to electron beam lithography. Thus, large scale systems become intractable to fabricate at a high throughput within a reasonable time-frame. We have studied the possibility to fabricate molecular motor-based devices using the high throughput, high resolution technique of nanoimprint lithography. Molecular motor-based devices require wide open regions (loading zones) to allow filaments to land for later propulsion into the nanoscale tracks. Such open zones are challenging to fabricate using nanoimprint lithography due to the large amount of material displaced in the process. We found that this challenge can be overcome by introducing nanoscaled pillars inside the loading zones, into which material can be displaced during imprint. By optimising the resist thickness, we were able to decrease the amount of material displaced without suffering from insufficient filling of the stamp. Furthermore, simulations suggest that the shape and positioning of the pillars can be used to tailor the overall cytoskeletal filament transportation direction and behaviour. This is a potentially promising design feature for future applications that however, requires further optimisations before experimental realisation.

## 1. Introduction

Molecular motors are a class of proteins that govern the directed and active transport in eukaryotic cells. These motor-systems can be isolated from the cell and used in so called *in vitro* motility assays [1–4], where motors, adsorbed onto a surface, propel the corresponding cytoskeletal filaments on a chip, in a highly energy-efficient manner ( $\sim 25$  kT/10 nm) [5–7] compared to e.g., nanofluidics. Such molecular motor systems on a chip in nanotechnological applications require directed movement along chemically [8, 9] and/or physically [10–15] defined tracks, fabricated by lithography. The unidirectional movement is strongly dependent on the persistence length of the cytoskeletal filaments [8, 11, 15, 16], e.g., the actin-myosin II motor system of muscle [17–19] requires very narrow tracks  $< 300$  nm [8, 11] to prevent U-turns because of the rather high flexibility of actin filaments compared to e.g., microtubules. On the other hand, the velocity of myosin II propelled actin filaments is faster than of kinesin propelled microtubules.

Nanotechnological device applications of molecular motors includes e.g., biocomputation [7] where mathematical problems are encoded into graphical networks of channels. As the cytoskeletal filaments move along the tracks, they explore all possible pathways, each corresponding to different solutions depending on the problem encoded. Molecular motors are also used within biosensing [20] for e.g., nanoseparation of analyte



molecules to concentration regions to increase the rate of collection analyte on the detector and to increase the sensitivity in detection [21]. Both these types of devices require large open surface areas patterned for adsorption of the motors in active form. These areas, here denoted loading zones, are important for initial landing of a large number of cytoskeletal filaments from solution, for later transportation into the more complex channel networks, see figure 1.

Currently, the loading zones and network structures are patterned by electron beam lithography (EBL) for the actin-myosin system [7, 11, 20]. However, as patterns grow larger and more complex, the costs and fabrication time scale become unmanageable. Nanoimprint lithography (NIL) is a promising high-resolution [22–24] technique as it offers high throughput at lower costs relative other lithography techniques. The principle of NIL is based on displacement of resist under pressure to replicate stamp features, so this method is not limited by diffraction during sample fabrication. NIL is very suitable for single-step lithography applications, and with high-resolution stamps it is possible to obtain features as small as 20 nm or below [25]. Furthermore, the effects of electrostatic charging and beam scattering [26, 27] need not be taken into account as compared to EBL. However, NIL becomes challenging if the difference between the height and width dimensions of the desired material displacement is large [28], which is the case in some parts of molecular motor based devices, e.g., the above mentioned loading zones.

It has been previously shown that NIL can be used to pattern narrow tracks (100–400 nm wide, 150 nm deep) in poly(methyl methacrylate) for actin-myosin devices [29]. However, to the best of our knowledge, no studies have been done to develop a method to imprint the larger and thus, more challenging loading zones, combined with narrow tracks.

In this paper we show how we redesigned the loading zones from previous EBL fabrication efforts [8, 20] and optimised the resist thickness to be able to imprint structures with a large width to height ratio without suffering from insufficient filling of the stamp. By using a thin resist layer and by adding nanoscaled pillars we were able to provide regions into which the laterally displaced imprint resist could flow. Subsequent to residual resist removal, we were able to observe successful actin-myosin motility. Furthermore, we present simulations showing that the structural design and placement of these pillars can be used to tailor the emptying rate of the loading zone as well as to guide the filaments towards different directions. The implications of these theoretical findings for improvements in pattern design are discussed.

## 2. Experimental

### 2.1. Stamp design and fabrication

Previous research [20] has shown that a funnel shaped loading zone is preferred over a circular one as the filaments are guided towards the funnel tip, providing an improved loading, i.e., emptying rate of filaments exiting the loading zone and entering the nanoscale channels as desired. Therefore, this funnel shape was preserved also for the loading zones used here. All EBL designs were made using the Raith150 software (Raith GmbH). To imprint shallow, wide loading zones, different types of nanopillar shapes were introduced into the pattern. Initial testing without these pillars had a variety of issues including incomplete resist displacement, inhomogeneous residual layers and large areas of resist peeling off during stamp removal.

A hard NIL master stamp with negative features was fabricated using a 4" Si (100) wafer in thermally oxidized (500 nm) SiO<sub>2</sub> (Siebert Wafer GmbH, Aachen, Germany). The wafer was patterned by electron beam lithography (EBL) and reactive ion etching (RIE). In the first processing step, a double layer hard-etch-mask consisting of 60 nm Cr and 30 nm SiO<sub>2</sub> was deposited on top of the SiO<sub>2</sub> layer by thermal evaporation (AVAC HVC600, Ltd) and atomic layer deposition (ALD) (Fiji F200, Veeco), respectively. The top SiO<sub>2</sub> layer served as the etch mask for patterning Cr, which in turn, was used for relatively deep etching of thermal oxide SiO<sub>2</sub>. A two-step RIE was required due to insufficient stability of the EBL resist to pattern the Cr layer directly.

In the second processing step, a layer of EBL resist CSAR 62 (Allresist GmbH, Strausberg, Germany) was spin-coated (Primus SB15, ATMgroup) onto the etch-mask at 3000 rpm for 30 s and baked on a hotplate for 2 min at 160 °C. The stamp pattern was defined by EBL (Raith150, GmbH) at 20 kV acceleration voltage, beam current ≈0.15 nA and dose 60 μC/cm<sup>2</sup>. The pattern was developed in *o*-xylene (VWR, Radnor, PA, USA) for 5 min at room temperature and rinsed in 2-propanol (VWR, Radnor, PA, USA). Resist residues were removed by ashing in oxygen plasma (Plasma Preen, Plasmatic Systems Inc.) for 15 s at 5 mbar.

In the third processing step, the top 30 nm SiO<sub>2</sub> was patterned by inductively coupled plasma reactive ion etching (ICP-RIE) (PlasmalabSystem100, Oxford Instruments) using a mixture of C<sub>4</sub>F<sub>8</sub> and O<sub>2</sub> gases (chamber pressure 1.0 · 10<sup>-6</sup> Torr, gas flow 78.7/3.2 sccm (C<sub>4</sub>F<sub>8</sub>/O<sub>2</sub>), RF power 268 W, ICP power 1194 W, DC bias 266 V). The CSAR 62 resist was used as a mask in this etch process. The underlying Cr was etched using a mixture of Cl<sub>2</sub> and O<sub>2</sub> gases, creating a stable mask for deep etching the thermal SiO<sub>2</sub> (chamber pressure 1.0 · 10<sup>-6</sup> Torr, gas flow 20/5 sccm (Cl<sub>2</sub>/O<sub>2</sub>), RF power 97 W, DC bias 129 V). In the final etching step, the structures were etched down ~380 nm into the 500 nm thick thermal SiO<sub>2</sub> by of C<sub>4</sub>F<sub>8</sub>/O<sub>2</sub> ICP-RIE (chamber pressure 1.0 · 10<sup>-6</sup> Torr, gas flow 78.8/0.9 sccm (C<sub>4</sub>F<sub>8</sub>/O<sub>2</sub>), RF power 248 W, ICP power 1986 W, DC bias 344 V). After the final etch, all fluorocarbon residues were removed by ashing the wafer in pure oxygen plasma for 10 min at 5 mbar. The remaining Cr mask was removed by wet etching in Chrome Etch 18 (Micro resist technology GmbH, Berlin, Germany) for 5 min. To provide an anti-sticking surface preventing resist adhesion during NIL, the structured SiO<sub>2</sub> was coated with a monolayer of fluorodecyltrichlorosilane (FDTS) by ALD (Fiji F200, Veeco).

The master stamp was used to fabricate transparent intermediate polymer stamps (IPS<sup>®</sup>) through thermal imprinting. The IPS<sup>®</sup> was replicated from the master stamp by heating it to 160 °C and imprinting at 50 bar for 2 min and then cooled down to 115 °C before lowering the pressure to atmospheric pressure.

## 2.2. Sample fabrication

All samples were fabricated on 2" SiO<sub>2</sub>/Si(100) wafers by imprinting the patterns in TU7-220 resist (Obducat, Lund, Sweden). A modified version of a standard IPS<sup>®</sup>-simultaneous thermal and UV-imprint (IPS<sup>®</sup>-STU<sup>®</sup>) process developed by Obducat, was used for the nanoimprinting. The wafers were patterned by the STU<sup>®</sup> process, and a separate IPS<sup>®</sup> was used for each wafer. Prior to the deposition of TU7, the wafers were treated in oxygen plasma at 5 mbar for 60 s to improve resist adhesion. To obtain an optimum resist thickness, a series of wafers were spin-coated for 30 s at five different spin-speeds: 1000, 1200, 1500, 2000 and 3000 rpm, and baked on a hotplate for 60 s at 95 °C.

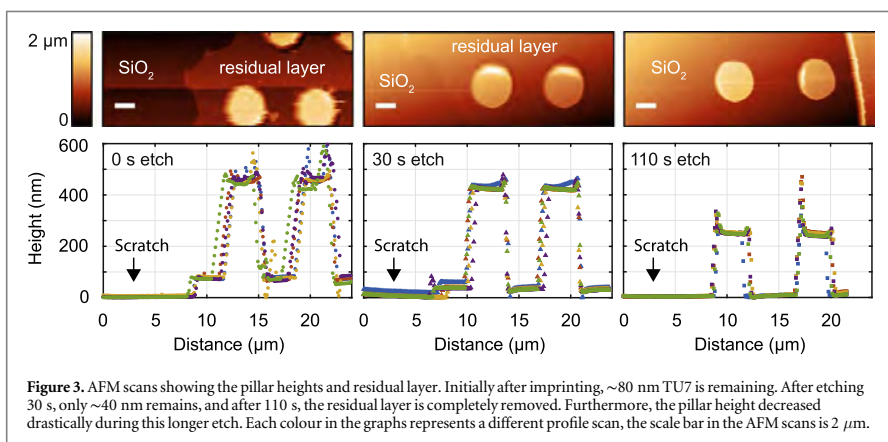
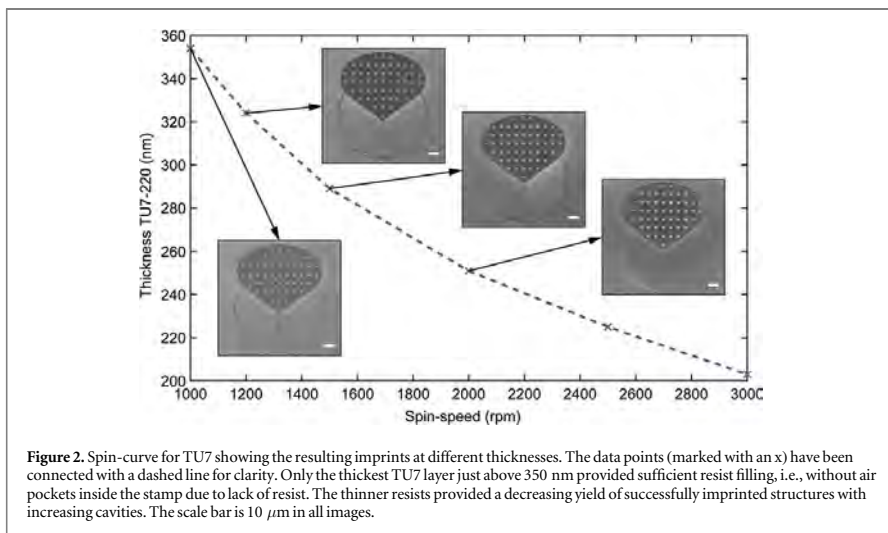
During imprint, the TU7 layer was heated to 75 °C and subjected to a pressure of 20 bar with subsequent exposure to 20 s of UV-light, with a wavelength of 370 nm and intensity of 34 mW cm<sup>-2</sup>, to cross-link the TU7 polymer. The pressure and temperature were maintained for 2 min and then decreased to ambient conditions. After imprinting, the wafers were examined in a scanning electron microscope (SEM) (Hitachi SU8010, Hitachi, Japan) to determine the minimum resist thickness which ensures sufficient filling of the stamp, see figure 2.

A new series of wafers with the spin-speed with the best results (1000 rpm) were fabricated and imprinted. These wafers were used to optimise the removal of the residual resist layer by reactive ion etching (Sirius T2, Trion Technology) in oxygen plasma. To examine the residual layer, a small scratch was made through the structured area and scanned in an atomic force microscope (AFM) (NaiAFM, NanoSurf) in non-contact mode with an ACLA tip, before and after etching for 10 s, 30 s and 110 s, see figure 3. The obtained data was analysed in the Gwyddion software [30].

The wafers were diced (Disco DAD 3320, Co) into to 10 × 10 mm samples and treated with trimethylchlorosilane (Sigma-Aldrich, Saint Louis, MO, USA) as previously described [31] for 64 min at 200 mbar.

## 2.3. In vitro motility assay

We performed *in vitro* motility assays [4] as previously described [31] at 26 °C, by infusing 120 μg/ml heavy mero myosin (5 min) and 200 nM Rhodamine-phalloidin labelled actin filaments (2 min) followed by an assay solution (pH 7.4) containing 1 mM MgATP and with an ionic strength of 60 mM. The motility assay was observed in a Zeiss Axio observer inverted microscope with Hg-lamp illumination, Zeiss Plan-APOCHROMAT



$63 \times 1.4$  NA oil immersion objective, TRITC filter set (excitation 532–554 nm, emission 570–613 nm, dichroic cut-on 562 nm) and a Hamamatsu EMCCD camera. The recorded data was analysed in ImageJ [32, 33] to study the filament behaviour.

#### 2.4. Monte Carlo simulations

To estimate the effect of different shaped pillars in the loading zones, we performed Monte Carlo simulations of the movement of filament tips on open surfaces and of their guiding at wall edges. The simulations take into account the filament rigidity, thermal motion and the guiding effect of the channel walls as described in previous work [15]. Briefly, the effect of the thermal fluctuations of filament tips moving at velocity ( $v$ ) was taken into account by updating the direction of motion at time intervals ( $\Delta t$ ) with an angular change, which was obtained from a Gaussian distribution with zero mean value and standard deviation ( $\sigma$ ) according to equation (1):

$$\sigma = (v\Delta t/L)^{0.5} \quad (1)$$

where  $L$  is the persistence length of the filament (in this case 10  $\mu\text{m}$ ). The MATLAB (Mathworks, Natick, MA) randn function with a Mersenne-Twister algorithm was used as random number generator for normal distributions. For each simulated device, the random number generator was initialised with the 'rng('shuffle')' command. Thereafter, individual random seeds for each filament were generated with the 'randi' function, ensuring that the random number generator for each filament was initialised with a unique random seed. After a

wall collision was detected, the direction of the filaments was changed such that the change in angle was minimal and the angle after collision followed the angle of the smooth wall at the collision point. Similar algorithms have been successfully used to optimise nanofabricated structures for the guiding of cytoskeletal filaments [7, 34].

### 3. Results and discussion

In standard NIL procedures, the resist is spun thicker than the stamp protrusions to prevent deformation and damaging of the stamp during imprinting. However, by using a two-step imprinting procedure with a soft IPS<sup>®</sup> this risk is completely eliminated. Due to the large difference between height and width being imprinted in the structures presented here (up to  $\sim 1:200$ ), we deliberately spun a thinner resist layer than the intended depth of the structures to try and obtain more capillary flow upwards to displace as much resist as possible vertically, into the stamp cavities. The thickness of the resist was varied by changing the spin-speed from 1000 rpm up to 3000 rpm. We found that the thinnest resist possible to use is just above 350 nm, while the thinner resists cause insufficient filling, see figure 2.

The residual layer of TU7 was removed by reactive ion etching in oxygen plasma. Initially  $\sim 80$  nm TU7 remained after imprinting. After a 30 s full wafer etch, only 40 nm remained. To ensure full removal of all TU7 in order to promote later myosin driven actin motility, a longer 110 s full wafer etch was performed, completely removing all remaining TU7 on the channels floors, see figure 3. A slightly shorter etch time can also be used to maintain higher pillars.

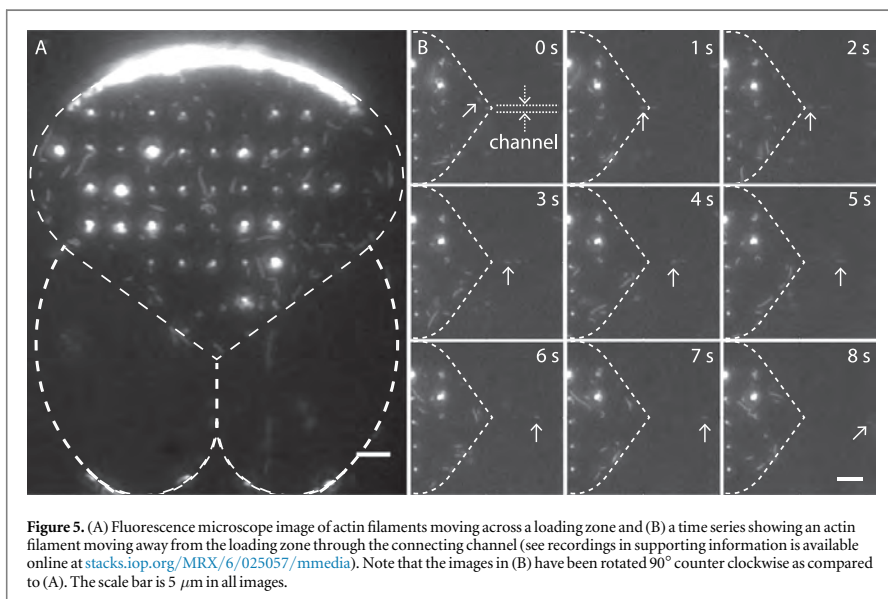
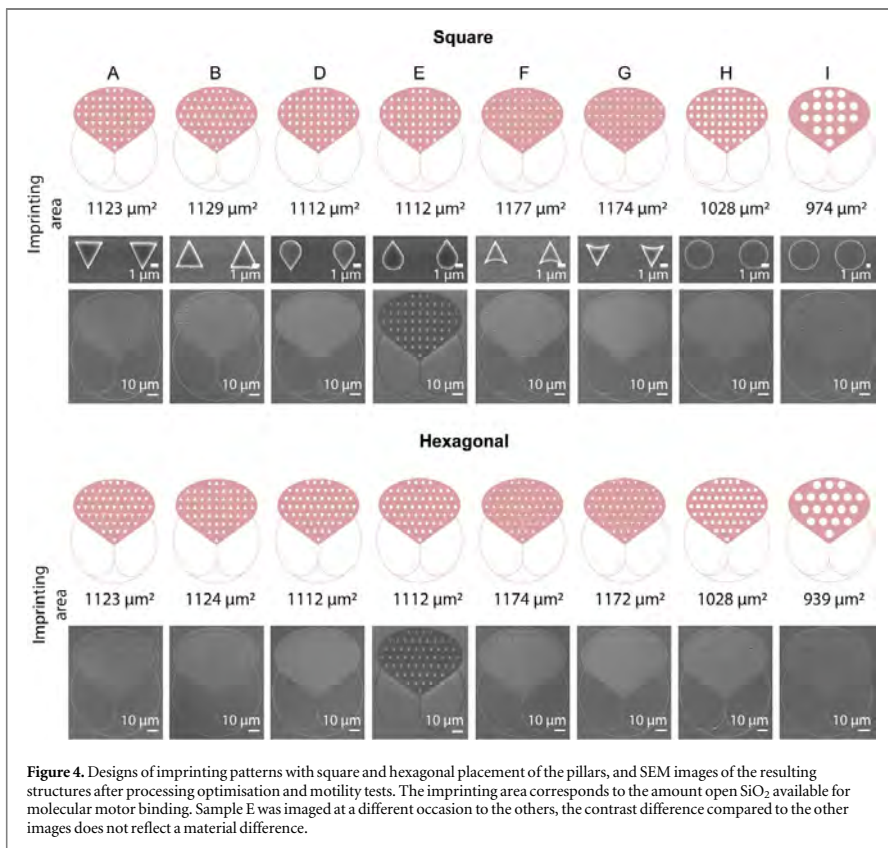
The pattern designs and resulting imprints that were fabricated with use of the optimisations described above, are depicted in figure 4.

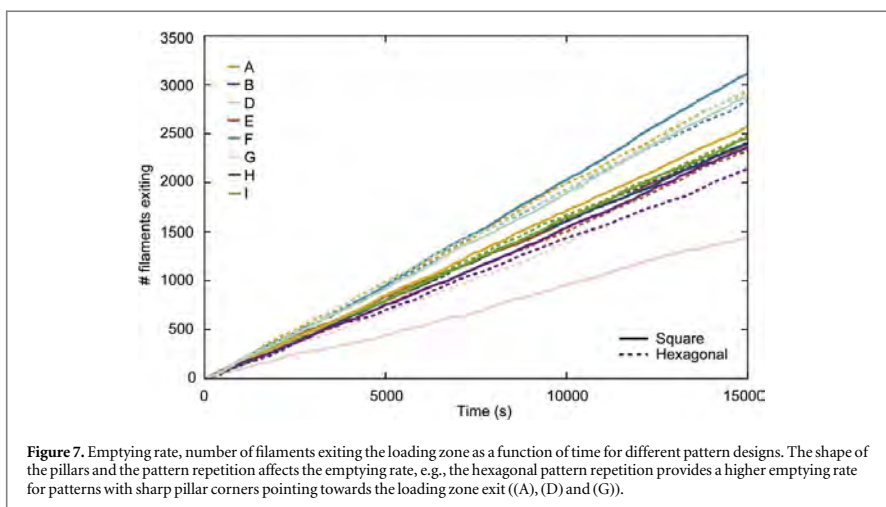
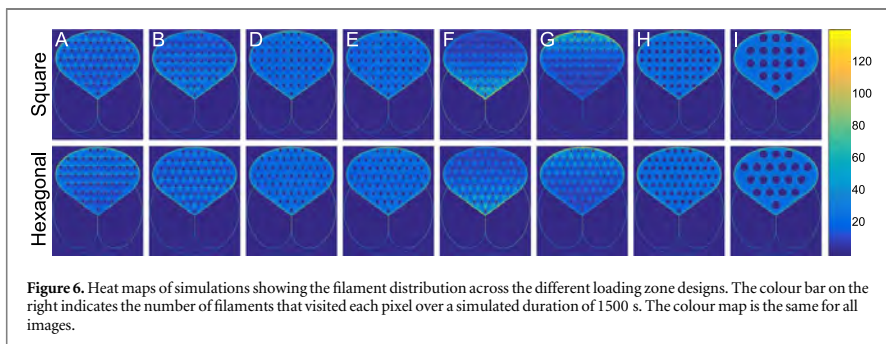
The imprinted structures supported motility inside both the loading zone and the connecting nanochannel, see figure 5, although the majority of filaments remained inside the loading zone without entering the channel. We observed filaments tracing the pillar-structures when approaching at a grazing incidence angle, but detachment was observed upon head-on collision, similar to what previous findings have suggested [8, 35]. The overall number of filaments observed in these structures is low, which is likely due to the increased number of obstacles as compared to open loading zones, causing an increased number of exiting events due to head-on collisions. Moreover, the decreased number of filaments is also attributed to a decreased surface area available for motor adsorption. The surface area is decreased to different extents from  $1200 \mu\text{m}^2$  without any pillars, depending on the different designs (figure 4). Nevertheless, as the filaments come in contact with the pillars, their trajectory path is also redirected, providing a good spread of filaments across the entire loading zones (figure 5). Such properties are desirable in applications where filament behaviour in a confined area is studied, e.g., in response to different chemical environments. Therefore, we hypothesized that a hexagonal and square pattern repetition would generate different filament spreading due to constant redirection upon impact, as filaments otherwise tend to trace the walls in confined spaces [11, 15]. However, no obvious difference was observed between the hexagonal and square pattern positions, both geometries provided good motility, this can likely be improved by further optimisation to increase the number of filaments studied.

In addition, Monte Carlo simulations suggest that the pillars introduced could also be able to tailor both the overall direction of filament movement as well as the emptying rate of filaments exiting the loading zone. For these simulations, the same number of filaments (240) were simulated for a time equivalent of 1500 s for each design. In an experimental set-up, the total number of filaments will also depend on the free  $\text{SiO}_2$  surface area available for molecular motor binding. Most designs have the same  $\text{SiO}_2$  area in both the square and hexagonal pattern repetitions (figure 4). However, depending on the number of pillars included and the pillar shape, the imprint areas vary slightly. Thus, the total number of filaments would not be consistent in each experiment. However, as is clear from figure 4, the difference would be small.

The overall simulated behaviour of the filaments can be seen in the heat maps presented in figure 6. The designs with three sharp corners (designs A, B, F, G in figure 4) present a larger difference in emptying rate (figure 7) between the square and hexagonal pattern repetition as compared to the pillar shapes with just one sharp corner (designs D and E in figure 4). The emptying rate with the completely symmetrical pillar shapes (see designs H and I) are close to identical, despite the difference in pillar diameter. Moreover, the symmetrical pillar shapes provide more evenly distributed filaments inside the loading zone (figure 6).

Another noticeable difference is that the emptying rate (figure 7) for square pattern repetitions is lower than for hexagonal pattern repetition if a sharp corner is pointing towards the exit (compare A and B, D with E, F and G). However, the overall emptying rate is still higher for patterns with a sharp corner pointing towards the exit (compare A, D with B, E). Interestingly, the pillar shape in designs F and G provide a slightly different filament movement. The heat map of design F (figure 6) clearly shows a larger density of filaments closer to the loading zone exit, while the opposite is true for design G. This is likely caused by the concave arc in the pattern that changes the angle of any filament hitting the concave wall towards (design F) or away from (design G) the exit,





which will affect the proceeding pathway [9]. The effect becomes more evident after comparison of emptying rates (figure 7) for filaments pushed towards an end of the loading zone, where designs F and G provide the two most extreme emptying rates.

The filament behaviour will of course vary for different molecular motor systems as a key factor affecting the trajectory path is the persistence length. Here we have used parameters that match the behaviour of the actin-myosin system in an *in vitro* motility assay, namely a persistence length of 10  $\mu\text{m}$  and a velocity of 10  $\mu\text{m}/\text{s}$ . Similar simulations have been successfully used to predict the behaviour of both actin-myosin and kinesin-microtubule motor systems in nanostructures [7, 34].

#### 4. Conclusion

We have shown that it is possible to fabricate structures with an aspect ratio up to  $\sim 1:200$  (height-to-width) for molecular motor devices by nanoimprint lithography. Key parameters are resist thickness and introduction of pillar shapes into large open areas such as loading zones for cytoskeletal filaments. The pillars provide sinks in the stamp into which polymer can be displaced. Furthermore, Monte Carlo simulations indicate that the introduced pillars could be used to tailor the behaviour of filament movement by varying the shape and configuration of the pillars. In contrast to previous attempts that created simple line patterns for the guiding of cytoskeletal filaments [29], our approach allows fabrication of complex molecular motor-powered nanodevices such as network-based biocomputers [7] or lab-on-a-chip diagnostic devices [6]. We envision that this technology will enable rapid mass-production of such devices at greatly reduced cost, bringing them closer to market maturity. Furthermore, the possibility to imprint structures with large differences in dimensions by

resist thickness optimisation may also find future applications within several other fields including nanopillar patterning for e.g., superhydrophobic surfaces [36] or cellular behaviour studies [37].

## Acknowledgments

Financially supported by the European Union's Horizon 2020 research and innovation FET programme under grant agreement No 732482 (Bio4Comp); NanoLund; MyFab; the Swedish Research Council (Projects 2015-05290 and 2015-0612); Linnaeus University, Faculty of Health and Life Sciences. A part of the current work has also been financed by the Swedish foundation for strategic research (SSF), within project 'Development of nanoimprint infrastructure at Lund Nano Lab as a key enable for large scale applications of nanowires', RIF14-0090.

## ORCID iDs

Frida W Lindberg  <https://orcid.org/0000-0001-5617-6337>

## References

- [1] Kron SJ and Spudich JA 1986 Fluorescent actin filaments move on myosin fixed to a glass surface *Proc. Natl. Acad. Sci. USA* **83** 6272–6
- [2] Howard J, Hudspeth A J and Vale R D 1989 Movement of microtubules by single kinesin molecules *Nature* **342** 154–8
- [3] Sheetz M P and Spudich J A 1983 Movement of myosin-coated fluorescent beads on actin cables *in vitro Nature* **303** 31–5
- [4] Kron SJ, Toyoshima Y Y, Uyeda T Q P and Spudich J A 1991 Assays for actin sliding movement over myosin-coated surfaces *Methods Enzymol.* **196** 399–416
- [5] Barclay C J 1998 Estimation of cross-bridge stiffness from maximum thermodynamic efficiency *J. Muscle Res. Cell Motil.* **19** 855–64
- [6] Korten T, Månsson A and Diez S 2010 Towards the application of cytoskeletal motor proteins in molecular detection and diagnostic devices *Curr. Opin. Biotechnol.* **21** 477–88
- [7] Nicolau D V J, Lard M, Korten T, Delft F V, Persson M, Bengtsson E, Månsson A, Diez S, Linke H and Nicolau D V 2016 Parallel computation with molecular motor-propelled agents in nanofabricated networks *PNAS* **113** 2591–6
- [8] Sundberg M et al 2006 Actin filament guidance on a chip: toward high-throughput assays and lab-on-a-chip applications *Langmuir* **22** 7286–95
- [9] Clemmens J, Hess H, Lipscomb R, Hanein Y, Böhringer K F, Matzke C M, Bachand G D, Bunker B C and Vogel V 2003 Mechanisms of microtubule guiding on microfabricated kinesin-coated surfaces: chemical and topographic surface patterns *Langmuir* **19** 10967–74
- [10] Hiratsuka Y, Tada T, Oiwa K, Kanayama T and Uyeda T Q P 2001 Controlling the direction of kinesin-driven microtubule movements along microlithographic tracks *Biophys. J.* **81** 1555–61
- [11] Bunk R, Sundberg M, Månsson A, Nicholls I A, Omring P, Tågerud S and Montelius L 2005 Guiding motor-propelled molecules with nanoscale precision through silanized bi-channel structures *Nanotechnology* **16** 710–7
- [12] Hess H, Matzke C M, Doot R K, Clemmens J, Bachand G D, Bunker B C and Vogel V 2003 Molecular shuttles operating under cover: a new photolithographic approach for the fabrication of structured surfaces supporting directed motility *Nano Lett.* **3** 1651–5
- [13] Nicolau D V, Suzuki H, Mashiko S, Taguchi T and Yoshikawa S 1999 Actin motion on microlithographically functionalized myosin surfaces and tracks *Biophys. J.* **77** 1126–34
- [14] Suzuki H, Yamada A, Oiwa K, Nakayama H and Mashiko S 1997 Control of actin moving trajectory by patterned poly (methylmethacrylate) tracks *Biophys. J.* **72** 1997–2001
- [15] Månsson A, Bunk R, Sundberg M and Montelius L 2012 Self-organization of motor-propelled cytoskeletal filaments at topographically defined borders *J. Biomed. Biotechnol.* **2012**
- [16] Clemmens J, Hess H, Doot R, Matzke C M, Bachand G D and Vogel V 2004 Motor-protein roundabouts: microtubules moving on kinesin-coated tracks through engineered networks *Lab Chip* **4** 83–6
- [17] Huxley H E 1969 The mechanism of muscular contraction *Science* **164** 1356–66
- [18] Huxley A F and Simmons R M 1971 Proposed mechanism of force generation in striated muscle *Nature* **233** 533–8
- [19] Huxley A F 1974 Muscular contraction *J. Physiol.* **243** 1–43
- [20] Lard M, ten Siethoff L, Kumar S, Persson M, te Kronnie G, Linke H and Månsson A 2013 Ultrafast molecular motor driven nanoseparation and biosensing *Biosens. Bioelectron.* **48** 145–52
- [21] Katira P and Hess H 2010 Two-stage capture employing active transport enables sensitive and fast biosensors *Nano Lett.* **10** 567–72
- [22] Chou S Y, Krauss P R, Zhang W, Guo L and Zhuang L 1997 Sub-10 nm imprint lithography and applications *J. Vac. Sci. Technol.* **15** 2897–904
- [23] Heidari B, Maximov I, Sarwe E-L and Montelius L 1999 Large scale nanolithography using nanoimprint lithography *J. Vac. Sci. Technol. B Microelectron. Nanom. Struct.* **17** 2961–4
- [24] Schiff H 2008 Nanoimprint lithography: an old story in modern times ? A review *J. Vac. Sci. Technol. B Microelectron. Nanom. Struct.* **26** 458–80
- [25] Graczyk M, Cattoni A, Rösner B, Seniutinas G, Löfstrand A, Kvennefors A, Mailly D, David C and Maximov I 2018 Nanoimprint steps with ultra-high resolution: optimal fabrication techniques *Microelectron. Eng.* **190** 73–8
- [26] Stepanova M and Dew S 2012 *Nanofabrication: Techniques and Principles* (Wien: Springer) 9783709104231
- [27] Gangnaik A S, Georgiev Y M and Holmes J D 2017 New generation electron beam resists: a review *Chem. Mater.* **29** 1898–917
- [28] Scheer H-C 1998 Problems of the nanoimprinting technique for nanometer scale pattern definition *J. Vac. Sci. Technol. B Microelectron. Nanom. Struct.* **16** 3917
- [29] Bunk R, Carlberg P, Månsson A, Nicholls I A, Omring P, Sundberg M, Tågerud S and Montelius L 2005 Guiding molecular motors with nano-imprinted structures *Jpn. J. Appl. Phys.* **44** 3337–40
- [30] Nečas D and Klapetek P 2012 Gwyddion: an open-source software for SPM data analysis *Cent. Eur. J. Phys* **10** 181–8

- [31] Lindberg F W, Norrby M, Rahman M A, Salhotra A, Takatsuki H, Jeppesen S, Linke H and Månsson A 2018 Controlled surface silanization for actin-myosin based nanodevices and biocompatibility of new polymer resists *Langmuir* **34** 8777–84
- [32] Rueden C T, Schindelin J, Hiner M C, DeZonia B E, Walter A E, Arena E T and Eliceiri K W 2017 ImageJ2: imagej for the next generation of scientific image data *BMC Bioinform.* **8** 1–26
- [33] Schindelin J *et al* 2012 Fiji: an open-source platform for biological-image analysis *Nat. Methods* **9** 676–82
- [34] Nitta T, Tanahashi A, Hirano M and Hess H 2006 Simulating molecular shuttle movements: towards computer-aided design of nanoscale transport systems *Lab Chip* **6** 881–5
- [35] Schroeder V, Korten T, Linke H, Diez S and Maximov I 2013 Dynamic guiding of motor-driven microtubules on electrically heated, smart polymer tracks *Nano Lett.* **13** 3434–8
- [36] Jung Y C and Bhushan B 2006 Contact angle, adhesion and friction properties of micro- and nanopatterned polymers for superhydrophobicity *Nanotechnology* **17** 4970–80
- [37] Dalby M J, Gadegaard N and Oreffo R O C 2014 Harnessing nanotopography and integrin-matrix interactions to influence stem cell fate *Nat. Mater.* **13** 558–69



# Paper III





# Nanofabrication technologies for molecular-motor-powered network-based biocomputation structures

Christoph Meinecke<sup>1,2</sup>, Till Korten<sup>3,4</sup>, Frida W. Lindberg<sup>5</sup>, Heiner Linke<sup>5</sup>, Georg Heldt<sup>2</sup>, Danny Reuter<sup>1,2</sup>, Stefan Diez<sup>3,4</sup>, Stefan E. Schulz<sup>1,2</sup>

## **Affiliations:**

1 TU-Chemnitz, Center for Microtechnologies, Chemnitz, Germany

2 Fraunhofer Institute for Electronic Nanosystems (ENAS), Chemnitz, Germany

3 B CUBE - Center for Molecular Bioengineering, Technische Universität Dresden, Dresden, Germany.

4 Max Planck Institute of Molecular Cell Biology and Genetics, Dresden Germany.

5 NanoLund and Solid State Physics, Lund University, Lund, Sweden

**Keywords:** Biocomputation, nanotechnology, molecular-motors, network-based computation

## **Abstract**

Network-based biocomputation relies on accurate guiding of cytoskeletal filaments. Here, we report on the fabrication and operation of a biocomputation network of a classical nondeterministic-polynomial-time complete (“NP-complete”) problem, the subset sum problem. The nanofabricated structures rely on a combination of physical and chemical guiding of the gliding of cytoskeletal filaments, e.g. microtubules or actin filaments along channels. Therefore, the nanochannels have to fulfil specific requirements for the biochemical treatment as well as the cytoskeletal guidance. The material stack used for the nanochannels was optimized such that the motor proteins are active only at the floor of the nanochannels. Further optimizations in the nanofabrication have greatly improved the smoothness of channel walls and floor, while optimizations in motor-protein expression and purification have improved the activity of the motor proteins. Together, these optimizations provide us with the opportunity to increase the longevity as well as the reliability of our devices. In the future, this will enable fabrication and operation of large-scale networks, intended to solve substantially larger computational problems that are too extensive and/or time-consuming for conventional computers.

## Introduction

Conventional computers solve problems sequentially, which limits their ability to compute intricate combinatorial problems. This concerns problems such as routing, design of error-free computer chips and software, calculation of efficient resource-use in industrial processes, or prediction of protein folding. The challenge is the exponential increase of the necessary calculations in relation to the size of the system. Even relatively small combinatorial problems can overwhelm a conventional, sequentially operating computer, with the number of arithmetical operations required to solve the problem. Alternative parallel computing approaches like DNA-computers [1] or quantum computers [2], could in principle solve such problems much more efficiently. However, so far these methods have not been scalable in practice.

Here, we present a novel strategy for parallel biological computation, using a combination of physical and chemical guiding of filaments by biomolecular motors. For this purpose, state-of-the-art nanofabrication methods such as electron beam lithography, are combined with biomolecular motors of the cell. This enabled us to control the motion and position of biomolecules with molecular scale precision. We used the biomolecular motor protein kinesin-1, which is robust in artificial environments, and its associated cytoskeletal filaments microtubules (MT), as well as heavy meromyosin together with its cytoskeletal filament, actin.

## Network-based Biocomputation

A network-based biocomputational device in general, comprises a conveniently designed computing network, with a pool of possible solutions that require a sufficient source of biological agents to explore all possible outcomes. Network-based biocomputation relies on accurate guiding of biological agents. The nanofabricated structures rely on a combination of physical and chemical guiding of the gliding of agents along channels.

### *A. Working Principle*

Here, we investigated the fabrication and operation of a biocomputation network that encodes the subset-sum problem (SSP), a classical nondeterministic-polynomial-time complete (“NP-complete”) problem.

The SSP is a well-known problem in computer science especially in cryptography and complexity theory [3]. SSP asks what possible sums, or alternatively, whether a target sum  $T$ , can be reached by summing up any combination of integers from a number set  $S$ .



### B. Network Layout

Two types of layouts for a computational network (Fig. 2), encoding for the specific instance  $\{10, 6, 5, 3\}$  of a subset-sum problem, were designed, one for the microtubule-kinesin I system, and one for the actin-myosin II system.

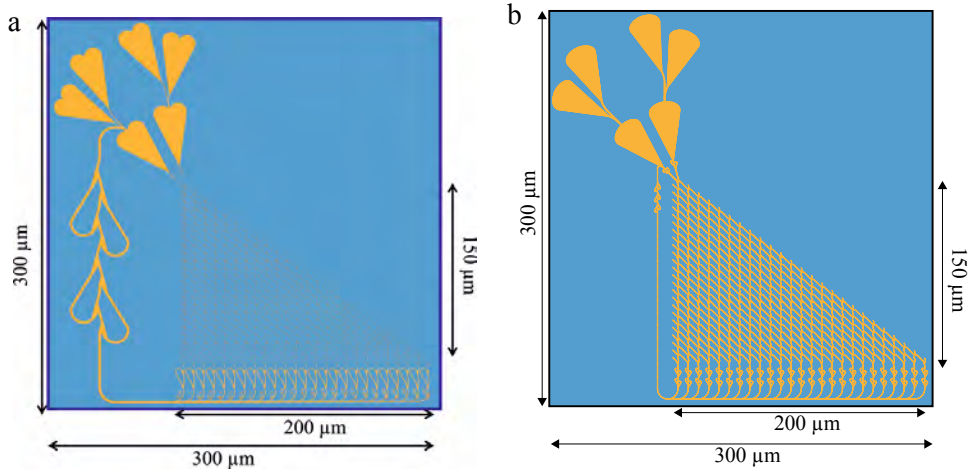


**Fig. 2: Layout of the biocomputation network encoding the SSP  $\{10, 6, 5, 3\}$  for a) microtubules and b) actin filaments.** Areas accessible to the cytoskeletal filaments (channels, loading zones and feedback loops) are indicated in yellow, walls and inaccessible areas are indicated in blue.

The processing of microtubule-kinesin devices was done at TU-Chemnitz/ZfM and Fraunhofer Institute ENAS and the processing of actin-myosin devices was done at Lund Nano Lab at Lund University, resulting in a network of nanofabricated guiding channels forming split and pass junctions. The biological functionalization and necessary surface treatments were performed at TU Dresden for microtubule-kinesin and at Linneaus University for actin-myosin.

Figure 3 shows the fabricated biocomputational networks for the SSP layouts. On the left, the scanning electron micrograph of the entire network for microtubules is given, and to the right an optical micrograph of the network for actin filaments is shown.

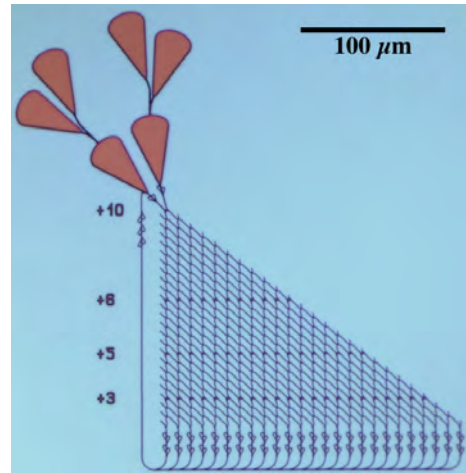
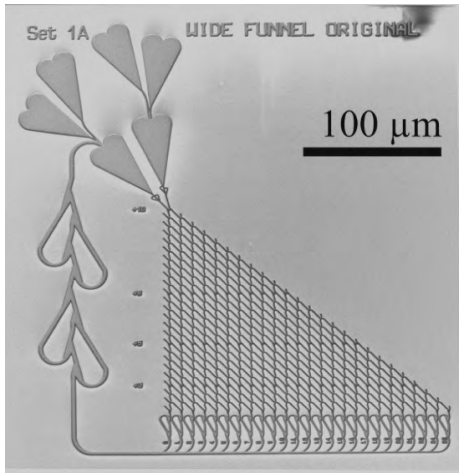


**Fig. 3: Fabricated biocomputational networks.** (left) Scanning electron micrograph of the fabricated network structure for microtubules and (right) optical micrograph of the network for actin filaments.

## Experimental

Reliable guiding of the cytoskeletal filaments (the biocomputing agents), through the network is based on two essential requirements: (I) Chemical guiding, where only the channel bottoms have functional motor proteins and walls do not have active motors, preventing the filaments from attaching to the surface anywhere but inside the channels. (II) Physical guiding, where the channel topography provides physical confinement. That means the filaments collide with the walls and are forced to follow the channel.

The combination of chemical and physical guiding results in very reliable guiding of the filaments in the desired direction (Fig. 4) [5, 6].

Two different types of motor-proteins and their corresponding filaments were investigated during the experiments:

- 1) The kinesin-microtubule system, using the biomolecular motor protein kinesin-1 – which is robust in artificial environments – to propel the cytoskeletal filament microtubules (MT) [7].
- 2) The actin-myosin system, using the biomolecular motor protein myosin-II – which is a very fast motor that is readily available from skeletal muscle – to propel actin filaments [8].

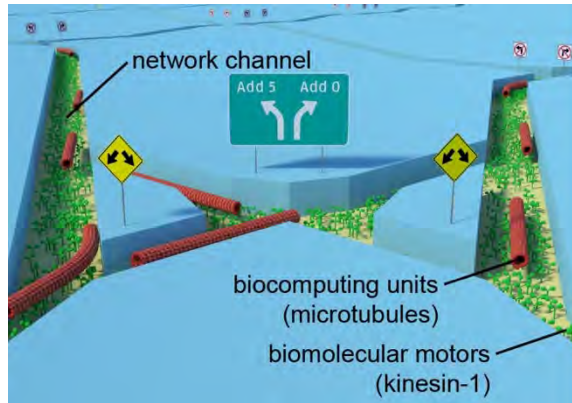


**Fig. 4: Chemical and physical guiding.** Scheme of filament guiding based on physical and biochemical confinement

#### *A. Network fabrication – kinesin-microtubule System*

The biocomputational network used for the microtubule-kinesin system consists of a network of SiO<sub>2</sub> channels, with a Au “floor” at the channel bottom, forming a system of hierarchical structures of pass/split-junctions. The SiO<sub>2</sub> is silanized with 2-[Methoxy(polyethyleneoxy)propyl]trimethoxysilane (PEG), such that the motor proteins (kinesin-1) can only adsorb onto the gold floor and not onto the surrounding SiO<sub>2</sub> walls.

The network structures were fabricated on a standard 6-inch, single side polished silicon wafer (625 μm) in four steps:

- 1) The initial layer on the Si-substrate is a 100 nm thick SiO<sub>2</sub> diffusion barrier layer made by dry thermal oxidation. The layer growing was carried out under oxygen atmosphere with 3% HCl. Afterwards a 100 nm Au layer was sputtered, sandwiched between two 10 nm thick Cr adhesion layers. Next, a 500 nm SiO<sub>2</sub> layer was deposited using a PE-CVD at 300°C. Finally, a 10 nm Cr layer acting as a hard mask for the SiO<sub>2</sub> patterning was sputtered onto the surface (see Fig. 5).

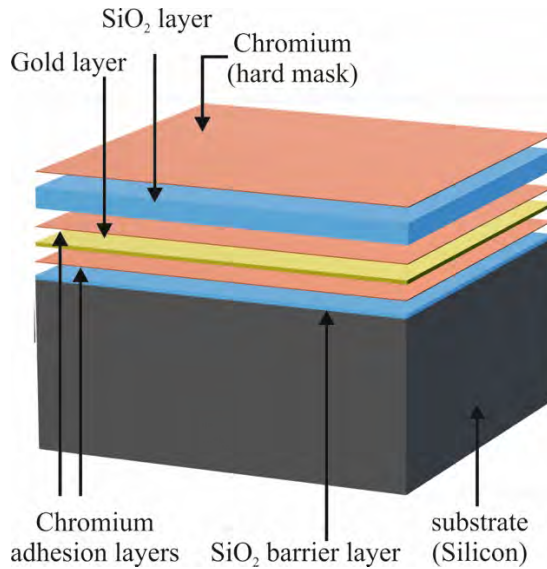


**Fig. 5: Layer structure for the devices used for the microtubule system.** Cross sectional view of the deposited layers on a silicon wafer.

- 2) The wafer was subsequently spin-coated with PMMA (ALLRESIST AR-P 679.04), a positive-tone electron-beam resist, to a resist thickness of 400 nm and hard-baked at 180°C for 5 minutes. For the exposure, an e-beam lithography system (Vistec SB254) was used at a dose of 650  $\mu\text{C}/\text{cm}^2$ . The PMMA was developed for 60 s at room temperature in a solution of methyl isobutyl ketone (MIBK) and isopropanol (IPA) (ratio 1:3), rinsed with IPA and flushed in a conductance-controlled DI-water bath. In a final step, all remaining surface humidity was removed in a commercial dryer. This leaves the wafer with a patterned resist mask on top ready to be used as etch mask for the underlying chromium layer.
- 3) The resilience of PMMA against plasma etching is quite low, therefore the resist pattern was transferred into a Cr-layer acting as a hard mask for the following structuring of the  $\text{SiO}_2$ -layer. Cr was used as mask material because it gives high pattern fidelity and smooth channel sidewalls, which is important for the next  $\text{SiO}_2$  etch step. Etching of the chromium hard mask was performed in a FHR MS-200-2-AE system using a mixture of  $\text{Cl}_2$  (100 sccm) and  $\text{O}_2$  (30 sccm) at a chuck temperature of 8°C for 150 seconds. The patterning of the  $\text{SiO}_2$  channels was subsequently performed at an ICP Oxford Plasmalab System 100 using a gas flow of 10 sccm  $\text{CHF}_3$  and 18 sccm  $\text{C}_4\text{F}_8$ . The etch duration was app. three minutes.

After successful nanofabrication of the channels (see also Fig. 3 left), surface passivation, biological functionalization and microtubule gliding motility assays, were performed by a procedure previously described [9, 10] that was upgraded for motility in nanochannels [11]. Briefly, The SiO<sub>2</sub> surface of the computational chip was passivated with 2-[Methoxy(poly-ethyleneoxy) propyl] trimethoxysilane] 90% (ABCR, SIM4492.7; 0.23% v/v in toluene·HCl) overnight at room temperature to prevent protein binding anywhere except onto the gold channel floors. Flow cells were constructed by placing stretched stripes of Parafilm on the chips next to the structures. The channels were closed with a glass coverslip (Menzel, (18×18) mm<sup>2</sup>) silanized with PEG, as described for the structures above. Flow cells were perfused with casein-containing solution (0.5 mg ml<sup>-1</sup>) in BRB80 and left to adsorb for 5 min. Next, 5 μl of kinesin solution (4 nM full-length kinesin), was perfused into the flow cells and incubated for another 10 min. Thereafter, a motility solution (1 mM ATP, 20 mM D-glucose, 20 μg ml<sup>-1</sup> glucose oxidase, 10 μg ml<sup>-1</sup> catalase, 10 mM DTT, 10 μM taxol in BRB80) containing rhodamine-labeled, taxol-stabilized microtubules, was applied.

Full-length kinesin-1 (kinesin) from *Drosophila* was expressed in insect cells and purified as described previously [11]. Tubulin was isolated from porcine brain and subsequently labeled with rhodamine as described previously [12].

### *B. Network fabrication actin-myosin-system*

The biocomputational network consists of a network of channels, which is formed by a system of hierarchical structures of pass/split-junctions in CSAR62 resist on a SiO<sub>2</sub>-coated Silicon substrate. (Fig. 6). The difference in charge and hydrophobicity of the channel walls and floors, enable myosin-motors to adhere in a motility promoting manner only on the channel floors.

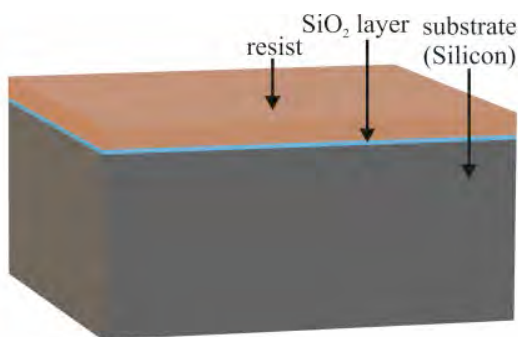


**Fig. 6 Layer structure.** Cross section of the deposited layers on a silicon wafer

The structures were fabricated on a single side polished 2-inch wafer Si(100) wafer in three steps:

- 1) A 70 nm thick SiO<sub>2</sub> layer was deposited onto the Si-substrate by atomic layer deposition (ALD) using pulses of bisdiethylaminosilane as precursor in oxygen plasma. The reason for this layer is two-fold: enabling surface derivatization by TMCS to modify the surface hydrophobicity and to enhance the contrast of fluorescently labelled actin filaments. The latter, known as fluorescence interference contrast (FLIC) enables signal enhancement through constructive interference of the emission signals of the fluorophores located on the filaments, excited by either direct light from the light source or light reflected by the Si surface.
- 2) A layer CSAR62 (ALLRESIST AR-P 6200) was spin-coated onto the SiO<sub>2</sub>, to a thickness around 360 nm and hard-baked at 180°C for 2 minutes. The network was patterned by electron beam lithography (Raith150) with a dose of 60  $\mu\text{C}/\text{cm}^2$ . The CSAR62 was developed for 2 min in O-xylene, rinsed with IPA and dried with N<sub>2</sub>-gas.
- 3) To remove any resist residues, and to activate the SiO<sub>2</sub> surface with hydroxyl groups, the devices were treated in oxygen plasma for 15 s at 5 mbar. Once activated, the surface was derivatized with trimethylchlorosilane by chemical vapor deposition as described in [13] at 200 mbar for 64 min, providing a water contact angle  $\sim 75^\circ\text{C}$ .

A microscopic image of the fabricated biocomputational network for the actin-myosin-system, comparable to the network used for the Microtubule-System, is shown in figure 3 (right).

Flow cells were built by gluing device face down to microscope cover slips (No. 0, Menzel-Gläser, Braunschweig, Germany) using two stretches of 60  $\mu\text{m}$  thick double-sided tape. The in vitro motility assays were performed at 22°C according to a modified protocol previously described [14], 120  $\mu\text{g}/\text{ml}$  heavy meromyosin was incubated for 3 min, 1 mg/ml bovine serum albumin (2 min), 50 nM rhodamine-phalloidin labelled actin filaments (2 min). The ionic strength was 60 mM and the MgATP concentration was 1 mM.

### *C. Image processing Microtubule System*

Fluorescence time-lapse movies were recorded with an Axiovert 200M inverted optical microscope (Zeiss) using a Tetra methyl Rhodamine Iso-Thiocyanate filter set (Chroma Technology; Ex 535/50, DM 565, BA 610/75). Time-lapse images were recorded at a rate of 0.5 frames per second with an exposure time of 100 ms using an EMCCD camera (iXon+EMCCD, DU-897E, Andor) in conjunction with Metamorph imaging software (Universal Imaging Corp.).

#### *D. Image processing Actin-Myosin-System*

The motility assays were imaged with a Nikon inverted microscope with a Mercury lamp using a x100 1.4 NA oil immersion objective and a TRITC filter set (excitation: 532-554 nm, emission: 570-613 nm, dichroic cut-on: 562 nm). The recordings were captured at a framerate of 5 frames per second using an EMCCD camera (Hamamatsu C9100) and analyzed with ImageJ [15].

## **Results and Discussion**

Biocomputation with biological agents would require several technological preconditions.

- Fabrication of smooth and narrow channels that reliably guide motility and do not allow the filaments to make U-turns [16].
- Fabrication of devices that would ensure continuous motility from the source of agents to the pool of possible solutions [17].

#### *A. Microtubule-kinesin system*

In order to achieve high pattern fidelity and smooth channel sidewalls, a Cr layer acting as hard mask during SiO<sub>2</sub> plasma etch was evaluated. Due to the resilience of PMMA against plasma etching being quite low, a Cr-layer acting as a hard mask for the following structuring of the SiO<sub>2</sub>-layer was used. Cr showed good plasma etching properties and a high selectivity against gold and SiO<sub>2</sub>. The Cr hard mask gives high pattern fidelity and the etching results in smooth channel sidewalls (see **fig. 7**), which is important for the motility of the agents in these channels.

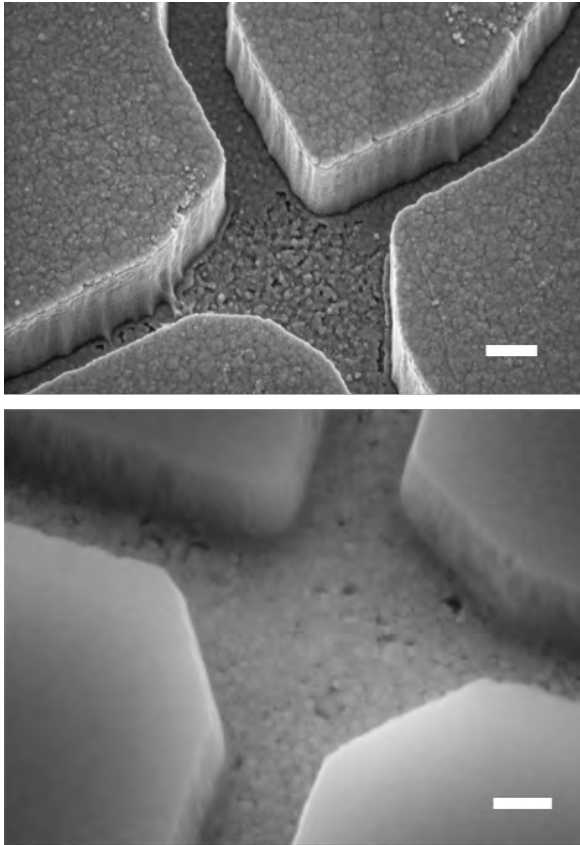


**Fig. 7: Smoothness of channel sidewalls.** (top) Rough SiO<sub>2</sub> sidewalls and Au channel bottom using PMMA for patterning. (bottom) Smooth channel surface using Cr as hard mask for SiO<sub>2</sub> patterning and as adhesion layer. The scale bar is 200 nm in both images.

Furthermore, two different adhesion layers (Titanium and Chromium) were investigated regarding their plasma etch durability and their selectivity against gold and SiO<sub>2</sub>. The Titanium adhesion layer was used in previous experiments for the fabrication of biocomputational networks [4]. However, during our investigation, the Ti was already attacked during the plasma etching of the SiO<sub>2</sub>, so that during the removal of this layer, the buried Au layer degraded resulting in an increase in surface roughness and deposition of the sputtered Au at the SiO<sub>2</sub> sidewalls (see fig. 8).

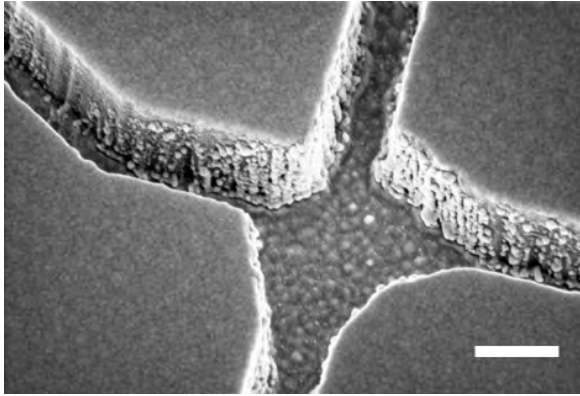


**Fig. 8: Surface roughness.** Scanning electron micrograph of a nanochannel with Au redeposited during the plasma etching at the SiO<sub>2</sub>-sidewalls

To increase the reliability and the yield of the network structures, Cr has been used as adhesion layer. This layer protects the Au surface during the SiO<sub>2</sub> etch and can be removed without leaving residues behind by an O<sub>2</sub>-dry etch process.

Functionalization tests with the cytoskeletal filaments moving through the network showed that samples with the Ti adhesion layer performed worse in the end due to the increased surface roughness of the Au layer rendering it unsuitable for biocomputing.

Another challenge was the ratio of large structures (landing zones) to small structures (network channels) (see Fig. 3 left) during the dry etch processes. The opening ratio of the areas influences the homogeneity and rate during the plasma etching critically. Due to the good selectivity of the Cr adhesion layer, longer etching times became possible without risking surface degradation of the underlying Au layer.

The channel width plays an important role for the motility and the behavior of the agents at the junctions, therefore the process-related broadening of the channel width during SiO<sub>2</sub> plasma etching was investigated. Seven network-structures were fabricated having the same overall layout but with different channel widths ranging from 200 nm up to 500 nm. Subsequently the channel widths of the different structures (rectifiers, split and pass-junctions) were analyzed using a scanning electron microscope (JSM 7800F) (see Fig. 9 right).

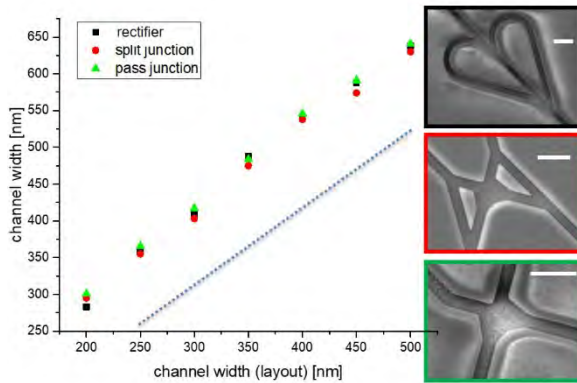


**Fig. 9: Size accuracy of nanofabrication.** Comparison of the channel broadening during SiO<sub>2</sub> plasma etch. The scale bar is 1 μm in all images.

The measurements in figure 9 reveal a linear dependence between the designed width and the resultant structure width at the end of the fabrication process. This finding enabled us to easily scale the designs to the channel sizes necessary to achieve good motility of the cytoskeletal filaments.

The biocomputational network for kinesin-microtubule motility encodes one particular four-variable instance of the SSP  $\{10, 6, 5, 3\}$ . The network was fabricated using the optimized technology and patterning parameters described in the experimental section. Observing microtubules exiting at the first 16 exits of the network (fitting into one field-of-view of our microscope), showed that significantly more microtubules exited at correct solutions than at incorrect solutions (Fig. 10). Thus, we were able to solve the specific instance  $\{10, 6, 5, 3\}$  of the SSP with twice as many possible solutions compared to [4], using electron beam lithography combined with the biomolecular motor kinesin-1 and their associated cytoskeletal filaments microtubules. Please note that almost all errors (filaments exiting at incorrect exits) result from microtubules that landed in the channels and not from microtubules that made a calculation error. In future devices, we will eliminate this source of error using microfluidic focusing to ensure that microtubules can land only in the loading zones of the device and not in the channels of the network.

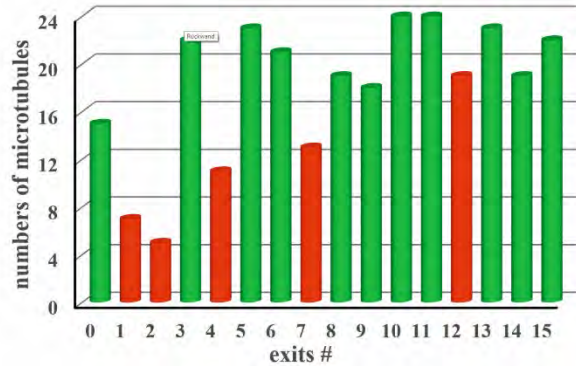
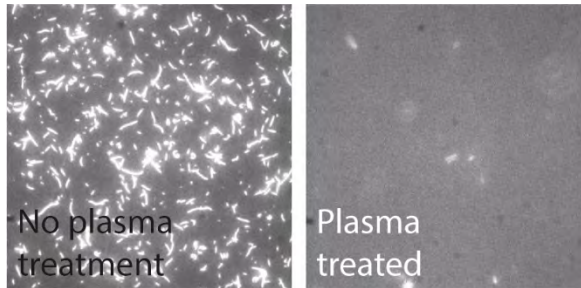


Fig. 10: **Result.** Results of microtubules exploring a {10, 6, 5, 3} SSP network

### B. Actin-myosin system

Early proof-of-principle networks for the actin-myosin system were relatively inexpensive to fabricate due to their size [4]. However, the increased dimensions associated with upscaling quickly makes fabricating these structures infeasible without process optimisation for high throughput. These earlier networks were patterned by electron beam lithography (EBL) in poly(methyl methacrylate) (PMMA) resist. PMMA requires high beam doses, whereas newer resists, such as CSAR62 (AllResist GmbH, Strausberg, Germany) can provide a better contrast and resolution at much lower doses, provided a suitable developer is selected.

As the overall device relies on biological function, it is critical that the polymer used is non-toxic for the particular protein system in use. Furthermore, the polymer also needs to inhibit myosin-binding to prevent motility on the channel walls. We performed *in vitro* motility assays on CSAR62 surfaces and observed good motility, comparable to that on TMCS-derivatized SiO<sub>2</sub> [13]. By treating a CSAR62 polymer surface with oxygen plasma, we were able to completely suppress the actin filament motility, see figure 11. These effects in combination make CSAR62 structures suitable for the actin-myosin system.



**Fig. 11: Filaments on ARP.** Fluorescence micrographs. The high motility on CSAR 62 suggests the resist is non-toxic for the actin-myosin system. By plasma treatment of the resist, the motility can be completely suppressed.

In order to determine the requirements for CSAR 62 patterning, four different EBL doses were tested; 30, 40, 50, 60  $\mu\text{C}/\text{cm}^2$ , with acceleration voltage 20 kV. All structures were developed in O-xylene and we found that it was not possible to achieve complete structures with a dose lower than 60  $\mu\text{C}/\text{cm}^2$  in our Raith 150 EBL system, see figure 12. Structures exposed at 60  $\mu\text{C}/\text{cm}^2$  instead of the 250  $\mu\text{C}/\text{cm}^2$  required by PMMA can be made roughly four times larger in the same amount of time.

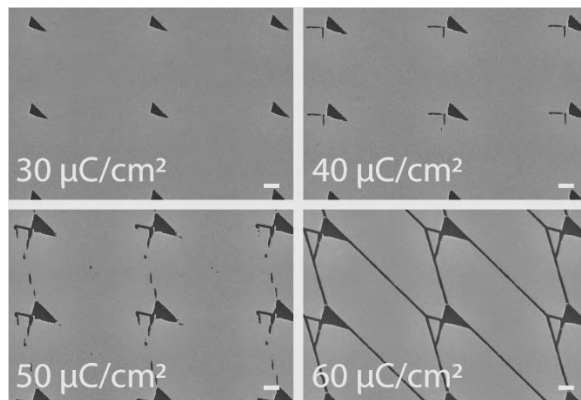


**Fig. 12: DoseTest.** Scanning electron micrograph of dose tests in CSAR62 resist. The scalebar is 1  $\mu\text{m}$  in all images.

Furthermore, we found that the exposed areas did not fully replicate the pattern design. This effect was found to be related to the orientation of the pattern (type 1) with respect to the electron beam raster. To resolve this issue, we redesigned the pattern (type 2) as shown in figure 13, and it now correctly exposes the pattern in any orientation. All structures have been exposed with a dose of 60  $\mu\text{C}/\text{cm}^2$  using a Raith 150 EBL at 20 kV acceleration voltage.

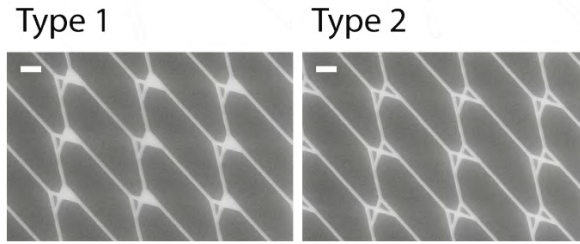


**Fig. 13: Pattern test.** Scanning electron micrographs of two types of pattern designs. Pattern type 1 did not replicate the pattern design due to the orientation of the electron beam raster. By redesigning the pattern, type 2, we were able to correctly replicate the pattern.

To enhance the patterning speed further, the aperture size of exposure was increased from 10  $\mu\text{m}$  diameter [4] to 20  $\mu\text{m}$  at 20 kV acceleration voltage. This increased the beam current from 0.014 nA to around 0.12 nA increasing exposure throughput by a factor 8.5. Figure 13 was exposed with a 20  $\mu\text{m}$  aperture with no noticeable loss of feature detail. No U-turns were observed during actin filament motion through nanochannels exposed with this aperture size (see video in supporting information). A stack of the maximum intensity can be seen in figure 14 for the structures exposed at 10  $\mu\text{m}$  and 20  $\mu\text{m}$ .

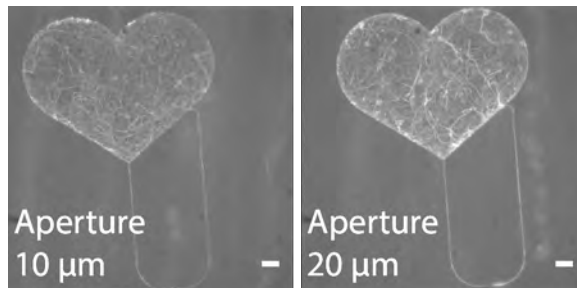


**Fig. 14: Aperture diameters used for exposure.** Fluorescence micrographs showing the maximum intensity for a 60 s time-lapse movie of an actin-myosin in vitro motility assay experiment with structures exposed with two different electron beam apertures, 10 and 20  $\mu\text{m}$ . The scale bar is 5  $\mu\text{m}$  in both images.

To further enhance speed, the patterning process was adapted to a Voyager EBL (Raith GmbH, Dortmund, Germany) with a 50 kV acceleration voltage and a 40  $\mu\text{m}$  diameter aperture. This resulted in a beam current of  $\sim 0.55$  nA and an even higher throughput increase. Even at these high speeds, well defined features were achieved, see figure 15.

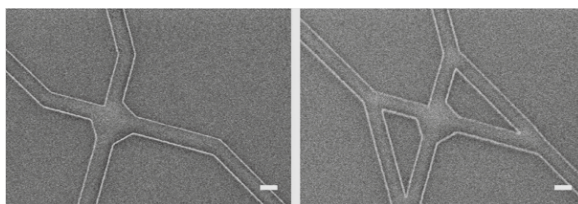


**Fig. 15: SEM micrographs of the junctions.** The images showing well preserved features even at higher electron beam exposure currents, here 0.55 nA using a 40  $\mu\text{m}$  aperture and 50 kV acceleration voltage.

Initial testing of the biocomputational networks for actin filaments have begun. Further optimizing is required to improve the longevity and number of filaments exploring the network to ensure enough filaments can reach all exits.

## Acknowledgments

This project has received funding from the European Union's Horizon 2020 research and innovation programme under grant agreement No 732482 (Bio4Comp).

## References

1. M. Scudellari, Proc. Natl. Acad. Sci. USA 2015, 112, no. 52, pp. 15771–15772)
2. T. D. Ladd, F. Jelezko, R. Laflamme, Y. Nakamura, C. Monroe, J. L. O'Brien, Nature 2010, 464, 45–53
3. M. Silvano, T. Paolo: "4 Subset-sum problem". Knapsack problems: Algorithms and computer interpretations. Wiley-Interscience 1990. pp. 105–136
4. D. V. Nicolau, Jr., M. Lard, T. Korten, F. C. van Delft, M. Persson, E. Bengtsson, A. Mansson, S. Diez, H. Linke, D. V. Nicolau, Proc. Natl. Acad. Sci. USA 2016, vol. 113, no. 10, pp. 2591-2596
5. J. Clemmens, H. Hess, R. Lipscomb, Y. Hanein, K. F. Boehringer, C. M. Matzke, et al.: Mechanisms of microtubule guiding on microfabricated kinesin-coated surfaces: chemical and topographic surface patterns. Langmuir 2003;19:10967–74.
6. M. Sundberg, R. Bunk, N. Albet-Torres, A Kvennefors, F. Persson, L. Montelius, et al.: Actin filament guidance on a chip: toward high-throughput assays and lab-on-a-chip applications. Langmuir 2006; 22:7286–95.
7. J. Howard, A. J. Hudspeth, R. D. Vale: Movement of microtubules by single kinesin molecules. Nature 1989;342:154–8.].
8. T. Q. P. Uyeda, S. J. Kron, J. A. Spudich: Myosin step size: estimation from slow sliding movement of actin over low densities of heavy meromyosin. J Mol Biol 1990;214:699–710.

9. B. Nitzsche V. Bormuth, C. Bräuer, J. Howard, L. Ionov, J. Kerssemakers, T. Korten, C. Leduc, F. Ruhnnow, *St Diez. Methods Cell Biology* vol. 95, 2010, p. 247–271
10. M. G. L. van den Heuvel, C. T. Butcher, R. M. M. Smeets, St. Diez, C. Dekker. *Nano Lett* 5(6):1117–1122, 2005] that was upgraded for motility in nanochannels
11. T. Korten, S. Chaudhuri, E. Tavkin, M. Braun, S. Diez, *IEEE Transactions on NanoBioscience* 2016, vol. 15, pp. 62-69.
12. M. Castoldi, A. V. Popov, *Protein Expression and Purification* 2003, 32, 83-88
13. F. W. Lindberg, M. Norrby, M. A. Rahman, A. Salhotra, H. Takatsuki, S. Jeppesen, H. Linke and A. Månsson: Controlled Surface Silanization for Actin-Myosin and Biocompatibility of New Polymer Resists. *Langmuir* 34, 8777-8784, (2018)
14. M. Persson, M. Gullberg, C. Tolf, A. M. Lindberg, A. Månsson, A. Kocer: Transportation of Nanoscale Cargoes by Myosin Propelled Actin Filaments. *PLoS One* 2013, 8 (2), e55931,
15. W. S. Rasband: ImageJ, U.S. National Institutes of Health, Bethesda, Maryland, USA, <http://imagej.nih.gov/ij/>, 1997–2012
16. R. Bunk, M. Sundberg, A. Månsson, I.A. Nicholls, P. Omling, S. Tågerud, L. Montelius, *Nanotechnology* 16 (2005) 710.
17. Y. Hiratsuka, T. Tada, K. Oiwa, T. Kanayama, T.Q.P. Uyeda, *Biophys. J.* 81 (2001) 1555

Paper IV





# Regeneration of assembled, molecular-motor-based bionanodevices

Mohammad A Rahman<sup>1,2</sup>, Cordula Reuther<sup>3,4</sup>, Frida W. Lindberg<sup>2,5</sup>, Martina Mengoni<sup>3,4</sup>, Heiner Linke<sup>2,5</sup>, Stefan Diez<sup>3,4</sup>, Alf Månsson<sup>1,2</sup>

## Affiliations:

1 Department of Chemistry and Biomedical Sciences, Linnaeus University, Kalmar, Sweden

2 NanoLund, Lund University, Lund, Sweden

3 B CUBE - Centre for Molecular Bioengineering, Technische Universität Dresden, Dresden, Germany.

4 Max Planck Institute of Molecular Cell Biology and Genetics, Dresden Germany.

5 Division of Solid State Physics, Lund University, Lund, Sweden

**Keywords:** Nanodevice regeneration, protein desorption, molecular motor based nanodevice, proteinase K, motility for nanotechnology, CSAR62 polymer resist.

## Abstract

Biomolecular motors (myosin, kinesin etc.) have been exploited for nanotechnological applications, e.g. in biosensing and biocomputation, where the motor-propelled filaments are guided along nanofabricated structures. Because the nanostructured chips are expensive and time consuming to produce it is crucial to develop a method that will allow repeated use without destroying the nanostructures or disturbing the surface chemistry. To that end, we here report a method with the potential to regenerate biomolecular motor-based nanodevices, enabling the re-use of the nanostructured chips and the associated fluidics system by addition of fresh proteins. We have used a small nonselective proteolytic enzyme, proteinase K (200 µg/ml), to cleave the surface adsorbed motor proteins (e.g. myosin II or kinesin-1) followed by a short treatment with SDS (5%) or Triton X100 (0.05%). This method was equally successful in regenerating trimethylchlorosilane-derivatized glass surfaces for actin-myosin motility and glass surfaces for microtubule-kinesin motility. We were able to regenerate both glass, trimethylchlorosilane derivatized glass and SiO<sub>2</sub> chips at least three times without any decrease in performance over time. Additionally, we found that polyethylene glycol derivatized glass/SiO<sub>2</sub> and

CSAR62 polymer resists on SiO<sub>2</sub>, used for motility inhibiting surface areas with microtubule-kinesin and actin-myosin, respectively, did not lose their motility inhibiting properties through the treatment. Furthermore, we observed regeneration of nanostructured surfaces: (a) trimethylchlorosilane derivatized SiO<sub>2</sub> chips surrounded by CSAR62, for actomyosin motility and (b) gold coated chips surrounded by polyethylene glycol derivatized SiO<sub>2</sub>, for kinesin-microtubule motility. This demonstrates the versatility of this regeneration method for several molecular motor-based systems. Thus, we also expect the method to be useful for regenerating nanodevices for other protein systems adsorbed to surfaces for various nanotechnological applications, e.g. in biosensing.

## Introduction

Protein adsorption to surfaces is a ubiquitous and extremely important phenomenon (Hlady and Buijs, 1996; Nakanishi, Sakiyama and Imamura, 2001; Kasemo, 2002; Rabe, Verdes and Seeger, 2011). Whereas it may be unwanted in several instances, it has also been widely exploited in biotechnology as well as in fundamental biophysical and biochemical investigations (Castner and Ratner, 2002). For instance, antibodies or other protein-based recognition molecules are adsorbed to detector surfaces in biosensing (Hock, Seifert and Kramer, 2002; Frasconi, Mazzei and Ferri, 2010; Arlett, Myers and Roukes, 2011; Kumar *et al.*, 2013; Sharma, Byrne and O’Kennedy, 2016) and proteomic (Dodo *et al.*, 2013; Sugimoto *et al.*, 2016) applications. In addition, fundamental functional studies may involve surface adsorbed receptors and other protein nanomachines (Wong *et al.*, 1997; Xu, Bauer and Siedlecki, 2014; Bell and Terentjev, 2017). One widely used assay of the latter type is the *in vitro* motility assay. In the gliding *in vitro* motility assay (Kron and Spudich, 1986), biomolecular motors isolated from cells, are adsorbed onto a surface enabling propulsion of fluorescently labelled cytoskeletal filaments that can be observed in fluorescence microscopes. Two commonly studied systems are the actin filaments propelled by myosin motors (Kron and Spudich, 1986; Harada *et al.*, 1987; Winkelmann *et al.*, 1995; Månsson *et al.*, 2008) and microtubules propelled by kinesin (Howard, Hudspeth and Vale, 1989) or dynein motors. These motor systems are responsible for cell motility (including muscle contraction) and intracellular cargo transport. The modified version of this assay may also be applied to non-cytoskeletal motors such as processive DNA enzymes (Wang *et al.* 1998; Mehta and Spudich 1998). The *in vitro* motility assay has enabled a variety of nanotechnological applications, e.g. in nanoseparation and biosensing (Bachand *et al.*, 2006; Korten, Månsson and Diez, 2010; Hess, 2011; Kumar *et al.*, 2012, 2013, 2016; Korten *et al.*, 2016; Kumar and Mansson, 2017) as well as more recently, parallel biocomputation (Nicolau *et al.*, 2016). Many of these applications require networks of nanochannels for filament transport, which involve different surface

materials and chemistry. It is also expected that these devices will be advanced further, e.g. by integrating (opto)- electronic components for automated read-out of filament positions, velocities etc.

The nanostructures used for molecular motor-based devices are expensive and time consuming to fabricate. Therefore, it is highly desirable to develop methods that enable effective regeneration and re-use of these nanostructures. In this process, all aged non-functional proteins are ideally replaced with freshly added functional proteins without having to disassemble the chip from its fluidic system. At the same time, it is also important that the surface regeneration is achieved without destroying the nanostructures or nanoelectronic components. Ideally, the process also preserves the motility-contrast between the nanofabricated channel floors and surrounding walls related to different surface chemistries (Månsson, 2012).

In previous efforts to regenerate surfaces, e.g., for biosensor use, a range of different approaches were attempted. These include rather gentle methods such as incubation with high ionic strength solutions (Radi *et al.*, 2005) and detergent (Andersson, Hämäläinen and Malmqvist, 1999; Albrecht, Kaepfel and Gauglitz, 2008; Mattos *et al.*, 2012), a combination of detergents and acids (Andersson, Hämäläinen and Malmqvist, 1999) as well as cleaning followed by overnight incubation with water (Sankiewicz, Tokarzewicz and Gorodkiewicz, 2015). However, the attempts also include harsher methods such as treating the surfaces with highly concentrated acid or oxygen plasma (Kumar Dixit, 2014). Whereas gentle methods may not be effective in removing the aged proteins, harsher methods may alter the surface chemistry as well as the physical properties of the nanostructures and electronic components. Moreover, some of the procedures (such as oxygen plasma treatment or overnight incubation with water) may require the disassembling of the biosensor device before and its reassembling after regeneration. These approaches are not suitable for miniaturized chips with critical nanostructures.

The aim of this work was to develop a suitable method for regenerating assembled, molecular motor-based bionanodevices while keeping the surface chemistry and embedded nanostructures intact. We hypothesized that either 1) surface treatment with a suitable detergent or buffer, 2) proteolysis of the molecular motors on the surface with an unspecific protease or 3) a combined treatment with protease and detergent would desorb the molecular motors and other proteins from the surface and thus, allow full surface regeneration by incubation with fresh motors. Finally, we hypothesized that these treatments would be gentle enough to preserve the critical surface properties and nanostructures without dissemblance of the chip-fluidic systems. Following extensive initial trials, we selected the detergents Sodium dodecyl sulfate (SDS) and Triton X100 as detergents as well as a quite extensively characterized (Betzler, Pal & Saenger, 1988; Petsch, Deckwer, & Anspach, 1998) nonspecific protease, 'proteinase K', for testing of our hypotheses (see further

below). Our results suggest that a combined treatment with Protease K and SDS or Triton X100 gives optimal regeneration of the surfaces in the sense that it allows their re-use for adsorption of fully functional motor proteins of general applicability both to the actin-myosin and microtubule-kinesin motor systems. Furthermore, our results suggest that regeneration is achievable without modifying the selective surface chemistry and nanostructures. The possible extension of the regeneration method to a range of non-motor applications is discussed in view of the broad importance of protein adsorption in diverse fields.

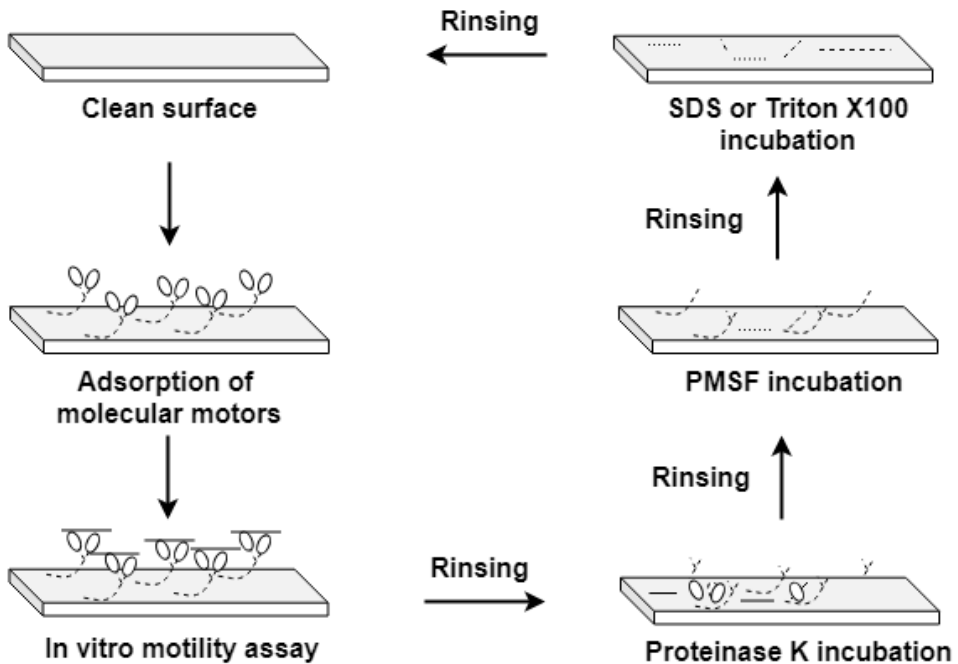


**Figure 1.** Schematic illustration of the method for regeneration of molecular motor-based bionanodevices.

## Materials and Methods

### *Ethical statement*

Rabbits for myosin and actin preparations were kept and sacrificed according to instructions approved by the Regional Ethical Committee for Animal experiments in Linköping, Sweden, reference number 73-14.

### *Materials*

Proteinase K from *Tritirachium album* was purchased from Sigma Aldrich (cat. no. P6556), diluted in dH<sub>2</sub>O (1 mg/ml), aliquoted and stored at -20°C. Rhodamine Phalloidin was obtained from Thermo Fisher Scientific (cat. no. R415). Dithiothreitol (DTT) was purchased from Sigma Aldrich (actin-myosin study) and Fermentas (microtubule-kinesin study). Adenosine triphosphate (ATP) is either from Sigma Aldrich (actin-myosin study) or from Roche (microtubule-kinesin study). MgCl<sub>2</sub> is either from Fisher Bioreagents (actin-myosin study) or from VWR (microtubule-kinesin study). KOH is either from Sigma Aldrich (actin-myosin study) or from Merck (microtubule-kinesin study). Sodium dodecyl sulfate (SDS) is either from Sigma Aldrich (actin-myosin study) or from VWR (microtubule-kinesin study). Other biochemical and reagents were of analytical and/or biotechnology grade and purchased from Sigma Aldrich.

### *Buffers and solutions*

Actin and myosin: A low ionic strength solution (Buffer A; pH 7.4) was composed of 10 mM 3-(N-morpholino)propanesulfonic acid (MOPS), 1 mM MgCl<sub>2</sub>, 0.1 mM Potassium Ethylene glycol-bis(β-aminoethyl ether)-N,N,N',N'-tetraacetic acid (K<sub>2</sub>EGTA). Assay solution (Buffer B) for gliding *in vitro* motility assays was prepared in Buffer A with 10 mM DTT, 45 mM KCl, 3 mg/ml glucose, 0.1 mg/ml glucose oxidase, 0.02 mg/ml catalase, 2.5 mM creatine phosphate, 0.2 mg/ml creatine phosphokinase and 1 mM MgATP. Wash Buffer (Buffer C) was prepared with 50 mM KCl and 1 mM DTT in Buffer A. Proteinase K and SDS were dissolved in dH<sub>2</sub>O. Phenylmethanesulfonyl fluoride (PMSF) stock (usually 200-400 mM) was prepared in 99.7% Ethanol and further diluted (5 mM) in dH<sub>2</sub>O just before use.

Microtubule and kinesin: All solutions for the gliding *in vitro* motility assays were prepared in Brinkley Reassembly Buffer 80 mM (BRB80) (Buffer D; pH 6.9) that was composed of 80 mM 1,4-piperazinediethanesulfonic acid (PIPES), 1 mM EGTA, 1 mM MgCl<sub>2</sub>. The motor buffer (Buffer E) contained 0.2 mg/ml casein, 1 mM ATP and 10 mM DTT in buffer D. The assay buffer (Buffer F) was prepared with 10 μM Taxol, 1 mM ATP, 40 mM D-glucose, 55 μg/ml glucose oxidase, 11 mg/ml catalase and 10 mM DTT in buffer D.

### *Protein preparations*

Actin and myosin: Actin and myosin were prepared from fast skeletal muscle of New Zealand white rabbits immediately after sacrifice according to ethical approval (see above). Actin was prepared as described earlier (Pardee and Spudich, 1982; Kron *et al.*, 1991). Myosin and heavy meromyosin (HMM) were prepared following a previously published protocol ((Margossian and Lowey, 1982), with modifications in (Kron *et al.*, 1991; Sata *et al.*, 1993)). Protein preparations were characterized by

sodium dodecyl sulfate polyacrylamide gel electrophoresis, as described previously (Rahman *et al.*, 2018).

**Microtubule and kinesin:** Microtubules were polymerized from 5  $\mu$ L rhodamine-labeled porcine brain tubulin in buffer D with 5 mM  $MgCl_2$ , 1 mM GTP, 5 % Dimethyl Sulfoxide (DMSO) at 37°C for 30 min. The microtubules were stabilized and diluted 60-fold in BRB80 containing 10  $\mu$ M Taxol. Full-length *Drosophila melanogaster* kinesin-1 molecules were expressed in insect cells and purified as described earlier (Korten *et al.*, 2016).

### *Surface preparation*

**Actin and myosin:** For *in vitro* motility assays with actin and myosin, glass coverslips (for control assays) were derivatized with trimethylchlorosilane (TMCS) as described earlier (Sundberg *et al.*, 2003; Albet-Torres *et al.*, 2007).

All partially patterned electron beam resist (CSAR62) coated  $SiO_2$  surfaces were fabricated on 10x10 mm Si(100) substrates with a 70 nm thick  $SiO_2$  layer deposited by atomic layer deposition (ALD). The chips were sonicated in acetone (VWR, Radnor, PA, USA) and isopropanol (VWR, Radnor, PA, USA) for 3 min each, prior to spin-coating a layer of CSAR62 (Allresist, Strausberg, Germany) dissolved to 9% in Anisole (VWR, Radnor, PA, USA) at 3000 rpm for 30 s. A thin strip of polydimethylsiloxane (PDMS) was placed in the center of the chip which was then spin-cleaned at 6000 rpm using S1165 (Sigma Aldrich, Saint Louis, MO, USA), acetone and isopropanol and dried under nitrogen flow. After drying, the PDMS strip was removed and the chip was baked on a hot-plate at 180°C for 2 min. The chips were treated with oxygen plasma at 5 mbar for 15 s and silanized with TMCS for 64 min at 200 mbar, as previously described (Lindberg *et al.*, 2018).

The nanostructured surfaces were made on 10x10 mm<sup>2</sup> Si(100) substrates with a 75 nm thick  $SiO_2$  layer grown by dry thermal oxidation. The chips were cleaned as described in the previous section and spin-coated with CSAR62 dissolved to 13% in Anisole at 5000 rpm for 30 s and baked on a hot-plate at 180°C for 2 min. Following baking, the polymer resist was patterned by electron beam lithography (Voyager, Raith GmbH, Dortmund GmbH) at 50 kV acceleration voltage, beam current  $\sim$ 0.55 nA and 250  $\mu$ C/cm<sup>2</sup> dose. The exposed polymer was developed in amyl acetate (Sigma Aldrich, Saint Louis, MO, USA) for 90 s, rinsed in isopropanol and dried under nitrogen flow. These chips were also treated with oxygen plasma at 5 mbar for 15 s and silanized with TMCS for 64 min at 200 mbar (Lindberg *et al.*, 2018).

**Microtubule and kinesin:** For kinesin-microtubule motility assays, glass coverslips (22 x 22 mm<sup>2</sup>, Corning) (for control assays) were cleaned by sonication in Mucosal/water (1 : 20; v=v) for 15 min followed by rinsing in deionized water for 2 min. In addition, coverslips were sonicated in ethanol/water (1:1; v=v) for 10 min

followed by rinsing in deionized water and MilliQ-water (2 min each) and finally dried using a nitrogen airflow.

The nanostructured devices for microtubule-kinesin motility assays were prepared as described earlier (van den Heuvel *et al.*, 2005). They consisted of an Au floor coated with kinesin-1 and 500 nm high SiO<sub>2</sub> walls that were coated with poly(ethyleneoxy)-silane (PEG-silane) to prevent binding of motor proteins. Briefly, a Si-wafer was sputter-deposited with 100 nm-thick Au, sandwiched between two 10nm-thick Cr adhesion layers. Next, a 500nm-thick quartz layer was deposited, followed by a resist layer. After exposure in an e-beam lithography system, the resist was developed and the quartz layer was dry-etched down to the Au layer. Afterwards, chips were cleaned for 10 min in acetone and rinsed with ethanol and nanopure water. The SiO<sub>2</sub> was PEGylated for 16 h using 2.4 mg/ml 2-[Methoxy(polyethyleneoxy) propyl]trimethoxysilane, (PEG-silane; 90%; ABCR, SIM4492.7) in Toluene-HCl. Finally, the chips were rinsed in Toluene, Ethanol and nanopure water.

#### *In vitro motility assays and recording*

**Actin and myosin:** The experiments were performed using flow-cells assembled with the TMCS derivatized glass coverslip (24 x 60 mm<sup>2</sup>) for the floor and untreated glass coverslip (18 x 18 mm<sup>2</sup>) for the ceiling of the cell, spaced with double-sided tape. For *in vitro* motility assays (Persson *et al.*, 2013; Rahman, Salhotra and Månsson, 2019), flow cells were incubated with HMM (120 µg/ml; 5 min) and then with Bovine Serum Albumin (BSA) (1mg/ml; 2 min), both in buffer C. Subsequently, the flow cells were rinsed with buffer C, incubated with 2-10 nM rhodamine-phalloidin labeled actin filaments and rinsed again with buffer C, prior to addition of the assay solution (buffer B). Image acquisition was performed using an inverted fluorescence microscope either from Nikon (Nikon TE300, Nikon corporation with a 100x objective, NA =1.4) or Zeiss (Axio Observer.D1, Zeiss, Germany, with a 63x objective, NA=1.4). For excitation, a Mercury short-arc lamp (OSRAM GmbH) was used together with suitable filter sets, allowing observation of rhodamine fluorescence. Image sequences were recorded using an electron multiplying charge-coupled device (EMCCD) camera (C9100-12PHX1, Hamamatsu Photonics) with pixel size (on sample) of 0.16x0.16 µm<sup>2</sup> and 0.24x0.24 µm<sup>2</sup> for 100x and 63x objective, respectively. The actin filament movements were recorded using a frame rate in the range 4-10 frames/second. Actin filament sliding velocities were calculated as described earlier (Månsson and Tågerud, 2003; Rahman *et al.*, 2018). The cut-off of the coefficient of variation (CV) (standard deviation of frame-to-frame velocity divided by average velocity in ten frames) for data inclusion in velocity analysis was set to ≤0.2.

**Microtubule and kinesin:** The experiments were performed in 3-mm-wide flow-cells. Flow cells of planar surfaces were assembled from a cleaned glass coverslip

(22 x 22 mm<sup>2</sup>) for the bottom, a (18 x 18 mm<sup>2</sup>) PEGylated coverslip (Papra, Gadegaard and Larsen, 2001) for the top, and two stripes of parafilm as spacers. For nanostructured devices, flow cells consisted of a (22 x 22 mm<sup>2</sup>) PEGylated coverslip for the bottom, the silicon wafer for the top, and two stripes of parafilm as spacers. Buffer D, containing 0.5 mg/ml casein, was perfused into the flow-cell and allowed to adsorb to the surface for 5 min. This solution was exchanged for a 10 µg/ml kinesin-1 solution in motor buffer and incubated for 5 min. Assay buffer (buffer F) containing 580 nM microtubules was added to the flow-cell. Image acquisition was performed using an inverted fluorescence microscope Zeiss Axiovert 200M (Zeiss, Germany) with a 100x oil immersion objective Plan-Neofluar NA = 1.3 (Zeiss, Germany) and an objective heater set to 27°C (for planar surfaces) and a 40x air objective Plan-Apochromat NA = 0.95 (Zeiss, Germany) (for nanostructured surfaces). For excitation a Lumen 200 metal arc lamp (Prior Scientific Instruments, USA) was applied. The data was recorded with an electron multiplying charge-coupled device (EMCCD) camera (iXon + EMCCD, DU-897E, Andor) having a pixel size of 16 µm. If not stated differently, images were acquired every 2 s with an exposure time of 100 ms using MetaMorph (Molecular Devices, USA). Microtubule gliding velocities were evaluated using a MATLAB-based tracking algorithm developed in-house and was described earlier in detail (Korten *et al.*, 2018).

### *Surface regeneration*

After performing an *in vitro* motility assay, the flow cell was rinsed three times with wash buffer (buffer C or D) followed by rinsing with dH<sub>2</sub>O. In the final optimized protocol, proteinase K was diluted in dH<sub>2</sub>O to 200 µg/ml and activated with 5 mM CaCl<sub>2</sub> at 37°C for 10 minutes, before being added to the flow cell and incubated for 1 hour at 37°C with gentle shaking. After the proteinase K treatment, all following steps were performed at room temperature (RT). Next, the flow cell was rinsed three times with dH<sub>2</sub>O followed by incubation with a PMSF-containing solution (5 mM) for 5 minutes. Finally, the flow cell was washed with dH<sub>2</sub>O (3x) and incubated with SDS (5 %) or Triton X100 (0.05%) for 5 minutes. To remove the SDS or Triton X100, the flow cell was rinsed 10 times with dH<sub>2</sub>O and then three times with wash buffer. In order to perform a new *in vitro* motility assay, fresh proteins (HMM and actin; see above) were added.

## **Results and discussions**

For the initial developments of an effective surface regeneration procedure, we predominantly used the actin–myosin motor system (Table S1; Figs. S1-S3). The initial studies involved tests of regeneration using only proteinase K (Fig. S2) or different detergents (Fig. S1, Table S1), as well as tests with varied incubation times

and concentrations of the different detergents (Fig. S1). The detergents are expected to weaken the hydrophobic interactions that are assumed to be central for the unspecific surface adsorption of HMM and several other proteins (Toyoshima, 1993), which suggests that they would be useful in a surface regeneration procedure.

Proteolytic enzymes, on the other hand, may be useful by appreciably lowering the local protein concentration through proteolysis followed by diffusional removal of the peptide fragments. We selected proteinase K as proteolytic enzyme for several reasons: (1) It has a high activity and (2) it is a non-selective (Betz et al., 1988) protease, attacking peptide bonds between several different amino acids. (3) It is a small protein (28.5 kDa) that limits steric hindrance of enzymatic attacks close to surface-adsorbed parts of a molecular motor within dense protein layers (Betz et al., 1988). (4) It has a high conformational stability (Bajorath, Hinrichs, Saenger, 1988) which is likely to limit its own surface-adsorption and associated inactivation. Finally, (5) proteinase K is well documented to cleave actin (Higashi-Fujime *et al.*, 1992) and is used in biotechnological applications such as nucleic acid isolation and cell lysis studies (Goldenberger *et al.*, 1995). We added proteinase K at a concentration of 200  $\mu\text{g/ml}$ , which is in the high range of the supplier's recommendation (50-200  $\mu\text{g/ml}$ ) for nucleic acid preparations (Sigma Aldrich), but lower than the concentration (400  $\mu\text{g/ml}$ ) in a study (Petsch *et al.* 1998) where proteinase K was used to remove endotoxin from cationic proteins. Incubation times between 30 min and 18 h were suggested by the manufacturer, but in earlier papers even longer times (30 h) were applied.

We tested different incubation times with proteinase K (Fig. S2), however, all led to only partial regeneration, characterized by lower actin-sliding velocity after the regeneration procedure). Based on a hypothesis that there might be some motor fragments left after proteolysis that prevent saturation of the surface with newly adsorbed motors, we added a brief SDS incubation step following the proteolysis to remove these remnants. Based on tests of different SDS concentrations (Fig. S3), we found that treatment with 5% SDS seemed optimal. Therefore, we decided on a standard, optimized, regeneration protocol (Fig. 1) where 1 h proteinase K treatment (200  $\mu\text{g/ml}$ ) is followed by 5 min treatment with SDS (5%).

This protocol (Fig. 1) was then applied to actin-myosin and microtubule-kinesin *in vitro* motility assays for quantitatively evaluating its performance on various substrate materials as well as chemically and topographically structured surfaces.

On standard surface substrates (TMCS derivatized glass and  $\text{SiO}_2$  chips for actin-myosin, and glass for microtubule-kinesin), we found that the test motility function (sliding velocity, fraction of motile filaments, and length of filaments) after regeneration was fully restored compared to the control, both for actin-myosin and microtubule-kinesin (Fig. 2 and 3).

We have found that, actin filament gliding was similar both before (control) and after the regeneration (Fig. 2a-d). Moreover, the fraction of motile filaments was not decreased on the regenerated surfaces (Fig. S3b). If the regeneration with the optimized protocol would not have effectively removed all surface-adsorbed proteins, one would see more stuck filaments because of the interaction between actin and denatured proteins or protein fragments on the surface. In addition, the average length of the paths travelled by the filaments would be shorter. Therefore, our results (Fig. 2a-d and S3b) suggests that the regeneration procedure with proteinase K (1h) and 5% SDS (5 min) effectively cleans the surfaces. The motor density is another important consideration for the *in vitro* motility assay, since the actin sliding velocity is lower at a reduced motor density on a surface. Moreover, in such a condition, one would expect to observe appreciably longer filaments because of reduction in breakdown by reduced number of myosin heads. Our results show that the actin filament length distribution (Fig. 3a) is similar both before and after regeneration. Furthermore, the actin-sliding velocity was not reduced after the regeneration (Fig. 3b). The differences in velocities on control surfaces in Figure 3b are due to the experiments being performed at different temperatures, in the range 20.6-25.4°C. However, these observations (Fig. 3) are consistent with the idea that the motor density was not reduced after the regeneration. Moreover, previous studies suggest that, actin sliding velocity is reduced when the surface chemistry is altered, for example at lower surface contact angles, because of an altered myosin binding pattern. Therefore, we argue that the surface regeneration process did not change the surface chemistry as we did not observe lower velocity after recycling of the surface.

After regenerating the flow channel and adsorbing new kinesin-1 molecules, microtubules moved smoothly and the fraction of stuck filaments did not increase (Table S2; Fig. S4). A comparison of a typical gliding assay before and after regeneration is shown in Figure 2e-h (and Supplementary movies). The microtubule length distribution is dependent on the actual population, especially the length of the shortest filaments able to move on a surface which is regulated by the active kinesin-1 density. Because the distributions before (control) and after the regeneration are comparable with respect to the shorter filaments (Fig. 3c) we can conclude that also a high motor density is achieved after regenerating the surface. The microtubule gliding velocities, which are independent of the kinesin-1 density on the surface, also remained nearly constant (Fig. 3d).

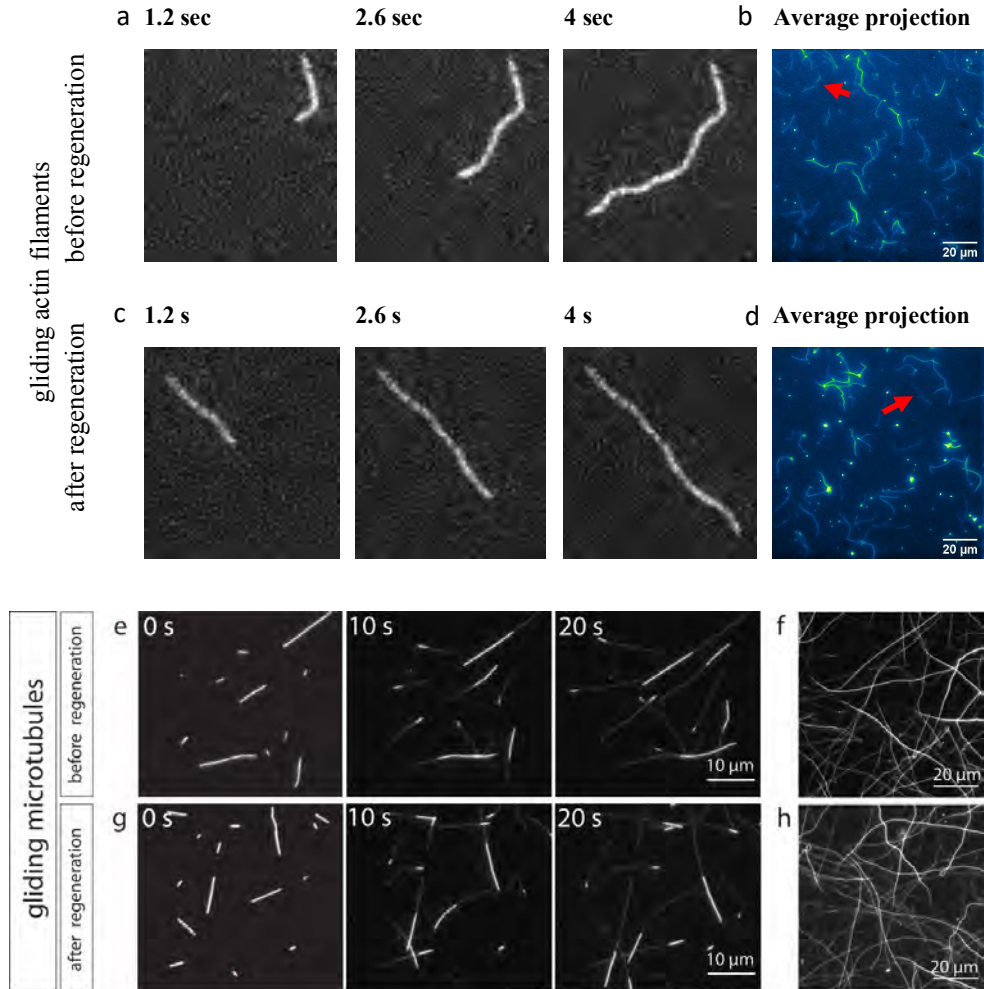


**Fig 2: Gliding motility assays before and after regeneration** **a+c)** Fluorescence micrographs zoomed areas showing a single actin filament gliding on a HMM coated TMCS derivatized glass surface before (a) and after (c) regeneration. Images are from maximum projections of time-lapse movies at different time points. **b+d)** Full field of view showing actin filament gliding on HMM coated TMCS derivatized glass surface before (b) and after (d) regeneration. The image is from average projection of a 4 s time-lapse movie. Scale bar: 20μm. **e+g)** Fluorescence images of microtubules gliding on kinesin-coated glass substrates at different time points before (e) and after (g) regeneration, overlaid to the summed traces (Z-projections) of the microtubules. **f+h)** Average projections of time-lapse movies (121 images; 1 image per second) of these exemplary assays (whole field of view) before (f) and after (h) regeneration.

We also tested whether or not it was possible to repeatedly regenerate surfaces. We have tested the repeated regeneration (3 times) using TMCS derivatized SiO<sub>2</sub> surfaces with the optimized protocol without observing any decrease in the actin sliding velocity (Fig.3). Similar results were found for the microtubule-kinesin motility on glass (Fig. 3). If devices are not immediately reused it is better to dry

the motility assay-supporting surface. We therefore tested if it is possible either to dry the surface before or after regeneration and then re-use it. This was tested for the microtubule-kinesin motility assay system on glass surfaces and we found that both approaches yielded successful regeneration (Fig.3; Table S2).

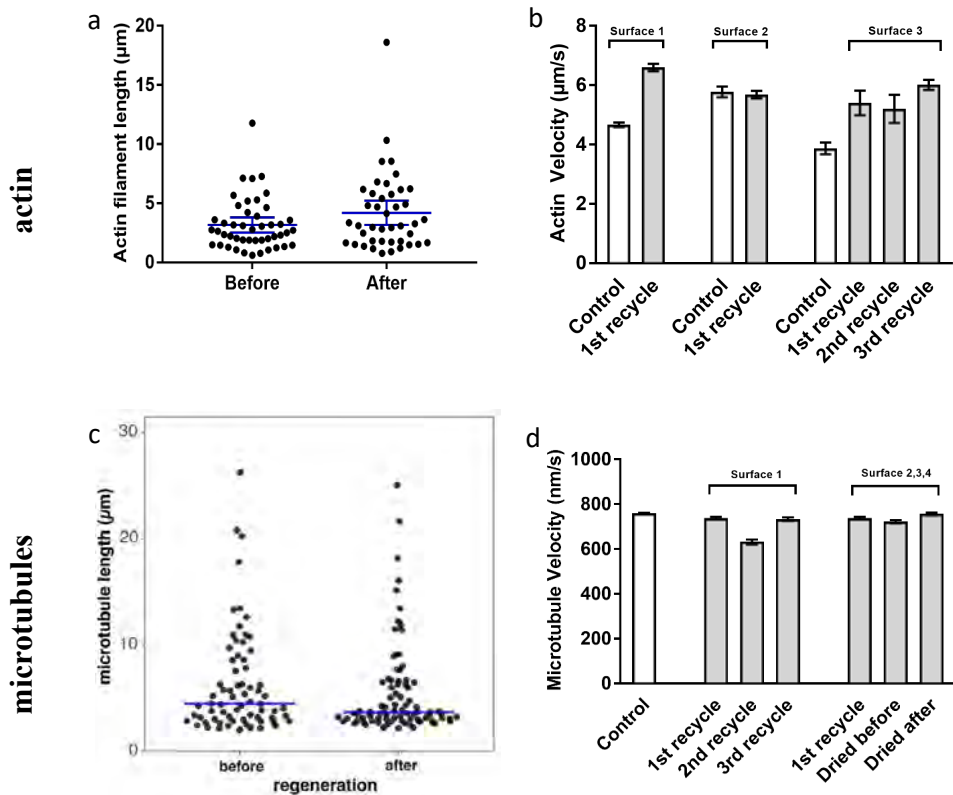


**Figure 3: Analysis of motility performance after regeneration** a) Actin filament length distribution on HMM adsorbed to TMCS derivatized  $\text{SiO}_2$  surfaces on 2 different experimental occasions before and after the regeneration. b) Actin sliding velocity on the HMM adsorbed to TMCS derivatized  $\text{SiO}_2$  surfaces; N= 3 surfaces where 1st and 2nd surfaces were regenerated one time (no further regeneration was attempted intentionally) while the third one was recycled for 3 times. In each individual experiment, 10-24 actin filaments were analyzed. c) Microtubule length distribution in a kinesin-1 gliding assay on glass surfaces before and after regeneration. d) Microtubule gliding velocity at 27°C on kinesin-1 adsorbed to glass surfaces; N= 4 surfaces where the 1st surface was recycled for 3 times; the 2nd surface was recycled for 1 time; the 3rd surface was first dried and then recycled for 1 time; the 4th surface was first recycled and then dried before performing a motility assay. For the 2nd to the 4th surfaces, no further regeneration was attempted intentionally. In each individual experiment, 277-664 microtubules were analyzed. Data are given as mean  $\pm$  95 % Confidence Interval (95 % CI).

After having proven that the regeneration of standard planar surfaces for gliding motility assays works reliably, we tested topographical structured surfaces with selective chemistry. For microtubule-kinesin this was realized by microstructuring silicon oxide on top of a gold coated silicon wafer (Fig. 4a). The silicon oxide walls

were chemically modified with PEG-silane to block protein binding, i.e., to allow motility only on the gold floors of the structures. Similar structures have been used earlier for kinesin-based devices (van den Heuvel *et al.*, 2005; Nicolau *et al.*, 2016). The control motility assay showed smooth gliding of filaments and motility was exclusively restricted to the structured “flower” area (Fig. 4b). The determined microtubule gliding velocities were around 700 nm/s and remained about constant over time (Fig. 4c). After regenerating the surface and adsorbing new proteins, motility was still only observed within the structures, clearly demonstrating that the chemical selectivity due to the PEG-coating of the silicon oxide walls was not destroyed by the regeneration procedure. Moreover, microtubules were nicely guided at the structure walls and did not get stuck more frequently: the fraction of stuck microtubules after regeneration  $f_{\text{regeneration}} = 0.09$  was comparable to the control value  $f_{\text{control}} = 0.07$ . The microtubules gliding velocities were with about 740 nm/s, slightly higher than the control, but also remained constant over time. The velocity increase after regeneration, might be explained by a slight increase of the ambient temperature in the course of the experiment. Altogether, these results indicate that our regeneration procedure is equally suitable for topographical structured surfaces and for planar ones, and even preserves chemical selectivity.

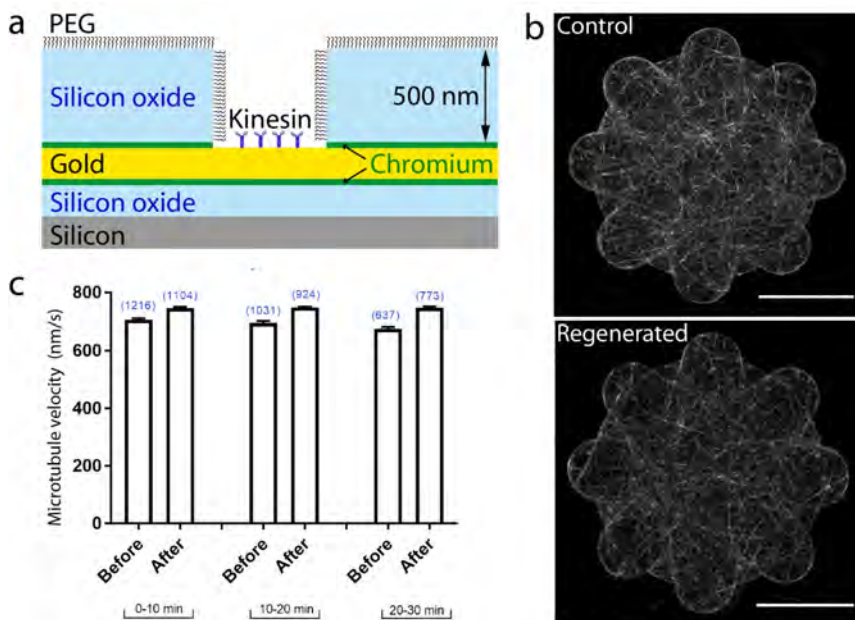


**Figure 4.** Regeneration of an assembled motility device with embedded nanostructures. **a**) Schematic cross-section of the nanostructured surface used for regeneration. On these surfaces, motility was restricted to the gold layers on the pattern floor of the microstructures. The rest of the surface was protein-repellent due to a PEG-silane coating. **b**) Summed traces (Z-projections of 10 min time-lapse movie) of fluorescently labelled microtubules gliding on kinesin-1 coated gold layers (pattern floor) before (control) and after regeneration. Scale bar: 50 $\mu$ m. **c**) Microtubule gliding velocity (nm/s) at different time points before and after regeneration; N= 3 surfaces. At each individual time point, 637-1216 microtubules were analyzed. Data are given as mean  $\pm$  95 % Confidence Interval (95 % CI).

In a next attempt, we tested the method to regenerate a SiO<sub>2</sub> surface, patterned using a surface chemistry adapted for the actin-myosin motility assay system. In this case, half the surface was covered with motility inhibiting CSAR62 polymer resist (Thomas and Macintyre J Vacuum Sci & Tech 2014) that may be used for nanofabrication of structures on a SiO<sub>2</sub> chip (Lindberg *et al.*, 2018). We found that the motility inhibition in the area covered with CSAR62 polymer resist was not altered by the regeneration procedure while the TMCS derivatized SiO<sub>2</sub> surface area without CSAR62 resist was fully regenerated (Fig. S5).

Next, we tried regenerating the simple nanostructure design in Fig. 5. Unfortunately, we found that a similar treatment as described above does generally not lead to successful regeneration of nanostructures for actomyosin motility with TMCS derivatized SiO<sub>2</sub> surrounded by motility suppressing CSAR62 polymer resist. We considered the idea that this is due to a lack of compatibility of CSAR62 with extended aqueous treatment. To test this possibility, we submerged some nanostructures under water for 8 hours but did not observe resist lift-off or other changes. We then hypothesized that use of SDS may cause the problem. The long hydrocarbon chain of SDS may interact with the ester group of CSAR62 polymer resist and change the properties of the resist. Another possibility could be that SDS, which is an anionic surfactant with appreciable net negative charge, transfers the negative charges to the CSAR62 polymer resist. The ideas that the use of SDS is the basis for the problems with regeneration of nanostructured surfaces is supported by results of experiments where SDS was substituted with a nonionic detergent Triton X100 (0.05%). In contrast to SDS, Triton X100 has neither the long hydrocarbon chain nor the negative charges. Interestingly, we found that Triton X100 is equally effective as SDS for regeneration of both TMCS derivatized glass and SiO<sub>2</sub> surfaces (Fig. 5) otherwise using the standard protocol (Fig 1). Both the actin sliding velocities and the mean filament lengths were maintained at the control value after regeneration, suggesting that the HMM surface density is unchanged compared to motility assays before regeneration (Fig. S6).

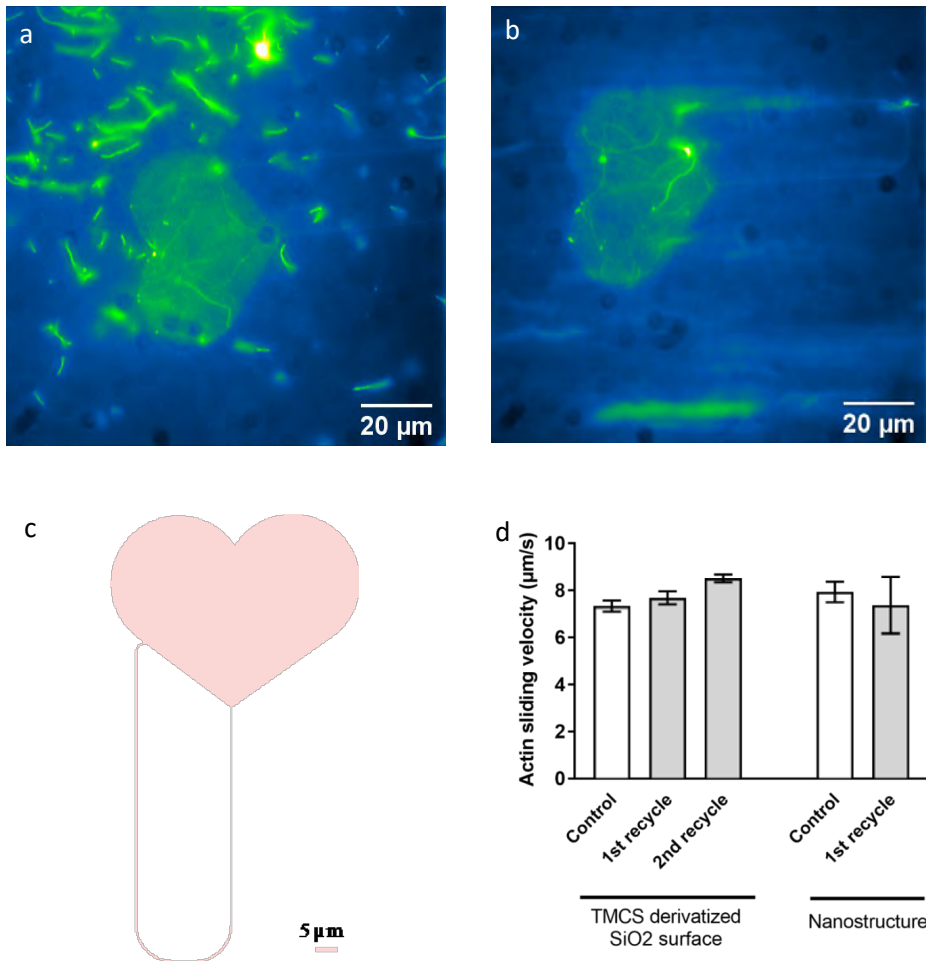


**Figure 5:** Efficiency of the optimized protocol (Proteinase K incubation (200 µg/ml; 1h; 37°C) followed by Triton X100 treatment (0.05%; 5min; RT)) to regenerate non-patterned motility assay surfaces and surfaces with nanostructures. **a** & **b**) Fluorescence micrographs showing actin filament gliding on HMM adsorbed to TMCS-derivatized SiO<sub>2</sub> in the nanostructure (see schematic design in Fig. 5c): **a**) control and **b**) after regeneration. Images are from maximum projections of 3.8 s time-lapse movies. Scale bar: 20µm. **c**) Schematic design of the nanostructure used for regeneration with topographically and chemically defined channels. The structure is made by electron beam lithography in CSAR 62 polymer walls with trimethylchlorosilane-derivatized-SiO<sub>2</sub> channel floors (pink). The HMM motor fragments bind to the TMCS-derivatized channel floors (pink) in a motility promoting manner, as binding to the surrounding CSAR 62 polymer walls is inhibited (Lindberg et al Langmuir 2018). The large heart shaped structure acts as a loading zone for the actin filaments, guiding them into the 500 nm wide feedback channel. **d**) HMM propelled actin sliding velocity (µm/s) on TMCS derivatized SiO<sub>2</sub> surfaces; N= 2 surfaces where the 1st surface was a flat chip and regenerated twice and the 2nd surface had an embedded nanostructure (Fig 5c). On the flat SiO<sub>2</sub> chip, 18-25 actin filaments were analyzed and on the loading zone of the nanostructure, 3-12 filaments were analyzed. Data are given as mean ± 95 % Confidence Interval (95 % CI).

The generally useful regeneration procedure that we describe in the present paper requires both the proteinase K incubation step and subsequent treatment with a

detergent (cf. Figs. S3-S6). We attribute the role of proteinase K in the regeneration process to effective cleavage of the motors, presumably into small peptide fragments, allowing these to readily diffuse away from the surface. The need to use SDS or Triton X100 for full regeneration suggests that small peptide fragments may re-adsorb to the surface after proteinase K digestion, preventing adsorption of fresh motor proteins. An important feature of a regeneration procedure, is that it does not destroy the nanostructures or the selective motility based on different surface chemistry. The present work suggests that the use of SDS is compatible with these aims for some surface patterning procedures (Fig. 4) but may need to be substituted by other detergents (e.g. Triton X100) in other cases (Fig. 5).

The fact that the regeneration was equally effective for actin-myosin and microtubule-kinesin 1 assays, is highly important for the development of motor driven nanodevices because these two motor systems are the ones most often used for these purposes. Furthermore, the surface treatment described in this paper did not affect the previously performed motility suppressing treatment on the CSAR62 polymer resist and did not affect the PEG-layers on the SiO<sub>2</sub> suppressing microtubule-kinesin motility.

## Conclusions

We describe a method to regenerate molecular motor-based bionanodevices, assembled together with a fluidic system, that is useful for both the actin-myosin and microtubule-kinesin systems, and has the potential to allow repeated use of such devices. Our findings are important also because the regenerated structures also rely on chemical confinement to create non-motile areas in nanostructured devices (Nicolau *et al.*, 2016; Lindberg *et al.*, 2018) for use in motor-driven biocomputation or biosensing applications. We found that these chemical treatments were unaffected by the regeneration procedures presented here. Future applications of the regeneration method can be extended to other motor-based devices with embedded nanostructures or nanoelectronics.

## Acknowledgements

This work was funded by European Union Seventh Framework FET Programme under contracts 613044 (ABACUS) and 732482 (Bio4comp), The Swedish Research Council (grant # 2015-05290), The Faculty of Health and Life Sciences at The Linnaeus University, NanoLund at Lund University.

## References

- Albet-Torres, N. *et al.* (2007) 'Mode of heavy meromyosin adsorption and motor function correlated with surface hydrophobicity and charge', *Langmuir*, 23(22), pp. 11147–11156. doi: 10.1021/la7008682.
- Albrecht, C., Kaepffel, N. and Gauglitz, G. (2008) 'Two immunoassay formats for fully automated CRP detection in human serum', *Analytical and Bioanalytical Chemistry*, 391(5), p. 1845. doi: 10.1007/s00216-008-2093-x.
- Andersson, K., Hämäläinen, M. and Malmqvist, M. (1999) 'Identification and Optimization of Regeneration Conditions for Affinity-Based Biosensor Assays. A Multivariate Cocktail Approach', *Analytical Chemistry*. American Chemical Society, 71(13), pp. 2475–2481. doi: 10.1021/ac981271j.
- Arlett, J. L., Myers, E. B. and Roukes, M. L. (2011) 'Comparative advantages of mechanical biosensors', *Nature nanotechnology*. 2011/03/27, 6(4), pp. 203–215. doi: 10.1038/nnano.2011.44.
- Bachand, G. D. *et al.* (2006) 'Active capture and transport of virus particles using a biomolecular motor-driven, nanoscale antibody sandwich assay', *Small*, 2. doi: 10.1002/sml.200500262.
- BAJORATH, J., HINRICHS, W. and SAENGER, W. (1988) 'The enzymatic activity of proteinase K is controlled by calcium', *European Journal of Biochemistry*, 176(2), pp. 441–447. doi: 10.1111/j.1432-1033.1988.tb14301.x.
- Bell, S. and Terentjev, E. M. (2017) 'Specific binding of a polymer chain to a sequence of surface receptors', *Scientific Reports*, 7(1), p. 17272. doi: 10.1038/s41598-017-17581-x.

BETZEL, C., PAL, G. P. and SAENGER, W. (1988) 'Three-dimensional structure of proteinase K at 0.15-nm resolution', *European Journal of Biochemistry*. John Wiley & Sons, Ltd (10.1111), 178(1), pp. 155–171. doi: 10.1111/j.1432-1033.1988.tb14440.x.

Castner, D. G. and Ratner, B. D. (2002) 'Biomedical surface science: Foundations to frontiers', *Surface Science*. North-Holland, 500(1–3), pp. 28–60. doi: 10.1016/S0039-6028(01)01587-4.

Dodo, C. G. *et al.* (2013) 'Proteome analysis of the plasma protein layer adsorbed to a rough titanium surface', *Biofouling*. Taylor & Francis, 29(5), pp. 549–557. doi: 10.1080/08927014.2013.787416.

Frasconi, M., Mazzei, F. and Ferri, T. (2010) *Protein immobilization at gold-thiol surfaces and potential for biosensing*, *Analytical and bioanalytical chemistry*. doi: 10.1007/s00216-010-3708-6.

Goldenberger, D. *et al.* (1995) 'A simple "universal" DNA extraction procedure using SDS and proteinase K is compatible with direct PCR amplification', *Genome Research*, 4(6), pp. 368–370. doi: 10.1101/gr.4.6.368.

Harada, Y. *et al.* (1987) 'Sliding movement of single actin filaments on one-headed myosin filaments', *Nature*. Nature Publishing Group, 326, p. 805.

Hess, H. (2011) 'Engineering Applications of Biomolecular Motors', *Annual Review of Biomedical Engineering*. Annual Reviews, 13(1), pp. 429–450. doi: 10.1146/annurev-bioeng-071910-124644.

van den Heuvel, M. G. L. *et al.* (2005) 'High rectifying efficiencies of microtubule motility on Kinesin-coated gold nanostructures', *Nano Letters*, 5(6), pp. 1117–1122. doi: 10.1021/nl0506554.

Higashi-Fujime, S. *et al.* (1992) 'Muscle actin cleaved by Proteinase K: Its polymerization and In Vitro motility', *Journal of Biochemistry*, 112(4), pp. 568–572. doi: 10.1093/oxfordjournals.jbchem.a123940.

Hlady, V. and Buijs, J. (1996) 'Protein adsorption on solid surfaces', *Current Opinion in Biotechnology*. Elsevier Current Trends, 7(1), pp. 72–77. doi: 10.1016/S0958-1669(96)80098-X.

Hock, B., Seifert, M. and Kramer, K. (2002) 'Engineering receptors and antibodies for biosensors', *Biosensors and Bioelectronics*. Elsevier, 17(3), pp. 239–249. doi: 10.1016/S0956-5663(01)00267-6.

Howard, J., Hudspeth, A. J. and Vale, R. D. (1989) 'Movement of microtubules by single kinesin molecules', *Nature*, 342(6246), pp. 154–158. doi: 10.1038/342154a0.

Kasemo, B. (2002) 'Biological surface science', *Surface Science*. North-Holland, 500(1–3), pp. 656–677. doi: 10.1016/S0039-6028(01)01809-X.

Korten, T. *et al.* (2016) 'Kinesin-1 Expressed in Insect Cells Improves Microtubule in Vitro Gliding Performance, Long-Term Stability and Guiding Efficiency in Nanostructures', *IEEE Transactions on NanoBioscience*, 15(1), pp. 62–69. doi: 10.1109/TNB.2016.2520832.

Korten, T. *et al.* (2018) 'An automated in vitro motility assay for high-throughput studies of molecular motors', *Lab on a Chip*. Royal Society of Chemistry, 18(20), pp. 3196–3206. doi: 10.1039/c8lc00547h.

Korten, T., Månsson, A. and Diez, S. (2010) 'Towards the Application of Cytoskeletal Motor Proteins in Molecular Detection and Diagnostic Devices', *Curr Opin Biotechnol*, 21. doi: 10.1016/j.copbio.2010.05.001.

Kron, S. J. *et al.* (1991) 'Assays for actin sliding movement over myosin-

coated surfaces', *Methods Enzymol*, 196. doi: 10.1016/0076-6879(91)96035-P.

Kron, S. J. and Spudich, J. A. (1986) 'Fluorescent actin filaments move on myosin fixed to a glass surface.', *Proceedings of the National Academy of Sciences of the United States of America*, 83(17), pp. 6272–6276. doi: 10.1073/pnas.83.17.6272.

Kumar Dixit, C. (2014) 'Surface Regeneration of Gold-Coated Chip for Highly-Reproducible Surface Plasmon Resonance Immunoassays', *Journal of Biosensors & Bioelectronics*, 05(02). doi: 10.4172/2155-6210.1000149.

Kumar, S. *et al.* (2012) 'Antibodies covalently immobilized on actin filaments for fast myosin driven analyte transport', *PLoS One*, 7. doi: 10.1371/journal.pone.0046298.

Kumar, S. *et al.* (2013) 'Magnetic capture from blood rescues molecular motor function in diagnostic nanodevices', *Journal of Nanobiotechnology*, 11(1), pp. 1–12. doi: 10.1186/1477-3155-11-14.

Kumar, S. *et al.* (2016) 'Sensing protein antigen and microvesicle analytes using high-capacity biopolymer nano-carriers', *Analyst*. The Royal Society of Chemistry, 141(3), pp. 836–846. doi: 10.1039/C5AN02377G.

Kumar, S. and Mansson, A. (2017) 'Covalent and non-covalent chemical engineering of actin for biotechnological applications', *Biotechnology Advances*, 35(7), pp. 867–888. doi: <https://doi.org/10.1016/j.biotechadv.2017.08.002>.

Lindberg, F. W. *et al.* (2018) 'Controlled Surface Silanization for Actin-Myosin Based Nanodevices and Biocompatibility of New Polymer Resists', *Langmuir*, 34(30), pp. 877–8784. doi: 10.1021/acs.langmuir.8b01415.

Månsson, A. *et al.* (2008) ‘In vitro assays of molecular motors – impact of motor-surface interactions Alf’, *Frontiers in Bioscience*, 6(44), pp. 21–25.

Månsson, A. (2012) ‘Translational actomyosin research: fundamental insights and applications hand in hand’, *J Muscle Res Cell Motil*, 33. doi: 10.1007/s10974-012-9298-5.

Månsson, A. and Tågerud, S. (2003) ‘Multivariate statistics in analysis of data from the in vitro motility assay’, *Analytical Biochemistry*, 314(2), pp. 281–293. doi: [http://dx.doi.org/10.1016/S0003-2697\(02\)00610-3](http://dx.doi.org/10.1016/S0003-2697(02)00610-3).

Margossian, S. S. and Lowey, S. (1982) ‘[7] Preparation of myosin and its subfragments from rabbit skeletal muscle’, in Enzymology, B. T.-M. in (ed.) *Structural and Contractile Proteins Part B: The Contractile Apparatus and the Cytoskeleton*. Academic Press, pp. 55–71. doi: [http://dx.doi.org/10.1016/0076-6879\(82\)85009-X](http://dx.doi.org/10.1016/0076-6879(82)85009-X).

Mattos, A. B. *et al.* (2012) ‘A dual quartz crystal microbalance for human cardiac troponin T in real time detection’, *Sensors and Actuators B: Chemical*. Elsevier, 161(1), pp. 439–446. doi: 10.1016/J.SNB.2011.10.058.

Nakanishi, K., Sakiyama, T. and Imamura, K. (2001) ‘On the adsorption of proteins on solid surfaces, a common but very complicated phenomenon’, *Journal of Bioscience and Bioengineering*, 91(3), pp. 233–244. doi: [https://doi.org/10.1016/S1389-1723\(01\)80127-4](https://doi.org/10.1016/S1389-1723(01)80127-4).

Nicolau, D. V *et al.* (2016) ‘Parallel computation with molecular-motor-propelled agents in nanofabricated networks’, *Proceedings of the National Academy of Sciences*, 113(10), pp. 2591–2596. doi: 10.1073/pnas.1510825113.

Papra, A., Gadegaard, N. and Larsen, N. B. (2001) ‘Characterization of Ultrathin Poly(ethylene glycol) Monolayers on Silicon Substrates’, *Langmuir*. American Chemical Society, 17(5), pp. 1457–1460. doi:

10.1021/la000609d.

Pardee, J. D. and Spudich, J. A. (1982) 'Purification of muscle actin', *Methods Cell Biol.*, 24. doi: 10.1016/S0091-679X(08)60661-5.

Persson, M. *et al.* (2013) 'Transportation of nanoscale cargoes by myosin propelled actin filaments', *PLoS One*, 8. doi: 10.1371/journal.pone.0055931.

Petsch, D., Deckwer, W. D. and Anspach, F. B. (1998) 'Proteinase K digestion of proteins improves detection of bacterial endotoxins by the *Limulus* ameobocyte lysate assay: application for endotoxin removal from cationic proteins.', *Analytical biochemistry*, 259(1), pp. 42–7. doi: 10.1006/abio.1998.2655.

Rabe, M., Verdes, D. and Seeger, S. (2011) 'Understanding protein adsorption phenomena at solid surfaces', *Advances in Colloid and Interface Science*. Elsevier, 162(1–2), pp. 87–106. doi: 10.1016/J.CIS.2010.12.007.

Radi, A.-E. *et al.* (2005) 'Reusable Impedimetric Aptasensor', *Analytical Chemistry*. American Chemical Society, 77(19), pp. 6320–6323. doi: 10.1021/ac0505775.

Rahman, M. A. *et al.* (2018) 'Blebbistatin Effects Expose Hidden Secrets in the Force-Generating Cycle of Actin and Myosin', *Biophysical Journal*, 115(2), pp. 386–397. doi: <https://doi.org/10.1016/j.bpj.2018.05.037>.

Rahman, M. A., Salhotra, A. and Månsson, A. (2019) 'Comparative analysis of widely used methods to remove nonfunctional myosin heads for the in vitro motility assay', *Journal of Muscle Research and Cell Motility*. doi: 10.1007/s10974-019-09505-1.

Sankiewicz, A., Tokarzewicz, A. and Gorodkiewicz, E. (2015)

‘Regeneration of surface plasmon resonance chips for multiple use  
Regeneration of surface plasmon resonance chips for multiple use’,  
(April).

Sata, M. *et al.* (1993) ‘Dynamic Interaction Between Cardiac Myosin Isoforms Modifies Velocity of Actomyosin Sliding In vitro’, *Circ Res*, 73(4), pp. 696–704. doi: 10.1161/01.RES.73.4.696.

Sharma, S., Byrne, H. and O’Kennedy, R. J. (2016) ‘Antibodies and antibody-derived analytical biosensors’, *Essays in biochemistry*. 2016/06/30. Portland Press Limited, 60(1), pp. 9–18. doi: 10.1042/EBC20150002.

Sugimoto, K. *et al.* (2016) ‘Proteomic analysis of bone proteins adsorbed onto the surface of titanium dioxide’, *Biochemistry and Biophysics Reports*. Elsevier, 7, pp. 316–322. doi: 10.1016/J.BBREP.2016.07.007.

Sundberg, M. *et al.* (2003) ‘Silanized surfaces for in vitro studies of actomyosin function and nanotechnology applications’, *Anal Biochem*, 323. doi: 10.1016/j.ab.2003.07.022.

Toyoshima, Y. Y. (1993) ‘How are Myosin Fragments Bound to Nitrocellulose Film?’, in Sugi, H. and Pollack, G. H. (eds) *Mechanism of Myofilament Sliding in Muscle Contraction*. Boston, MA: Springer US, pp. 259–265. doi: 10.1007/978-1-4615-2872-2\_25.

Winkelmann, D. A. *et al.* (1995) ‘Flexibility of myosin attachment to surfaces influences F-actin motion’, *Biophysical Journal*, 68(6), pp. 2444–2453. doi: 10.1016/S0006-3495(95)80426-1.

Wong, J. Y. *et al.* (1997) ‘Direct Measurement of a Tethered Ligand-Receptor Interaction Potential’, *Science*, 275(5301), p. 820 LP-822. doi: 10.1126/science.275.5301.820.

Xu, L.-C., Bauer, J. W. and Siedlecki, C. A. (2014) 'Proteins, platelets, and blood coagulation at biomaterial interfaces', *Colloids and Surfaces B: Biointerfaces*. Elsevier, 124, pp. 49–68. doi: 10.1016/J.COLSURFB.2014.09.040.

# Supporting Materials and Methods

## Materials

The detergents Tween 20 and Triton X100 were diluted in dH<sub>2</sub>O before use. The radioimmunoprecipitation assay (RIPA) buffer was composed of 150 mM NaCl, 1% sodium deoxycholate, 25 mM Tris base, 0.1% SDS, 1% NP40 and prepared before use.

## Regeneration using non-standard protocols

In the course of optimizing the protocol, we performed experiments generally following the protocol in the main Fig. 1 but eliminating either the proteinase K or the detergent incubation step. We also varied the Proteinase K incubation time (1-24 h) and the SDS concentration (0.05 to 5%). Furthermore, we tested other detergents than SDS.

To regenerate surfaces with different detergents, after performing an *in vitro* motility assay (“control assay”) on a trimethylchlorosilane (TMCS) derivatized glass surface, the flow cell was rinsed with wash buffer C (5x) followed by a series of rinse (3x), incubation (2h) and rinse (3x) with a detergent solution (concentrations were varied for different detergents). Next, the flow cell was rinsed (10x) with the buffer C before a new motility assay (“test assay”), i.e., adsorbing new molecular motors, was performed on surfaces.

## Supporting results

We tested different detergents (Tween 20, SDS, Triton X100) and RIPA buffer which have previously been found to be useful for desorption of proteins from surfaces (Mattos et al 2012; Albrecht et al 2008; Andersson et al 1999; Kratz et al 2015). None of the tested agents alone led to a full recovery of motility. We hypothesized that the reason could be that 1) an extended (2 hours) incubation with detergent changes the surface chemistry or 2) detergent molecules themselves adsorb to the surface hence disturbing new protein binding. To test these hypotheses, we first used appreciably shorter incubation time periods with SDS (0.5-2 min) as well as different SDS concentrations (0.05-1%). None of these approaches was, however, effective to regenerate TMCS derivatized glass surfaces for subsequent *in vitro* motility assays. We also incubated a fresh control surface with SDS (0.05%, 30 sec) before adding proteins and that did not decrease the performance of the motility assay (Table S1; Fig. S1). One explanation for the failed regeneration with use of detergent alone, might be the high local surface

concentration of motors proteins. This might lead to aggregation of the denatured motors, thus, preventing surface desorption. Such an idea is consistent with the observation of macroscopic precipitates following treatment with 10% SDS (Table S1).

We then treated the motility assay surfaces with proteinase K (see details in the manuscript) to effectively cleave the surface adsorbed proteins. The flow cells of the control assays were incubated (1-24 h at 37°C) with proteinase K followed by several rinsing steps. We found that the myosin motility in the subsequent test assay was successfully regenerated, although the actin gliding velocity was significantly reduced. However, the incubation time did not impact the effectiveness of the regeneration, as the gliding velocities in the respective test assays (Fig. S2a) were not significantly different. Therefore, in the following, a proteinase K incubation time of 1 h was used unless otherwise stated.

In addition to a reduction in velocity, we noticed that the fraction of motile actin filaments was higher in the test motility assays after regeneration (Fig. S2b). Moreover, the tendency for short filaments to detach from the surface was increased, and the filaments were, on average, appreciably longer (Fig. S2 c-e) than before regeneration. These observations point toward a lower myosin (HMM) surface density compared to the control assay (Uyeda et al. 1990; Toyoshima et al. 1990). One reason for this may be the reduced adsorption of new functional HMM molecules due to an incomplete removal of the proteins from the surface during the washing steps after the proteinase K treatment. For the microtubule-kinesin system, we found that the motility performance in the test assays varied if only proteinase K and not the detergent step was included during the regeneration. In most instances, more microtubules were stuck or detached from the surface. Similarly, to the actin-myosin system, these results indicate the presence of fewer and/or inactive motors, caused by residues on the surface.

The above results suggest that removal of remaining motor fragments following proteinase K treatment could further improve the regeneration efficiency. Therefore, we included a short SDS incubation step (0.05-5%; 5 min), followed by proteinase K treatment (1h at 37°C). We found that SDS inclusion after proteinase K improved the regeneration of surfaces and at 5% SDS actin sliding velocity was fully recovered (main paper and Fig. S3).

## Supporting Figures

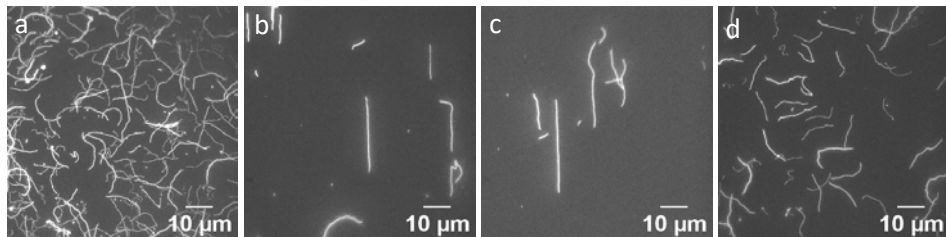


**Figure S1.** Fluorescence micrographs showing rhodamine phalloidin labelled actin filaments on heavy meromyosin coated trimethylchlorosilane derivatized glass surface: **a)** actin filament gliding on a control surface (before 0.05% SDS incubation); **b)** non motile actin filaments on the surface after 0.05% SDS incubation for 2 min; **c)** non motile actin filaments on the surface after 0.05% SDS incubation for 30 sec; **d)** actin gliding on the surface (0.05% SDS incubation on a control surface before protein adsorption);

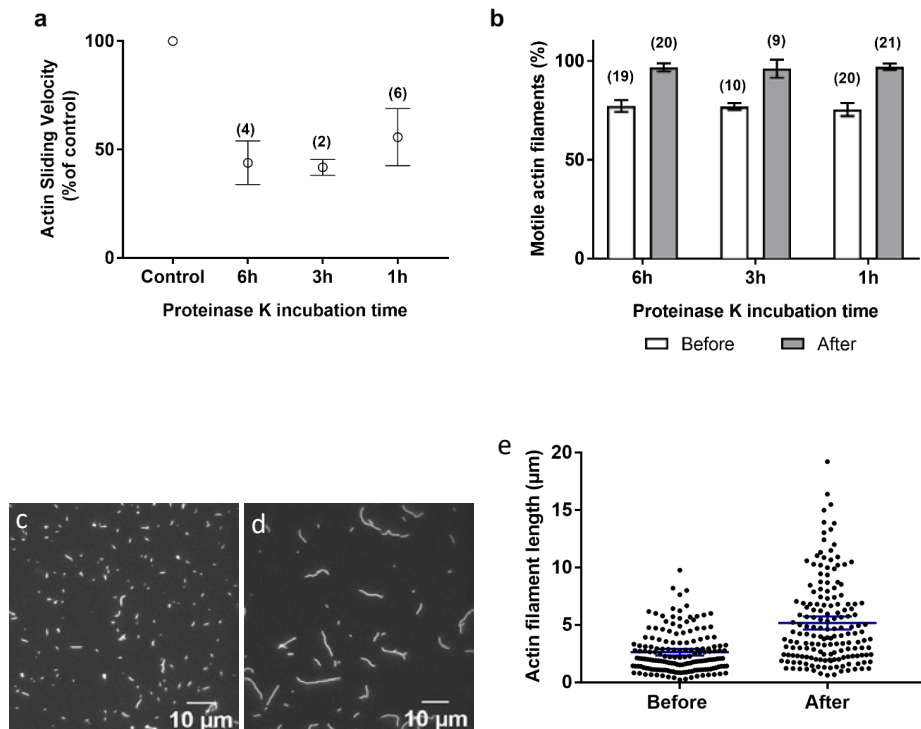


**Figure S2:** Efficiency of proteinase K alone in regenerating trimethylchlorosilane derivatized glass surfaces for use in actomyosin in vitro motility assays. **a)** Actin sliding velocity (% of control) on the regenerated surfaces; N= number of surfaces (in parentheses); In each individual experiment, 9-30 actin filaments were analyzed. Mean actin sliding velocities on surfaces after proteinase K treatment are normalized to the mean actin sliding velocity of the same surface before regeneration. Mean values from normalized actin sliding velocities (% of control) from all experiments are plotted. **b)** Fraction of motile actin filaments (%) before and after the proteinase K treatments; N= number of image areas (in parentheses) in the flow cell. **c & d)** Fluorescence micrographs showing rhodamine phalloidin labelled actin filaments on the same surface before **c)** and after **d)** the regeneration, respectively. **e)** Actin filament length (µm) distribution on the surfaces in 6 different experimental occasions before and after the regeneration. Data are given as mean  $\pm$  95 % confidence interval (95 % CI).

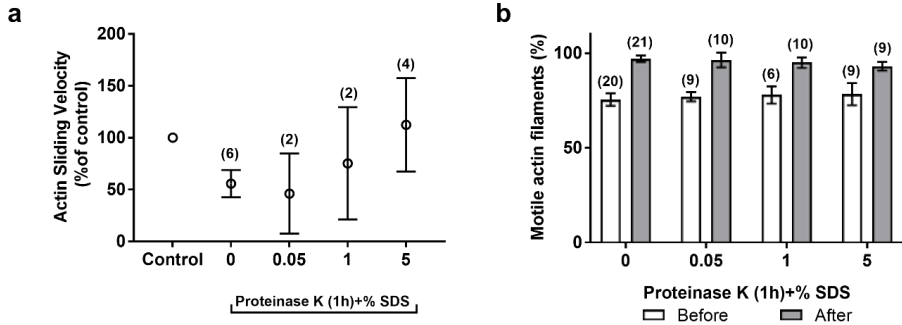


**Figure S3:** Efficiency of SDS (0-5%) inclusion after proteinase K (1h) treatment for regenerating trimethylchlorosilane derivatized glass surfaces for use in the in vitro motility assay. a) Actin sliding velocity (% of control) on the regenerated surfaces; N= number (in blue) of surfaces; In each individual experiment, 9–30 actin filaments were analyzed. Mean actin sliding velocities on surfaces after proteinase K treatment are normalized to the mean actin sliding velocities of the same surface before regeneration. Mean values from normalized actin sliding velocities (% of control) from all experiments are plotted. b) Motile actin filaments (%) before and after the proteinase K and SDS treatments; N= number (in blue) of image areas in the flow cell. Data are given as mean  $\pm$  95 % confidence interval (95 % CI).

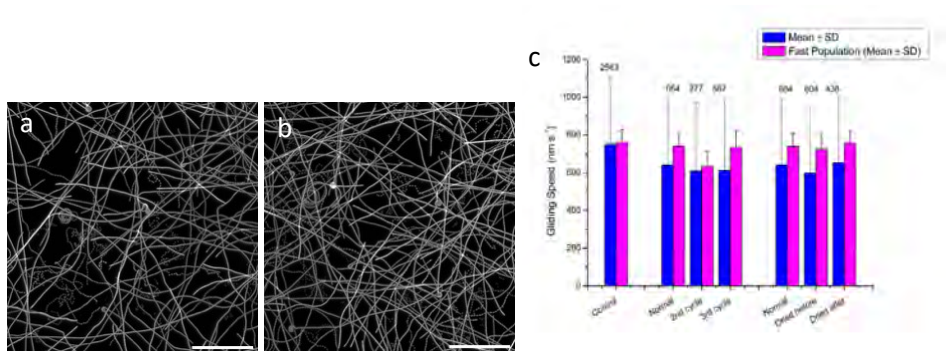


**Figure S4.** Efficiency of the optimized protocol (proteinase K incubation (200  $\mu$ g/ml; 1h; 37°C) followed by SDS treatment (5%; 5min; RT)) to recycle motility assay surfaces (glass) using the microtubule-kinesin 1 system. **a & b**) Fluorescence micrographs showing microtubule gliding on a kinesin-1 coated glass surface: **a**) control and **b**) after regeneration. Images are from maximum projections of 2 min time-lapse movies. Scale bar: 20 $\mu$ m. **c**) Microtubule gliding speeds (slow vs fast) on regenerated glass surfaces: The mean speeds for microtubules gliding at 27°C on glass surfaces were evaluated before (control) and after regeneration (normal – without drying, 2<sup>nd</sup> /3<sup>rd</sup> cycle – repeated regeneration on the same surface). The number of evaluated microtubules are stated above each box.

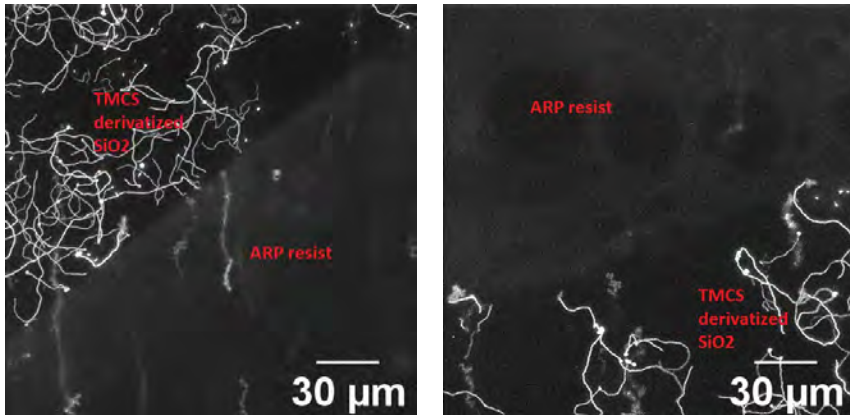


**Figure S5.** Actin filament gliding on a heavy meromyosin coated TMCS derivatized  $\text{SiO}_2$  surface, where half of the surface was covered by a motility inhibiting resist ARP: left-control and right-after recycling with proteinase K and 5% SDS (ARP resist layer is undisturbed and inhibited motility). Images are from maximum projections of 19.7 sec time lapse movies. Scale bar: 30  $\mu\text{m}$ .

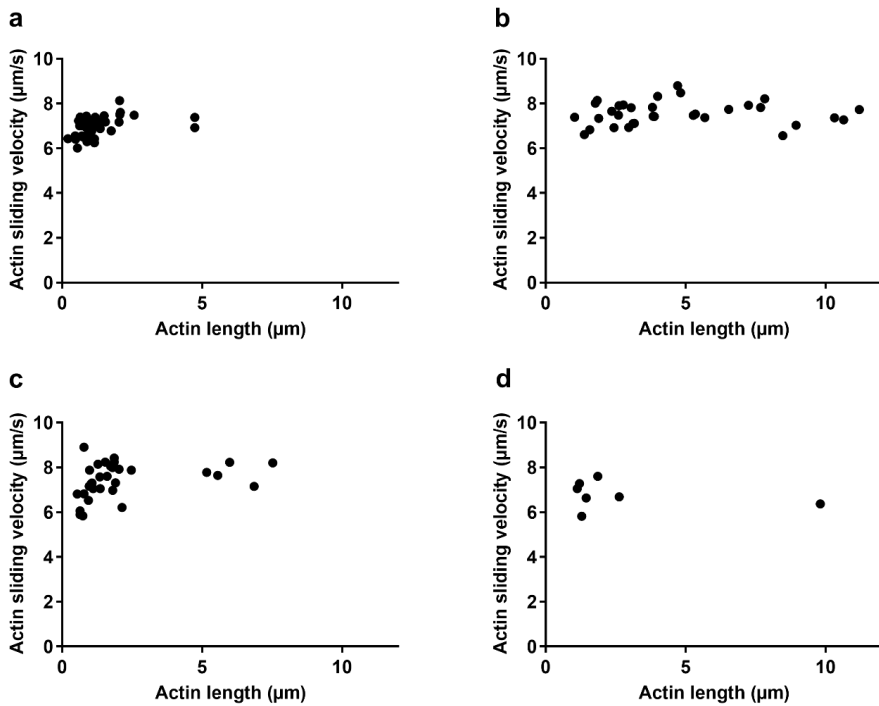


**Figure S6.** Efficiency of the optimized protocol (proteinase K incubation (200  $\mu\text{g/ml}$ ; 1h; 37°C) followed by Triton X100 treatment (0.05%; 5min; RT)) to recycle motility assay surfaces and surfaces with embedded nanostructure. Actin sliding speed plotted against actin filament length for all analyzed filaments in all experiments in main Fig. 5a. **a-b)** TMCS derivatized flat  $\text{SiO}_2$  surface before and after regeneration. **c-d)** TMCS derivatized nanostructured  $\text{SiO}_2$  surface before and after regeneration.

## Supporting Tables

**Table S1.** Summary of different approaches to test recycling of TMCS derivatized glass surfaces.

SL	Regeneration strategies	Treatment/Incubation strategy	Result/observation	
1	RIPA buffer	2 h incubation at RT	Regeneration was not successful. Actin filaments were floating in the solution.	
2	Tween 20 (0.1%)	2 h incubation at RT	Regeneration was not successful. Actin filaments were floating in the solution.	
3	SDS	10%	2 h incubation at RT	White precipitation on the surface
4		1%	2 min incubation at RT	Regeneration was not successful. Actin filaments were stuck.
5		0.1%	2 min incubation at RT	Regeneration was not successful. Actin filaments were stuck.
6		0.05%	2 min incubation at RT	Regeneration was not successful. Actin filaments were stuck.
		0.05%	30 sec incubation at RT	Regeneration was not successful. Actin filaments were stuck.
		0.05%	30 sec incubation at RT (On a fresh surface before protein adsorption)	Actin gliding was similar to control (Fraction of motile filaments were 83.7 and 86.8 % respectively on surfaces without and with 0.05% SDS incubation before protein adsorption)
7		Proteinase K	200 µg/ml	24 h incubation at 37°C
8		200 µg/ml	6 h incubation at 37°C	Actin sliding velocity was 43.91 +/- 6.29% of the control

9		200 µg/ml	3 h incubation at 37°C	Actin sliding velocity was 41.77 +/- 0.4% of the control
10		200 µg/ml	1 h incubation at 37°C	Actin sliding velocity was 55.72 +/- 12.57% of the control
11	Proteinase K &	200 µg/ml	1 h incubation at 37°C	Actin sliding velocity was 46.15 +/- 4.29% of the control
	SDS	0.05%	5 min at RT	
12	Proteinase K &	200 µg/ml	1 h incubation at 37°C	Actin sliding velocity was 75.33 +/- 6.02% of the control
	SDS	1%	5 min at RT	
13	Proteinase K &	200 µg/ml	1 h incubation at 37°C	Actin sliding velocity was fully restored
	SDS	5%	5 min at RT	
14	Proteinase K &	200 µg/ml	1 h incubation at 37°C	Regeneration was not successful. Actin filaments were floating in the solution.
	Tween 20	1%	5 min at RT	
16	Proteinase K &	200 µg/ml	1 h incubation at 37°C	Actin sliding velocity was fully restored
	Triton X100	0.05%	5 min at RT	

**Table S2.** Fraction of stuck microtubules in a motility assay before (control) and after surface regeneration (normal – without drying, 2<sup>nd</sup> /3<sup>rd</sup> cycle – repeated regeneration on the same surface)

	Fraction of stuck microtubules
Control	0.010
Normal	0.008
2 <sup>nd</sup> cycle	0.014
3 <sup>rd</sup> cycle	0.011
Dried before	0.013
Dried after	0.009

Paper V





# Nanoscaled patterning of active molecular motor structured surfaces for switchable motility

Frida W. Lindberg<sup>1\*</sup>, Jingyuan Zhu<sup>1\*</sup>, Till Korten<sup>4,5</sup>, Christoph Meinecke<sup>2,3</sup>, Stefan Diez<sup>4,5</sup>, Heiner Linke<sup>1</sup>

## **Affiliations:**

1 NanoLund and Solid State Physics, Lund University, Lund, Sweden

2 TU-Chemnitz, Center for Microtechnologies, Chemnitz, Germany

3 Fraunhofer Institute for Electronic Nanosystems (ENAS), Chemnitz, Germany

4 B CUBE - Centre for Molecular Bioengineering, Technische Universität Dresden, Dresden, Germany.

5 Max Planck Institute of Molecular Cell Biology and Genetics, Dresden Germany.

**Keywords:** Molecular motors, programmable gating, microtubule-kinesin, nanostructure, PNIPAM, PGMA, switchable motility

## **Abstract**

Nanotechnology devices using molecular motors typically use a combination of chemical and physical confinement to define pathways or channels to guide filament motion. Being able to change what pathways are available will allow the creation of complex, programmable structures, within e.g., network-based biocomputation. Here, we demonstrate a method to tune the motility in selective areas on a surface. Specifically, we used the negative tone electron beam lithography resist polyglycidyl methacrylate (PGMA) as a polymer linker for the thermo-responsive polymer poly(N-isopropylacrylamide) (PNIPAM) to physically block and un-block molecular motors bound to a surface. We developed the processing parameters for patterning PGMA on both flat surfaces and inside nanoscaled channels, enabling us to selectively graft PNIPAM in specific regions. We were able to achieve successful motility switching in selective areas on a flat surface, demonstrating the ability to locally tune the paths for molecular motor propelled filaments. These results provide a possibility for encoding switchable encodings in network-based bio-computation and the ability to create versatile sensing devices with paths that can be switched on and off.

## Introduction

Directing and guiding the motion of nanomachines such as cytoskeletal motor protein systems has enabled a multitude of nanotechnology applications<sup>1-7</sup>. Motor proteins convert chemical energy into mechanical work, propelling filamentous proteins in a highly energy-efficient manner<sup>4,8,9</sup>. These motor systems can be isolated from the living cell and adsorbed onto a surface with maintained function in the *in vitro* motility assay<sup>10-13</sup>. Recently, the two motor-systems, namely actin-myosin II and microtubule-kinesin 1, were used to provide a proof of concept of network-based biocomputation (NBC) using biomolecular motors<sup>4</sup>. NBC is a parallel computation technique where a mathematical problem is encoded into a network of channels and junctions. Each pathway represents a different solution, which can be explored by filamentous agents propelled by molecular motors bound to the surface. A limitation of existing NBC devices<sup>4</sup> is the fact that one network hard-encodes one specific instance of a problem, without the ability to program the encoding. The ability to change what pathways are available will enable programmable networks allowing dynamic encodings. These programmable gating mechanisms could be created by switching the motility of filamentous agents in selective areas.

Tunable motility can e.g., be achieved by changing the amount of motor-fuel (ATP) present<sup>14</sup> or by applying an electric field across a junction, steering the motion of filaments by interacting with the leading tip<sup>15</sup>. More locally switchable motility can be achieved by using the thermo-responsive polymer poly(N-isopropylacrylamide) PNIPAM<sup>16,17</sup>, where the motors are physically blocked and unblocked. At low temperatures, below a lower critical solution temperature (LCST), PNIPAM is soluble in aqueous solution and the polymer chain resides in an extended form<sup>18</sup> (see **Figure 1**). This blocks the motors on the surface and prevents filaments from binding and being propelled. If the temperature is raised above the LCST, which for PNIPAM is around 30-35°C<sup>19</sup>, the polymer undergoes a conformational change and aggregates into a collapsed, insoluble globule which exposes the molecular motors, re-enabling filament propulsion.

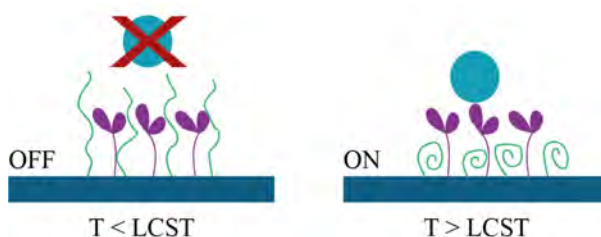


**Figure 1.** Schematic illustrations of PNIPAM above and below the lower critical solution temperature (LCST). At temperatures below the LCST, the PNIPAM polymer resides in an extended form, blocking the molecular motors and inhibit motility (OFF state). At temperatures above the LCST, the PNIPAM polymer collapses, exposing the molecular motors, enabling motility (ON state).

In the first experiments demonstrating the ability to turn microtubule-kinesin motility on and off<sup>16,17</sup>, the entire surface was covered with PNIPAM, grafted onto a polymer linker, poly-glycidyl methacrylate (PGMA). The ability to switch motility along pre-defined pathways was demonstrated by Schroeder et al.<sup>17</sup>, who chemically confined the motor system onto Au tracks that could be selectively heated. However, because these tracks lacked the physical walls usually employed in molecular motor devices<sup>20-23</sup>, the ability to guide filaments was limited. An aim is thus, to combine the ability to switch molecular motor motility inside physical channels. In other words, the challenge is to create guiding channels (optimally below a width of below 1  $\mu\text{m}$ )<sup>22</sup>, with PNIPAM coated locally on channel floors.

Here we present a method of selectively grafting PNIPAM in local areas, enabling switching in specific regions only, by using the PGMA polymer as a negative tone electron beam lithography resist<sup>24</sup>. We present the necessary processing parameters for PGMA on both flat surfaces and inside channel structures and demonstrate successful motility switching in selective areas on flat surfaces.

## Experimental

### *Device preparation*

Samples for examining local PNIPAM grafting on PGMA patches were fabricated on 10x10 mm Si(100) chips with a 30 nm layer of SiO<sub>2</sub> deposited by atomic layer deposition. The samples were spin-coated a layer 1.6% PGMA (Polymer Source Inc., Quebec, Canada) dissolved in Anisole (VWR AB, Lund, Sweden) and 98x98  $\mu\text{m}^2$  squares were patterned by electron beam lithography (Raith150, Raith GmbH) at a 20 kV acceleration voltage using dose 10  $\mu\text{C}/\text{cm}^2$  to cross-link the polymer. The samples were developed in methyl ethyl ketone for 2 min, rinsed in isopropanol and dried in N<sub>2</sub>-gas. After exposure and development, a 7 nm residual layer of PGMA remained in the non-exposed areas which could not be removed by longer development but only by oxygen plasma treatment (Plasma Preen, Plasmatic Systems Inc.). After PNIPAM grafting (see below), we performed *in vitro* motility assay (IVMA) experiments on these samples (see also below).

Samples for examining the processing parameters of PGMA in 500 nm and 2  $\mu\text{m}$  channels were fabricated on 6" Si(100) wafers. A 100 nm SiO<sub>2</sub> diffusion barrier was thermally oxidised with 3% HCl, followed by sputtering a 100 nm Au layer between two 10 nm Cr adhesion layers. A ~500 nm SiO<sub>2</sub> layer for the channel structures was deposited by plasma enhanced chemical vapour deposition at 300°C and a 10 nm Cr hard mask was sputtered on top. Finally, a 400 nm layer of poly(methyl methacrylate) resist (AR-P 679.04, AllResist GmbH, Strausberg, Germany) was spin-coated and baked at 180°C for 5 min. The channels were patterned by electron beam lithography (Vistec SB254, Vistec GmbH) at kV using dose 650  $\mu\text{C}/\text{cm}^2$  and

developed for 60 s in a mixture of methyl isobutyl ketone and isopropanol (1:3), rinsed in isopropanol followed by deionised water and dried in an oven. The channel structures were etched through the Cr layer by reactive ion etching (FHR MS-200-2-AE) using a mixture of Cl<sub>2</sub> (100 sccm) and O<sub>2</sub> (30 sccm) for 150 s and then etched into the thick SiO<sub>2</sub> by inductively coupled plasma reactive ion etching (Oxford Plasmalab System 100, Oxford Instruments) using a mixture of CHF<sub>3</sub> (19 sccm) and C<sub>4</sub>F<sub>8</sub> (18 sccm) for ~3 min. The remaining Cr hard mask and Cr on the channel floor removed by dry-etching in oxygen plasma (R3T STP 2020, Muegge), leaving SiO<sub>2</sub> channel walls with Au channel floors. The samples were spin-coated a layer of 1% and 6% PGMA at 4000 rpm. PGMA (1%) patterns were defined by EBL (Voyager, Raith GmbH) at 50 kV using dose 12 μC/cm<sup>2</sup> and developed as described above. The resulting thickness of the PGMA on the flat surface and inside the channels was measured by AFM.

Samples for examining the etch rate of PGMA were fabricated on 10x10 mm Si (100) chips and spin-coated a layer of PGMA 1% at 4000 rpm. The samples were etched in oxygen plasma (Moorfield nanoETCH, Moorfield Nanotechnology Ltd) at 15 W for various times,  $t = 30-90$  s. The remaining thickness was measured by AFM.

#### *Atomic force microscope measurements*

The PGMA thickness in different channel widths and in scratches on flat surfaces was measured by atomic force microscopy (Bruker ICON, Bruker Co). The scans were obtained in tapping mode using a high aspect ratio (5:1) tip (TESPA-HAR 42 N/m, 320 kHz, Aluminium Reflective Coating). The scans were analysed in Gwyddion (GNU GPL developed by the Czech Metrology Institute).

#### *PNIPAM grafting*

COOH-terminated PNIPAM was grafted to the developed PGMA at elevated temperatures. Depending on the PGMA thickness, optimal grafting densities were usually achieved at 140-180°C. PNIPAM was dissolved at a concentration of 1 % (w/v) in chloroform. The surface of the chips was then completely covered with a droplet of the PNIPAM solution. After the chloroform evaporated, the chip was mounted overlapping two Peltier elements which were held at a temperature of 140°C and 180°C, respectively (**Figure 4A**). This assembly was placed in a desiccator and incubated for 1 h at 50-100 mbar pressure. Afterwards, the sample was rinsed with 70°C chloroform to remove unbound PNIPAM.

#### *Motility assay and data collection*

IVMA experiments were performed in flow cells made on glass coverslips (Menzel, 18×18 mm<sup>2</sup>). Two pieces of Parafilm were stretched out and placed on the structured side of the chips which in turn, were placed (face down) on the glass slide. The

entire flow cell was heated on a hot plate at 50°C while gently pressing on the chip to seal the sides with parafilm. The flow cells were incubated with a casein-containing solution (0.5 mg ml<sup>-1</sup>) in BRB80 for 5 min, followed by 10 min incubation with 5 µl of kinesin solution (4 nM full-length kinesin from *Drosophila*, expressed and purified as previously described<sup>25</sup>). Next, a solution (1 mM ATP, 20 mM D-glucose, 20 µg ml<sup>-1</sup> glucose oxidase, 10 µg ml<sup>-1</sup> catalase, 10 mM DTT, 10 µM taxol in BRB80) with rhodamine-labelled, taxol-stabilized microtubules (from porcine brain, prepared as previously described<sup>26</sup>) was added.

To image the fluorescently labelled microtubules we used an Axiovert 200M inverted optical microscope (Zeiss) with a Tetra methyl Rhodamine Iso-Thiocyanate filter set (Chroma Technology; Ex 535/50, DM 565, BA 610/75) and a Zeiss 40x 0.95 NA apochromat objective. The data was recorded at 0.5 frames/s (exposure time 100 ms) by an EMCCD camera (iXon+EMCCD, DU-897E, Andor) using the Metamorph imaging software (Universal Imaging Corp.).

## Results and discussion

### *PGMA processing in nanochannels*

The thickness of PGMA diluted in Anisole to 1% and 6%, was measured with AFM by scanning across a scratch made on a flat surface spin-coated with PGMA. The PGMA 1% was ~15 nm thick, while the PGMA 6% created a much thicker ~146 nm layer (**Figure 2a and b**). To prevent the filaments from encountering a large step in switchable areas, we wanted the PGMA to be as thin as possible. To examine how the two PGMA concentrations deposit inside channel structures we also measured the channel height before and after PGMA deposition (**Figure 2c and d**). On the structured samples, we observed a larger accumulation inside the channels for the higher concentration of PGMA 6%. In the narrower, 500 nm channels, the PGMA 6% was approximately 249 nm (measured channel width before PGMA deposition (532 nm) subtracted by the measured channel height after PGMA deposition (283 nm)) and approximately 126 nm. We also observed some accumulation of the thinner PGMA 1% inside the narrower channels (57 nm PGMA in 500 nm channels), but not inside the wider channels (13 nm PGMA in 2 µm channels). The exact thickness is, however, difficult to measure inside the channel structures due to possible AFM tip broadening effects. Nonetheless, the lower concentration PGMA 1% is preferred over the thicker 6% PGMA due to accumulation.

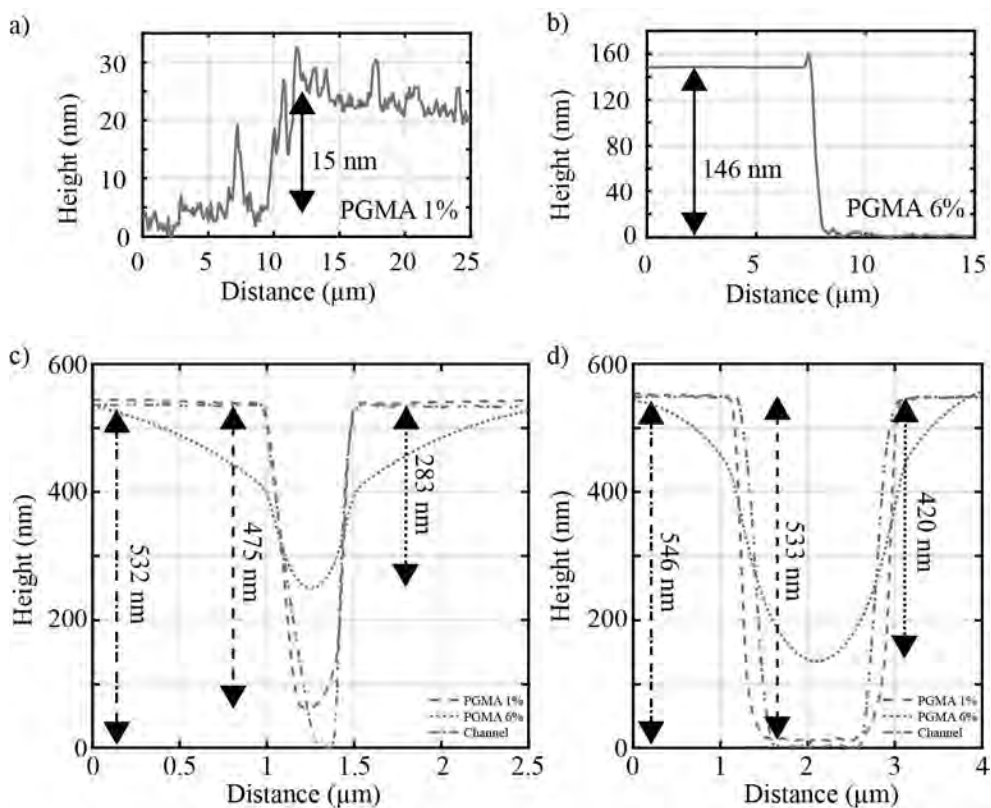


**Figure 2.** AFM profile scans of a) PGMA 1% and b) 6% across a scratch made on a flat surface to measure the PGMA film thickness. The spin-thickness inside a) 500 nm wide channels and b) 2  $\mu\text{m}$  wide channels were also measured for both PGMA 1% and PGMA 6%. The PGMA 6% accumulated in both channel widths, more in the narrower channel. The PGMA 1% deposited seemingly uniform inside the wider channel but showed some accumulation inside the narrower channel. Each scan profile is 50 px wide.

The guiding of microtubules is very dependent on the channel width, both in terms of filament flexibility<sup>22,27,28</sup> and depending on the microtubule-wall interaction<sup>22,23</sup>, where narrower channels improve the overall guiding<sup>22,29</sup>. To examine the processing parameters in a computational device with narrow channels (300 nm) we created a network encoding the subset sum problem, which in principle would switch between two number encodings (2, 3, 7) and (5, 7). The network design is seen in **Figure 3a**, as well as the areas patterned with PGMA (marked in green on the purple junctions seen in the insets). **Figure 3bc** shows an AFM of the PGMA thickness inside a test structure made with the same channel width as in the network. The measured PGMA thickness after EBL patterning in these 300 nm wide channels is  $\sim 27$  nm which is slightly lower than in un-patterned PGMA in the 500 nm wide channels (**Figure 2c**). It should be pointed out that the thickness is calculated from the height difference between patterned and un-patterned area. The enhanced

proximity increased the size of the pattern together with an extra residual film formed (7-8 nm) on both structured and unstructured SiO<sub>2</sub>, although other excess, un-exposed PGMA was removed during development. By considering the residual layer on the flat surface and clean channel depth 519 nm (before processing), the PGMA thickness is ~35 nm ((519+8)-492 = 35). The PGMA thickness can be further reduced by oxygen plasma treatment., and is a necessity to remove the residual un-exposed PGMA to prevent PNIPAM grafting across the entire surface.

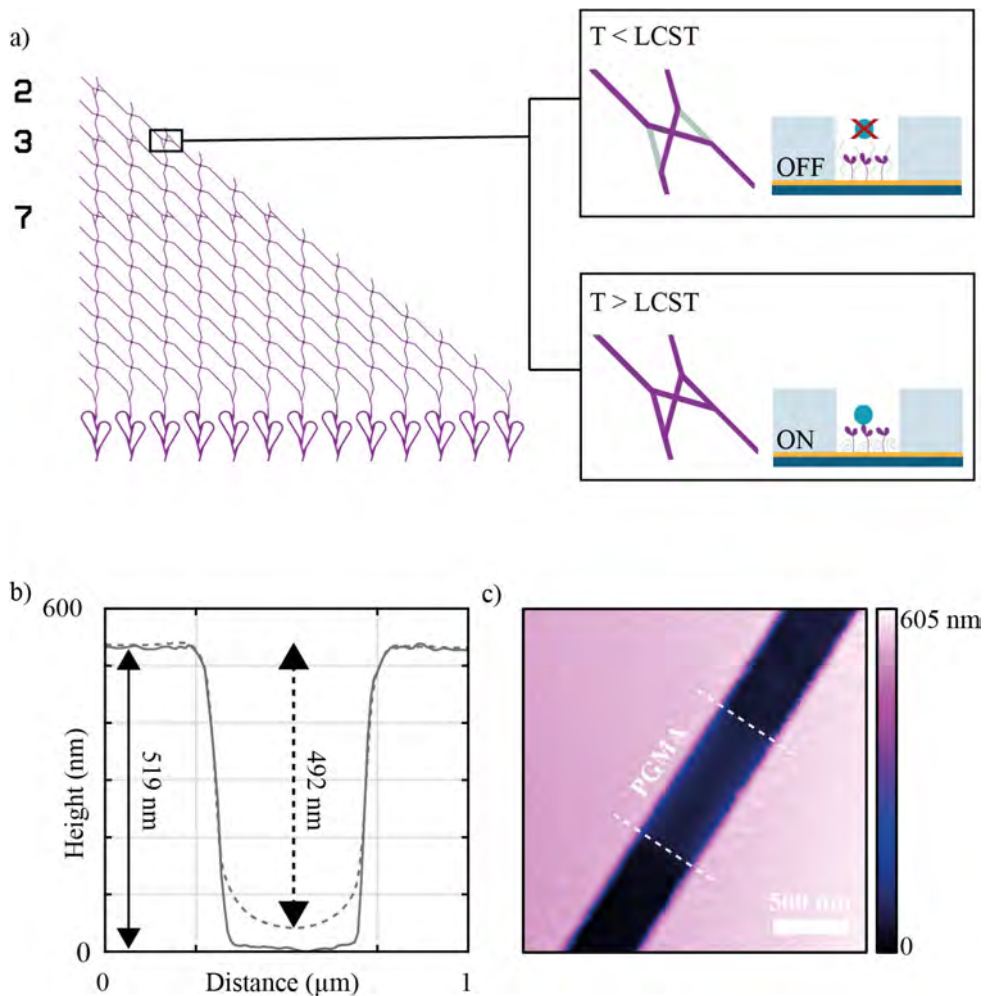


**Figure 3.** a) Network design for the subset sum problem network that would encode the number set (2, 3, 7) before switching and the number set (5, 7) after switching. The insets show how the PGMA/PNIPAM patches will change the possible pathways available to the filaments. b) AFM profile plot of the AFM scan in c) showing the PGMA (marked between white dashed lines) thickness inside a 300 nm wide channel.

### *Local switching on PGMA patches*

The local switching of motility was examined on  $98 \times 98 \mu\text{m}^2$  patches of PGMA grafted with PNIPAM. The PNIPAM grafting density is crucial for successful switching. The grafting density can be controlled by the temperature at which the grafting reaction occurs. Therefore, we constructed a temperature gradient stage (see **Figure 4A**) which allowed us to test a whole range of grafting temperatures on one sample, significantly reducing the load on sample manufacturing and improving the efficiency of protocol optimization. We found successful motility switching at two different grafting temperatures,  $140^\circ\text{C}$  and  $143^\circ\text{C}$ . The fluorescence micrographs in **Figure 4BC** show how motility is first inhibited when the temperature is below the LCST ( $25^\circ\text{C}$ , PNIPAM polymers are expected to be in their extended form), while in **Figure 4DE** when the temperature is above the LCST ( $35^\circ\text{C}$ , when PNIPAM is expected to collapse) the filaments can move across the entire surface. The PNIPAM grafting temperature is known to affect density<sup>16</sup>. If the density is too low, the motors will still be able to bind and propel filaments even when the PNIPAM is extended. However, if the PNIPAM density is too high, no motors will be able to bind to the surface and instead, the motility will be completely inhibited. A noticeable difference in **Figure 4** is that at the lower PNIPAM grafting temperature ( $140^\circ\text{C}$ ) seems to not be dense enough to completely block the motility as a few microtubules still appear in focus on the PGMA patch (although to a smaller extent than above the LCST). At the higher grafting temperature ( $143^\circ\text{C}$ ) however, slightly fewer microtubules are transported across the PGMA patch when  $T > \text{LCST}$ , indicating that the PNIPAM density might be slightly too high and could be tuned further.

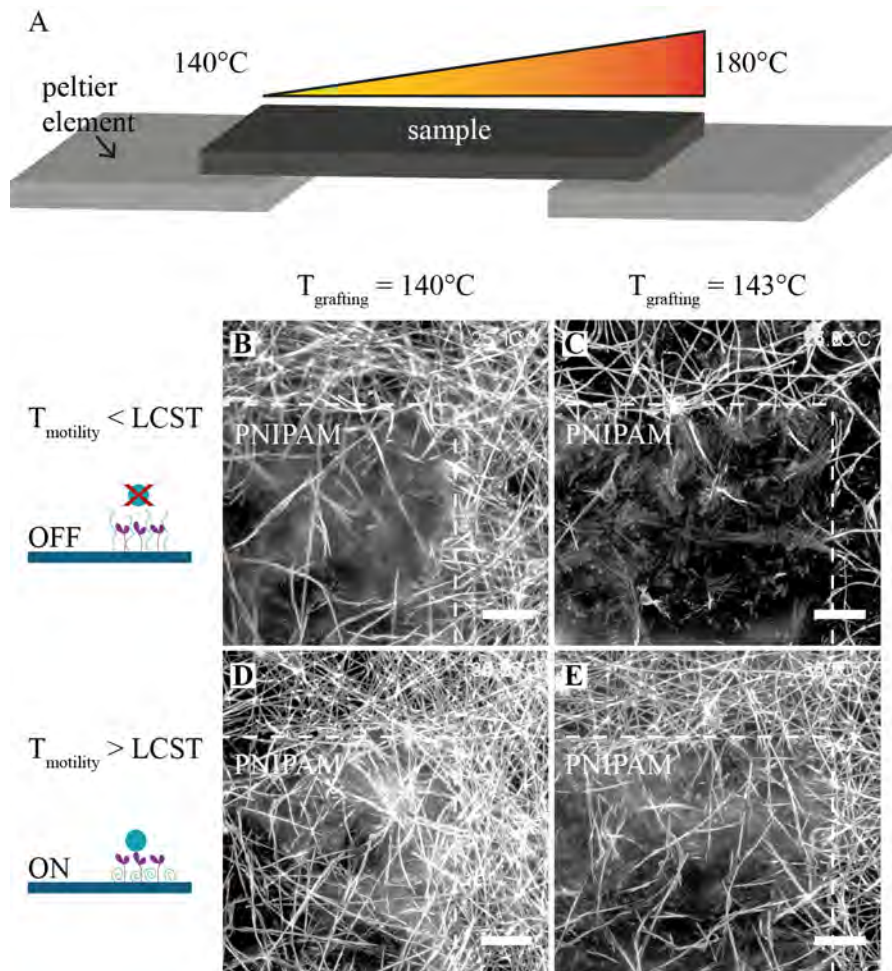


**Figure 4.** Local PNIPAM grafting. A) Sample layout and illustration of 140°C-180°C heat gradient used for PNIPAM grafting. B) The maximum projections of 85s long fluorescence micrograph corresponding to a PNIPAM grafting temperature of 140°C and C) 143°C. The effect of the extended PNIPAM repelling microtubules at D)  $T < LCST$  (25°C) and the collapsed PNIPAM permitting gliding at E)  $T > LCST$  is indicated by the lack- or presence of straight fluorescence traces on the PNIPAM patches. The scalebar is 20  $\mu\text{m}$  in all images.

## Conclusion

We describe a method for processing and patterning the negative tone polymer resist PGMA by electron beam lithography. By patterning PGMA we were able to demonstrate motility switching of the microtubule-kinesin system in local areas on patches grafted with PNIPAM. If implemented into computational devices, switchable motility could be used to program encodings to create versatile NBC problems. Furthermore, local control of motility could also be useful within

biosensing applications to tune the pathway of target analytes transported by molecular motors. Studies have shown<sup>30</sup> that the conformational changes of PNIPAM can also cause a change in the surface energy as measured by the water contact angle (WCA). Below the LCST, the WCA can be as low as 30°, while above the LCST the WCA can be tuned to up to ~90°. The slightly longer motor system heavy meromyosin II with a surface-to-filament distance ~38 nm<sup>31</sup>, is very sensitive to changes in the water contact angle<sup>32–34</sup>. Therefore, gating methods based on PNIPAM could potentially also be applied to other motor systems where motility switching could be achieved by switching the chemical property of the surface at the locations shown in **Figure 3a** (green) instead of by physically blocking the motors.

## Acknowledgements

Financially supported by the European Union's Horizon 2020 research and innovation programme under grant agreement No 732482 (Bio4Comp) and from NanoLund.

## References

1. Lin, C.-T., Kao, M.-T., Kurabayashi, K. & Meyhofer, E. Self-Contained, Biomolecular Motor-Driven Protein Sorting and Concentrating in an Ultrasensitive Microfluidic Chip. *Nano Lett.* **8**, 1041–1046 (2008).
2. Katira, P. & Hess, H. Two-stage capture employing active transport enables sensitive and fast biosensors. *Nano Lett.* **10**, 567–572 (2010).
3. Lard, M. *et al.* Ultrafast molecular motor driven nanoseparation and biosensing. *Biosens. Bioelectron.* **48**, 145–152 (2013).
4. Nicolau, D. V. J. *et al.* Parallel computation with molecular motor-propelled agents in nanofabricated networks. *PNAS* **113**, 2591–2596 (2016).
5. Bunk, R. *et al.* Actomyosin motility on nanostructured surfaces. *Biochem. Biophys. Res. Commun.* **301**, 783–788 (2003).
6. ten Siethoff, L. *et al.* Molecular motor propelled filaments reveal light-guiding in nanowire arrays for enhanced biosensing. *Nano Lett.* **14**, 737–742 (2014).
7. Månsson, A. Translational actomyosin research: Fundamental insights and applications hand in hand. *J. Muscle Res. Cell Motil.* **33**, 219–233 (2012).
8. Barclay, C. J. Estimation of cross-bridge stiffness from maximum thermodynamic efficiency. *J. Muscle Res. Cell Motil.* **19**, 855–864 (1998).
9. Korten, T., Månsson, A. & Diez, S. Towards the application of cytoskeletal

- motor proteins in molecular detection and diagnostic devices. *Curr. Opin. Biotechnol.* **21**, 477–488 (2010).
10. Kron, S. J. & Spudich, J. A. Fluorescent actin filaments move on myosin fixed to a glass surface. *Proc. Natl. Acad. Sci. U. S. A.* **83**, 6272–6276 (1986).
  11. Howard, J., Hudspeth, A. J. & Vale, R. D. Movement of microtubules by single kinesin molecules. *Nature* **342**, 154–158 (1989).
  12. Sheetz, M. P. & Spudich, J. A. Movement of myosin-coated fluorescent beads on actin cables in vitro. *Nature* **303**, 31–35 (1983).
  13. Kron, S. J., Toyoshima, Y. Y., Uyeda, T. Q. P. & Spudich, J. A. Assays for Actin Sliding Movement over Myosin-Coated Surfaces. *Methods Enzymol.* **196**, 399–416 (1991).
  14. Hess, H., Clemmens, J., Qin, D., Howard, J. & Vogel, V. Light-Controlled Molecular Shuttles Made from Motor Proteins Carrying Cargo on Engineered Surfaces. *Nano Lett.* **1**, 235–239 (2001).
  15. van den Heuvel, M. G., de Graaff, M. & Dekker, C. Molecular sorting by electrical steering of microtubules in kinesin-coated channels. *Science (80-. )*. **312**, 910–4 (2006).
  16. Ionov, L., Stamm, M. & Diez, S. Reversible switching of microtubule motility using thermoresponsive polymer surfaces. *Nano Lett.* **6**, 1982–1987 (2006).
  17. Schroeder, V., Korten, T., Linke, H., Diez, S. & Maximov, I. Dynamic Guiding of Motor-Driven Microtubules on Electrically Heated, Smart Polymer Tracks. *Nano Lett.* **13**, 3434–3438 (2013).
  18. Nath, N. & Chilkoti, A. Creating " 'Smart' Surfaces Using Stimuli Responsive Polymers. *Adv. Mater.* **14**, 1243–1247 (2002).
  19. Schild, H. G. POLY(N-ISOPROPYLACRYLAMIDE ): EXPERIMENT , THEORY AND APPLICATION. *Prog. Polym. Sci.* **17**, 163–249 (1992).
  20. Moorjani, S. G., Jia, L., Jackson, T. N. & Hancock, W. O. Lithographically patterned channels spatially segregate kinesin motor activity and effectively guide microtubule movements. *Nano Lett.* **3**, 633–637 (2003).
  21. Hiratsuka, Y., Tada, T., Oiwa, K., Kanayama, T. & Uyeda, T. Q. P. Controlling the direction of kinesin-driven microtubule movements along microlithographic tracks. *Biophys. J.* **81**, 1555–1561 (2001).
  22. Clemmens, J. *et al.* Mechanisms of microtubule guiding on microfabricated kinesin-coated surfaces: Chemical and topographic surface patterns. *Langmuir* **19**, 10967–10974 (2003).
  23. Hess, H. *et al.* Molecular Shuttles Operating Undercover: A New Photolithographic Approach for the Fabrication of Structured Surfaces

- Supporting Directed Motility. *Nano Lett.* **3**, 1651–1655 (2003).
24. Taniguchi, Y. *et al.* PGMA as a High Resolution , High Sensitivity Negative Electron Beam Resist. *Jpn J Appl Phys* **18**, 1143–1148 (1979).
  25. Korten, T., Chaudhuri, S., Tavkin, E., Braun, M. & Diez, S. Kinesin-1 Expressed in Insect Cells Improves Microtubule in Vitro Gliding Performance, Long-Term Stability and Guiding Efficiency in Nanostructures. *IEEE Trans. Nanobioscience* **15**, 62–69 (2016).
  26. Castoldi, M. & Popov, A. V. Purification of brain tubulin through two cycles of polymerization- depolymerization in a high-molarity buffer. *Protein Expr. Purif.* **32**, 83–88 (2003).
  27. Bunk, R. *et al.* Guiding motor-propelled molecules with nanoscale precision through silanized bi-channel structures. *Nanotechnology* **16**, 710–717 (2005).
  28. Clemmens, J. *et al.* Motor-protein roundabouts : Microtubules moving on kinesin-coated tracks through engineered networks. *Lab Chip* **4**, 83–86 (2004).
  29. Hess, H. *et al.* Ratchet patterns sort molecular shuttles. *Appl. Phys. A Mater. Sci. Process.* **75**, 309–313 (2002).
  30. Huber, D. L., Manginell, R. P., Samara, M. A., Kim, B.-I. & Bunker, B. C. Programmed adsorption and release of proteins in a microfluidic device. *Science (80-. )*. **301**, 352–354 (2003).
  31. Persson, M. *et al.* Heavy meromyosin molecules extending more than 50 nm above adsorbing electronegative surfaces. *Langmuir* **26**, 9927–9936 (2010).
  32. Hanson, K. L. *et al.* Polymer surface properties control the function of heavy meromyosin in dynamic nanodevices. *Biosens. Bioelectron.* **93**, 305–314 (2017).
  33. Albet-Torres, N. *et al.* Mode of heavy meromyosin adsorption and motor function correlated with surface hydrophobicity and charge. *Langmuir* **23**, 11147–11156 (2007).
  34. Lindberg, F. W. *et al.* Controlled Surface Silanization for Actin-Myosin Based Nanodevices and Biocompatibility of New Polymer Resists. *Langmuir* [acs.langmuir.8b01415](https://doi.org/10.1021/acs.langmuir.8b01415) (2018). doi:10.1021/acs.langmuir.8b01415



There is a broad range of applications for multivariable, combinatorial problems such as electronic circuit optimisation, drug development, cryptography and route optimisation, just to mention a few. These problems are very challenging to solve in a sequential manner, and instead, parallel computation methods become a necessity.

This thesis describes the development of several techniques used to expand the capabilities of parallel computation with molecular motors: how problems are encoded, the physical and chemical requirements and different architectural elements to optimise the system.

